AN EXPERIMENTAL AND COMPUTATIONAL INVESTIGATION INTO INTERMOLECULAR INTERACTIONS

Does the Bottom Effect the Top?

JACK MATTHEW LESLIE HENRY

UNIVERSITY OF LEEDS

Department of Physics and Astronomy

June 2022

Submitted in accordance with the requirements for the degree of

Doctor of Philosophy

The candidate confirms that the work submitted is his own and that appropriate credit has been given where reference has been made to the work of others.

SUPERVISORS:
Dr Adam Sweetman
Prof Stephen Evans

EXPERIMENTAL MENTOR:
Dr Philip Blowey

COMPUTATIONAL MENTOR:
Dr Shashank S. Harivyasi

"You're not the only one cursed with knowledge."

— Thanos, Infinity War (2018). Acquisition of the Time Stone.

"Perfectly balanced, as all things should be."

— Thanos, Infinity War (2018). Thanos during his adoption of Gamora, Daughter of Thanos.

Too far to the experimental side, and additional knowledge from a computational investigation may be missed. Too far to the computational side, and the simulated systems risk entering the purely hypothetical realm.

ABSTRACT

Decades of surface science studies on adsorbed molecules have shown the surface a molecule is adsorbed on can effect the molecule's electronic and geometric structure [1]. However, the change in reactivity of a single molecule, induced by the presence of a surface, has not been rigorously investigated.

In this work, the influence of molecule-substrate bonding on the interactions experienced by a Scanning Probe Microscopy (SPM) tip were investigated both experimentally and computationally. Non-Contact Atomic Force Microscopy (NC-AFM) experiments were performed under Ultra-High Vacuum (UHV) conditions at $5\,K$, and reinforced with complementary atomistic *ab initio* Density Functional Theory (DFT) simulations of Simulated Non-Contact Atomic Force Microscopy ($_s$NC-AFM) to gain a deeper understanding of the studied system.

A system comprised of C_{60} molecules adsorbed on the Cu(111) surface was selected for this work as it provides an ideal system for investigating the effects of molecule-substrate bonding. Previous work on this system has shown the C_{60}-Cu(111) interface can be controlled to form two distinct structures, with quantifiable differences in the geometric and electronic properties of the interface [2][3]. Furthermore, the molecules in both structures regularly adsorb in the same orientation [4]. This allows any difference in the interaction between the tip and the adsorbed C_{60} molecules to be attributed to differences in the molecule-substrate bonding, rather than differences in the presenting face of the adsorbed C_{60} molecule. Previous work has also investigated the use of C_{60} functionalized tips. The studies have shown C_{60} functionalized tips to be stable and passivized relative to metallic tips [5][4]. This provided the opportunity for this work to investigate the C_{60}-Cu(111) interface using both reactive Copper tips and C_{60} functionalized tips.

In the computational side of this work, developments in Simulated Non-Contact Atomic Force Microscopy ($_s$NC-AFM) were made. It was discovered multiple methods exist to calculate the force and potential spectra from the converged Fritz Haber Institute *ab initio* molecular simulations (FHI-aims) DFT simulations. Where the choice of method can have significant effects on the $_s$NC-AFM spectrum, affecting how analogous the $_s$NC-AFM is to the Experimental Non-Contact Atomic Force Microscopy ($_e$NC-AFM). Furthermore, it was deduced the use of periodic boundary conditions to accurately represent a metallic surface can lead to systematic overestimation of the $_s$NC-AFM spectra. Therefore theory for a periodicity correction was developed.

ACKNOWLEDGMENTS

I would like to give a huge thank you to my supervisory team, Dr Adam Sweetman and Prof Steven Evans, my mentors, Dr Shashank S. Harivyasi and Dr Phillip Blowey, and my colleges, Dr Tim Brown and Dylan Barker. We faced a multitude of challenges outside of our control, involving poorly constructed yet crucial equipment, the effects of the pandemic and social distancing measures, and chronic illness suffered by both myself and members of my supervisory team. Without our light-hearted approach to challenging situations, and our general ability to adapt and move forwards, the completion of this PhD would not have been possible.

I would like to thank my examination team, comprised of Dr Joseph Barker and Dr Samuel P. Jarvis, and many members of staff from the University Of Leeds, for their support and understanding. We worked together to create an examination process which was both fair, and allowed someone of my unprecedented limitations to complete the oral examination of a PhD.

Finally, I would also like to give a huge thank you to my parents, Sue Leslie and Nick Henry, and my sister, Louise Henry. Without their unwavering support throughout the duration of my PhD, especially in the later years as my caregivers, this PhD would not have been possible.

Thank you to everyone who has helped me, lets not do this again.

CONTENTS

AFM Atomic Force Microscopy

NC-AFM Non-Contact Atomic Force Microscopy

$_e$NC-AFM Experimental Non-Contact Atomic Force Microscopy

$_s$NC-AFM Simulated Non-Contact Atomic Force Microscopy

a_{Cu} lattice constant of the Copper FCC Bravais Lattice unit cell

C-C a single bond between two Carbon atoms

C=C a double bond between two Carbon atoms

C6 pairwise power law corresponding to $n = 6$ ($C_6 R^{-6}$)

C3 pairwise power law corresponding to $n = 3$ ($C_3 R^{-3}$)

C_{3v} 120° rotational symmetry with three vertical mirror planes containing the axis of rotation

C_3 120° rotational symmetry with no mirror planes

C_{60} the Buckminsterfullerene allotrope of Carbon comprised of 60 Carbon atoms

$C_{60,u}$ C_{60} adsorbed on the unreconstructed Cu(111) surface

$C_{60,r}$ C_{60} adsorbed on the 7 atom vacancy Cu(111) surface reconstruction

$C_{60,g}$ a gaseous C_{60} molecule

C_{60}-h a C_{60} molecule oriented to present a hexagonal face

C_{60} Tip C_{60} functionalized AFM tip

Cu Tip copper functionalized AFM tip

CO Tip CO functionalized AFM tip

Cu(111)-(4x4) A semi infinite copper slab (periodic along the a and b directions) cleaved along the (111) plane (defined using miller indices). The unit cell vectors a and b have length $a = b = 10.2700$Å, allowing for 4 Cu atoms along the a and b directions of the unit cell. Unit vector $c = 100$Å, resulting in most of the unit cell being vaccum space. The number of atomic layers along the vertical direction varies from n=3 to n=15, where n denotes the number of complete layers in the slab

Cu(111)-fcc a face centred cubic hollow site on the Cu(111) surface

Cu_u unreconstructed copper (111) surface

Cu_r reconstructed copper (111) surface

DFT Density Functional Theory

D3 Grimme's D3

et al and other authors

FCC Face Centered Cubic

FHI-aims Fritz Haber Institute *ab initio* molecular simulations

FHI-aims-SE Fritz Haber Institute *ab initio* molecular simulations System Energy method

FHI-aims-TF Fritz Haber Institute *ab initio* molecular simulations Tip Forces method

FHI-aims-SF Fritz Haber Institute *ab initio* molecular simulations Surface Forces method

HPA Hirshfeld Population Analysis

$H_2O@C_{60}$ H_2O contained within a C_{60} molecule

$H_2O@C_{60,u}$ the $H_2O@C_{60}$ molecular complex adsorbed on the Cu_u surface

$H_2O@C_{60,r}$ the $H_2O@C_{60}$ molecular complex adsorbed on the Cu_r surface

$H_2O@C_{60,g}$ the $H_2O@C_{60}$ molecular complex in a gaseous state

$H_2O@C_{60}$-h hexagonal face of a $H_2O@C_{60}$ molecule

HOMO Highest Occupied Molecular Orbital

KS Kohn-Sham

LSS FHI-aims 2010 default Light Species Settings

LSA Large Separation Approximation

LUMO Lowest Unoccupied Molecular Orbital

LT Low Temperature

MBD Many Body Dispersion

MPA Mulliken Population Analysis

On-Curve NC-AFM spectra taken over a site of interest

Off-Curve NC-AFM spectra taken over the (usually unperturbed) substrate to remove the long range background interaction

OVITO A scientific visualization and data analysis solution for atomistic and other particle-based models

PBE Perdew–Burke–Ernzerhof

SPM Scanning Probe Microscopy

STM Scanning Tunnelling Microscopy

STS Scanning Tunnelling Spectroscopy

TSS FHI-aims 2010 default Tight Species Settings

TS Tkatchenko-Scheffler vdW and vdW^{surf}

UHV Ultra-High Vacuum

vdW van der Waals

xc exchange-correlation

$_e$Tip experimental NC-AFM tip comprised of the Microscopic Tip Base ($_e$MTB) and the Nanoscopic Tip Apex ($_e$NTA)

$_e$Sample experimental NC-AFM sample comprised of the Bulk Surface ($_e$BS) and the Adsorbed Molecule ($_e$AM),if one is present

$_e$MTB Microscopic Tip Base

$_e$NTA Nanoscopic Tip Apex

$_e$BS Bulk Surface

$_e$AM Adsorbed Molecule

$_s$Tip $_s$NC-AFM tip

$_s$Surface $_s$NC-AFM surface

$_s$Tip Base the metal section of the $_s$NC-AFM tip, which can be further functionalized with additonal molecules (such as C_{60}, CO, or Cu tip apex)

$_s$Tip Molecule the molecule adsorbed on the functionalized $_s$Tip Base

$_s$Tip Apex the atoms in the $_s$Tip involved in short range interactions with the $_s$Surface

$_s$Surface Base the underlying surface, analogous to the experimental surface

$_s$Surface Molecule the molecule adsorbed on the underlying surface, analogous to the deposited molecule in an experiment

$_s$Surface Apex the atoms in the $_s$Surface involved in short range interactions with the $_s$Tip

$_s$Tip-Sample Junction the region of the system where the $_s$Tip Apex and the $_s$Surface Apex interact

Intra-Cellular the interactions between groups of atoms occurring within a Cluster Calculation, or the original unit cell of a Periodic System

Inter-Cellular the interactions between groups of atoms in a Periodic System, where one of the interacting groups exists in the original unit cell, and the other group of atoms exists in the periodic replications of the unit cell

PT-OS periodic replications of the $_s$Tip interacting with the original $_s$Surface

PS-OT periodic replications of the $_s$Surface interacting with the original $_s$Tip

TB-SM interaction between the original $_s$Tip Base and the original $_s$Surface Molecule

TM-SM interaction between the original $_s$Tip Molecule and the original $_s$Surface Molecule

TB-SB interaction between the original $_s$Tip Base and the original $_s$Surface Base

TM-SB interaction between the original $_s$Tip Molecule and the original $_s$Surface Base

TB_{PBC}-SM the interaction between the periodic replications of the $_s$Tip Base and the original $_s$Surface Molecule

TM_{PBC}-SM the interaction between the periodic replications of the $_s$Tip Molecule and the original $_s$Surface Molecule

TB_{PBC}-SB the interaction between the periodic replications of the $_s$Tip Base and the original $_s$Surface Base

TM_{PBC}-SB the interaction between the periodic replications of the $_s$Tip Molecule and the original $_s$Surface Base

TB-SM_{PBC} the interaction between the original $_s$Tip Base and the periodic replications of the $_s$Surface Molecule

TM-SM_{PBC} the interaction between the original $_s$Tip Molecule and the periodic replications of the $_s$Surface Molecule

TB-SB_{PBC} the interaction between the original $_s$Tip Base and the periodic replications of the $_s$Surface Base

TM-SB_{PBC} the interaction between the original $_s$Tip Molecule and the periodic replications of the $_s$Surface Base

Part I

EXPERIMENTAL INVESTIGATION

"Reality is often disappointing."

— Thanos, Infinity War (2018). Acquisition of the Reality Stone.

1 SCANNING PROBE MICROSCOPY

The field of Scanning Probe Microscopy (SPM) was founded by G.Binnig and H.Rohrer with the invention of the Scanning Tunelling Microscope (and the Scanning Tunnelling Microscopy (STM) technique) in the 1981 paper *'Tunnelling through a controllable vacuum gap'* [6]. The potential of STM to image surfaces was later demonstrated in 1982, with images of Au(110) and Si(111) surfaces containing visible atomic scale terraces [7]. Interest in the STM technique further increased when the technique's atomic scale resolution was demonstrated on the Si(111)-7x7 surface reconstruction, helping to end a longstanding debate on the reconstructed surface structure [8]. Since the invention of the STM, various new SPM techniques have been developed. The most notable being the Atomic Force Microscopy (AFM) [7]. Of the various SPM techniques AFM is one of the most widely used along side STM. Furthermore, the history of AFM is closely linked to that of STM, as AFM was conceived when Binnig realised the STM tip was experiencing measurable forces as it interacted with the the surface being scanned. Traditionally, the main limitation of the STM is it can only image on conducting surfaces. Whereas AFM provides an imaging technique for use with insulating surfaces as well as conducting ones.

1.1 SCANNING TUNELLING MICROSCOPY

STM is a SPM technique which uses electron tunnelling to generate image contrast. A metallic tip, ideally atomically sharp, approaches the sample surface. This creates two electron reservoirs, separated by a vacuum gap (a potential barrier). At small enough tip sample separations, electrons are able to quantum mechanically tunnel between atoms in the tip and atoms in the sample, producing a measurable current (the tunnel current). The applied bias between the tip and sample determines whether the electrons tunnel into or out of the tip. Furthermore, larger biases allow electrons to simultaneously tunnel into and out of a greater range of orbitals, thereby increasing the tunnel current. The tunnel current is exponentially proportional to the tip-sample separation, a relationship which allows STM to achieve atomic resolutions because it ensures only the tip apex atom(s) will contribute to the image contrast in an atomically sharp tip. Therefore, the image produced is very sensitive to movement of the tip in the Z direction, and the topology of the sample, as these factors effect the tip sample separation. To produce an image, the tip scans across the surface in a plane parallel to the surface, and the tip position in

the Z direction is adjusted. The Z position of the tip is controlled by a feedback loop which, analyses the tunnel current in real time **(see Section 1.1.1)**. As with all SPM techniques, the pixels in the image are taken serially in a raster pattern, rather than in parallel. This can become an issue as it enables drift; movement of the sample relative to the original scan origin during the scan [9]. Much of the theory behind image formation in STM with a metallic tip was developed by Tersoff and Hamann in the 1980s [10], who based their approach off the research carried out on multi-electron tunnelling between two reservoirs by J.Bardeen in 1960 [11].

1.1.1 *Image Contrast in Scanning Tunelling Microscopy*

Image contrast can be produced in a variety of ways while performing STM. In constant height mode the tip is scanned along the XY plane, parallel to the plane of the surface. In this mode, the image contrast comes directly from variations in the tunnel current. A drawback to this method is the tip can easily crash into the surface due to thermal drift and piezo creep, or while imaging large topological features (see black arrow in **Figure 1.1**). This limits constant height STM to imaging on very flat surfaces, however, feedback loops are not needed. To image surfaces containing features with relatively large protrusions, while also avoiding tip-sample crashes, constant current mode can be used. This method obtains image contrast from the height of the tip, and feedback loops adjust said height to maintain a constant current (see red arrow in **Figure 1.1**). When applying Tersoff Hamann theory to STM constant current images, the images can be interpreted as proportional to a contour map of constant local density of states of the sample [10]. Although STM is a key tool in surface science, it is only capable of probing the electronic structure of the sample. This is an important distinction as the electronic structure of the sample may not strongly resemble the geometric structure. An example of this phenomena is the ability to image electron standing waves on noble metals [12].

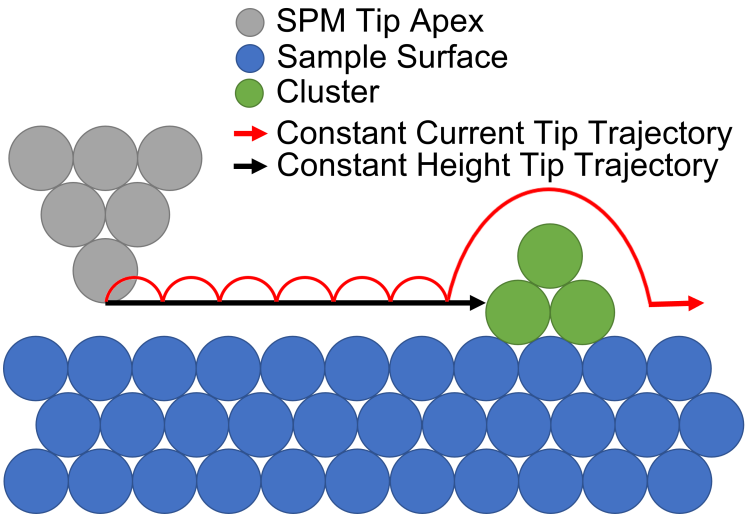

Figure 1.1: Representations of SPM tip trajectories for constant current and constant height imaging modes. Grey circles represent atoms forming the $_e$NTA, blue circles represent atoms forming an atomically flat metallic surface, green circles represent metal atoms forming a cluster protruding from the surface. The red and black arrows represent the tip trajectory in the constant current and constant height imaging modes.

1.2 ATOMIC FORCE MICROSCOPY

The invention of the AFM allowed insulating surfaces to be probed on the atomic scale with SPM techniques. AFM enabled this ability as the contrast in AFM comes from the forces acting on the tip, rather than an electrical current (which requires conducting materials). The earliest Atomic Force Microscopes used an aluminium foil cantilever with a diamond tip, and a STM tunnel current to measure the cantilever displacement [13].

1.2.1 *Atomic Force Microscopy Operating Modes*

There are three main operating modes for AFM. Contact mode, Non-Contact Atomic Force Microscopy (NC-AFM), and tapping mode. In contact mode AFM the cantilever deflection, and so the force acting on the cantilever, remain approximately constant throughout the imaging process. Therefore, the image is a contour of constant force. However, this imaging technique suffers from relatively large lateral frictional forces, which can deform the sample. Additionally, contact mode AFM suffers from snap to contact [14]. The snap-to-contact effect occurs during the attractive regime, when the interaction force gradient is larger than the cantilever spring constant (stiffness). When this condition is met, the cantilever deflection rapidly increases as the cantilever is deflected towards the surface. This poses a problem for two reasons;

The process can destroy the Nanoscopic Tip Apex ($_e$NTA), and a region of attractive interaction between the $_e$Tip and the $_e$Sample becomes inaccessible to the experiment. Where we define $_e$Tip as experimental NC-AFM tip comprised of the Microscopic Tip Base ($_e$MTB) and the Nanoscopic Tip Apex ($_e$NTA) ($_e$Tip), and $_e$Sample as experimental NC-AFM sample comprised of the Bulk Surface ($_e$BS) and the Adsorbed Molecule ($_e$AM),if one is present ($_e$Sample). Furthermore, the attractive interaction made inaccessible by snap-to-contact is often of scientific high interest. Therefore, the use of contact mode AFM is limited to imaging strongly bound materials, such as ionic crystals, and dynamic methods such as NC-AFM were developed to investigate samples with greater sensitivity.

To regularly achieve sub molecular and atomic resolution, modern techniques such as NC-AFM are performed. To obtain the highest resolution, NC-AFM is regularly performed under Ultra-High Vacuum (UHV) and Low Temperature (LT) conditions. Using UHV-LT-AFM, it is possible to resolve the individual atomic bonds in organic molecules, on a variety of surfaces. Furthermore, this technique has been applied to identify the chemical structure of molecules adsorbed on a surface [1][15][1][16][17][18][19][20].

LT conditions are often used in NC-AFM experiments as the signal to noise ratio influences the resolution of data, and is strongly dependent on temperature. NC-AFM apparatus are regularly cooled by liquid nitrogen down to $77\,K$, or by liquid helium down to $5.7\,K$, however experiments been carried out at temperatures in the mK regime. Further advancements in the NC-AFM field have extended the ability of the technique to identify the chemical structure of adsorbed molecules at room temperature [19][21].

1.2.2 *NC-AFM Imaging Modes*

In Non-Contact Atomic Force Microscopy (NC-AFM) the tip of the cantilever oscillates above the sample, reducing the forces acting on the tip apex and sample, allowing the tip apex and sample structures to be preserved over multiple scans. There are two modes for imaging with NC-AFM, amplitude modulation mode and frequency modulation mode. In amplitude modulation mode the cantilever oscillates near it's resonant frequency, and changes in the amplitude of oscillation are mapped to produce image contrast. In frequency modulation mode, the cantilever oscillates at it's resonant frequency, and changes in the resonant frequency of the cantilever are measured to produce image contrast [22]. In this situation, changes in resonant frequency of the cantilever are induced by changes in forces acting on the AFM tip as it interacts with the sample. For small oscillation amplitudes we can describe the frequency shift as proportional to the force gradient experienced by the tip, however this is a first order approximation

which breaks as the oscillation amplitude increases. In this regime, the images produced by NC-AFM can be interpreted as maps of the vertical force gradient ($\frac{dF_z}{dz}$) experienced by the tip [23].

In NC-AFM, images are often take in constant current mode. However, this approach can result in the tip colliding with protrusions on the surface **(see Figure 1.1)**, or drifting towards (or away) from the surface over time. To tackle these issues, NC-AFM experiments have been performed which utilize feedback loops, the advantage being the feedback loops regulate the tip-sample separation during NC-AFM imaging. Two main approaches for this type of NC-AFM imaging exist, STM constant current [24][25], and NC-AFM constant frequency shift [26]. A drawback to taking NC-AFM images in feedback modes becomes apparent when interpreting the images. The NC-AFM image contrast is a convolution of the varying tip height, and corrugation of the sample. Furthermore, when using STM feedback, the corrugation of the sample measured STM is not necessarily analogous to the corrugation of the sample measured by NC-AFM.

1.2.3 *The qPlus Sensor*

Quartz tuning forks were initially introduced as an alternate cantilever material to silicon, the benefits being the tuning fork's high spring constant, and the piezoelectric properties of quartz. The high spring constant allows a low oscillation amplitude to be used, and the piezoelectric properties of quartz allow the tuning fork to be both self driving, and measure it's own oscillation amplitude (self-sensing). The self-sensing property of the quartz tuning fork removes the need for a diode laser system to track the movement of the cantilever [27].

Development of the qPlus quartz tuning fork cantilever yielded the first atomic resolution images obtained with NC-AFM whilst using a quartz tuning fork setup [14]. A key advancement made with the qPlus technique was the process of gluing the prong (without the tip) onto a custom made substrate. The qPlus experimental setup is well suited to NC-AFM performed under UHV and LT conditions as the eigenfrequency of the quartz cantilever can be assumed to be constant within the temperature range of $0\,K$ to $298\,K$ [28]. However, the qPlus quartz tuning fork still has its drawbacks, mainly in the inconsistency from sensor to sensor. The amount of epoxy used to attach the tip to the free prong, as well as the position of the tip on the prong, and mass of the tungsten tip itself, can have large effects on the change in resonant frequency of the tuning fork when the tip is added. As a result, in an ideal experiment the resonant frequency and spring constant of each individual qPlus tuning fork needs to be individually determined. This becomes an issue when quantitative NC-AFM measurements need to be made, as both the resonant frequency and cantilever stiffness can affect the measured force value. Therefore, research into the production of

qPlus tips with reliable and known spring constants has been carried out [29].

1.3 FORCE MEASUREMENTS IN NC-AFM

Measuring and investigating the forces present in an NC-AFM experiment is non-trivial feat. There are multiple forces present in an NC-AFM experiment, each causing the tip to interact with the surface in a unique way. Some of these interactions are desired, others not. Furthermore, in frequency modulation NC-AFM the force can not be measured directly, and is instead calculated from a measurable quantity defined as the frequency shift. In **Section 1.3**, the origins and types of tip-sample interactions shall be described. This is followed by the description of a simple mathematical model which describes the origin of the frequency modulation NC-AFM frequency shift. Furthermore, the approach used in this work to calculate the force from the frequency shift is detailed.

1.3.1 *Force Origins*

The interactions investigated with NC-AFM can be broken down into four main groups; Pauli repulsive, van der Waals (vdW), chemical, electrostatic, and magnetic. Pauli repulsive and vdW interactions are widely known from the Lennard Jones potential, which models the interaction between two inert atoms. In **Equation 1.1**, the Lennard Jones potential has been defined in terms of the depth of the potential well (ϵ_{LJ}, dimensions energy), and the equilibrium bond length, which we define as the coordinate at which the potential passes through zero (σ_{LJ}, dimensions length);

$$U_{LJ}(r) = 4\epsilon_{LJ}\left[\left(\frac{\sigma_{LJ}}{r}\right)^{12} - \left(\frac{\sigma_{LJ}}{r}\right)^{6}\right]. \tag{1.1}$$

In **Equation 1.1**, r is the inter-atomic separation, and $U_{LJ}(r)$ is the value of the Lennard Jones potential at the inter atomic separation r (dimension energy). In **Equation 1.1**, the Pauli repulsive interaction (between two atoms) is modeled with an r^{-12} power law, and the vdW interaction (between two atoms) is modeled with an r^{-6} power law. The difference in the power laws is particularly significant in NC-AFM. The vdW interaction between the tip and sample occurs over larger tip-sample separations than the repulsive Pauli interaction due to the difference in the power laws. Furthermore, as the numbers of interacting atoms increase, the order of the power law modeling the vdW interaction decreases, further increasing the length scale over which the tip and sample will experience an attractive interaction [30].

When two atoms interact through chemical bonding, the depth of the potential well is larger, and the attractive interaction grows more

rapidly as z decreases, therefore making the Lennard Jones potential less applicable. The Morse potential is another simple model, used to describe two atoms interacting via chemical bonding;

$$U_{Morse}(r) = \epsilon_{Morse}\left[e^{-2\lambda(r-\sigma_{Morse})} - e^{-\lambda(r-\sigma_{Morse})}\right]^2, \tag{1.2}$$

where $U_{Morse}(r)$ is the value of the Morse potential at the inter atomic separation r, ϵ_{Morse} is the depth of the potential well, σ_{Morse} is the equilibrium bond length, and λ is the inverse decay length which controls the width of the potential well. The simplest form of an electrostatic interaction is given by Coulombs law, which models the electrostatic interaction between two point charges,

$$F(r) = \frac{k_e q_1 q_2}{r^2}. \tag{1.3}$$

Where r is the distance between two interaction point charges, $F(r)$ is the magnitude of the force acting between the interacting charges at a separation r, q_1 and q_2 are the charges, and k_e is Coulomb's constant. However, the electrostatic interaction within an NC-AFM experiment is more complex. The bias used to produce a tunnel current image **(see Section 1.1)** can produce a relatively large electrostatic interaction between the tip and the sample [31][32][4]. In addition, the tip apex can contain much smaller scale dipoles, which also interact with the surface. A well known example is the *CO* terminated tip [33][18].

Chemical interactions can be defined as the NC-AFM tip forming a chemical bond with the surface. As this interaction arises from bond formation, it is an attractive interaction which occurs on a much shorter length scale than the electrostatic and vdW interactions. However, the presence of strong chemical interactions is not always desired. Therefore, NC-AFM tips are regularly passivated to reduce this interaction. Common examples being the *CO* [1][16] and C_{60} functionalized tips [34][35][36][37][38][5][4][3]. Magnetic forces were not investigated in this work, and were not a significant component of the total tip-sample interaction in the systems studied in this work.

1.3.2 *Frequency Modulated Atomic Force Microscopy*

In NC-AFM, the force is not measured directly. Instead, in the case of frequency modulation NC-AFM, changes to the resonant frequency of the cantilever are recorded. In this situation, changes in resonant frequency of the cantilever are induced by changes in forces acting on the AFM tip as it interacts with the sample, thereby allowing the force to be recovered from the frequency shift. This change in resonant frequency is measured using a phase-locked loop, and can be converted to a force measurement through algorithms such as the Sader-Jarvis algorithm (**Section 1.3.2.1**, the approach used in this work), the MATRIX algorithm, or the small angle approximation. In this work, frequency

modulation NC-AFM was used exclusively with the Sader-Jarvis force inversion. The following section details the process of obtaining force measurements in frequency modulation NC-AFM from the measured frequency shift.

The AFM tip-cantilever system, oscillating out of contact with the surface, can be modeled as a driven harmonic oscillator, described by **Equation 1.4**

$$f_0 = \frac{1}{2\pi}\sqrt{\frac{k_c}{m_{eff}}}. \tag{1.4}$$

Where f_0 is the resonant frequency of the cantilever, k_c is the spring constant of the cantilever, and m_{eff} is the effective mass of the cantilever[1]. As the tip approaches (and interacts with) the surface, an additional force acting between the tip and the sample is experienced by the tip (F_{ts}). The addition of this interaction can be modeled through an adjustment to **Equation 1.4** by modifying k_c;

$$f_0 + \Delta f = \frac{1}{2\pi}\sqrt{\frac{k_c + k_{ts}}{m_{eff}}}, \tag{1.5}$$

where k_{ts} is the spring constant modification term which describes the tip-sample force F_{ts}, and Δf is the change in resonant frequency of the cantilever system caused by the tip-sample interaction (the frequency shift).

At this point we apply an approximation known as the *small amplitude approximation*, where we assume k_{ts} is constant over the full z range of the cantilever oscillation. With this approximation, we can utilize the fact that k_{ts} is a spring constant, and so can be expressed as differentials of corresponding force (F_{ts}) and potentials (U_{ts}), shown in **Equation 1.6**

$$k_{ts} = -\frac{\partial F_{ts}}{\partial z} = \frac{\partial^2 U_{ts}}{\partial z^2}. \tag{1.6}$$

We can make a further simplification through knowing $k_{ts} << k_c$, and thus expand $\sqrt{k_c + k_{ts}}$ in **Equation 1.5** as a Taylor series. From there, we can substitute **Equation 1.6** into **Equation 1.5**, and arrive at **Equation 1.7**

$$\Delta f \simeq \frac{-f_0}{2k_c}\frac{\partial F_{ts}}{\partial z}. \tag{1.7}$$

Equation 1.7 demonstrates how the *measured* frequency shift of the cantilever is related to the *gradient* of the force, rather than the force itself. The small amplitude approximation was first demonstrated by Giessibl and other authors (*et al*) 1997 [39]. It can be phrased in many

1 The effective mass (m_{eff}) corrects for the mass being distributed along the length of the spring (cantilever), allowing us to model the system as if the mass exists at the end of the spring (cantilever).

ways; the assumption the tip-sample separation (at closest approach) is much larger than the oscillation amplitude ($z_0 >> a$) [39], the assumption the tip-sample forces are constant over the whole z range of a cantilever oscillation [23], or that $k_{ts} << k_c$ (as detailed above).

In addition to linking the force and frequency shift in the small amplitude regime, Giessibl also derived **Equation 1.8**, a more general relationship between the force and frequency shift .

$$\Omega(z) = \frac{\Delta f}{f_0} = -\frac{1}{\pi a k_c} \int_{-1}^{1} F_{ts}\left[z_0 + a\left(1+u\right)\right] \frac{u}{\sqrt{1-u^2}} du, \tag{1.8}$$

Where a is the amplitude of oscillation, z_0 is the distance of closest approach between tip and sample, and the substitution $u = cos\varphi$ was performed.

1.3.2.1 *Sader-Jarvis Inversion*

Equation 1.8 provides the groundwork for calculating the force from the frequency shift. However, it needs to be inverted to arrive at a general formula for calculating the force (F_{ts}) from the experimentally measurable frequency shift (Δf). Starting from **Equation 1.8**, Sader and Jarvis derived a general formula for calculating the force **(Equation 1.9)** and **(Equation 1.9)** potential from the frequency shift [40][41];

$$F(z) = 2k_c \int_{z_0}^{\infty} \left(1 + \frac{a^{1/2}}{8\sqrt{\pi(t-z_0)}}\right) \Omega(t) - \frac{a^{3/2}}{\sqrt{2\left(t-z_0\right)}} \frac{d\Omega(t)}{dt} dt, \tag{1.9}$$

and

$$U(z) = 2k_c \int_{z_0}^{\infty} \Omega(t) \left((t-z_0) + \frac{a^{1/2}}{4}\sqrt{\frac{t-z_0}{\pi}} + \frac{a^{3/2}}{\sqrt{2\left(t-z_0\right)}}\right) dt, \tag{1.10}$$

where t is the tip-sample separation, which is integrated over z_0 (the point of closest approach) to ∞, and $\Omega(t)$ is $\Omega(z)$ from **Equation 1.8**. In this work, the potential was calculated from the frequency shift using **Equation 1.10**, then differentiated to calculated $F(z)$. A key success of **Equations 1.9 & 1.10** is their ability to reproduce the findings from the small and large amplitude approximations [39][42][43]. Unfortunately, the integrals in **Equations 1.9 & 1.10** are improper due to a pole at $t = z_0$, therefore a correction term is often implemented when the analytical form of **Equations 1.9 & 1.10** is used with experimental data [44][45].

Later inspection of **Equations 1.9 & 1.10** found certain combinations oscillation amplitudes and spectrum shapes produced ill-posed results, leading to a significantly larger uncertainty in the conversions from frequency shift [46][47]. The spectra in **Chapter 2** were checked for

ill-posedness using the approaches laid out in [46][47], and found to be satisfactory.

1.3.2.2 *Dynamic Scanning Tunelling Microscopy*

It is routine to measure both the frequency shift and the tunnel current simultaneously. However, the measured tunnel current is dissimilar to the conventional static STM tunnel current. During dynamic STM, the tip is oscillating at a frequency much higher than the sample rate of the tunnel current. Therefore the measured current is the time average of the tunnel current over the full oscillation of the cantilever ($\langle I_{tc}(z)\rangle$). To compare dynamic STM measurements to conventional STM, formula have been developed to calculate the instantaneous tunnel current at the point of closest approach during a cantilever oscillation ($I_{tc}(z)$) . **Equation 1.11** relates the measured time averaged tunnel current to the instantaneous tunnel current [48][49], analogous to how **Equation 1.8** relates the frequency shift to the tip-sample interaction force;

$$\langle I_{tc}(z)\rangle = \frac{1}{\pi}\int_{-1}^{1}\frac{I_{tc}(z)\left[z+a\left(1+u\right)\right]}{\sqrt{1-u^2}}du. \tag{1.11}$$

We then invert **Equation 1.11** to produce a general formula for calculating the instantaneous tunnel current from the measurable time averaged tunnel current measured dynamic STM [48][49]

$$I_{tc}(z) = \langle I_{tc}(z)\rangle_{(z+a)} - \int_{z_0}^{\infty}\sqrt{\frac{2a}{\tau-z_0}}\left[\frac{d\left\langle I_{tc}(\tau)\right\rangle}{d\tau} - \sqrt{\frac{2}{\pi}\frac{d\left\langle I_{tc}(\tau+a)\right\rangle}{d\tau}}\right]d\tau. \tag{1.12}$$

Like with **Equations 1.9 & 1.10**, the integral in **Equation 1.12** is improper due to a pole at $\tau = z_0$, therefore a correction term is often implemented when the analytical form of **Equations 1.12** when it is used with experimental data [44][45].

1.3.3 *Off-Curve Subtraction*

In NC-AFM, the tip-sample interaction is often partitioned into the non-site-specific and non-site-specific interactions. Speaking in general terms, the site-specific interaction is often the quantity of interest, therefore experiments are designed to minimize and remove the non-site-specific interaction from the measured quantity. **Figure 1.2** demonstrates how an experimental On-Curve and Off-Curve pair is used to remove the non-site-specific interaction from an NC-AFM spectrum by performing an off-curve subtraction. Where we define the On-Curve as NC-AFM spectra taken over a site of interest (On-Curve), and the Off-Curve as NC-AFM spectra taken over the (usually unperturbed) substrate to remove the long range background interaction (Off-Curve).

Looking at **Figure 1.2** we can see the site-specific interaction is comprised of the {Microscopic Tip Base ($_e$MTB) – Adsorbed Molecule ($_e$AM)} interaction and the {Nanoscopic Tip Apex ($_e$NTA) – Adsorbed Molecule ($_e$AM)} interaction. Whereas the non-site-specific interaction is comprised of the {Microscopic Tip Base ($_e$MTB) – Bulk Surface ($_e$BS)} interaction and the {Nanoscopic Tip Apex ($_e$NTA) – Bulk Surface ($_e$BS)} interaction. Thus, performing the off-curve subtraction removes the non-site-specific interaction from the quantity measured by the On-Curve. However, **Figure 1.2** and the above theory relies on the underlying assumption that *the presence of the $_e$AM is not affecting the $_e$MTB – $_e$BS interaction*. Strictly speaking, when an off-curve subtraction is performed, we are calculating the change in interaction between the experimental NC-AFM tip comprised of the Microscopic Tip Base ($_e$MTB) and the Nanoscopic Tip Apex ($_e$NTA) ($_e$Tip) and the experimental NC-AFM sample comprised of the Bulk Surface ($_e$BS) and the Adsorbed Molecule ($_e$AM),if one is present ($_e$Sample). Where the change in interaction has been caused by the presence of the $_e$AM.

Furthermore, if we apply **Equations 1.10&1.9** to **Figure 1.2**, then we can come up with an experimental condition for the upper limit of the integration during force spectroscopy. When applying **Equations 1.10&1.9** to calculate the site-specific interaction from a pair of On-Curve as NC-AFM spectra taken over a site of interest (On-Curve), the tail end of the off-curve subtraction spectrum must equal zero.

1.3.3.1 *Controlled Tip Preparation*

After performing the off-curve subtraction, we are left with the $_e$MTB – $_e$AM and the $_e$NTA – $_e$AM site-specific interactions. However, this is still not the ideal situation. Often, in NC-AFM experiments, the quantity of interest is the interaction between the $_e$NTA and the $_e$AM. Furthermore, the shape and atomic (or molecular) species at the $_e$NTA have a large effect on SPM images. Therefore there is a strong desire to be able to accurately shape, and characterize, the $_e$Tip's $_e$MTB and $_e$NTA.

The mass of the $_e$MTB can be reduced by creating a thinner taper to the $_e$NTA. This can be done by electro-chemically etching the tip to produce a thinner $_e$MTB [51][52], followed by further shaping the $_e$Tip with a Focused Ion Beam [53][54]. Furthermore, it is possible to image the $_e$NTA, with atomic resolution, using Field Ion Microscopy. The Field Ion Microscopy technique can be further extended to thin the $_e$MTB, and produce an atomically sharp $_e$NTA, through a spatially controlled field-assisted reaction with nitrogen [55].

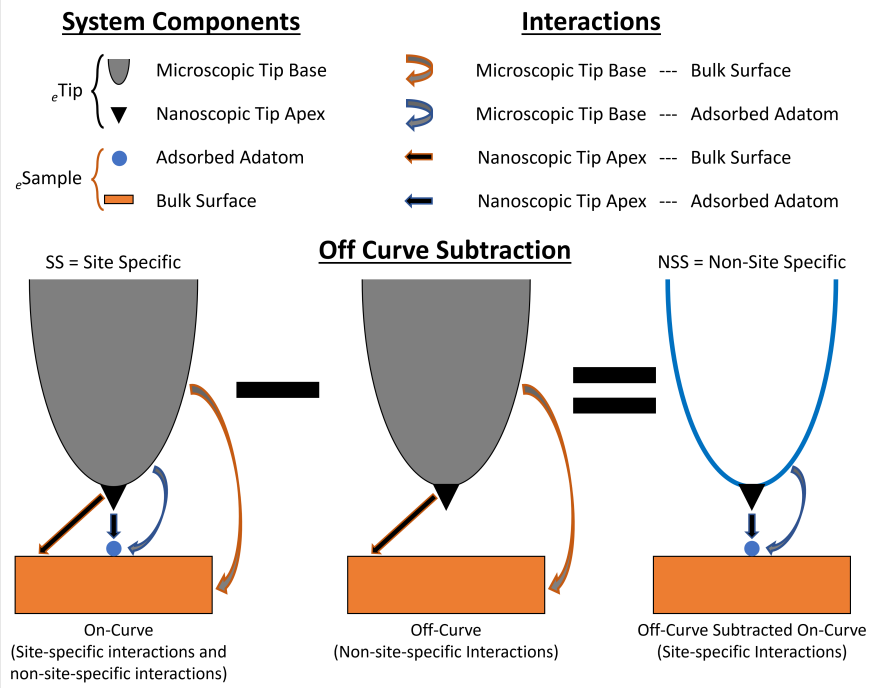

Figure 1.2: Diagrams of the site-specific and non-site-specific interactions, an On-Curve and Off-Curve pair, and how the off-curve subtraction is applied to separate out the site-specific and non-site-specific interactions. **Figure 1.2** was reproduced and edited, with permission, from **Figure 2.6 c** of the thesis of Samuel P. Jarvis [50].

2

EXPERIMENTAL METHODS & RESULTS

This chapter details the results from a series of experiments performed during a two week research trip to the University Of Nottingham, in March 2020. The research trip aimed to determine if the underlying Cu(111) surface reconstruction was detectable using NC-AFM spectra.

The experiments were performed with a surface comprised of islands of C_{60} molecules adsorbed on the Cu(111) surface. Through careful temperature control, and during repeated depositions, an underlying surface reconstruction of the Cu(111) surface was induced under a portion of the adsorbed molecules **(see Section 2.1.1)**. To investigate a possible change in the reactivity of the adsorbed C_{60} molecules, induced by the Cu(111) surface reconstruction, force spectra were taken atop the adsorbed C_{60} molecules. The force minimum of each spectrum was further calculated, providing a quantitative measurement for the reactivity of the adsorbed C_{60} molecule **(see Section 2.1.2)**.

The experiment was designed to allow a measured difference in force minima, taken over $C_{60,r}$ and $C_{60,u}$, to be assigned to differences in how adsorbed C_{60} molecules are bonded to the surface (the 'backbonding'). In particular, changes to the reactivity of the molecule induced by the underlying surface. A key feature of the C_{60} on Cu(111) system is the atomic positions of the carbon atoms at the top of the adsorbed C_{60} molecules are unperturbed by the bonding of the the C_{60} to the Cu(111) surface. A review of the literature suggested the 7 adatom vacancy Cu(111) surface reconstruction was expected to transfer $\sim -3e$ to the adsorbed C_{60} molecule [56][2], and the relatively unperturbed unreconstructed Cu(111) surface is expected to transfer $< -1e$ to the adsorbed C_{60} molecule [57][58][2]. Where this difference in the charge transfer suggests a significant difference in the 'backbonding' of the adsorbed C_{60} molecules.

2.1 EXPERIMENTAL METHODS

2.1.1 *Sample Preparation*

The experiments were performed using the generation 2 Scienta Omicron UHV-LT-AFM/STM system installed at the University Of Nottingham. The system was controlled using the Matrix controller, and the experiments performed at 5.4 K (liquid Helium cooled), under UHV conditions.

A bar shaped Cu(111) sample was introduced into the UHV system for sample preparation. To prepare the Cu(111) surface, three sputter-anneal cycles were performed. Where one cycle involved sputtering the sample with Argon for ~30 *mins*, followed by annealing the sample at 600 °*C* for ~30 *mins*. However, due to a malfunction of the sputter gun, a pristine sample could not be prepared (see insets to **Figures 2.4 A & 2.10 A**), and no further sputter-anneal cycles could be performed.

The surface was prepared to contain islands of C_{60} molecules adsorbed on both the reconstructed and unreconstructed Cu(111) surface. To form islands of C_{60} molecules, small amounts of C_{60} were deposited onto the surface, the coverage checked with STM constant current images, and further depositions performed if needed. This approach was taken to avoid the need for further sputter-anneal cycles, which could not be reliably performed due to the malfunctioning sputter gun. During C_{60} depositions, the sample was cooled with LN_2 to prevent Cu(111) surface reconstructions occurring at room temperature [3]. To form the first islands of C_{60} molecules, C_{60} was deposited at 1.4 *V* (15.0 *A*) for ~30 *mins*, followed by a second ~30 *min* deposition at 1.5 *V* (16.0 *A*), and a third ~15 *min* deposition at 1.8 *V* (18.0 *A*). The planned experiments required islands of adsorbed C_{60} containing C_{60} adsorbed on both the unreconstructed, and reconstructed, Cu(111) surface. Therefore, after the first set of C_{60} depositions, the sample was annealed to ~200°*C* to induce the 7 adatom displacement surface reconstruction [2]. The presence of the surface reconstruction was confirmed with STM constant current images through an analysis of the molecular adsorption heights [2][3], then a final C_{60} deposition was performed onto the LN_2 cooled sample for ~20 *min*, at 1.8 *V* (18.0 *A*). The final deposition produced an adequate coverage of C_{60} molecules adsorbed on the unreconstructed Cu(111) surface, along side C_{60} molecules adsorbed reconstructed Cu(111) surface.

2.1.2 *Experimental Procedure*

All SPM data in this work was gathered using a single qPlus sensor. All constant current frequency shift images, and force spectra, in this work were taken with an oscillation amplitude of 285 pm, where the oscillation amplitude was calibrated using the tunnel current method from Sugimoto *et al* [48].

Suitable islands of adsorbed C_{60} molecules were located with constant current STM images. Once found, further constant height NC-AFM images were taken over small sections of the islands, where the frequency shift and tunnel current were simultaneously recorded. These images can be seen in **Figures 2.1, 2.4, 2.7, 2.8, & 2.10**. Using the constant height NC-AFM images, suitable On-Curve spectrum sites atop the adsorbed C_{60} molecules were identified. This process was carried out using copper functionalized AFM tips (*Cu* Tips), and C_{60} functionalized

AFM tips (C_{60} Tips). To produce a *Cu* Tip, the tip was crashed into the surface to coat the Nanoscopic Tip Apex ($_e$NTA) with Cu. To produce a C_{60} Tip, a metallic tip was positioned above a C_{60} molecule adsorbed on the unreconstructed Cu(111) surface, and then approached towards the surface until the C_{60} molecule was picked up by the tip. The successful creation of a C_{60} Tip was confirmed by scanning the same molecular island; if the C_{60} Tip was created then the adsorbed C_{60} molecule will be missing from the island, and the image features of the adsorbed C_{60} molecules will also change.

Z spectroscopy was performed over C_{60} molecules adsorbed in both geometries. Both frequency shift and tunnel current (in addition to the excitation and oscillation amplitude) were recorded during the spectroscopy. However, due to a known cross-talk issue between the tunnel current and frequency shift channels, the junction bias was minimized to minimize the tunnel current. This increased the accuracy of the frequency shift measurement, and the following force conversion. However, it increased the uncertainty in the bias to a minimum of ± 100 %, which increased the uncertainty in the calculated conductance by the same amount. Due to this large uncertainty, the conductance data was not included in this work, as no reliable conclusions could be drawn from it.

The force minimum of the Z spectra was used as the measure of the interaction with the tip and the sample. With a C_{60} Tip, the force spectra were smoothed to separate out the higher frequency noise from the low frequency signal, increasing the accuracy of the extracted force minimum. When analyzing data taken with a *Cu* Tip, it was decided no smoothing would be applied. This decision was made because the length scale over which the signal about the force minimum varies is similar to that of the noise, therefore the noise could not be removed from the measurement without also removing some of the signal and artificially altering the force minimum.

2.1.3 *Experimental Difficulties*

Unique difficulties and challenges were faced during the research trip to the University Of Nottingham. Difficulties and challenges such as; The helium liquifier developing a fault and shutting down, the sputter gun on the system developing a fault, long term health issues of the writer of this work, and the start of the COVID-19 Pandemic. In particular, the beginning of the pandemic caused changes to the planned experiments, and eventually resulted in the closure of the lab before the planned end date of the trip.

The experiments were planned to be carried out at the University Of Nottingham to mitigate the effects of the long-term equipment issues at the University Of Leeds, leading to the equipment not being available to contribute to this work. This PhD project was originally

planned to be carried out on the generation 3 Scienta Omicron UHV-LT-AFM/STM system, purchased by the University Of Leeds. However, the instrument could not be signed off due an ongoing a failure to meet acceptance criteria, and was eventually taken back to Germany for repairs. The system was installed at the University Of Leeds for a second time during the start of 2022, with continuing ongoing issues around the purchase of the instrument and, the long-term reliability of the instrument, ability of the instrument to meet the original acceptance criteria.

2.2 C_{60} TIP RESULTS

The three distinct C_{60} Tips were created, and force spectra taken with them. Two of the C_{60} Tips had indistinguishable force minimum values, therefore the data gathered with these two C_{60} Tips was analyzed together, and named C_{60} *Tip Dataset 1*. The Data named C_{60} *Tip Dataset 2* was one continuous set of data, taken within a single fill cycle of the cryostats, over the same region of the surface. A single C_{60} Tip was created to take the data, however there were small tip changes during the data gathering which needed to be accounted for.

2.2.1 C_{60} *Tip Dataset 1*

Figure 2.1 contains a constant current STM image **(A)**, and simultaneously taken constant height frequency shift and tunnel current images taken over the same region **(B,C,D,E)**. There appears to be more C_{60} molecules adsorbed on the unreconstructed surface in image **A** than in images **B-E**. This is due to a double tip which was only visible in constant current STM imaging. The molecules in **A** which are not present in the constant current images have been circled in blue.

Figure 2.2 contains example On-Curve and Off-Curves taken atop C_{60} adsorbed on the unreconstructed Cu(111) surface ($C_{60,u}$), and C_{60} adsorbed on the 7 atom vacancy Cu(111) surface reconstruction ($C_{60,r}$). **A, B, C, & D** display example force spectra from C_{60} *Tip Dataset 1*, **E, F, G, & H** display example force spectra from C_{60} *Tip Dataset 2*. Looking at **A**, one can see the two C_{60} Tips analyzed together as C_{60} *Tip Dataset 1* have different non-site-specific (background) frequency shift signals. However, when the non-site-specific interactions are removed with the off-curve subtraction, the site-specific interactions are indistinguishable in **B, C, & D**.

Figure 2.3 contains box and scatter plots of the force spectrum minima in C_{60} *Tip Dataset 1*. In total, 62 spectra were taken which reached their force minimum. These spectra, and corresponding images, were further inspected for tip changes in post processing. Spectra taken with C_{60} Tips that only gathered data over $C_{60,u}$ or $C_{60,r}$ molecules were excluded from further analysis and **Figure 2.3**, reducing the number

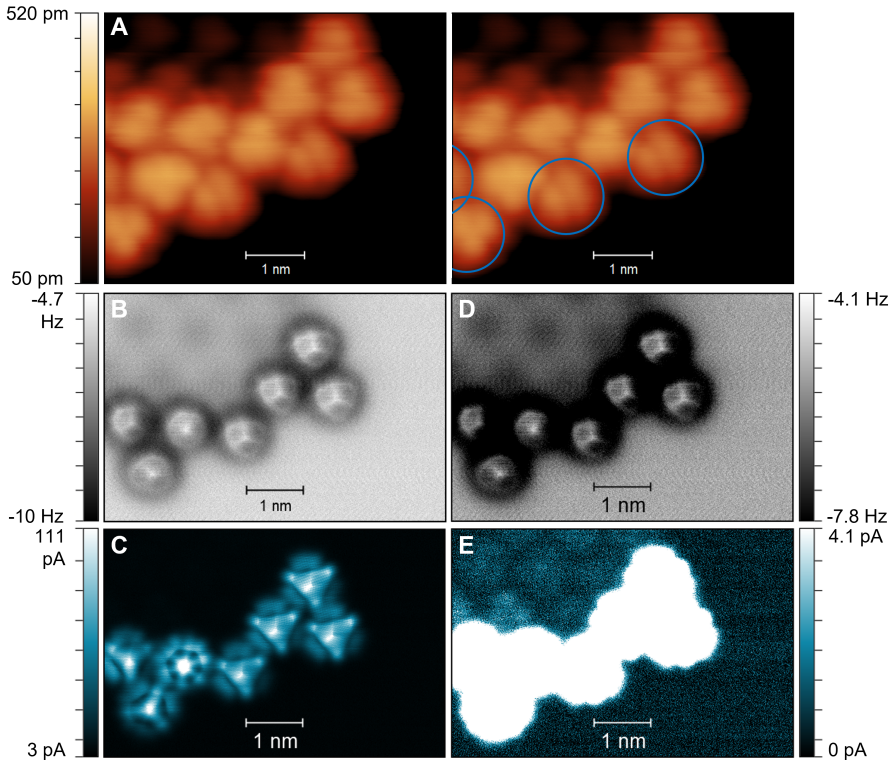

Figure 2.1: STM and AFM images over an island of $C_{60,r}$ and $C_{60,u}$ molecules which was investigated with C_{60} Tip 1. **A:** Constant current Z height image at a bias of $0.5\,V$ and set-point of $50\,pA$. **B&D:** The same constant height frequency shift image. **C&E:** The same constant height tunnel current image. Images **B&C** (and thus **D&E**) were taken simultaneously at a bias of $1\,mV$. The colour bar range in images **B&C** has been adjusted to optimize image contrast over the $C_{60,u}$ molecules, in **D&E** the colour bar has been adjusted to optimize image contrast over the $C_{60,r}$ molecules.

of valid spectra to 49. This approach of excluding certain spectra was taken as a small tip change can change the value of the force minimum. If this change is not present in both the $C_{60,u}$ and $C_{60,r}$ data being averaged over, then the tip change will effect the average of one and not the other, introducing an artificial difference of the force minima on comparison. An analysis performed on the full data set can be found in **Figure A.1** in **Appendix A**. From averaging over all valid force minima, the following values were obtained: $F_{min,r}^{C_{60}\ Tip\ D1} = -0.306\,nN$ and $F_{min,u}^{C_{60}\ Tip\ D1} = -0.298\,nN$. Where $F_{min,r}^{C_{60}\ Tip\ D1}$ and $F_{min,u}^{C_{60}\ Tip\ D1}$ correspond to the average force minimum of the $C_{60,r}$ and $C_{60,u}$ data for C_{60} *Tip Dataset 1*.

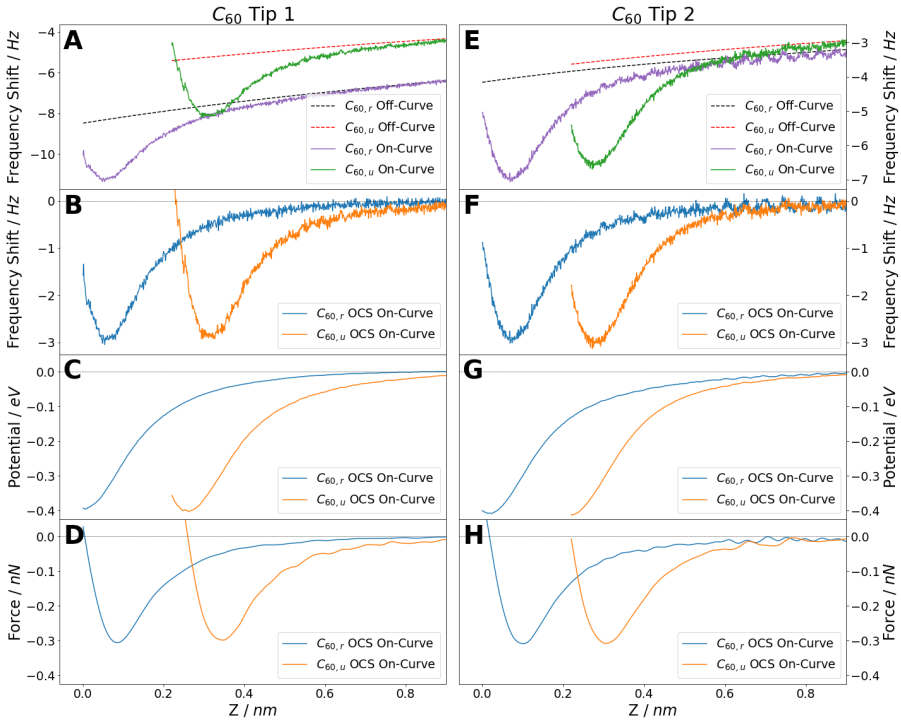

Figure 2.2: Example $_e$NC-AFM force spectra, taken over $C_{60,r}$ and $C_{60,u}$ molecules, with C_{60} Tips 1 **(A,B,C,D)** and 2 **(E,D,G,H)**. **A&E** show frequency shift data for the $C_{60,r}$ and $C_{60,u}$ On-Curves (purple and green solid lines), and Off-Curves (black and red dashed lines). **B&F** show the off-curve subtracted On-Curve frequency shift data. **C&G** show the corresponding potential data, calculated from the curves in **B&F** by applying the Sader-Jarvis Algorithm [40][41]. **D&H** show the corresponding force data, calculated from the curves in **C&G** by applying a Lanczos Derivative [59] with the minimum differential width of 3 points. A spline fit [60] was then applied to the force data to remove the high frequency noise about the force minima. The Off-Curves in **A&E** (red and black dashed lines), and the off-curve subtracted On-Curves in **D&H**, have been smoothed using a spline to remove the maximum amount of noise, without changing the overall shape of the spectra.

.

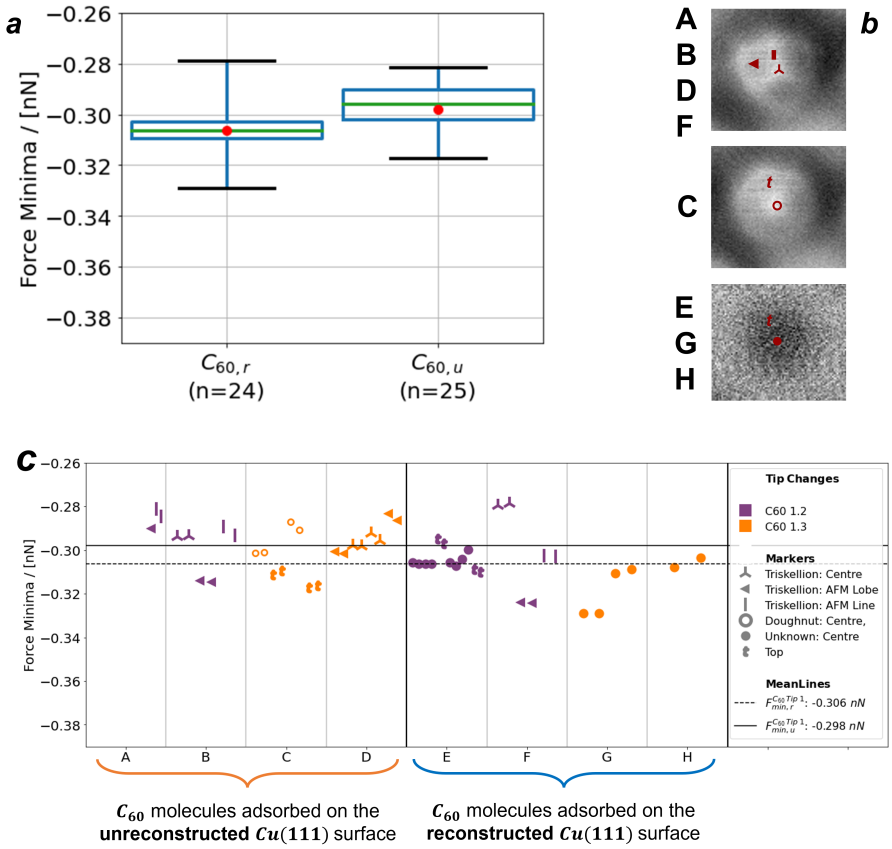

Figure 2.3: Box and scatter plots **(*a* & *c*)** of the force minimum data, taken over $C_{60,r}$ and $C_{60,u}$ molecules, with C_{60} Tip 1. In ***a***, the green lines and reds dot correspond to the median and mean values of the spectra, where spectra taken over the $C_{60,r}$ and $C_{60,u}$ molecules have been plotted separately. In ***b***, sites where the spectra were taken have been pictorially defined. In ***c***, the colours correspond to tip changes, and the markers correspond to the site over which the spectrum was taken **(see *b*)**. The solid black and dashed black horizontal lines in ***c*** mark the average force minimum for the spectra taken over the $C_{60,u}$ and $C_{60,r}$ molecules. Only data from tip changes that included spectra taken over both $C_{60,u}$ and $C_{60,r}$ molecules were plotted, and averaged over, in **Figure 2.3**. See **Figure A.1** in **Appendix A** for all the data taken with C_{60} Tip 1.

2.2.2 C_{60} *Tip Dataset 2*

Figure 2.4 contains a constant current STM image **(A)**, and simultaneously taken constant height frequency shift and tunnel current images taken over the same region **(B, C, D, E)**. Unlike in **Figure 2.1**, there is no double tip in the constant current STM image. Comparing the raw frequency shift data in **Figure 2.2 E** to that in **A**, one can see the non-site-specific interaction is smaller for C_{60} *Tip Dataset 2* than for C_{60} *Tip Dataset 1*. However, when the non-site-specific interactions are removed with the off-curve subtraction, the site-specific interactions are very similar for C_{60} *Tip Dataset 1* and C_{60} *Tip Dataset 2* by comparing **B, C, & D** to **F, G, & H** (site-specific frequency shift, site-specific potential, site-specific force).

Figure 2.5 contains box and scatter plots of the force spectrum minima gathered with C_{60} *Tip Dataset 2*. In total, 250 spectra were taken which reached their force minimum. These spectra, and corresponding images, were further inspected for tip changes in post processing. Only spectra taken with tips that gathered data over both the $C_{60,u}$ or $C_{60,r}$ molecules were included in **Figure 2.5**, and further analysis. This approach reduced the number of valid spectra to 146. The decision to exclude these spectra was taken for the following reason; a small tip change can change the value of the force minimum. If this change is not present in both the $C_{60,u}$ and $C_{60,r}$ data, then when the average force minima value is calculated, the tip change will effect the average over one geometry and not the other, introducing an artificial difference of the force minima on comparison. An analysis performed on the full data set can be found in **Figure A.2** in **Appendix A**. The following value was obtained by averaging over all the valid spectra taken atop $C_{60,r}$ molecules in C_{60} *Tip Dataset 2*: $F_{min,r}^{C_{60}\,Tip\,D2} = -0.307\,nN$. The average value for spectra taken atop $C_{60,u}$ molecules in C_{60} *Tip Dataset 2* is more complex. Looking at **Figure 2.5**, the force minima of the spectra taken over the $C_{60,u}$ molecules appear to be distributed in a bimodal distribution. One of the modes can be assigned an average force minimum of $F_{min,u,M1}^{C_{60}\,Tip\,D2} = -0.303\,nN$, which is $4\,pN$ less than $F_{min,r}^{C_{60}\,Tip\,D2} = -0.307\,nN$. The second mode has an average force minimum of approximately $F_{min,u,M2}^{C_{60}\,Tip\,D2} = -0.342\,nN$, which is $35\,pN$ more attractive than $F_{min,r}^{C_{60}\,Tip\,D2} = -0.307\,nN$.

In an attempt to determine the source of the unexpected bi-modal distribution, the data was checked for correlations with the following criteria; the instantaneous current and conductance, the time averaged current and conductance, the position of the $C_{60,u}$ molecule in the island, the image contrast over the adsorbed $C_{60,u}$ molecule (doughnut or triskellion), the order the spectra were taken in, the lag time between the On-Curve and Off-Curve, the image from which the spectrum posi-

tions were defined, the tip changes, and which adsorbed $C_{60,u}$ molecule the spectrum was taken over.

For C_{60} *Tip Dataset 2*, it can be stated *a specific* C_{60} *Tip, paired with a specific adsorbed* $C_{60,u}$*, produces a set of force minima that lie in the same mode of the bimodal distribution*. However, the mode which the force minima will lie in (when gathered with a specific tip over a specific $C_{60,u}$ molecule) can not be predicted using the gathered data. In contrast to the unreconstructed phase, spectra taken atop C_{60} molecules adsorbed in the reconstructed phase show a more uniform distribution of force minima. The difference between the two adsorption geometries arises from the $C_{60,r}$ geometry bring prepared with an additional high temperature anneal step at ~200°C, whereas the $C_{60,u}$ geometry was adsorbed onto a LN_2 cooled sample, and then further cooled to *LHe* temperatures. It is also worth noting that the shape of the force spectra is more varied in C_{60} *Tip Dataset 2* compared to C_{60} *Tip Dataset 1*. However, the forwards and backwards curves were always in agreement unless a tip change was noted. This suggests the possibility the tip or sample were conforming more in some spectra than others in C_{60} *Tip Dataset 2*, but not producing permanent changes to the tip structure whilst doing so. Overall, an explanation for the bi-modal distribution is not known.

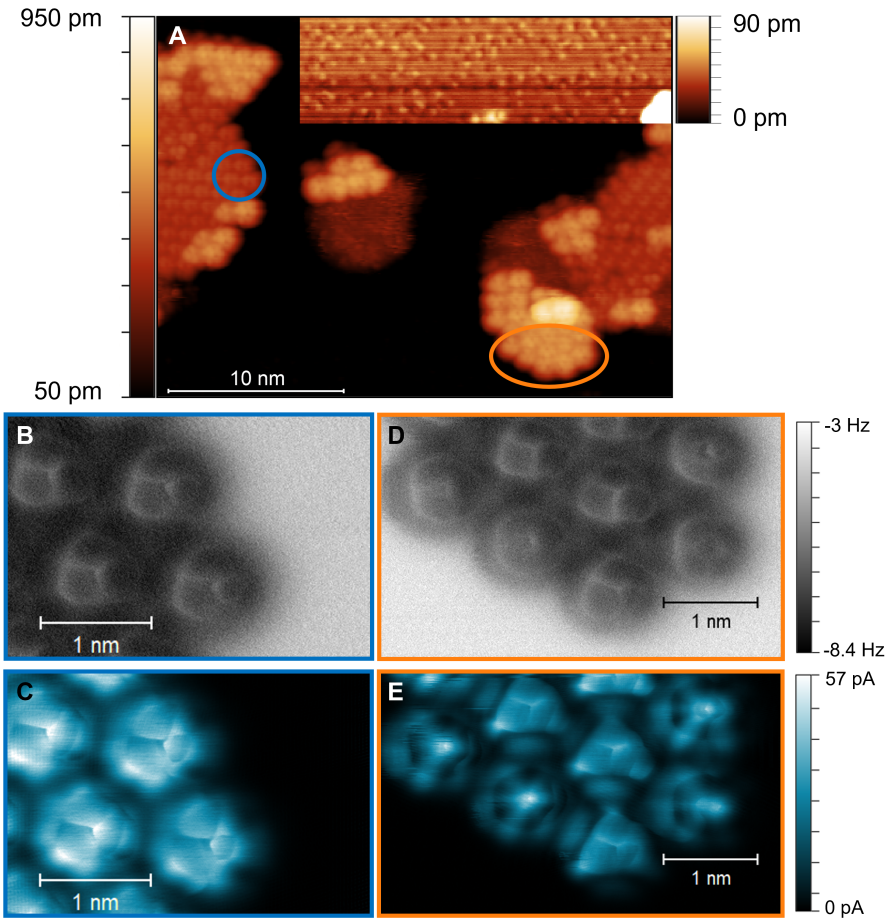

Figure 2.4: STM and AFM images over an island of $C_{60,r}$ and $C_{60,u}$ molecules which was investigated with C_{60} Tip 2. **A:** constant current Z height image at a bias of $0.5\,V$ and set-point of $50\,pA$. In the main image the colour bar has been adjusted to show contrast over the islands of C_{60}. In the inset the colour bar has been adjusted to show contrast over the Cu(111) surface. **B&C:** Constant height frequency shift and tunnel current images, taken simultaneously at a bias of $1\,mV$, over the $C_{60,r}$ molecules within the blue circle in **A**. **D&E:** Constant height frequency shift and tunnel current image, taken simultaneously at a bias of $0.5\,mV$, over the $C_{60,u}$ molecules within the orange circle in **A**.

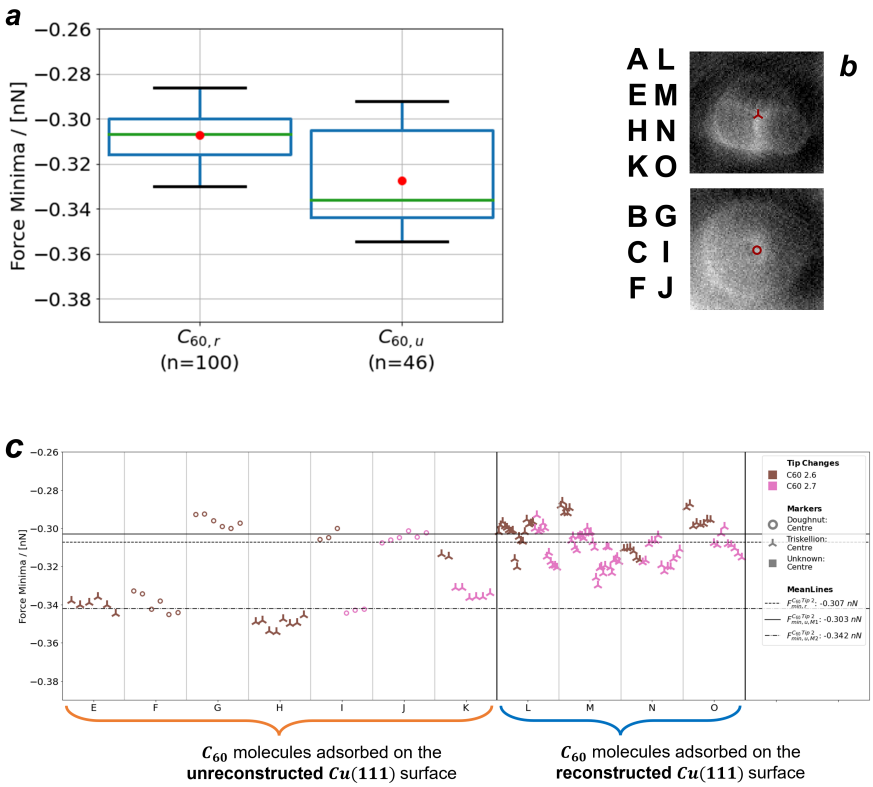

Figure 2.5: Box and scatter plots **(*a* & *c*)** of the force minimum data, taken over $C_{60,r}$ and $C_{60,u}$ molecules, with C_{60} Tip 2. In ***a***, the green lines and reds dot correspond to the median and mean values of the spectra, where spectra taken over the $C_{60,r}$ and $C_{60,u}$ molecules have been plotted separately. In ***b***, sites where the spectra were taken have been pictorially defined. In ***c***, the colours correspond to tip changes, and the markers correspond to the site over which the spectrum was taken **(see *b*)**. The solid black and dashed black horizontal lines in ***c*** mark the average force minimum for the spectra taken over the $C_{60,u}$ and $C_{60,r}$ molecules. Only data from tip changes that included spectra taken over both $C_{60,u}$ and $C_{60,r}$ molecules were plotted, and averaged over, in **Figure 2.5**. See **Figure A.2** in **Appendix A** for all the data taken with C_{60} Tip 2.

2.3 METAL TIP RESULTS

Two distinct *Cu* Tips were created, and the force spectra taken with them grouped into two datasets; *Cu Tip Dataset 1* and *Cu Tip Dataset 2*. The data in each dataset is one continuous set of data, taken within a single fill cycle of the cryostats, over the same region of the surface. A single *Cu* Tip was created to take each set of data, however there were small tip changes during the data gathering which needed to be accounted for.

2.3.1 *Cu Tip Dataset 1*

Figure 2.7 A contains a constant current STM image of an island of adsorbed C_{60} molecules. In **B** a constant current image was taken over a smaller section of the same island. **C & D** display simultaneously taken constant height frequency shift and tunnel current images taken over the same region image in **B**. Images **E & F** contain simultaneously taken constant height frequency shift and tunnel current images at a lower height over the $C_{60,r}$ molecules outlined by the red box in **C & D**. The brighter, circular features in **E** correspond to a $C_{60,r}$ molecule adsorbed with a pentagonal face presenting upwards. This is confirmed in **Figure 2.8** by counting the vertices of the adsorbed $C_{60,r}$ molecules in the constant height AFM image. A pentagon can be seen in the box outlined in red, and a hexagon in the box outlined in blue.

Figure 2.6 contains example On-Curve and Off-Curves taken atop the $C_{60,r}$ and $C_{60,u}$ molecules. **A, B, C, & D** display example force spectra for *Cu Tip Dataset 1*, **E, F, G, & H** display example force spectra for *Cu Tip Dataset 2*. Comparing **A** and **E** one can see the frequency shift values in **B** are lower indicating the background non-site-specific interactions are smaller for *Cu Tip Dataset 2*.

Figure 2.9 contains box and scatter plots of the force spectrum minima in *Cu Tip Dataset 1*. In total, 54 spectra were taken which reached their force minimum. These spectra, and corresponding images, were further inspected for tip changes in post processing. Spectra taken with tips that only gathered data over $C_{60,u}$ or $C_{60,r}$ molecules were excluded from further analysis and **Figure 2.9**, reducing the number of valid spectra to 38. This approach of excluding certain spectra was taken as a small tip change can change the value of the force minimum. If this change is not present in both the $C_{60,u}$ and $C_{60,r}$ data being averaged over, then the tip change will effect the average of one and not the other, introducing an artificial difference of the force minima on comparison. An analysis performed on the full data set can be found in **Figure A.3** in **Appendix A**. From averaging over all valid force minima, the following values were obtained: $F_{min,r}^{Cu\,Tip\,1} = -1.723\,nN$ and $F_{min,u}^{Cu\,Tip\,2} = -1.441\,nN$. Where $F_{min,r}^{Cu\,Tip\,1}$ and $F_{min,u}^{Cu\,Tip\,1}$ correspond to the average force minimum of the $C_{60,r}$ and $C_{60,u}$ data for C_{60} *Dataset 1*.

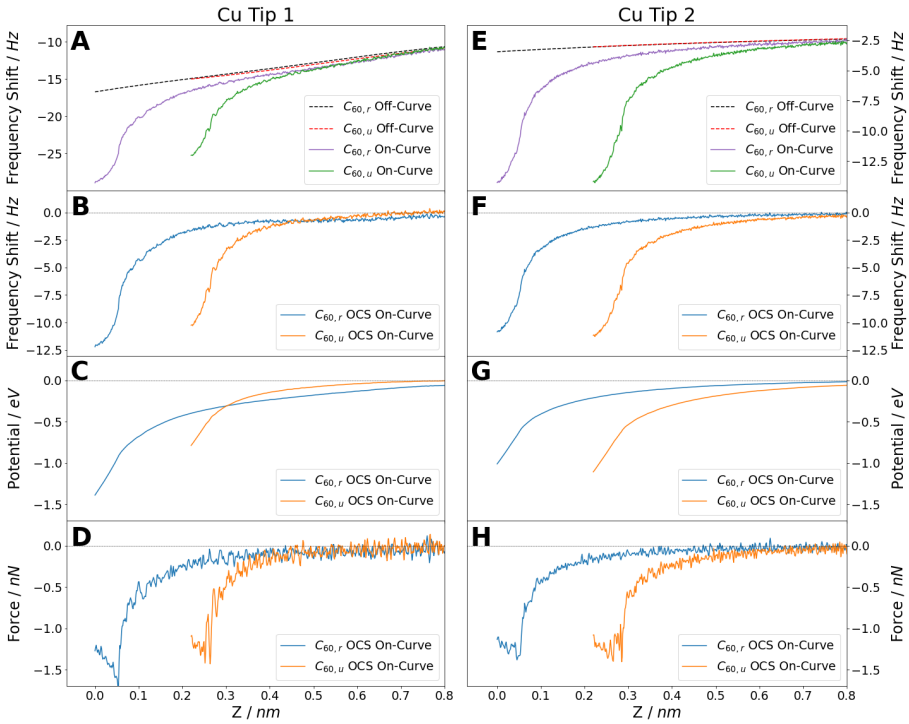

Figure 2.6: Example $_e$NC-AFM force spectra, taken over $C_{60,r}$ and $C_{60,u}$ molecules, with *Cu* Tips 1 **(A,B,C,D)()** and 2 **(E,D,G,H)()**. **A&E** show frequency shift data for the $C_{60,r}$ and $C_{60,u}$ On-Curves (purple and green solid lines), and Off-Curves (black and red dashed lines). **B&F** show the off-curve subtracted On-Curve frequency shift data. **C&G** show the corresponding potential data, calculated from the curves in **B&F** by applying the Sader-Jarvis Algorithm [40][41]. **D&H** show the corresponding force data, calculated from the curves in **C&G** by applying a Lanczos Derivative [59] with the minimum differential width of 3 points. The Off-Curves in **A&E** (red and black dashed lines), and off-curve subtracted On-Curves in **D&H**, have not been smoothed as it was not possible to smooth the data without removing part of the real signal.

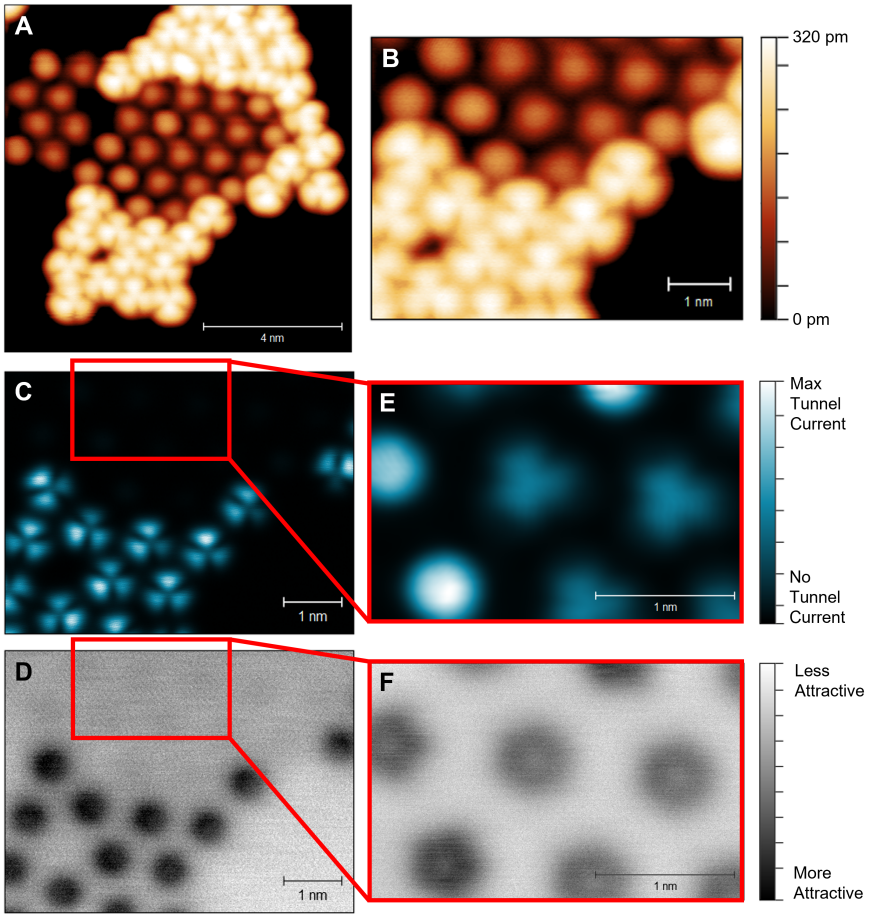

Figure 2.7: STM and AFM images over an island of $C_{60,r}$ and $C_{60,u}$ molecules which was investigated with Cu Tip 1. **A&B:** The same constant current Z height image at a bias of $0.1\,V$ and set-point of $50\,pA$. **C&D:** Constant height tunnel current and frequency shift images, taken simultaneously at a bias of $1\,mV$, over $C_{60,u}$ and $C_{60,r}$ molecules. **E&F:** Constant height tunnel current and frequency shift images, taken simultaneously at a bias of $1\,mV$, over $C_{60,r}$ molecules.

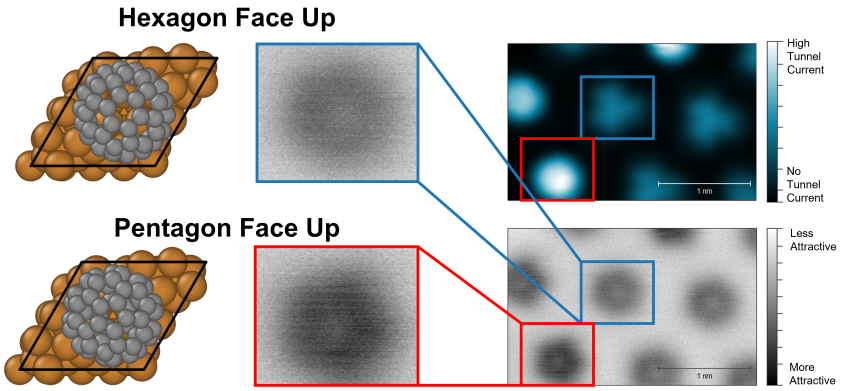

Figure 2.8: The same Constant height images in **Figure 2.7 E&F**. Constant height tunnel current and frequency shift images, taken simultaneously at a bias of $1\,mV$, over $C_{60,r}$ molecules. The section of the image outlined in red has been enlarged so one can see it is a pentagonal face of an $C_{60,r}$. The section of the image outlined in blue has been enlarged so one can see it is a hexagonal face of an $C_{60,r}$.

2.3.2 *Cu Tip Dataset 2*

Figure 2.10 A contains a constant current STM image taken over an island of adsorbed C_{60} molecules, the inset in **A** is the same image with the colour bar altered to highlight the image contrast over the surface. In **B** a constant current image was taken over a smaller section of the same island. **C & D** display simultaneously taken constant height frequency shift and tunnel current images taken over the same region imaged in **B**. Images **E & F** are the same images as **C & D** with the colour bar altered to highlight the image contrast over the $C_{60,r}$ molecules. All the C_{60} molecules **B, C, D, & E** have adsorbed with a hexagon facing upwards.

Figure 2.11 contains box and scatter plots of the force spectrum minima gathered with *Cu Tip Dataset* 2. In total, 237 spectra were taken which reached their force minimum. These spectra, and corresponding images, were further inspected for tip changes in post processing. Only spectra taken with tips that gathered data over both the $C_{60,u}$ or $C_{60,r}$ molecules were included in **Figure 2.11**, and further analysis. This approach reduced the number of valid spectra to 150. The decision to exclude these spectra was taken for the following reason; a small tip change can change the value of the force minimum. If this change is not present in both the $C_{60,u}$ and $C_{60,r}$ data, then when the average force minima value is calculated, the tip change will effect the average over one geometry and not the other, introducing an artificial difference of the force minima on comparison. An analysis performed on the full data set can be found in **Figure A.4** in **Appendix A**. The following values were obtained by averaging over all the valid spectra in *Cu*

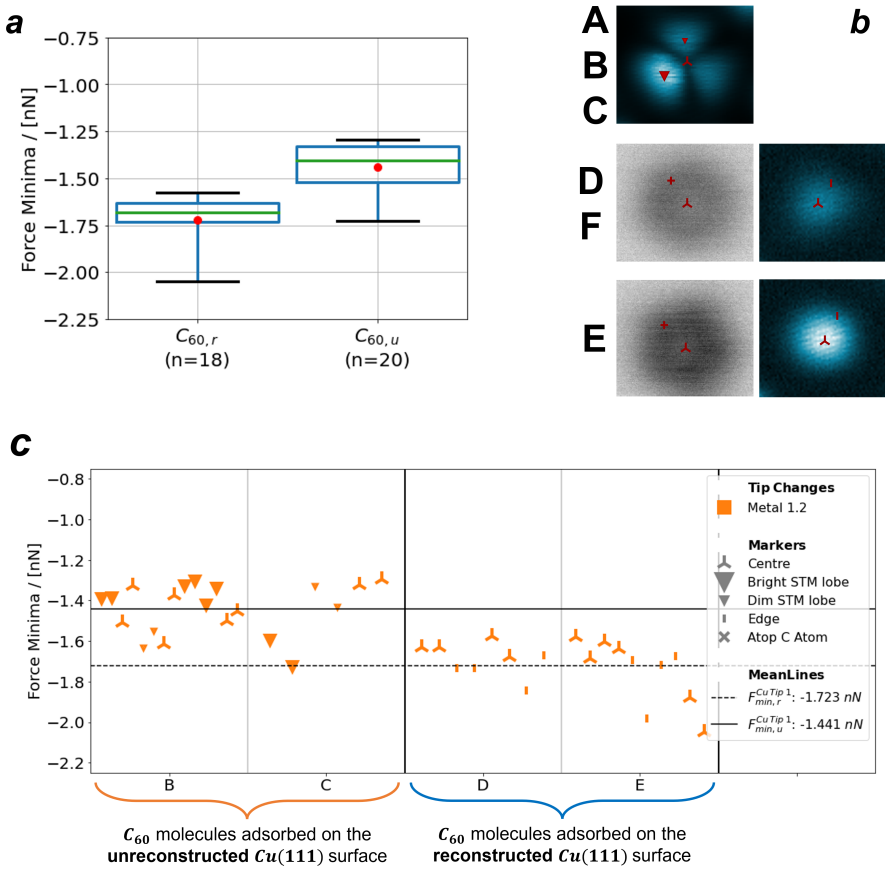

Figure 2.9: Box and scatter plots **(*a* & *c*)** of the force minimum data, taken over $C_{60,r}$ and $C_{60,u}$ molecules, with *Cu* Tip 1. In ***a***, the green lines and reds dot correspond to the median and mean values of the spectra, where spectra taken over the $C_{60,r}$ and $C_{60,u}$ molecules have been plotted separately. In ***b***, sites where the spectra were taken have been pictorially defined. In ***c***, the colours correspond to tip changes, and the markers correspond to the site over which the spectrum was taken **(see *b*)**. The solid black and dashed black horizontal lines in ***c*** mark the average force minimum for the spectra taken over the $C_{60,u}$ and $C_{60,r}$ molecules. Only data from tip changes that included spectra taken over both $C_{60,u}$ and $C_{60,r}$ molecules were plotted, and averaged over, in **Figure 2.9**. See **Figure A.3** in **Appendix A** for all the data taken with C_{60} Tip 1.

Tip Dataset 2: $F_{min,r}^{Cu\ Tip\,2} = -1.385\,nN$ and $F_{min,u}^{Cu\ Tip\,2} = -1.407\,nN$. Where $F_{min,r}^{Cu\ Tip\,2}$ and $F_{min,u}^{Cu\ Tip\,2}$ correspond to the average force minimum of the $C_{60,r}$ and $C_{60,u}$ data for *Cu Tip Dataset 2*.

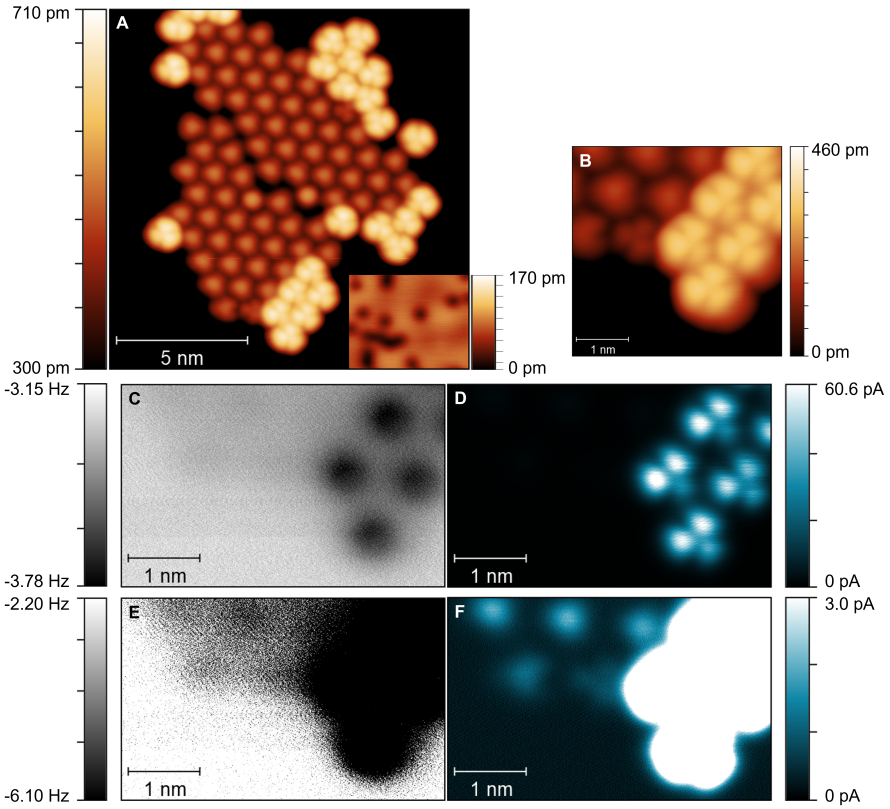

Figure 2.10: STM and AFM images over an island of $C_{60,r}$ and $C_{60,u}$ molecules which was investigated with Cu tip 2. **A:** Constant current Z height image, taken at a bias of 0.01 V and set-point of 40 pA, over a large island of C_{60} molecules. In the main image the colour bar has been adjusted to show contrast over the island of C_{60}. In the inset the colour bar has been adjusted to show contrast over the Cu(111) surface. **B:** Constant current Z height image, taken at a bias of 0.01 V and set-point of 40 pA, over the section of the C_{60} island imaged in **C,D,E,F**. **C&E:** The same constant height frequency shift image. **D&F:** The same constant height tunnel current image. Images **C&D** (and thus **E&**F) were taken simultaneously at a bias of 1 mV. The colour bar range in images **C&D** has been adjusted to optimize image contrast over the $C_{60,u}$ molecules, in **E&F** the colour bar has been adjusted to optimize image contrast over the $C_{60,r}$ molecules.

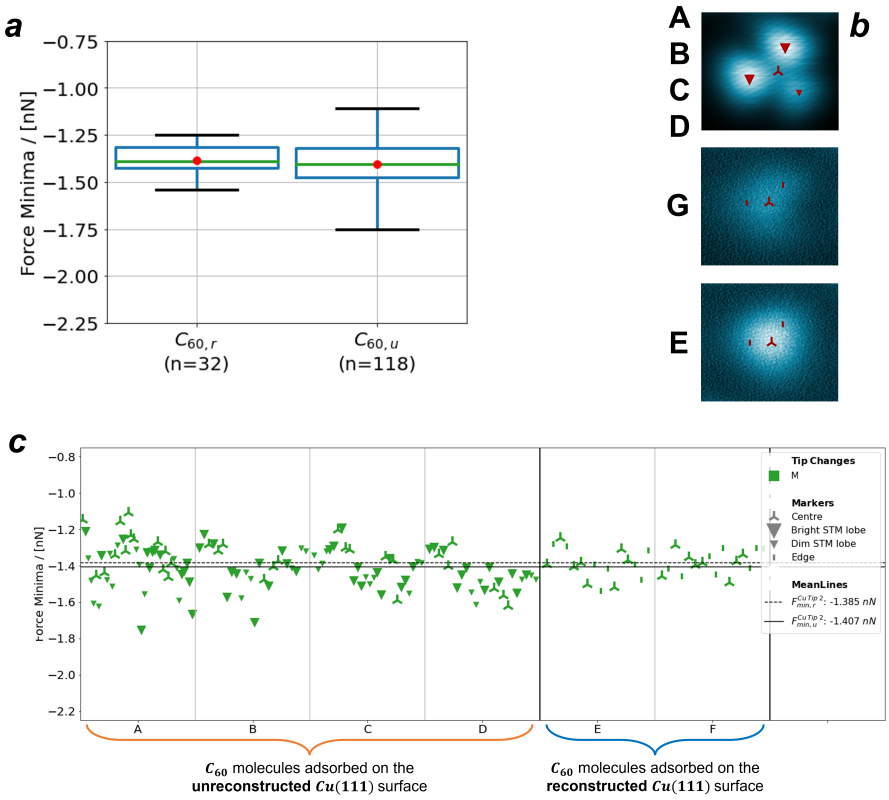

Figure 2.11: Box and scatter plots **(*a* & *c*)** of the force minimum data, taken over $C_{60,r}$ and $C_{60,u}$ molecules, with Cu tip 2. In ***a***, the green lines and reds dot correspond to the median and mean values of the spectra, where spectra taken over the $C_{60,r}$ and $C_{60,u}$ molecules have been plotted separately. In ***b***, sites where the spectra were taken have been pictorially defined. In ***c***, the colours correspond to tip changes, and the markers correspond to the site over which the spectrum was taken **(see *b*)**. The solid black and dashed black horizontal lines in ***c*** mark the average force minimum for the spectra taken over the $C_{60,u}$ and $C_{60,r}$ molecules. Only data from tip changes that included spectra taken over both $C_{60,u}$ and $C_{60,r}$ molecules were plotted, and averaged over, in **Figure 2.11**. See **Figure A.4** in **Appendix A** for all the data taken with Cu tip 2.

2.4 EXPERIMENTAL UNCERTAINTIES

When giving a mean as a final result, one would normally quote the standard error on the mean as the final uncertainty. Where the standard error is calculated by **Equation 2.1** below

$$\sigma_{\bar{x}} = \frac{\sigma_x}{\sqrt{n_x}} \tag{2.1}$$

, with $\sigma_{\bar{x}}$, σ_x, and n_x being the standard error, standard deviation, and sample size, respectively for sample x. Using **Equation 2.1** we can produce two uncertainty values:

- $\sigma_{\overline{C_{60}\,Tip}} \approx 1\,pN$
- $\sigma_{\overline{Cu\,Tip}} \approx 30\,pN$

where $\sigma_{\overline{C_{60}\,Tip}}$ is the standard error for C_{60} Tips, $\sigma_{\overline{Cu\,Tip}}$ is the standard error for the *Cu* Tips. In this methodology, given the approximate nature of error quoting, the individual uncertainties calculated for each surface reconstruction for each tip (C_{60} Tip or *Cu* Tips) are similar enough to allow us to quote a single standard error for all C_{60} Tips, and a second value for all *Cu* Tips.

Unfortunately, on close inspection of the experiential data, it becomes clear we have an unusual situation. *The standard error on the mean is not the most suitable uncertainty to quote with the final values of this work*. The perfect average value (mean) is taken over a series of values expected to be identical, with the variation produced by random noise following a gaussian distribution. However, for the following reasons, this is not the case with the experimental data in this work:

1. In **Figures 2.3, 2.5, 2.9, and 2.11**, it can be clearly seen that the data consists of spectra taken over multiple different sites atop adsorbed C_{60} molecules, where it is expected the spectrum site will have an effect on the force minimum, and was not accounted for when performing the experiments in this work. This reasoning is also complemented by how the structure of the tip is unknown (past inverse imaging the apex atoms on small adsorbed molecules surface), and therefore how stiff or flexible the tip apex (not the cantilever) is remains unknown. Therefore, it is unknown know how much the experimental tips can bend towards the site they prefer to bond with. In this context, the simulations are in contrast to the experiments. The metal tips were carved out of perfect metal crystals to produce neat and well structured pyramids, and in the case of the C_{60} Tip, they were simulated as a monolayer of C_{60} which locks itself into place.

2. In **Figures 2.1, 2.4, 2.7, and 2.10**, one can see the location of the adsorbed C_{60} molecules relative to the other adsorbed C_{60} molecules (in particular the number of nearest neighbors) varies.

This is expected to effect the value of the force minimum in a spectrum, and was not accounted for when performing the experiments in this work.

3. The location of the underlying copper atoms relative to the tip varies. This can effect how the adsorbed C_{60} molecule can cleave off the surface when it interacts with the tip (likely only relevant for the *Cu* Tip data). It is considered this could effect the force minimum, however this was not experimentally, computationally, or theoretically investigated in this work.

4. The off-curve for the $C_{60,r}$ system is an overestimate for the off-curve due to the 7 adatom vacancy caused by the surface reconstruction. Therefore the off-curve subtraction adds a change of unknown magnitude to the force minimum when comparing the $C_{60,r}$ and $C_{60,u}$ systems.

5. The STM contrast over the adsorbed C_{60} molecule changes with the surface reconstruction. This poses a problem for the metal tip data, as the STM images were used to decide the spectrum locations. Therefore it becomes difficult, if not impossible, to take spectra at identical sites for both the $C_{60,r}$ and $C_{60,u}$ systems (with a metal tip).

In this work we have calculated a mean force minimum for a spectra taken atop an adsorbed C_{60} molecule. However, due to the effects discussed above, the uncertainty on our mean values is greater than the standard error calculated for our mean values. We also continue to treat the bimodal distribution of C_{60} Tip dataset 2 as two separate mean values for this error analysis.

We can see from looking at **Figures 2.3, 2.5, 2.9, and 2.11** the variation in force minimum (due to the location of the spectrum atop the adsorbed C_{60} molecule) is not reliably quantifiable with data of the precision gathered in this work. Furthermore this data was also checked against the position of the adsorbed C_{60} molecule in the island, however this effect was also deemed to be unquantifiable with data of the precision gathered in this work. However that does not stop the expected variation from influencing the value of the mean. Furthermore, if one was to repeat this experiment and measure spectra over the different sites, in different ratios, then it is reasonable to predict the value of the mean will be effected to a different degree. Yet this variation is not accounted for in the calculated standard error. Therefore a more all seeing uncertainty for our mean values, which accounts for this variation, needs to be deduced.

Given we can not obtain experimental values for these discussed (and unaccounted for) uncertainties from the data presented in this work, we fall to this works simulations and theory to find estimates for the above uncertainties. Where the strong agreement between the

simulations and experiments (see **Chapter 8**) gives us the confidence to do so.

2.4.1 *C60 Tip Uncertainty*

1. Not explicitly calculated, however the rotation data in **Figures 7.1&4.16** gives us an estimate of $\sim 10\,pN$.
2. **Section 6.2.5** estimates this to correction to range from $0\,pN$ for a totally isolated C_{60} molecule, to $17\,pN$ for a complete mono-layer of C_{60} molecules. Given we have neither totally isolated molecules, or a mono-layer, $\sim 10\,pN$ is a reasonable estimate.
3. Not calculated
4. Not calculated
5. Not applicable

We can combine the C_{60} tip uncertainties by adding in quadrature using **Equation 2.2**

$$\Delta W = \sqrt{\Delta X^2 + \Delta Y^2 + \Delta Z^2} \tag{2.2}$$

to get the value of $14\,pN$, rounded to 2 significant figures. Where this uncertainty value is expected to be larger than the one calculated by **Equation 2.1** as we specifically don't want the uncertainty arising from the lines of reasoning in 1., 2., 3., 4., and 5. to be reduced by the sample size we are averaging over.

2.4.2 *Metal Tip Uncertainty*

1. We have simulated data for spectra taken with a Cu Tip, atop $C_{60,u}$ and $C_{60,r}$ molecules, at all 4 different sites (center of a C atom, a C-C bond, a C=C bond, and the center of the adsorbed C_{60} molecule). The value for the spectra taken at the center of the C_{60} was significantly less attractive than the other sites, a result not consistent with the experiment. This suggests the experimental system is more flexible than the computational system. Excluding the obvious inconsistency for the central site, we find a variation of $\sim 10\,pN$ and $\sim 100\,pN$ for the $C_{60,u}$ and $C_{60,r}$ systems respectively. Given we also know there are inconsistencies with the variation in site data between the experimental and computational data, likely being caused by how stiff/flexible the two systems are, we can apply the $\sim 100\,pN$ to both systems as a conservative estimate.
2. No estimate for a Cu Tip, however it is likely of the same order as for the C_{60} Tip so we can give an estimate of $\sim 10\,pN$.

3. Not explicitly investigated, however this effect is convoluted with the measured variation due to the site atop the adsorbed C_{60} (see 1.), therefore we can use the conservative estimate of $\sim 100\,pN$.

4. Not calculated

5. The STM contrast in the images, which were used to select the spectrum location, varies considerably between the $C_{60,u}$ and $C_{60,r}$ molecules. This means is it possible the sites being compared are not truly comparable (in addition to the ratios of the sites measured). This variation can also be estimated using the variation over the simulated sites ($\sim 100\,pN$) as it is another uncertainty stemming from variation due to the spectrum sites measured atop the adsorbed C_{60} molecule.

We can combine the metal tip uncertainties by adding in quadrature. Using **Equation 2.2** we get the value $170\,pN$, rounded to 2 significant figures. Where this uncertainty value is expected to be larger than the one calculated by **Equation 2.1** as we specifically don't want the uncertainty arising from the lines of reasoning in 1., 2., 3., 4., and 5. to be reduced by the sample size we are averaging over.

Part II

COMPUTATIONAL INVESTIGATION

"Now, reality can be whatever I want it to be."

— Thanos, Infinity War (2018). Acquisition of the Reality Stone.

3

DENSITY FUNCTIONAL THEORY

The following discussion of Density Functional Theory (DFT) was adapted from the textbooks *'Electronic Structure Basic Theory and Practical Methods'* and *'Introduction to Computational Chemistry'*, by Richard M. Martin [61] and Frank Jensen [62] respectively. The theses of *D. Egger* [63], *R. Maurer* [64], and *S.S. Harivyasi* [65], and the paper that describes Fritz Haber Institute *ab initio* molecular simulations (FHI-aims) by *V. Blum et al* [66] were also taken into consideration. Furthermore, the introductory reviews for DFT by *Burke et al* [67] and *Morgante et al* [68], and by *Grimme et al* [69] for van der Waals (vdW) interactions, were found to be particularly useful at the start of the authors studies for this work.

3.1 THE HAMILTONIAN

Density Functional Theory (DFT) is a technique used to simulate atomistic systems at a quantum mechanical level. In principle one needs to numerically solve the time-independent Schrödinger Equation

$$\hat{H}\Psi = E\Psi \tag{3.1}$$

to understand the quantum mechanical properties of a system. Where $\hat{H}$, Ψ, and E are the Hamiltonian operator, many-particle wavefunction, and energy eigenvalue of the system respectively. To solve the above eigenvalue problem, we need to define the Hamiltonian for a many-body interacting system. For a many-body interacting system comprised of N electrons and M nuclei; the Hamiltonian can be defined as follows:

$$\begin{aligned}\hat{H} = &- \overbrace{\frac{\hbar^2}{2m_e}\sum_{i=1}^{N}\nabla_i^2}^{\text{Electronic Kinetic energy}} - \overbrace{\frac{\hbar^2}{2}\sum_{a=1}^{M}\frac{1}{M_a}\nabla_a^2}^{\text{Nuclear Kinetic Energy}} \\ &+ \underbrace{\frac{1}{2}\sum_{i=1}^{N}\sum_{\substack{j=1\\ j\neq i}}^{N}\frac{e^2}{|\boldsymbol{r_i}-\boldsymbol{r_j}|}}_{\text{Electron-Electron Repulsion}} + \underbrace{\frac{1}{2}\sum_{a=1}^{M}\sum_{\substack{b=1\\ b\neq a}}^{M}\frac{Z_a Z_b e^2}{|\boldsymbol{R_a}-\boldsymbol{R_b}|}}_{\text{Nucleus-Nucleus Repulsion}} - \underbrace{\sum_{i=1}^{N}\sum_{a=1}^{M}\frac{Z_a e^2}{|\boldsymbol{r_i}-\boldsymbol{R_a}|}}_{\text{Electron-Nucleus Attraction}}\end{aligned} \tag{3.2}$$

where

m_e	mass of an electron
$\boldsymbol{r_i}, \boldsymbol{r_j}$	position vector of the i^{th} and j^{th} electron respectively
M_a, M_b	mass of the a^{th} and b^{th} nucleus respectively
Z_a, Z_b	atomic number of the $a^{th}$and b^{th} nucleus respectively
$\boldsymbol{R_a}, \boldsymbol{R_b}$	position vector of the $a^{th}$and b^{th} nucleus respectively
e	elementary charge (the charge of a proton)

The first two terms of **Equation** 3.2 are the kinetic energy for the electrons and nuclei, the last three terms are the electrostatic electron-electron, nucleus-nucleus, and electron-nucleus interactions derived from Coulomb's law. In **Equation** 3.2 we ignore the effects of magnetic fields, relativistic effects, and quantum electrodynamics. Despite these simplifications, solving the Schrödinger Equation analytically for systems larger than a hydrogen atom is currently too computationally expensive. Therefore, DFT makes a number of approximations and ansatz, as well as reframing the problem at hand, to make the calculations manageable on today's supercomputers.

3.2 BORN-OPPENHEIMER APPROXIMATION

The Born-Oppenheimer approximation from 1927 [70] uses the knowledge that the mass of an electron is much smaller than the mass of a hydrogen nucleus

$$m_e \lesssim \frac{M_a}{1840} \tag{3.3}$$

to simplify the Hamiltonian (**Equation** 3.2). The nuclei are more massive than the electrons, therefore they move more slowly. This allows us to approximate the nuclei as stationary in the reference frame of the electrons. Making this assumption sets the nuclear kinetic energy term to zero, and the nuclear repulsion term becomes a constant, which can be ignored. This simplifies **Equation** 3.2 to

$$\hat{H} = \underbrace{-\frac{\hbar^2}{2m_e}\sum_{i=1}^{N}\nabla_i^2}_{\substack{\text{Electronic}\\ \text{Kinetic Energy}}} + \underbrace{\frac{1}{2}\sum_{i=1}^{N}\sum_{\substack{j=1\\ j\neq i}}^{N}\frac{e^2}{|\boldsymbol{r_i}-\boldsymbol{r_j}|}}_{\substack{\text{Electron-Electron}\\ \text{Repulsion}}} - \underbrace{\sum_{i=1}^{N}\sum_{\substack{a=1\\ a\neq i}}^{M}\frac{Z_a e^2}{|\boldsymbol{r_i}-\boldsymbol{R_a}|}}_{\substack{\text{Electron-Nucleus}\\ \text{Attraction}}} \tag{3.4}$$

which can be condensed into the operator form

$$\hat{H} = \hat{T} + \hat{V}_{int} + \hat{V}_{ext} \tag{3.5}$$

where $\hat{T}$ is the kinetic energy of the electrons, $\hat{V}_{int}$ is the (internal) potential of the electrons repelling each other, and $\hat{V}_{ext}$ is the (external) potential of the stationary nuclei attracting the electrons.

3.3 HOHENBERG-KOHN THEOREMS

Despite reducing the nuclear contribution to a constant, $\Psi(\boldsymbol{r})$ is still a complicated interacting many-body wave-function

$$\Psi(\boldsymbol{r}) = \Psi(\boldsymbol{r_1}, ..., \boldsymbol{r_N}, \boldsymbol{R_1}, ..., \boldsymbol{R_M}) \Longrightarrow \Psi(\boldsymbol{r_1}, ..., \boldsymbol{r_N}) \tag{3.6}$$

comprised of N-electrons. In 1964 Hohenberg and Kohn theorized, and proved, that the N-electron wave-function can be replaced with an electron density [71], see **Figure** 3.1.

$$\begin{array}{ccc} \hat{\boldsymbol{V}}_{ext}(\boldsymbol{r}) & \overset{HK}{\Longleftarrow} & \boldsymbol{\rho_0}(\boldsymbol{r}) \\ \downarrow & & \uparrow \\ \boldsymbol{\Psi_i}(\boldsymbol{r}) & \rightarrow & \boldsymbol{\Psi_0}(\boldsymbol{r}) \end{array}$$

Figure 3.1: Schematic representation of Hohenberg-Kohn theorem. The smaller arrows denote the usual solution to the Schrödinger equation where the potential $V_{ext}(\boldsymbol{r})$ determines all states of the system $\Psi_i(\boldsymbol{r})$, including the ground state $\Psi_0(\boldsymbol{r})$and ground state electron density $\rho_0(\boldsymbol{r})$. The long arrow labeled 'HK' denotes the Hohenberg-Kohn theorem, which completes the circle. **Figure 3.1** was reproduced from **Figure 6.1** of Martin *et al* [61], with variable names changed to be consistent with this work.

The relationships depicted in **Figure** 3.1 can be described as follows;

{THEOREM I} For any system of interacting particles in an external potential $V_{ext}(\boldsymbol{r})$, this potential is determined uniquely, except for a constant, by the ground state particle density $\rho_0(\boldsymbol{r})$.

{THEOREM II} A universal functional for the energy $E(\rho(\boldsymbol{r}))$ in terms of the density $\rho(\boldsymbol{r})$ can be defined, valid for any external potential $V_{ext}(\boldsymbol{r})$. For any particular $V_{ext}(\boldsymbol{r})$, the exact ground state energy of the system is the global minimum value of this functional, and the density $\rho(\boldsymbol{r})$ that minimizes the functional is the exact ground state density $\rho_0(\boldsymbol{r})$.

When we also take into account **Equation** 3.7, which shows that integrating over the electron density returns N,

$$N = \int \rho_0(\boldsymbol{r}) d\boldsymbol{r} \quad \text{where} \quad \rho_0(\boldsymbol{r}) \geq 0 \tag{3.7}$$

and that the potential originating from the atomic nuclei ($V_{ext}(\boldsymbol{r})$) is external to the electrons, theorem I brings us to the conclusion that $\rho_0(\boldsymbol{r})$ completely satisfies the Hamiltonian. Thus $\rho_0(\boldsymbol{r})$ can be used to calculate the ground state energy E_0 in place of the N-electron wave-function,

$$E_0(\rho_0(\boldsymbol{r})) = E_0(\Psi_0(\boldsymbol{r})) \tag{3.8}$$

Hohenberg and Kohn produced two major contributions to DFT. Firstly, they expanded on the original Thomas-Fermi-Dirac DFT [1]to formulate density functional theory as an exact many-body system theory. In addition, with Theorem **II**, Hohenberg and Kohn show we can partition the energy calculation into an internal and external contribution, which provides a frame work to calculate the ground state electron density

$$E_0[\rho_0(\boldsymbol{r})] = F_{HK}[\rho_0(\boldsymbol{r})] + \int V_{ext}(\boldsymbol{r})\rho_0(\boldsymbol{r})d^3\boldsymbol{r} \tag{3.9}$$

where the second term describes the effect of the external potential from the nuclei acting on the electrons, and the first term is the 'Hohenberg-Kohn' functional which incorporates all the internal (kinetic and potential) energies of an interacting electron gas,

$$F_{HK}[\rho_0(\boldsymbol{r})] = T[\rho_0(\boldsymbol{r})] + E_{int}[\rho_0(\boldsymbol{r})] \tag{3.10}$$

with $T[\rho_0(\boldsymbol{r})]$ and $E_{int}[\rho_0(\boldsymbol{r})$ representing the functionals for the kinetic energy and internal interactions of the electrons. Unfortunately, Hohenberg-Kohn Theorems do not provide a method of determining the F_{HK} functional, only proof of its existence.

3.4 KOHN-SHAM ANSATZ

We have applied the Born-Oppenheimer approximation to remove two of the three terms involving the nuclei, **Equation** 3.5, and used Hohenberg-Kohn theory to reframe the problem in terms of the N-electron electron density (**Equations 3.9 & 3.10**). However, the system we want to solve is still a complex N-interacting-bodies problem. In 1965 Kohn and Sham made an additional ansatz to reduce the complexity of the system at hand [75]; *The interacting electron density can be replaced with an identical non-interacting electron density, provided the external potential has been modified to mimic the effect of the electron interactions*, see **Figure 3.2**.

This ansatz reduces the problem from N-interacting-bodies to N-non-interacting-bodies, providing a framework which makes the problem computationally feasible. However, no rigorous mathematical proof has been conceived. Using the Kohn-Sham (KS) approach we can alter **Equation 3.9**

$$E_0[\rho_0(\boldsymbol{r})] \cong T_{KS}[\rho_0(\boldsymbol{r})] + E_{KS}[\rho_0(\boldsymbol{r})] \tag{3.11}$$

where the $\cong$ represents we have made an anzats, $T_{KS}[\rho_0(\boldsymbol{r})]$ is the kinetic energy for our fictitious system of non-interacting electrons, and $E_{KS}[\rho_0(\boldsymbol{r})]$ is the energy calculated from the modified external

1 The 'plum pudding' model of an atom proposed by Thomas [72] and Fermi [73] in 1927. The model was later extended by Dirac [74] in 1930 to include a local exchange approximation, which modern methods are still based upon.

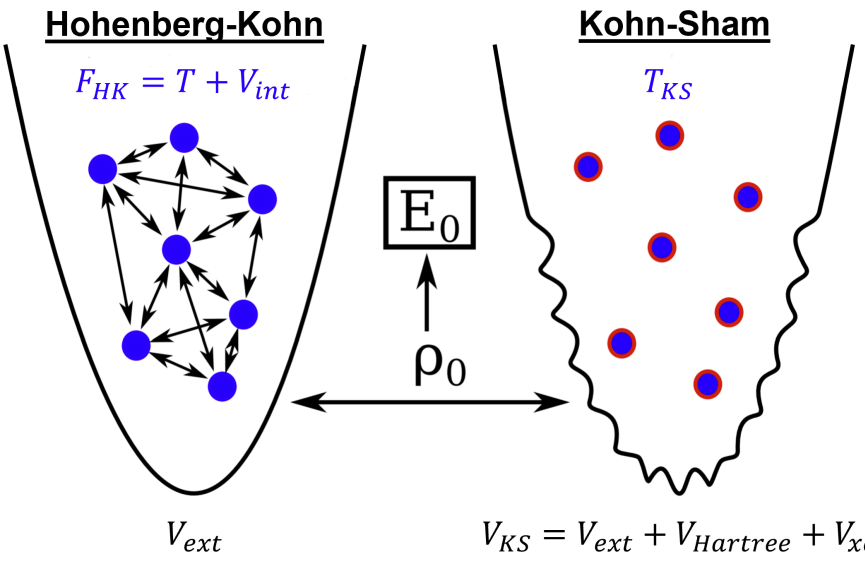

Figure 3.2: Schematic illustration of the Hohenberg-Kohn interacting electron problem (left) and the KS non-interacting electron problem (right). When moving from the system on the left to the system on the right, the method used to incorporate the electron-electron interactions is rephrased from an internal interaction potential (blue equations at the top) to an external interaction potential (black equations at the bottom) acting on non-interacting electrons (the KS ansatz) . **Figure 3.2** was reproduced and edited, with permission, from **Figure 3.2** of the thesis of Reinhard J. Maurer [64].

potential as defined in the KS anzats. We can further expand the $E_{KS}[\rho_0(\boldsymbol{r})]$ term from **Equation 3.11** to separate the classical coulombic repulsion, and external potential from the nuclei, from the more complicated electron-electron interactions terms. In doing so we define a new term, the exchange-correlation (xc) energy ($E_{xc}[\rho_0(\boldsymbol{r})]$)

$$E_0[\rho_0(\boldsymbol{r})] \cong T_{KS}[\rho_0(\boldsymbol{r})] + \underbrace{E_{Hartree}[\rho_0(\boldsymbol{r})] + E_{xc}[\rho_0(\boldsymbol{r})] + E_{ext}[\rho_0(\boldsymbol{r})]}_{E_{KS}[\rho_0(\boldsymbol{r})]} \tag{3.12}$$

where $E_{Hartree}[\rho_0(\boldsymbol{r})]$, $E_{xc}[\rho_0(\boldsymbol{r})]$, and $E_{ext}[\rho_0(\boldsymbol{r})]$ correspond to the Hartree potential, the xc interaction calculated by an xc functional, and the external potential of the real system acting on the electrons in our fictitious system. $E_{Hartree}[\rho_0(\boldsymbol{r})]$ is defined in **Equation 3.13** below, and is analogous to the electron-electron repulsion in **Equation 3.4**;

$$E_{Hartree}(\rho(\boldsymbol{r})) = \frac{1}{2}\int \frac{\rho(\boldsymbol{r})\rho(\boldsymbol{r}')}{|\boldsymbol{r}-\boldsymbol{r}'|} d\boldsymbol{r}d\boldsymbol{r}'. \tag{3.13}$$

We can express $E_{xc}[\rho(\boldsymbol{r})]$ in terms of the Hohenberg-Kohn functional

$$E_{xc}[\rho(\boldsymbol{r})] \cong F_{HK}[\rho_0(\boldsymbol{r})] - T_{KS}[\rho_0(\boldsymbol{r})] - E_{Hartree}[\rho_0(\boldsymbol{r})] \tag{3.14}$$

which is accomplished by equating **Equation 3.9** to **Equation 3.12** and rearranging. By substituting **Equation 3.10** into **Equation 3.14** we can express $E_{XC}[\rho(\boldsymbol{r})]$ in terms of the kinetic and potential energies

$$E_{xc}[\rho(\boldsymbol{r})] \cong \underbrace{T[\rho_0(\boldsymbol{r})] - T_{KS}[\rho_0(\boldsymbol{r})]}_{\substack{\text{Kinetic Correlation} \\ \text{Energy}}} + \underbrace{E_{int}[\rho_0(\boldsymbol{r})] - E_{Hartree}[\rho_0(\boldsymbol{r})]}_{\substack{\text{Potential Exchange} \\ \text{Correlation Energy}}} \tag{3.15}$$

which shows E_{xc} provides the kinetic correlation energy, and the potential exchange-correlation energy. As mentioned earlier, applying the KS anzats simplifies the problem down to N-non-interacting electrons, which allows us to construct a solvable Schrödinger Equation

$$[-\frac{\hbar^2}{2m_e}\nabla^2 + V_{KS}(\boldsymbol{r})]\psi_i(\boldsymbol{r}) = \varepsilon_i\psi_i(\boldsymbol{r}) \tag{3.16}$$

where $\psi_i(\boldsymbol{r})$ are the KS orbitals, and ε_i are the corresponding KS energy eigenvalues, and $V_{KS}(\boldsymbol{r})$ is the modified external potential introduced by the KS anzats for approximating the electron interactions

$$\begin{aligned} V_{KS}(\boldsymbol{r}) &= V_{ext}(\boldsymbol{r}) + \frac{\delta E_{Hartree}}{\delta\rho_0(\boldsymbol{r})} + \frac{\delta E_{xc}}{\delta\rho_0(\boldsymbol{r})} \\ &= V_{ext}(\boldsymbol{r}) + V_{Hartree}(\boldsymbol{r}) + V_{xc}(\boldsymbol{r}). \end{aligned} \tag{3.17}$$

We can see from **Equation 3.16** that solving the KS Schrodinger equation returns us a set of wave-functions (orbitals). By definition (of the KS approach), we can link the KS orbitals to the interacting system via the ground state density

$$\rho_0(r) = \sum_{i=1}^{N} |\psi_i(\boldsymbol{r})|^2. \tag{3.18}$$

However, the isolated wave functions constructed by Kohn-Sham DFT bare little physical significance as they are the solution to the fictitious KS system they emerge from.

SELF CONSISTENT CYCLE The KS equations involve coupled quantities (V_{KS} and $\rho_0(\boldsymbol{r})$), therefore they need to be solved self-consistently, within a self consistent field cycle, for a specific geometry. To start the process, an initial guess for the KS potential $V_{KS} = V_i$ and the corresponding electron density $\rho_0(\boldsymbol{r}) = \rho_i$ (for example the electron densities of the isolated gaseous atoms and corresponding V_{KS}) needs to be supplied and solved. The results from this step are then used to construct a new, better, guess; $V_{KS} = V_{i+1}$ and a corresponding

electron density $\rho_0(\boldsymbol{r}) = \rho_{i+1}$. This process repeats $V_i \rightarrow \rho_i \Rightarrow V_{i+1} \rightarrow \rho_{i+1} \Rightarrow V_{i+2} \rightarrow \rho_{i+2}$ until the system is converged. Where we define system convergence as when the change of the system between two iterations is smaller than the predefined convergence criteria.

3.5 THE EXCHANGE-CORRELATION FUNCTIONAL

An exact form of the xc functional is yet to be found, if one exists at all. Many attempts have been made to create xc functionals, resulting in an explosion of new approaches since 2005, see **Figure 3.3**. We can broadly separate xc functionals into two groups; local density approximation, and generalized gradient approximation. The local density approximation approach was first suggested by Kohm and Sham in their original 1965 paper [75]

$$E_{xc}^{LDA}[\rho_0(\boldsymbol{r})] = \int \rho_0(\boldsymbol{r}) \epsilon_{xc}^{LDA}(\rho_0(\boldsymbol{r}), \boldsymbol{r}) dr \tag{3.19}$$

where $\epsilon_{xc}^{LDA}(\rho_0(\boldsymbol{r}), \boldsymbol{r})$ is the energy density at point $\boldsymbol{r}$ as a function of the electron density $\rho_0(\boldsymbol{r})$. As the energy density for a given point is related only to the electron density at the given point this approach is defined as local. The generalized gradient approximation expands this approach to incorporate the gradient of the local electron density

$$E_{xc}^{GGA}[\rho_0(\boldsymbol{r})] = \int \rho_0(\boldsymbol{r}) \epsilon_{xc}^{GGA}(\rho_0(\boldsymbol{r}), \nabla\rho_0(\boldsymbol{r}), \boldsymbol{r}) dr \tag{3.20}$$

where $\epsilon_{xc}^{GGA}(\rho_0(\boldsymbol{r}), \nabla\rho_0(\boldsymbol{r}), \boldsymbol{r})$ is the energy density at point $\boldsymbol{r}$ as a function of the electron density $\rho_0(\boldsymbol{r})$, and the gradient of the electron density $\nabla\rho_0(\boldsymbol{r})$.

In this work the generalized gradient approximation type xc functional Perdew–Burke–Ernzerhof (PBE) was used exclusively throughout. The PBE functional was selected as it provides reliability for both the geometric [77] and electronic structure [78] of metal-organic interfaces

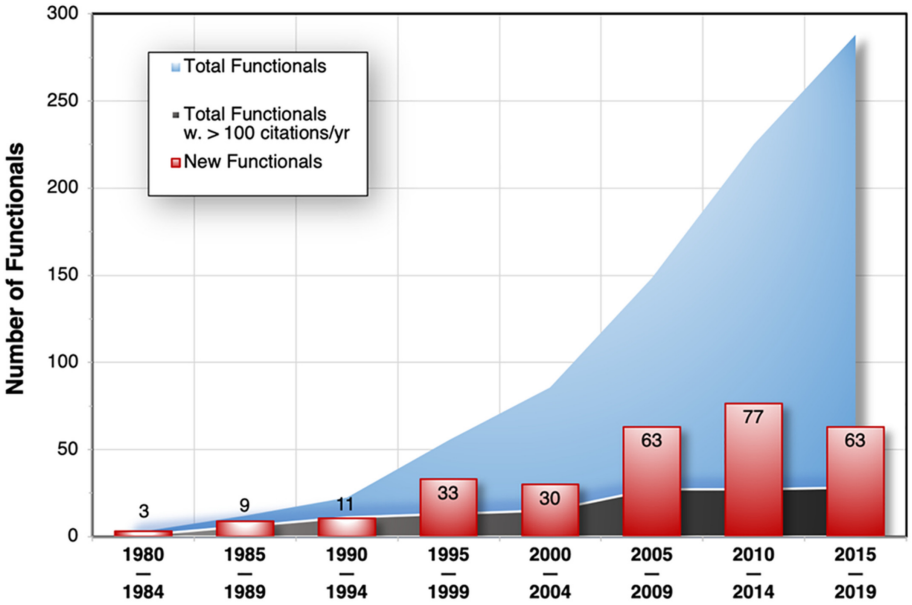

Figure 3.3: Estimate of the total number of exchange-correlation functional approximations created since 1980. The black area represents the number of functionals averaging more than 100 citations per year. The assessment was obtained by cross-referencing databases maintained by the *Department of Biomedical and Chemical Engineering and Science at the Florida Institute of Technology* [76] with those released in the LibXC software library and by using Google Scholar to estimate the number of citations for each functional [68]. **Figure 3.3** is reproduced with permission from **Figure 1** of Morgante *et al* [68].

3.6 VAN DER WAALS INTERACTIONS IN DFT

Van der Waals (vdW) interactions are largely a quantum mechanical electron correlation effect. However, most commonly used xc functional approximations (i.e. local density approximation and generalized gradient approximation) are semi-local, and therefore do not treat vdW interactions in the long-range regime. It is also known that failing to incorporate the missing interaction can result in less accurate simulated results, particularly in systems where the interactions of interest are governed by processes other than chemical bonding. Therefore, the practical DFT+vdW approach has been developed. In this scheme, the DFT calculation is supplemented with an additional potential. This potential is specifically designed to complete the description of vdW interactions when paired with the xc functional. Fortunately, most xc functionals are able to adequately describe the vdW interactions in the short range regime. This means the problem of accurately modeling the vdW interaction outside of DFT is reduced to only modeling the vdW interactions accurately in the long range regime.

A common theoretical base for vdW corrections is a pairwise interaction taking the form of a simple power law power. **Equation 3.21** gives a pairwise power law of the n^{th}power,

$$U_{vdW} = \frac{C_n}{R^n} \tag{3.21}$$

where n, U_{vdw}, R, and C_n are; the integer determining the power law, and the resultant vdW potential, the inter-atomic spacing, and the corresponding coefficient for the n^{th} power, respectively.

A commonly used power law for vdW corrections is a pairwise power law corresponding to $n = 6$ (C_6R^{-6}) (C6). It can be found in many modeling methods, such as the well known Lennard-Jones potential, Grimme's D3 (D3) **(Section 3.6.1)**, and the Tkatchenko-Scheffler vdW and vdW^{surf} (TS) methods (detailed in **Section 3.6.2**) [79][80][81] . However, more complex power laws may also need to be considered. Effects such as electron shielding can be incorporated into the TS vdW^{surf} method through a pairwise model including a pairwise power law corresponding to $n = 3$ (C_3R^{-3}) (C3) **(Section 3.6.2)**. On the other hand, the Many Body Dispersion (MBD) [82] **(Section 3.6.3)** moves away from a simplistic pairwise interaction by introducing a harmonic oscillator model. This framework results in the natural implementation of multiple power laws, as well as extending the scope of the vdW correction to include many body calculations on top of pairwise interactions [69].

As the vdW corrections described above are calculated separately to the DFT, it is possible the range the vdW corrections cover will overlap with the range in which vdW interactions are inherently accounted for by DFT. This effect gives rise to the 'double counting' issue. The double counting problem is resolved by introducing a damping function,

which decays the long range vdW potential in the short range regime (where the DFT naturally accounts for the vdW potential).

In this work three types of vdW correction were used in conjunction with the Perdew–Burke–Ernzerhof (PBE) xc; Grimme's D3 (D_3) [83], the Tkatchenko-Scheffler *vdW* and vdW^{surf} (TS) methods [79][80][81], and the Many Body Dispersion (MBD) method [82].

3.6.1 *Grimme's D3*

Grimme's D3 (D_3) is a well parameterized semi-empirical pairwise scheme primarily calculating C6 interactions. D_3 requires only the atomic positions to function, making it a cheap and versatile scheme. The atomic geometry is used to calculate the coordination number of each atom, allowing the interaction strength between the two atoms to be adjusted based on their coordination numbers. The effect of the coordination number on the strength of an atom's vdW interaction has been parameterized in advance using DFT simulations of various systems tailored to calculating the long range interaction [83]. In addition, the damping function has been parameterized to better complement commonly used xc functionals such as PBE [69].

An important difference between D_3 and the other vdW correction schemes discussed in this work in the input data required to calculate the vdW corrections. The TS and MBD methods require the electron density calculated from DFT, thus these methods are usually carried out on a supercomputer along with the DFT calculations. D_3, on the other hand, is carried out independently to how a particular geometry was created, as it requires only the atomic geometries. Therefore, a particularly useful feature of D_3 , is the fact that it can be easily computed on a conventional computer. This feature enabled an easy comparison between other vdW corrections, aiding the process of finding the best vdW correction for the system being modeled.

3.6.2 *Tkatchenko-Scheffler's* vdW *and* vdW^{surf}

The Tkatchenko-Scheffler *vdW* and vdW^{surf} (TS) approach incorporates the electron density from DFT into the calculation of C6 interactions [79]. The C6 coefficient between two free atoms of dissimilar species ($C_{6,AB}$) is calculated from the C6 coefficients between two free atoms of the same species ($C_{6,AA}$ and $C_{6,BB}$), and the static polarizability of the free atoms. The TS method applies the knowledge that the polarizability of an atom is directly related to the effective volume of an atom. Here, the effective volume is defined as the volume occupied by the electron density belonging to the atom, as determined by Hirshfeld partitioning of the DFT electron density. The effective volume of the atom in question is thus used to modify the C6 coefficients to obtain

coefficients specific to each atom in its local environment for use in the pairwise vdW interactions [79].

The TS method is known to give poor results when the atoms can not be thought of as having a volume surrounding the nuclei containing the electron density of that atom, such as systems with delocalized electrons. To help remedy this inaccuracy, a further C3 interaction for metals can be considered under the following assumption; the bulk metal being modeled is a semi infinite slab (infinite in the X and Y directions, and along the Z direction moving into the bulk crystal) [80][81].

3.6.3 *Many Body Dispersion*

The Many Body Dispersion (MBD) approach can be thought of as an extension to the TS approach. Compared to TS approach, the MBD approach includes a more theoretically complete description of complex electron screening effects, as well as many body contributions (3 or more interacting bodies). This is achieved using a quantum harmonic oscillator model, in addition to the atomic portability used in TS (**Figure 3.4**). The MBD approach is more theoretically complete than TS and thus tends to yield more accurate results, however comes at the cost of computational expense. For details on the theory behind MBD see Tkatchenko *et al* [82] and Grimme *et al* [69].

Multiple versions of MBD have been released as the theory behind the method is improved. In this work, the default MBD@rsSCS implementation from FHI-aims pre-2019 [84] was used exclusively.

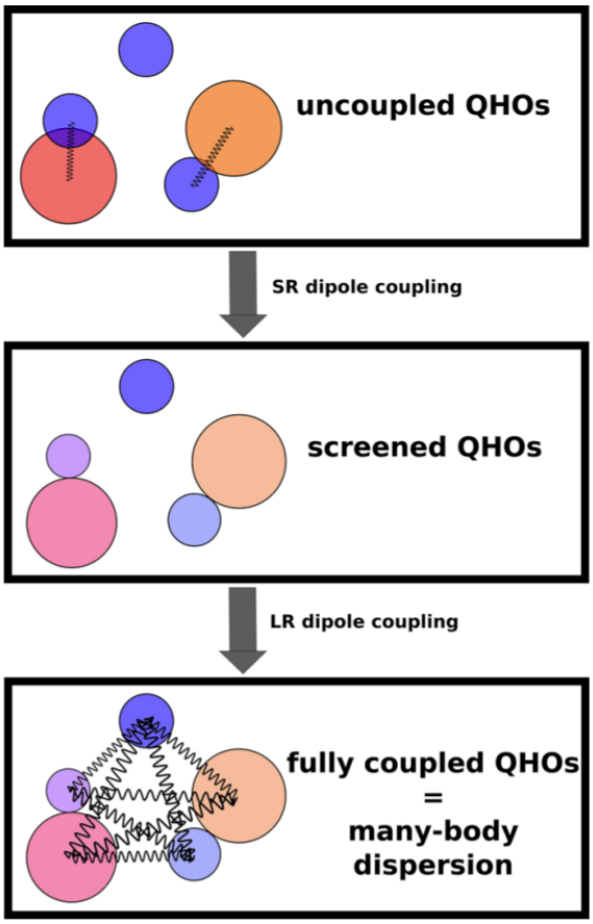

Figure 3.4: Schematic illustration of how to arrive at the Many Body Dispersion (MBD) energy based on the Tkatchenko-Scheffler vdW and vdW^{surf} (TS) method. The starting points are the oscillators from the TS model, which are depicted as differently sized and colored circles. First, these are coupled at short range via dipole–dipole interactions. A self consistent solution of these coupled oscillators yields a new set of screened oscillators. This is schematically depicted as a change in size and color of initially overlapping circles. Note that the isolated oscillator (depicted as the non-overlapping circle) is not affected by short-range dipole–dipole coupling and remains unchanged. In the last step, the screened oscillators interact through dipole–dipole coupling at long range, which yields the final many-body dispersion energy. **Figure 3.4** is reproduced with permission from **Figure 10** of Grimme *et al* [69].

3.6.4 *Choice of van der Waals Correction*

The choice of vdW correction used in a calculation is dependent on the type of calculation being performed. Being right for the wrong reason is a possible issue users can run into. It occurs when a result given by a vdW correction appears correct initially, but ends up being correct for the wrong reasons. For example, the correction scheme could overestimate the attraction caused by Cu-C interactions, but underestimate attraction caused by C-C atoms. These errors could then combine in such a way that the two errors cancel out and produce what appears to be an accurate vdW correction for that specific calculation, but not in future calculations. To avoid this situation, one needs to understand how a vdW correction works, and when it is likely to be accurate or inaccurate. This is especially important in this work as the vdW correction provides a large component of the simulated force spectra.

In this work, we have the luxury of modeling a well studied physical system. Therefore our system has well known and experimentally measured parameters which can help guide us when deciding which vdW correction to use (examples being force minima, charge transfer, adsorption geometry). In the case of this work, the final value of interest is primarily the force minima of the force spectra. Therefore the vdW correction used for the simulated force spectra was selected based on how well the scheme replicated the experimental force spectra measured in this work.

Four vdW corrections were considered in this work **(see Sections 3.6.1, 3.6.2, & 3.6.3)**. It was found both forms of the TS correction overestimated the force minimum by an approximate factor of two. This result is not surprising as the TS method has no robust consideration of electron shielding, meaning systems with delocalized electrons (such as the ones in the work) tend to be overestimated.

The D_3 and MBD corrections, on the other hand, were in close agreement with both each other and the experimental data for the metallic and C60 functionalized tips. This result is also expected. The D_3 correction scheme is an empirical approach that has been fitted from many thousands of accurately calculated systems, including systems involving C_{60} molecules and other carbon based molecules. Whereas the MBD correction scheme is a more theoretically rigorous approach which crucially includes methods to incorporate the effects of delocalized electrons and subsequent electron shielding (something the TS approach lacked). Given the D_3 correction scheme is not implemented in FHI-aims, this leaves the MBD correction scheme as the only accurate and practical correction scheme to be used for this work. We can further check the results from the calculations with MBD by applying the D_3 correction using the geometry converged with the MBD scheme. All the simulated force spectra presented in this work

were calculated using the MBD vdW correction scheme, and checked with the D_3 scheme.

3.7 IMPLEMENTING DFT IN FHI-AIMS

In practice, a computational physicist does not need the ability to perform DFT calculations from first principle, or be able to code ways to self-consistently solve the KS equations. Instead, vast software packages such as Fritz Haber Institute *ab initio* molecular simulations (FHI-aims) exist. These software packages perform the quantum mechanical calculations for the user, making it the user's job to understand how to provide accurate input parameters to avoid *the garbage in garbage out* trap, where a calculation is not setup correctly resulting in the results being inaccurate.

3.7.1 *Why FHI-aims*

FHI-aims by Blum et al. [66] was selected for this work after taking into account practical factors such as;

1. The supervisory team's prior expertise with compiling and using FHI-aims on various local, regional, and national high performance clusters, with varying hardware configurations.

2. The large array of implemented techniques including; various vdW correction schemes that were being actively worked on, multiple charge partitioning schemes, native calculation of density of states.

3. The FHI-aims package has been tested and bench marked for a variety of systems, including systems comprised of aromatic organic molecules on coinage metals Hofmann et al. [78], Liu, Tkatchenko, and Scheffler [77]. Given this work involves C_{60} on copper, this testing is particularly relevant for this work.

4. In FHI-aims calculations are performed using numeric atom-centered orbitals. This allows for periodic ***or*** open boundary conditions to be used, allowing the efficient calculation of both periodic systems (C_{60} adsorbed on the Cu(111) surface, **Chapters 4,5,6**) and cluster/gaseous systems (gaseous C_{60}, **Chapters 4,5,6,7**) without needing to approximate either of the situations.

5. An additional benefit of the numeric atom-centered orbitals approach used by FHI-aims is the ability to get a breakdown of the force and energy components assigned to individual atoms. The implications of this are discussed at great length in **Chapter 5**, where multiple methods for calculating force and potential spectra, or correcting for approximations, were developed.

6. FHI-aims has the ability to use a converged electronic structure of similar geometry as a starting point of a new geometry. The utilization of this feature greatly reduced the cost of simulating force spectra in DFT.

7. Looking at the practical side of FHI-aims, we see it has been optimized for efficient parallelization via ELPA, a package designed for solving eigenvalue problems in electronic structure calculations Marek et al. [85]. This aided in running FHI-aims on multiple high perforce clusters of varying capacity, with a huge variation in the number of nodes and processors available for each calculation.

Versions of FHI-aims used in this work:

- *Fritz Haber Institute ab initio molecular simulations: FHI-aims 200112_2* [86]
- *Fritz Haber Institute ab initio molecular simulations: FHI-aims 210226* [87]
- *Fritz Haber Institute ab initio molecular simulations: FHI-aims 210716_1* [84]

3.7.2 *Self Consistent field Cycle*

The process of a self consistent cycle is described in **Section 3.4**, however in theory this process could iterate on forever, with ever smaller changes between each cycle. Therefore a set of convergence criteria need to be defined to tell FHI-aims when the self consistent field cycle has attained an acceptable level of accuracy.

3.7.3 *Geometry Optimization*

When finding a converged system, the atomic core positions are allowed to relax in addition to the electron density. A reasonable starting geometry (initial guess) is supplied to the Fritz Haber Institute *ab initio* molecular simulations (FHI-aims) package. This geometry is calculated using molecular dynamics or previous DFT work, then the electron density optimized for the atomic core positions. This is carried out using the self consistent field procedure described above. The forces acting on each atom are calculated using the converged electron density, and the atomic core positions moved (relaxed) accordingly. This sequence of events is repeated until the system geometry is converged based on a set of convergence criteria, such as the maximum resultant force acting on any single atom. The effect of the geometry relaxation is to minimize the maximum force acting on individual atoms, which has the effect of minimizing total energy of the system.

Geometry relaxation can be considered a computationally expensive step. Therefore, reducing the number of atoms being relaxed in larger systems can be advantageous. When relaxing organic molecules on metal surfaces, such as C_{60} on $Cu(111)$, it can be assumed only the top few layers of Cu atoms will be geometrically perturbed, with the lower layers undergoing minimal or no movement. Therefore only the top 3 layers of the metal slab need to be unconfined, with the lower layers being confined under the approximation they do not relax. This approximation saves computational resources.

4

SIMULATED NC-AFM SYSTEMS AND SYSTEM CONVERGENCE

4.1 BULK COPPER

To accurately describe systems involving the Cu(111) surface in FHI-aims, convergence tests for Cu in bulk form were preformed. In **Section 4.1**, convergence is defined as the minimum energy of the system with respect to a varying input parameter. The bulk copper was simulated as an infinite Face Centered Cubic (FCC) crystal, with the FCC bravais lattice unit cell being used for all convergence testing (**Figure 4.1**). The convergence of the Cu system was tested against k-point sampling, and for the lattice constant of the Copper FCC Bravais Lattice unit cell (a_{Cu}). Where the k-point sampling in this context is how one samples the first Brillouin zone, and arises if the system is periodic [88]. The FCC geometry was generated using the atomic simulation environment python library. Using the atomic simulation environment, the atoms were placed at the correct crystallographic lattice points for an Face Centered Cubic (FCC) unit cell, and not allowed to relax during the DFT convergence calculations as this approach is consistent with using the primitive unit cell. All bulk copper convergence testing was performed on the Intel based University Of Leeds Arc4 HPC [89], using the 210716_1 FHI-aims release [84]. The FHI-aims parameters and self consistent field convergence criteria given in **Table 4.1** were used, unless otherwise stated. The FHI-aims 2010 species default parameters were used exclusively throughout this works.

4.1.1 *K-Point Sampling*

Convergence of the k-point sampling was calculated using the infinite Cu FCC bravais lattice unit cell described in **Section 4.1** above. K-points from 1 to 60 in all three directions ($k_{abc} = k_a = k_b = k_c$) were convergence tested using both the FHI-aims 2010 default Light Species Settings (LSS) and FHI-aims 2010 default Tight Species Settings (TSS), for lattice constants of $a_{Cu} = 3.6310$ Å, and $a_{Cu} = 3.6315$ Å. Where $a_{Cu} = 3.6310$ Å is a preferred lattice constant for the TSS, and $a_{Cu} = 3.6315$ Å a preferred lattice constant for LSS, as discussed in **Section 4.1.2**. The k-points were specified in the control file for FHI-aims using the **`k_grid n1 n2 n3`** parameter, where **`n1 = n2 = n3`** due to the symmetry of the system. **Figure 4.2** shows the k-point convergence data described above. From **Figure 4.2** we can see moving from LSS to TSS, or changing the lattice constant from $a_{Cu} = 3.6315$ Å to $a_{Cu} = 3.6310$ Å, has no

FHI-aims Parameter Key	FHI-aims Parameter Value	Comments
xc	**pbe**	
charge	**0**	
spin	**none**	
relativistic	**atomic_zora scalar**	
adjust_scf	**always 2**	
occupation_type	**gaussian 0.1**	
mixer	**pulay**	
n_max_pulay	**8**	
sc_accuracy_etot	**10^{-6}, 10^{-8},or 10^{-10}**	**10^{-6}** was exclusively used for k-point sampling convergence testing
sc_accuracy_eev	**10^{-3}, 10^{-4},or 10^{-5}**	**10^{-3}** was exclusively used for k-point sampling convergence testing
k_grid	**n1 n2 n3**	**n1=n2=n3** for FCC bravais lattice unit cell. Values of **25**, **42**, and **50** were used for lattice vector convergence testing

Table 4.1: Simulation parameters for bulk Cu convergence testing

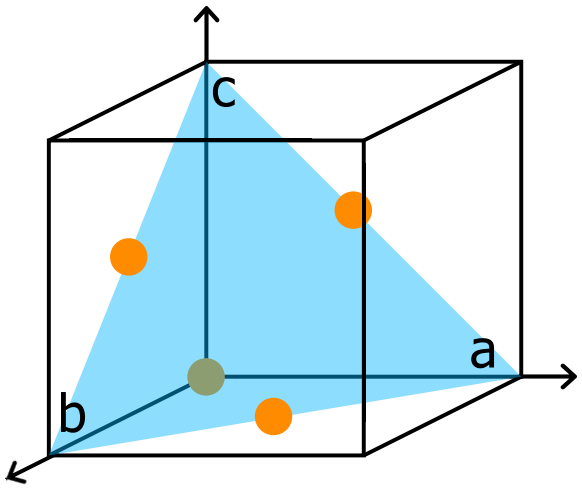

Figure 4.1: FCC bravais lattice unit cell. The 4 atoms are marked as orange circles. The (111) plane, as defined using miller indices, is visualized as a shaded blue region. The unit vectors along the X, Y and Z directions are labeled a, b, and c respectively, where a=b=c.

significant effect on the distribution of the relative energies or the values of the individual relative energies. The grey, red, and green shaded regions in **Figures 4.2 A&B** show that using k_{abc} values of 25, 42 and 50 give corresponding uncertainties of up to $\pm 0.6\,meV$, $\pm 0.05\,meV$, and $\pm 0.02\,meV$ respectively for the full system. These uncertainty values can then be divided by four to give the error per atom values of; $\Delta E_{Cu,atom} = \pm 0.15\,meV$, $\pm 0.0125\,meV$, and $\pm 0.005\,meV$. Where the uncertainty is calculated relative to data points of larger k_{abc} values, under the assumption the system is more converged (and thus more accurately simulated) for larger k_{abc} values. Visually, this can be described as comparing data for k_{abc} values at the coloured vertical dashed lines to the data located to the right of the coloured vertical dashed lines.

When applying these results to different sized systems, the k-points need to be scaled relative to the difference in the lattice vectors of the system of interest and the system the k-point convergence was calculated for. If the lattice vector in a given direction is doubled, then the number of k-points along that direction should be halved. **Equation 4.1** represents this statement analytically,

$$\frac{a_{1,n}}{a_{2,n}} = \frac{k_{2,n}}{k_{1,n}} \tag{4.1}$$

where $a_{1,n}$ and $a_{2,n}$ are the lattice vectors of systems 1 and 2 in the n^{th} direction, and $k_{1,n}$ and $k_{2,n}$ are the number of k-points for systems 1 and 2 in reciprocal space, corresponding to the n^{th} direction defined by the real space lattice vector a_n. **Equation 4.1** needs to be applied 3 times for a 3 dimensional system; once along each lattice vector direction.

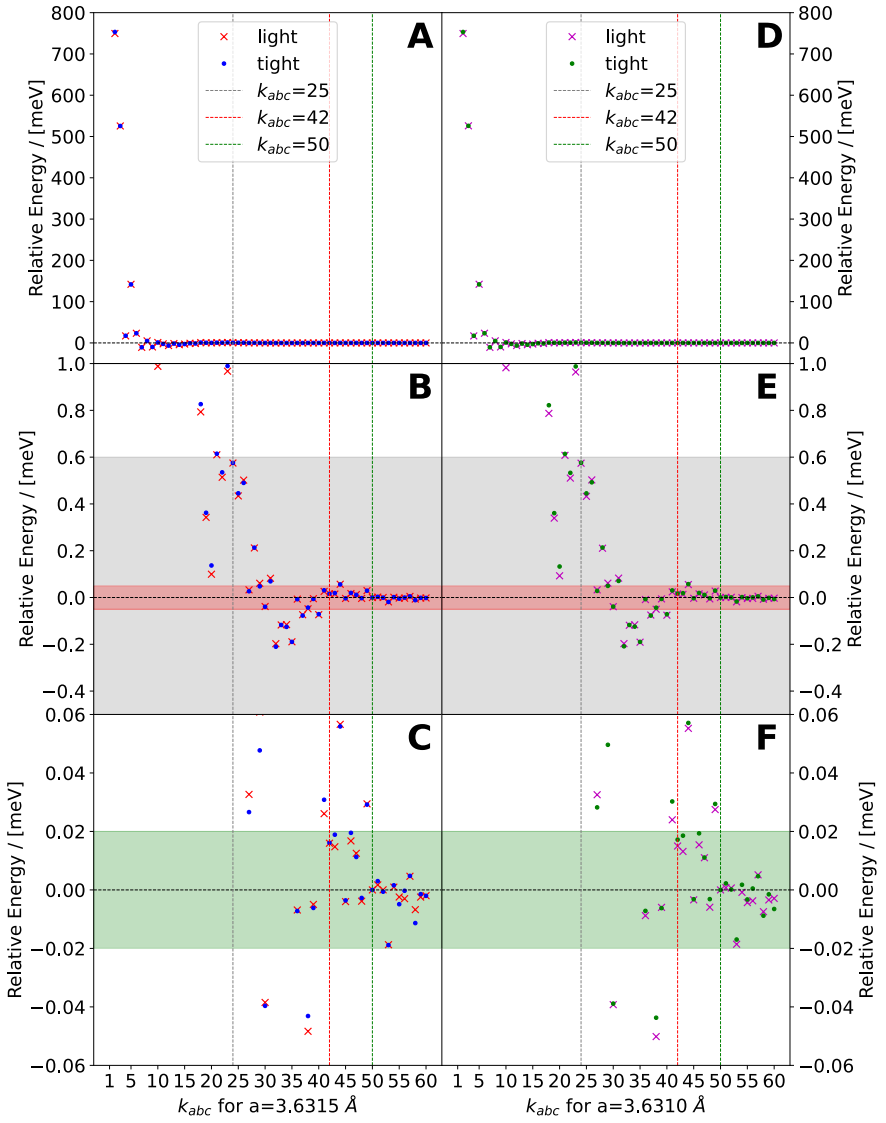

Figure 4.2: K-point sampling convergence data for the FCC bravais lattice system for the lattice constants $a_{Cu} = 3.6315$ Å and $a_{Cu} = 3.6310$ Å. K-points from 1 to 60 were tested for $k_{abc} = k_a = k_b = k_c$ using the LSS (crosses) and TSS (dots). The grey, red, and green vertical dotted lines mark $k_{abc} = 25, 42$, and 50 respectively. The grey, red and green shaded regions represent the uncertainty of the energy for the $k_{abc} = 25, 42$, and 50 systems respectively. The uncertainty is calculated relative to data points of larger (more converged) k_{abc} values, located to the right of the corresponding vertical lines. Plots **A**, **B**, and **C** display the same data corresponding to $a_{Cu} = 3.6315$ Å, with the y axes displaying progressively smaller relative energy ranges. Plots **D**, **E**, and **F** display the same data corresponding to $a_{Cu} = 3.6310$ Å, with the same y axes limits as plots **A**, **B**, and **C**. The relative energy is calculated and plotted relative to the energy of the $k_{abc} = 50$ system.

In this work the following copper geometry is incorporated within more complex systems (see **Figure 4.7 A, B, and C** for a visual definition of the Cu(111)-(4x4) system); A semi infinite copper slab (periodic along the a and b directions) cleaved along the (111) plane (defined using miller indices). The unit cell vectors a and b have length $a = b = 10.2700$Å, allowing for 4 Cu atoms along the a and b directions of the unit cell. Unit vector $c = 100$Å, resulting in most of the unit cell being vaccum space. The number of atomic layers along the vertical direction varies from n=3 to n=15, where n denotes the number of complete layers in the slab (Cu(111)-(4x4)). The convergence data for the FCC bravais lattice system therefore needs to be applied to the new Cu(111)-(4x4) system using **Equation 4.1**, where $a_2 = 2.828\, a_1$, $b_2 = 2.828\, b_1$, and $c_2 = 27.537\, c_1$. **Figure 4.3** contains a graphical representation of **Equation 4.1** being applied to the Cu(111)-(4x4) system when calculating the k_{ab}-points with respect to the convergence data in **Figure 4.2**. Although 18 k_{ab}-points for the Cu(111)-(4x4) system is ideal (corresponding to an uncertainty of $\pm 0.005\, meV$ per atom), a lower value of 8 k_{ab}-points was selected (corresponding to an uncertainty of $\pm 0.15\, meV$ per atom). This decision was made to balance the trade-off between computational cost and system k-point convergence, as explained in **Section 4.1.3**.

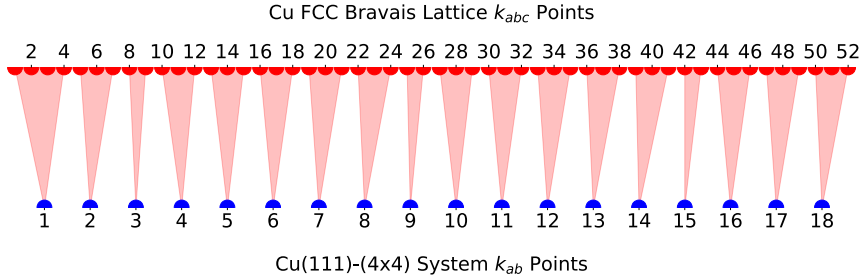

Figure 4.3: A graphical representation of **Equation 4.1** being applied to the Cu(111)-(4x4) system when calculating the k_{ab}-points with respect to the convergence data in **Figure 4.2** for an infinite Cu FCC system. The red dots on the top axis represents the k_{abc}-points in the infinite Cu FCC system, the Blue dots on the bottom axis represent the k_{ab}-points of the Cu(111)-(4x4) system.

When applying the energy uncertainty per atom values to the simulated force spectrum systems in **Section 4.3**, the errors coming from each Cu atom need to be added in quadrature using **Equation 4.2**

$$\Delta E_{system,Cu} = \sqrt{n_{Cu}(\Delta E_{Cu,atom})^2}, \tag{4.2}$$

where $\Delta E_{system,Cu}$ is the portion of the error in the energy of the total system coming from the Cu atoms, n_{Cu} is the number of Cu atoms in the system, and $\Delta E_{Cu,atom}$ is the error on a single Cu atom for the specified convergence criteria. For the $C_{60,r}$ system described

in **Figure 4.18**, $n_{Cu} \approx 100$, and $\Delta E_{Cu,atom} = 0.15$ meV (see **Figure 4.3** and **Equation 4.1**). Applying **Equation 4.2**, one gets an uncertainty of $\Delta E_{system,Cu} \leq 1.5$ meV for all the systems in **Section 4.3**. Given the energy of the system is $\sim 4.5 \times 10^6$ eV, this gives a relative error of $\frac{1}{3} \times 10^{-9}$ %. Furthermore, this uncertainty is an upper limit estimate for two reasons. Firstly, the system comprised of a Cu Tip probing a $C_{60,r}$ surface **(Figure 4.18)** contains the most Cu atoms. Secondly, the simulated force spectra are calculated relative to the point of furthest tip-sample separation. As the Cu atoms at the bottom/top of the slabs (bottom for the surface, top for the tip) are minimally perturbed during the spectrum, the uncertainty from those atoms acts more like a systematic offset, which is accounted for naturally during the post-processing of simulated force spectrum data (see **Section 5**). This error analysis also serves as an upper bound estimate for the uncertainty arising from the lattice constant, as the uncertainty values in **Section 4.1.2** are of a similar magnitude.

4.1.2 *Copper Lattice Constant (a)*

Convergence of the lattice constant for the FCC bravais lattice system described in **Section 4.1** was calculated for both LSS and TSS. The calculations were performed using k_{abc} values of 25, 42 and 50. The k-points were specified in the control file for FHI-aims using the **`k_grid n1 n2 n3`** parameter, where **`n1=n2=n3`** due to the symmetry of the system. **Figure 4.4** displays how the lattice constant (a) converges for the k_{abc} values 25, 42, and 50. **Figures 4.4 A&B** display data gathered using LSS species settings, whereas **Figures 4.4 C&D** contain data gathered with TSS. Looking at **Figures 4.4 B&D** we can see the lattice constant for LSS species settings lies in the range $a_{Cu} = 3.6315$ Å to $a_{Cu} = 3.6318$ Å, whereas for TSS the lattice constant lies in the range $a_{Cu} = 3.6309$ Å to $a_{Cu} = 3.6312$Å. Looking closely at **Figures 4.4 B&D**, there appears to be greater numerical noise as the k_{abc} value increases, seen as the blue dotted line appearing as the smoothest line on both plots. Is is plausible that more stringent convergence criteria were needed for accurate data at larger k_{abc} values, with small numerical noise being present in the data at less robust convergence criteria. To test this hypothesis, further calculations were performed. **Figure 4.5 A** concerns the **`sc_accuracy_etot`** criteria. This figure shows the energy of the system is not fully converged at **`sc_accuracy_etot = 10^-6`**, as the yellow dotted line and blue triangle line are not identical. However, setting **`sc_accuracy_etot < 10^-6`** does not have a significant impact on the smoothness of the line, or the lattice constant corresponding to the minimum energy. **Figure 4.5 B** shows setting **`sc_accuracy_eev < 10^-3`** has no effect on the data about the energy minimum as all three lines are identical. Overall **Figure 4.5** suggests the roughness of the lattice constant convergence data is likely not just computational noise within this FCC Cu system simulated in the FHI-aims environment. In **Figure 4.5 A** the value **`sc_accuracy_eev = 10^-5`** was used to ensure the **`sc_accuracy_eev`** parameter was not the limiting factor of the calculations. In **Figure 4.5 B** a value **`sc_accuracy_tot = 10^-8`** was used to ensure the **`sc_accuracy_tot`** parameter was not the limiting factor of the calculations. See **Section 4.1.1** for representative comparison of these energy uncertainties with the full systems in **Section 4.3**.

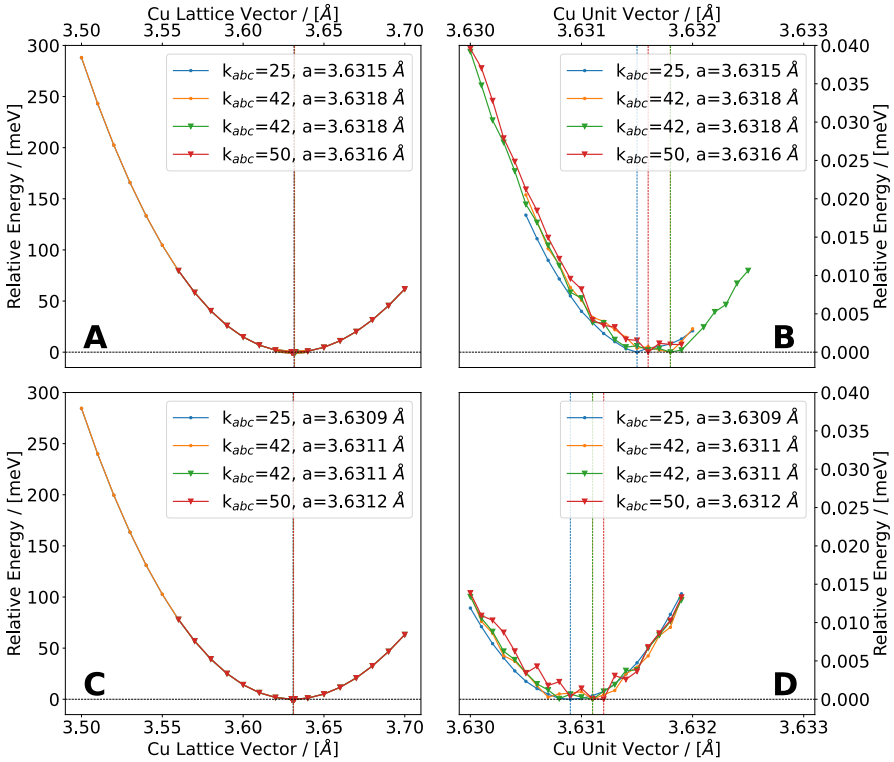

Figure 4.4: Lattice vector convergence data for the infinite Cu FCC system described in **Section 4.1**, **A&B:** LSS, **C&D:** TSS. The vertical dotted lines show the energy minima for the correspondingly coloured line. k_{abc} values are given in the legend, along with each line's minimum energy lattice vector. Dots represent data taken with the convergence criteria **`sc_accuracy_etot = 10^-8`**, triangles **`sc_accuracy_etot = 10^-10`**. **Figures A&B** contain data for LSS, **Figures C&D** for TSS. **Figures A&B** show the same LSS data, over different ranges. **Figures A** show the full range of lattice vectors tested (3.500 Å to 3.700 Å), **Figures B** show data taken at a 0.0001 Å resolution about the energy minima (3.6300 Å to 3.6330 Å). **Figures C&D** show the TSS data over the same ranges as **Figures A&B**.

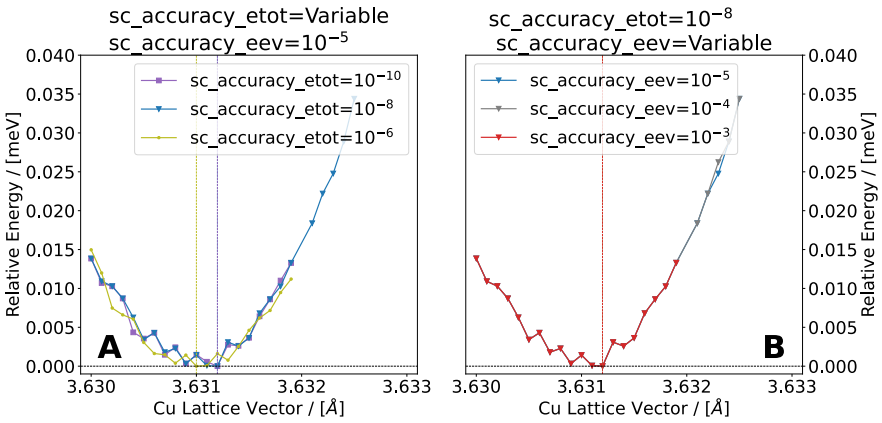

Figure 4.5: Lattice vector convergence data for the infinite Cu FCC system described in **Section 4.1**. This figure displays data taken with more stringent convergence criteria than **Figure 4.4**, with the aim of testing whether the convergence criteria used in **Figure 4.4** were adequate. The data in **Figure A** was calculated using a constant **`sc_accuracy_eev = 10^-5`**, with **`sc_accuracy_etot`** being varied from **`10^-6`** to **`10^-10`**. The data in **Figure B** was calculated with **`sc_accuracy_eev`** being varied from **`10^-3`** to **`10^-5`**, at a constant **`sc_accuracy_etot = 10^-8`**. All calculations were performed with $k_{abc} = 50$ using TSS. As with **Figure 4.4**, dots, triangles, and (additionally) squares represent data taken with convergence criteria values for **`sc_accuracy_etot`** of **`10^-6`**, **`10^-8`**, and **`10^-10`**. The blue triangle line in **A&B** is the same data plotted twice. The red triangle line in **B** is the same data as the red triangle line in **Figure 4.4 B.**

4.1.3 *Time Considerations*

When performing computationally expensive simulations, a practical balance between system convergence and computational cost has been made. Although the data above suggests system is most converged at 50 k-points, the time per atom in **Figure 4.6 B** is 10x and 5x larger for $k_{abc} = 50$ compared to $k_{abc} = 25$ for LSS and TSS respectively. Applying this result to one of the computational force spectra in **Section 6** (calculated using LSS species settings) we find each force spectra would have taken 100,000 CPU hours rather than 10,000 CPU hours. A similar situation arises when **Figures 4.6 C&D** are taken into account. Comparing the yellow dots to the blue triangles in **Figure 4.5** one can see that the system is not fully converged as the lines are not identical. However, using the lower value of **`sc_accuracy_etot = 10^-6`** (compared to **`sc_accuracy_etot = 10^-8`**) changes the lattice constant at the minimum energy by 0.0002 Å. In contrast, using **`sc_accuracy_etot = 10^-8`** increases the CPU hours required by 1.6x, or 6000 CPU hours per spectrum, when when applied to the computational force spectra in **Section 6**. A large increase in computational cost for a relatively small change in the value of the lattice constant.

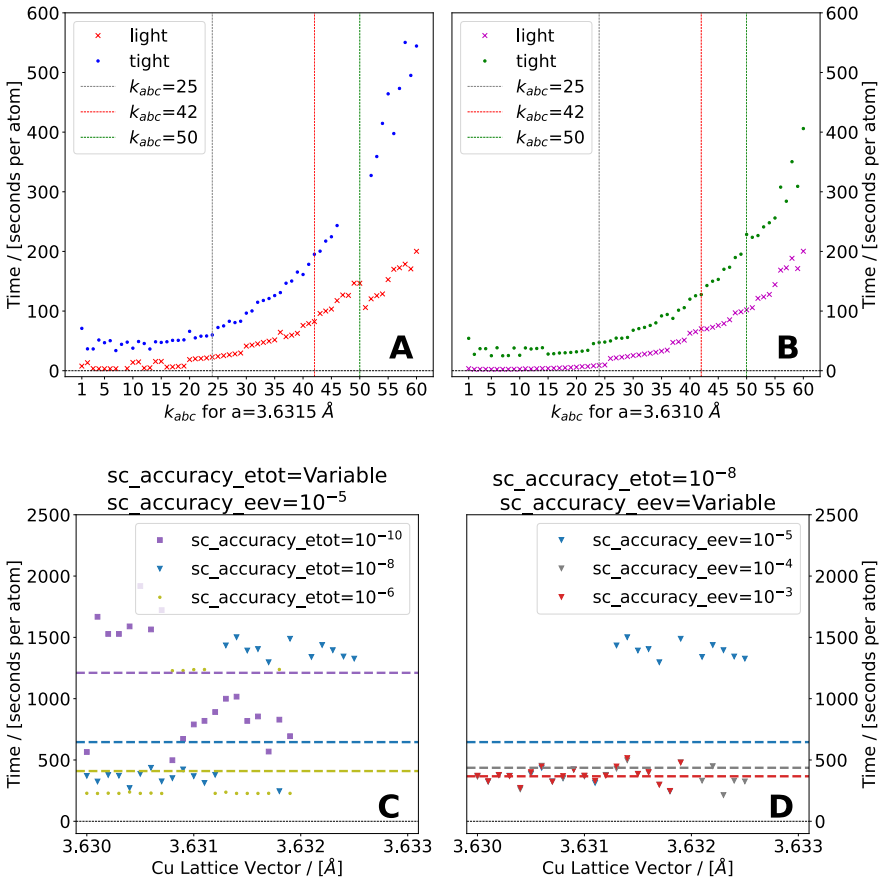

Figure 4.6: Time taken for systems to convergence, given as time per atom. **A&B** show time taken per atom as a function of k_{abc} points, and correspond to the data presented in **Figure 4.2**. K-points from 1 to 60 were tested for $k_{abc} = k_a = k_b = k_c$ using the LSS (crosses) and TSS (dots). The grey, red, and green vertical dotted lines mark $k_{abc} = 25, 42$, and 50 respectively. Plot **A** corresponds to data taken using a lattice constant of $a = 3.6315$ Å, plot **B** corresponds to data taken using a lattice constant of $a = 3.6310$ Å. **C&D** show time taken per atom as a function of a_{Cu}, and correspond to the data presented in **Figure 4.5**. The data in **C** was calculated using a constant **sc_accuracy_eev = 10^{-5}**, with **sc_accuracy_etot** being varied from **10^{-6}** to **10^{-10}**. The data in **D** was calculated with **sc_accuracy_eev** being varied from **10^{-3}** to **10^{-5}**, at a constant **sc_accuracy_etot = 10^{-8}**. All calculations were performed with $k_{abc} = 50$ using TSS. As with **Figure 4.4&4.5**, dots, triangles, and squares represent data taken with convergence criteria values for **sc_accuracy_etot** of **10^{-6}**, **10^{-8}**, and **10^{-10}**. The blue triangle line in **C&D** is the same data, and the red triangle line in **D** is the same data as the red triangle line in **Figure 4.4**. The horizontal dashed lines represent the average time taken to reach convergence, calculated over all the all tested lattice constants for each set of convergence criteria. In **A**; purple, blue and yellow correspond to **sc_accuracy_etot** values of **10^{-10}**, **10^{-8}**, and **10^{-6}** respectively, and in **B**; blue, grey and red correspond to **sc_accuracy_eev** values of **10^{-5}**, **10^{-4}**, and **10^{-3}**, respectively.

4.2 C_{60} ON CU(111)

It is well known in the literature that C_{60} readily adsorbs in islands, or as a mono-layer, on a Cu(111) surface with a Cu(111)-(4x4) periodicity [90][2]. It is also known that the presence of C_{60} molecules on a metal surfaces can induce a multitude of electronic and geometric surface reconstructions [91][92][93][2][94][95][3]. When C_{60} is adsorbed on the Cu(111) surface, a variety of surface reconstructions can form depending on the deposition conditions. These geometries include the 7 atom vacancy reconstruction, 1 atom vacancy reconstruction, and no reconstruction at all [2][3]. In this work, two unique adsorptions of C_{60} on the Cu(111) surface are considered and simulated. C_{60} adsorbed on the unreconstructed Cu(111)-(4x4) surface, and C_{60} adsorbed on the reconstructed Cu(111)-(4x4) surface. The surface reconstruction considered in this work is defined as a 7 surface atom vacancy in the top Cu(111) layer, directly underneath the adsorbed C_{60} molecule. This results in the C_{60} embedding down 1 atomic layer into the Cu(111) surface, perturbing the positions of remaining 9 surface atoms in the top layer from their lattice positions. The resulting geometry resembles a warped kagome structure. This particular surface reconstruction is described in detail by Woei *et al* [2].

Figure 4.7 displays front and top viewpoints of the Cu(111)-(4x4) and C_{60} systems investigated in DFT throughout this work. **Figure 4.7** plots **{A, B, C}** are the bare Cu(111)-(4x4) surface, **{D, E, F}** are C_{60} adsorbed on the unreconstructed Cu(111) surface ($C_{60,u}$), and **{G, H, I}** are C_{60} adsorbed on the 7 atom vacancy Cu(111) surface reconstruction ($C_{60,r}$). **{A, D, G}** and **{B, E, F}** display the isolated unit cells of the systems, **{C, F, I}** display a top down view of a section of the replicated unit cells, visualizing how the systems are simulated as infinite. Convergence of the metal slab was calculated as described in **Section 4.1**, a lattice constant for Cu of $a_{Cu} = 3.6310$ Å was used for all simulated systems from this point onwards. This results in lattice vectors for the Cu(111)-(4x4) system of $\overrightarrow{a} = (10.27002, 0, 0)$ **Å** and $\overrightarrow{b} = (5.135009, 8.894097, 0)$ Å. Lattice vector $\overrightarrow{c}$ was manually set as $\overrightarrow{c} = (0, 0, 100)$ Å. A corresponding **`k_grid 8 8 1`** was selected as a balance between Cu convergence and computational expense. The **`k_grid`** value of **`1`** along the Z direction arises as a result of the systems extending 100Å along the Z direction (calculated with **Equation 4.1** and **Figure 4.3**). The large lattice constant along the Z direction is to leave adequate space for the simulated AFM tip to be added to the systems in future calculations. Enough space needs to be available to contain the AFM tip atoms in addition to ensuring the top of the tip slab and the bottom of the surface slab do not interact.

To create the geometry of C_{60} adsorbed on the 7 atom vacancy Cu(111) surface reconstruction ($C_{60,r}$) the Cu surface was generated in the atomic simulation environment python library, and the C_{60} po-

sitioned 1Å above the FCC adsorption site. The system was relaxed, with the top two Cu layers (plus the reconstructed layer if applicable) unconfined, and all lower layers of the Cu(111)-(4x4) slab confined. As a result, the number of confined layers changes depending on the thickness of the slab. This setup results in the C_{60} adsorbing onto the Cu surface in a local minima dependent on the azimuth rotation of the C_{60} molecule relative to the Cu(111) surface. The FCC adsorption site was selected based on the findings by Woei *et al* [2] suggesting the FCC site is ~0.02 $eV/cell$ lower in energy on adsorption than the hexagonal close packed site for the $C_{60,r}$ system at slab thicknesses of 18 to 30 layers or more. The FCC adsorption site was also selected for the geometry of C_{60} adsorbed on the unreconstructed Cu(111) surface ($C_{60,u}$). This was to ensure the surface reconstruction is the only difference between the two systems, however Woei *et al* [2] did find the $C_{60,u}$ system favors the hexagonal close packed site by ~0.02 $eV/cell$. Experimental evidence for the $C_{60,u}$ or $C_{60,r}$ systems preferring a particular hollow site for adsorption is limited [96].

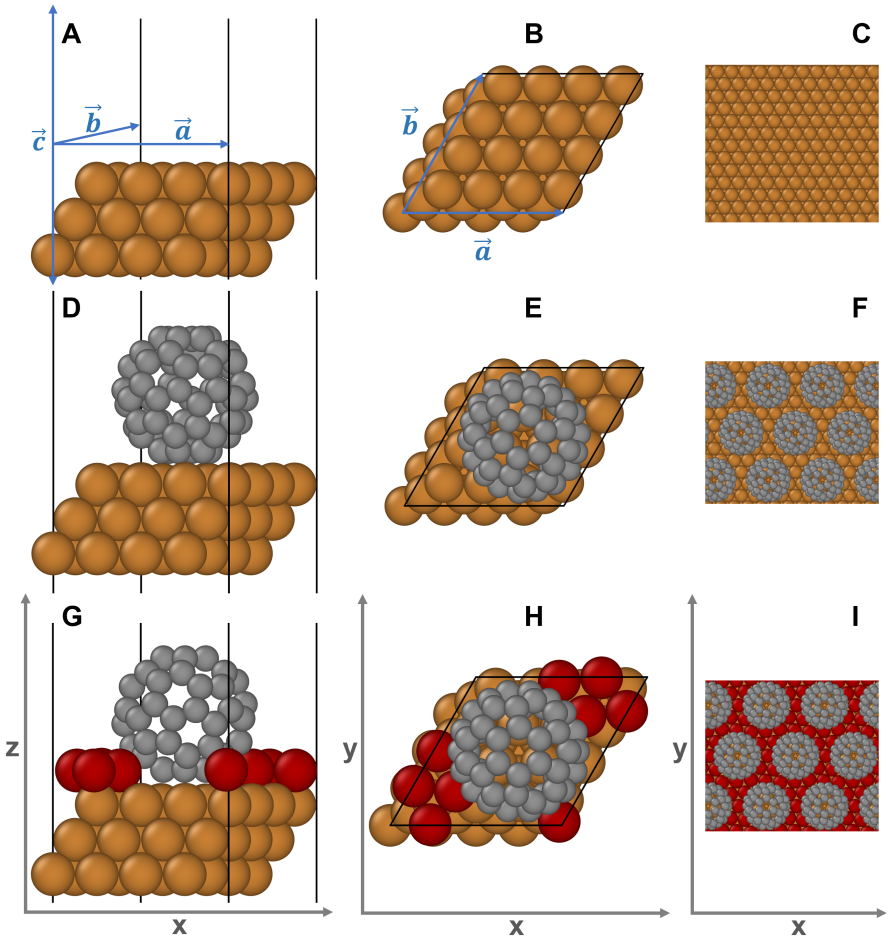

Figure 4.7: **{A, B, C}** show the geometry of the Cu(111)-(4x4) surface from the side (**A**), top (**B**), and the top as a continuous surface (**C**). **{D, E, F}** show the geometry of C_{60} adsorbed on the unreconstructed Cu(111) surface ($C_{60,u}$) from the side (**D**), top (**E**), and the top as mono-layer (**F**). **{G, H, I}** show the geometry of C_{60} adsorbed on the 7 atom vacancy Cu(111) surface reconstruction ($C_{60,r}$) from the side (**G**), top (**H**), and the top as a mono-layer (**I**). The remaining 9 atoms in the top (reconstructed) layer of the Cu(111) slab have been coloured red in **{G, H, I}**. The black lines represent the periodic unit cell. The grey arrows in **{G, H, I}** represent the axes orientations relative to the viewing angle in **{A, D, G}** and **{B, E, H}** and **{C, F, I}** respectively. The blue arrows in **A&B** represent the unit vectors $\vec{a} = (10.27002, 0, 0)$ **Å**, $\vec{b} = (5.135009, 8.894097, 0)$ Å, and $\vec{c} = (0, 0, 100)$ Å, which are consistent over all three unique systems. $\vec{c} = (0, 0, 100)$ Å is shown as an arrow pointing in both the upwards and downwards directions to represent how it extends over a larger range than is shown in the diagrams. The space above and below the atoms in **{A, D, G}** can be thought of as an infinite vacuum. Atoms are represented as spheres. With orange, red, and grey, representing Cu, Cu in the surface reconstruction, and C in the C_{60} molecules, respectively. All 3D atomic geometry visualizations in this work were created using OVITO [97].

4.2.1 *System Convergence*

Prior to the system in **Figure 4.7** being used for force spectrum calculations, convergence tests need to be performed. In the case of C_{60} relaxing onto the Cu(111)-(4x4) surface, the system convergence criteria of charge transfer, and system energy, were tested with respect to the number of complete Cu layers in the Cu(111)-(4x4) surface. The FHI-aims parameters used for the convergence testing in all parts of **Section 4.2.1** are given in **Table 4.2**. In addition to optimizing the electronic structure for a given geometry, the geometry (atomic core positions) was also allowed to relax, and thus was optimized to minimize the total energy of the system. The TS vdW correction was implemented. However, Cu-Cu interactions were omitted under the following assumption; including the Cu-Cu interactions provides an insignificant accuracy improvement to the simulation, but increases the computational cost. In addition to the general description given at the start of **Section 4.2**, the following procedure was followed for relaxing C_{60} on Cu(111)-(4x4) slabs of varying thicknesses (where n denotes the number of complete layers in the slab);

1. First, the $n = 5$ $C_{60,r}$ system was simulated first. The C_{60} was positioned above an FCC adsorption site, ~ 1Å above the adsorption height, in the desired azimuth rotation. This system was relaxed using the FHI-aims convergence criteria given in **Table 4.2**. Only atoms in the C_{60} molecule and slab layers $n = 1$ and $n = 2$ were allowed to relax, with all other atoms confined in the XYZ directions. The reconstructed layer does not count as a complete layer in the Cu(111)-(4x4) slab.

2. Second, $C_{60,r}$ systems corresponding to more or less than 5 slab layers ($n \neq 5$) were simulated. Cu slab layers were added or removed from the relaxed $n = 5$ $C_{60,r}$ system, and the edited system relaxed for a second time. As with the $n = 5$ system, only atoms in the C_{60} molecule and slab layers $n = 1$ and $n = 2$ were allowed to relax, with all other atoms being confined in the XYZ directions.

3. Finally, the $C_{60,u}$ system was simulated with a slab thickness of $n = 9$. The C_{60} was positioned above an FCC adsorption site, ~ 1Å above the adsorption height, in the same starting azimuth rotation as the $C_{60,r}$ $n = 5$ system. This system was relaxed using the FHI-aims convergence criteria given in **Table 4.2**. As with the $C_{60,r}$ system, only atoms in the C_{60} molecule and slab layers $n = 1$ and $n = 2$ were allowed to relax, with all other atoms being confined in the XYZ directions.

FHI-aims Parameter Key	FHI-aims Parameter Value	Comments
`xc`	`pbe`	
`vdw_correction_hirshfeld`	*N/A*	TS vdW correction
`vdw_pair_ignore`	`Cu Cu`	
`charge`	`0`	
`spin`	`none`	
`relativistic`	`atomic_zora scalar`	
`adjust_scf`	`always 2`	
`occupation_type`	`gaussian 0.1`	
`mixer`	`pulay`	
`n_max_pulay`	`8`	
`sc_accuracy_etot`	10^{-6}	
`sc_accuracy_eev`	10^{-3}	
`sc_accuracy_forces`	10^{-4}	
`sc_accuracy_rho`	0.5×10^{-5}	
`relax_geometry`	`trm` 10^{-2}	
`k_grid`	`8 8 1`	As discussed in **Section 4.1.1**

Table 4.2: Simulation parameters for C_{60} on Cu(111)-(4x4) convergence testing

4.2.1.1 *Charge Transfer*

In this work involving C_{60} adsorbed on the Cu(111)-(4x4) surface, a key quantity of interest when comparing the $C_{60,u}$ to the $C_{60,r}$ system is the charge transferred into the adsorbed C_{60} molecule. Therefore the primary convergence criteria to take into account for this system in the regime of this work is the charge transfer. The charge transfer values were calculated by applying the Mulliken Population Analysis (MPA) [98] and Hirshfeld Population Analysis (HPA) schemes [79] to the systems[1]. Once the partial charges were calculated, the charges on all the C atoms or all the Cu were summed over to give the charge transfer to/from the C_{60} molecule. **Figure 4.8 A&B** show the charge transferred from the reconstructed copper (111) surface (Cu_r) into the $C_{60,r}$ is $\Delta Q_{C_{60}} = -1.01 \pm 0.01e$, whereas the charge transferred from the unreconstructed copper (111) surface (Cu_u) into the $C_{60,u}$ is half as much at $\Delta Q_{C_{60}} = -0.51e$. The grey shaded area represents $\pm 0.01e$ about the charge transferred into the $C_{60,r}$. The charge on the individual atoms, as calculated by HPA, is displayed in **Figure 4.9**.

In addition to the HPA and MPA data, the species projected density of states for the Carbon atomic species has be calculated. This data is comparable to Scanning Tunnelling Spectroscopy (STS) data gathered from SPM experiments with metallic tips. Looking at **Figure 4.10,** one can see a clear and progressive shifting of the LUMO position (relative to the fermi Level). This LUMO shifting is consistent with charge transfer to the C_{60} (**Figure 4.8**). For the isolated $C_{60,g}$ molecule, there is a clear energy gap between the HOMO and LUMO. Upon adsorption onto the Cu_u surface, hybridization between the metal surface and the adsorbed C_{60} molecule occurs. This causes a widening of the LUMO along with a shift in the LUMO peak energy towards fermi level. Upon adsorption of the C_{60} molecule onto the Cu_r surface, more pronounced hybridization between the metal surface and the adsorbed C_{60} molecule occurs. This causes a greater widening of the LUMO, and a greater shift in the LUMO location such that it is centered on fermi level. This LUMO shifting is in agreement with the experimental and DFT results reported by Pai *et al* [2].

Figure 4.8 B shows the variation in charge transfer over the slab thickness range of 3 to 15, for both the MPA and HPA schemes. The variation in charge transferred to the $C_{60,r}$ over the range of 3 to 15 layers is 1% of the total charge transfer and can be considered insignificant. Therefore a relatively thin slab of 3 layers can be considered converged with regards to charge transfer. This finding is further reinforced when the partial charges on the atoms is visualized in **Figure 6.8**. **Figure 4.8 B** also allows us to compare the two charge partitioning schemes. Comparing the charge transferred to the $C_{60,r}$, we can see that both methods agree to within $0.01e$, or within 1% of the total

1 The Hirshfeld Population Analysis (HPA) scheme is used by the TS and MBD vdW correction schemes and therefore always calculated in systems including vdW corrections

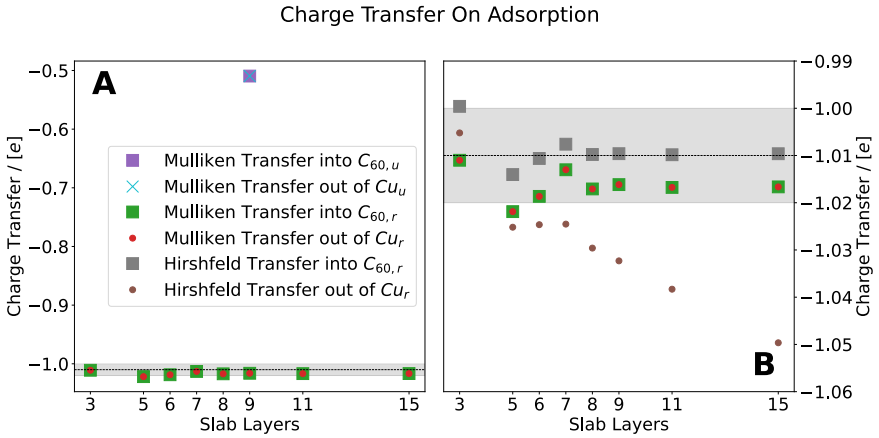

Figure 4.8: Charge transfer on adsorption data for the $C_{60,u}$ and $C_{60,r}$ systems. **Figure A** contains charge transfer data (calculated using MPA) comparing the $C_{60,u}$ system to the $C_{60,r}$ system. **Figure B** contains charge transfer data calculated with MPA and HPA. The green squares, purple squares, red dots, and cyan crosses represent the charge transferred into the $C_{60,r}$, into the $C_{60,u}$, out of the Cu_r, and out of the Cu_u respectively, calculated with MPA. The grey squares and brown dots represent the charge transferred into the $C_{60,r}$ and out of the Cu_r respectively, calculated with HPA. The horizontal black dashed line, and surrounding shaded region, correspond to the calculated charge transfer into the $C_{60,r}$ of $-1.01 \pm 0.01e$, with the grey shaded area marking out the $\pm 0.01e$ uncertainty.

charge transfer. In addition, it appears the main difference between the charge calculated by the two methods is a constant charge offset. However, when looking at the charge transferred out of Cu_r, the value calculated using HPA diverges from the $C_{60,r}$ value as the number of slab layers increases.

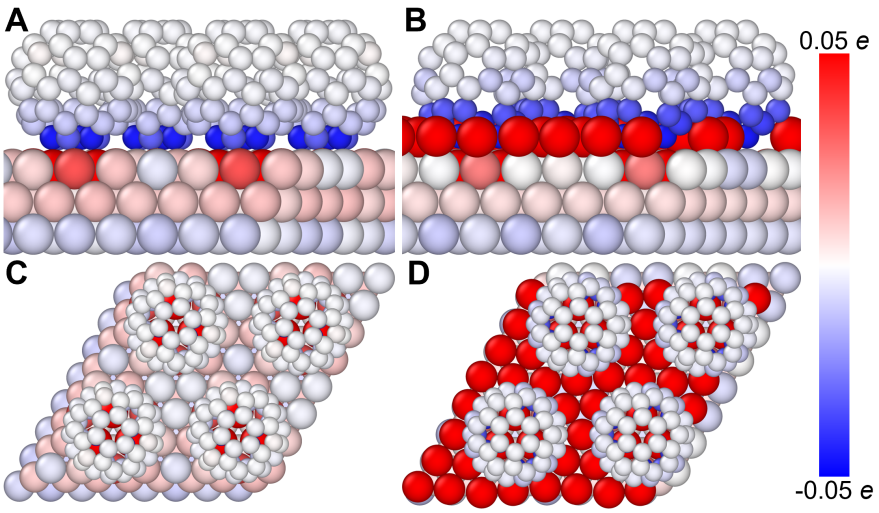

Figure 4.9: Partial charge per atom as calculated by HPA.

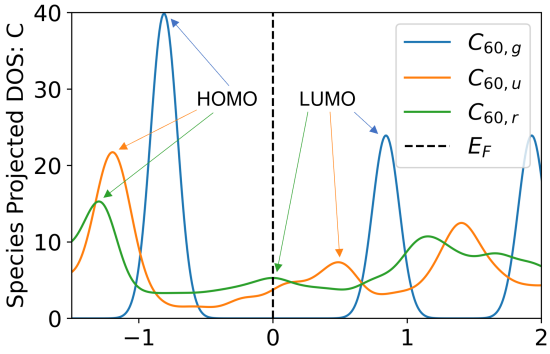

Figure 4.10: Species projected density of states data for the Carbon atomic species in the $C_{60,g}$, $C_{60,u}$, and $C_{60,r}$ systems (green, orange, and blue lines respectively). The fermi level, as calculated by FHI-aims, is plotted as a vertical dashed line. The $C_{60,u}$ and $C_{60,r}$ were simulated with a slab thickness of $n = 9$, and the TS vdW correction. The $C_{60,g}$ system was included as a reference to highlight the effect of the Cu_u and Cu_r surfaces on the C_{60} molecule.

The method of charge partitioning employed can affect the calculate charge transfer values, therefore alternative schemes were considered for this work. Bader charge analysis [99][100][101][102][103] is an alternative charge partitioning scheme. It is capable of assigning partial charges to individual atoms, and has been previously applied to systems involving C_{60} on the Cu(111) surface [58]. However, given the good agreement between the HPA and MPA schemes for the systems in this work, it was felt a third approach was not needed. See Saha *et al* [104] for a wider comparison between the MPA and HPA approaches. In addition, the HPA and MPA are implemented within FHI-aims where as bader charge analysis is not. One can also implement schemes which calculate the the charge transfer within a system without assuming that the charge density can be divided between individual atoms. One such method involves calculating the charge transfer of the whole system along the vertical direction by integrating the change in electron density on adsorption of the system. This approach has been used to study the adsorption of organic molecules on multiple metal surfaces, including the Cu(111) surface [105]. The plane integral approach could be beneficial as it is calculated directly from the DFT electron density, thereby producing a charge transfer value independent on any particular charge partitioning scheme. However, there are conditions for the use of this approach. The atomic coordinates of the adsorbed molecule and the substrate must be separable along the Z axis. As the $C_{60,r}$ system contains C atoms at lower Z coordinates than Cu atoms, the charge transferred along the Z direction can not be described a charge transfer from Cu atoms to C atoms, thus making this approach inapplicable to the $C_{60,r}$ system.

The charge transfer values calculated in this work are in possible disagreement with previous studies. Similar MPA [98] calculations for $C_{60,u}$ on Cu(111) were performed by Ogawa *et al* [57]. They reported a charge transfer of $\Delta Q_{C_{60,u}} \leq -0.889\,e$ to the $C_{60,u}$ molecule. However, these calculations were performed as cluster calculations comprised of less Cu atoms than the periodic systems used in this work, and thus are not directly comparable. A similar charge transfer value of $\Delta Q_{C_{60,u}} = -0.8\,e$ for the $C_{60,u}$ system was obtained by Wang *et al* [58] using two methods; Integration of the partially filled t_{1u} state [58], and a modified bader charge analysis approach [99]. These calculations involved a periodic system coupled with an $n = 7$ Cu(111)-(4x4) slab. More abstract theoretical work on a single Cu atom interacting with a C_{60} molecule has also been carried out. A charge transfer of $\Delta Q = -0.3\,e$ to the C_{60} [106] was calculating using the bader charge analysis scheme [100][101][102][103]. A theoretical and experimental value of $\Delta Q_{C_{60.r}} = -3\,e$ for the charge transferred to a $C_{60,r}$ molecule has been published by Pai *et al* [2]. The theoretical value was not obtained via a charge partitioning scheme. Other experimental values for the charge transfer from Cu(111) into C_{60} have been published,

however these values also need to be interpreted with caution. It is known that C_{60} on Cu(111) can adsorb on the surface in various geometries arising from multiple types of surface reconstructions **(Section 4.2.3)** [2][3], with each adsorption geometry having the potential to correspond to a unique charge transfer, and the underlying surface reconstruction being sensitive to preparation temperatures. As this array of possible geometries was not well understood until the 2010s or even the 2020s, it is difficult to equate experimental charge transfer values to specific adsorption geometries and surface reconstructions. One can find experimental values ranging from $-1\,e < \Delta Q < -3\,e$ [107][56][2]. See **Table 4.3** below for an overview of the literature.

Ref.	Surface Reconstruction	$\Delta Q_{C_{60}}$ / e	$\Delta Q_{C_{60}}$ Method
[107]	Unknown	$-1.5 \leq Q \leq -2$	LUMO shift measured by Near-Edge X-ray-Absorption Spectroscopy compared to the LUMO shift of K-doped C_{60} by Chen *et al* [108], and Photoemission Spectroscopy (independently)
[57]	$C_{60,u}$	$-0.563 \leq Q \leq 0.637$	MPA [98] applied to DFT simulations of C_{60} adsorbed on a 10 atom Cu(111) cluster.
[57]	$C_{60,u}$	-0.889	MPA [98] applied to DFT simulations of C_{60} adsorbed on a 34 atom Cu(111) cluster.
[58]	Inferred to be $C_{60,u}$	$-0.8 \leq Q \leq -0.9$	Integration of the partially filled t_{1u} state as calculated by DFT. DFT calculations involved a periodic system coupled with an $n = 7$ Cu(111)-(4x4) slab and no vdW correction.

[58]	Inferred to be $C_{60,u}$	-0.8	A modified bader charge analysis approach applied to the DFT charge density [99]. DFT calculations involved a periodic system coupled with an $n = 7$ Cu(111)-(4x4) slab, and no vdW correction.
[56]	Inferred to be $C_{60,r}$ due to the 600 K annealing temperature	-2.9	Angle-resolved photoemission
[2]	$C_{60,r}$	~ -3	Angle-resolved photoemission spectroscopy
[2]	$C_{60,r}$	~ -2.9	Angle-integrated photoemission spectroscopy
[2]	$C_{60,r}$	~ -3	STS LUMO position
[2]	$C_{60,u}$	< -1	Simulated Partial Density Of States LUMO position. DFT calculations involved a periodic system including aCu(111)-(4x4) slab of up to 30, and no vdW correction. correction.
[2]	$C_{60,r}$	~ -3	Simulated Partial Density Of States LUMO position. DFT calculations involved a periodic system including aCu(111)-(4x4) slab of up to 30, and no vdW correction. correction.
[106]	Single Cu atom interacting with C_{60}	-0.3	Bader charge analysis applied to DFT calculations [100][101][102][103].

4.2.1.2 *Adsorption Energy*

The adsorption energy of the system was calculated by subtracting the energy of both the isolated C_{60} mono-layer, and the isolated slab, from the energy of the full system (**Equation 4.3**),

$$E_{ads} = E_{system} - (E_{C_{60}} + E_{slab}) \tag{4.3}$$

where E_{ads} is the calculated adsorption energy, E_{system} is the energy of the full system (**Figure 4.7** rows 2&3), $E_{C_{60}}$ is the energy of the C_{60} mono-layer relaxed in same unit cell as the full system without the presence of of the slab, and E_{slab} is the energy of the relaxed slab in same unit cell as the full system without the presence of the C_{60} mono-layer. Due to the periodicity of the system this method is calculating the adsorption energy per unit cell of the system. In addition, the calculated adsorption energy does not take into account then energy penalty of forming the reconstructed Cu surface. The adsorption energy of the $C_{60,r}$ system at $n = 15$ is $E_{ads,C60_r} = -7.37\,eV$, where as the $C_{60,u}$ system has an adsorption energy of $E_{ads,C_{60,u}} = -3.04\,eV$ for $n = 9$. The adsorption energy of the $n = 3$ $C_{60,r}$ system is $E_{ads,C_{60,r}} = -7.21\,eV$, within $\pm 2\%$ of the more converged $n = 15$ value (within $0.16\,eV$). However, $\sim 0.1\,eV$ of this energy differences originates from the TS vdW energy, with only $\sim 0.05\,eV$ coming from the DFT energy. This suggests the DFT calculation of the system is more converged with respect to the adsorption energy at a slab thickness of $n = 3$ than the adsorption energy first suggests.

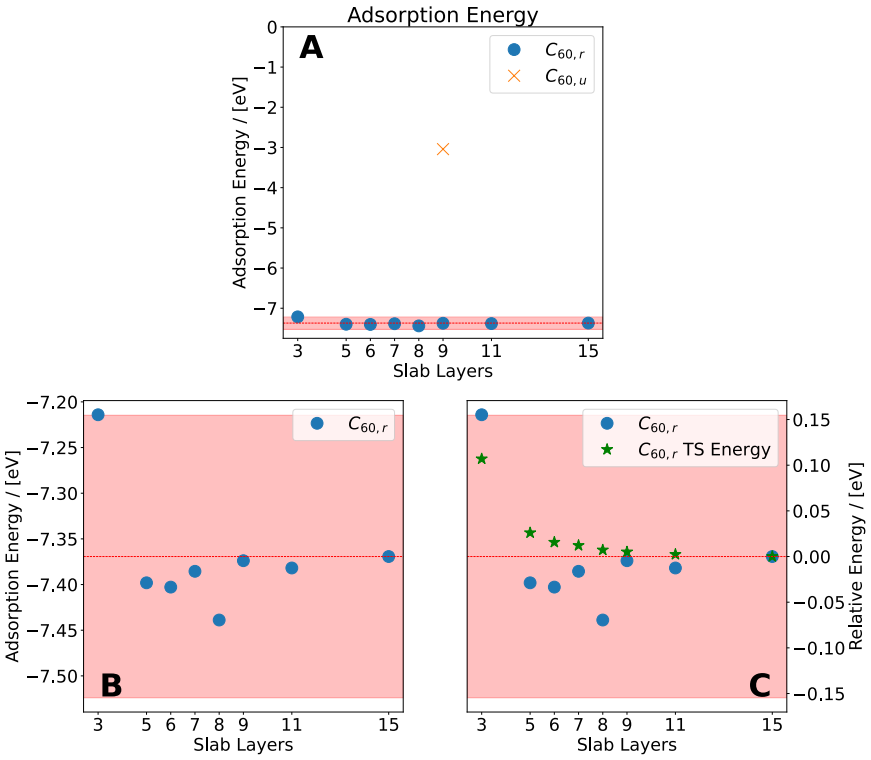

Figure 4.11: Adsorption energy data for the $C_{60,u}$ and $C_{60,r}$ systems. **A** contains data for both systems. In **B** the y axis has been cropped over the $C_{60,r}$ system data. In **C** the y axis given the adsorption energy relative to the system with slab a thickness of 15 layers (the $n = 15$ system). The blue circles in **{A, B, C}** represent adsorption energy for the $C_{60,r}$ system, and the orange cross in **A** the adsorption energy for the $C_{60,u}$. The green stars in **C** display the TS vdW energy relative the $n = 15$ system for the $C_{60,r}$ system. In **C** a positive energy is less favorable, and a negative value more favorable relative to the $n = 15$ system. The red dashed line marks the energy of the $n = 15$ system, and the red shaded region marks the energy of the $n = 15$ system $\pm 2.1\%$.

Simulated and experimental values for the adsorption energy of C_{60} adsorbed on the Cu(111) surface are available in the literature, and span the range $-0.8 \leq E_{ads,C_{60,u}} \leq 2.479\,eV$. However the simulated values can not be directly compared to the values given in this work. The values found in the literature are calculated without vdW corrections (see **Table 4.4** for values), therefore that provide a lower bound limit for calculations of the adsorption energy including vdW corrections. The importance of including vdW interactions when simulating C_{60} molecules has been shown in the literature [109][110], a finding which agrees with **Figure 4.11** from this work. Thus, any adsorption energy values calculated without the presence of a vdW correction should be considered as a lower bound estimate for the adsorption energy, independent to the thickness of Cu(111) slab used. Furthermore, based on this conclusion, one can also deduce a calculation of the adsorption energy which utilities a vdW correction scheme, but in a cluster calculation, is also likely a lower bound estimate for the adsorption energy. This arises because the simulation will be missing the long range vdW interactions of the adsorbed C_{60} molecule with the Cu(111) surface from neighboring cells.

Ref.	E_{ads} / eV	Surface	Periodic or Cluster	vdW	Slab Thickness (n)	DFT Method
[57]	-1.358	Cu_u	Cluster	None	2	10 Cu atom cluster with the azimuthal rotation angle fixed to the experimental X-ray Photon Diffraction value
[57]	-1.624	Cu_u	Cluster	None	2	10 Cu atom cluster
[57]	-2.479	Cu_u	Cluster	None	3	32 Cu atom cluster
[58]	$-1.9 \leq E_{ads}$ $E_{ads} \leq 2.4$	Cu_u	Periodic	None	7	Cu(111)-(4x4) surface
[96]	$-2.20 \leq E_{ads}$ $E_{ads} \leq -2.39$	Cu_u	Cluster	None	3	55 Cu coin shaped cluster
[2]	~ -0.8	Cu_u	Periodic	None	up to 30	

[2]	~ -3.0	Cu_r	Periodic	None	up to 30	
[106]	-0.98	N/A	Periodic	D3 [83]	N/A	Single Cu atom interacting with C_{60}

4.2.2 *Time Considerations*

Similar to **Section 4.1.3**, a practical balance between system convergence and computational cost has to be made. When simulating an AFM force spectrum over an adsorbed $C_{60,r}$, the tip can be treated as a mirror of the sample. Therefore the number of atoms in the system will be doubled relative to just the $C_{60,r}$ system. **Figure 4.12** displays time data for the $C_{60,r}$ adsorption relaxations discussed in **Figures 4.8 & 4.11** (green squares). In **B** the time data is extrapolated to estimate the time taken for a full force spectrum (red stars). It is assumed the time taken to relax the full system scales linearly with the adsorption time. This optimistic scaling was used as this is the best reported scaling for FHI-aims (achieved with systems of < 100 atoms), and the use of overlap matrices between spectrum steps improved the efficiency of the calculations. Furthermore, each force spectrum is assumed to be comprised of 60 geometric relaxations. The linear scaling provides a best case scenario time prediction, the 60 geometric relaxations was selected because it provides a time estimate for the $n = 3$ system that matches the force spectrum data presented in **Chapter 6** when using **Equation 4.4**,

$$\tau_{spectrum} = \alpha_{scale}\, \Re_{relax}\, \tau_{ads,n} \tag{4.4}$$

where $\tau_{spectrum}$ is the predicted time for a whole force spectrum, α_{scale} is the scaling factor based on the number of electrons in the system, $\Re_{relax}$ is the predicted number of steps in the force spectrum, and $\tau_{ads,n}$ is the time taken to adsorb C_{60} on a Cu(111)-(4x4) slab of thickness n. The work performed by Pai *et al* [2] suggests the largest slab which can be afforded should be used. However, analysis of **Figures 4.8 & 4.11** suggest the $n = 3$ system is adequate. Furthermore, this slab thickness has previously been used for cluster calculations of C_{60} on Cu(111) [57][96]. Looking at **Figure 4.12** we can see each force spectrum using a slab of $n = 9$ would take 60,000 CPU-hours (or more), compared to only 11,000 CPU-hours for the $n = 3$ system. This is a 6x increase in computational cost for a 1-2% increase in accuracy **(see Sections 4.2.1.1&4.2.1.2)**, therefore the $n = 3$ system visualized in **Figure 4.7** was selected for simulating force spectra. Given this work has access to $\leq 120,000$ CPU hours for performing force spectra this decision was the difference between completing ~2 force spectra, or ~10.

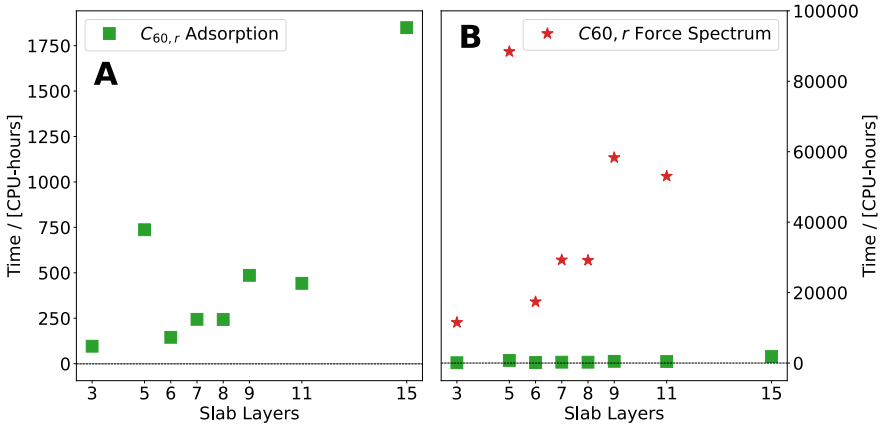

Figure 4.12: **A** displays the total time for the $C_{60,r}$ adsorption relaxations discussed in **Figures 4.8 & 4.11** (green squares). In **B** the total time data is extrapolated to estimate the time taken for a full force spectrum (red stars). The extrapolation is performed using **Equation 4.4**, with $\alpha_{scale} = 2$ and $\Re_{relax} = 60$, and $\tau_{ads,n}$ is the green squares in **A&B**. $n = 15$ Cu layers was predicted to take over 200,000 CPU hours and is not visible on this scale.

4.2.3 *Orientation*

It has been found, both experimentally and computationally, that C_{60} can adsorb on a variety of surfaces in a variety of different geometries. This large variety of adsorption orientations allows for different parts of the C_{60} cage to be presenting upwards; such as: hexagon up, pentagon up, and C=C or C-C bond up. In addition, in the case of a C_{60} molecule, the section of the molecule facing upwards is equivalent to the section facing downwards after an azimuthal rotation. For the Hexagon, Pentagon, C=C Bond, and C-C Bond up orientations, the relative rotation between the top and bottom faces is 60°, 72°, 0°, and 180°, respectively. A generalization of these different configurations is demonstrated in **Figure 4.13**[90][111][112][57][113][96][114][2][115][3].

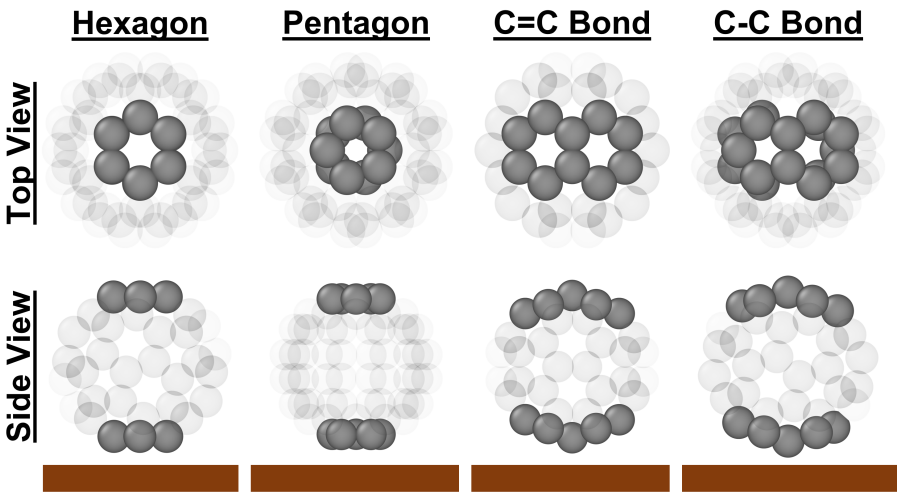

Figure 4.13: Representative orientations of a C_{60} molecule adsorbed on a surface, rendered from the top view and side view perspectives. C atoms forming the C_{60} cage are represented as grey spheres. Some of the C atoms have been rendered as partially transparent to highlight the section of the C_{60} molecule being presented to the surface (and SPM tip). The surface is depicted as a brown rectangle in the side view perspective. Although the section of the C_{60} molecule at the top and bottom are the same, the faces are azimuthally rotated relative to each other. For the Hexagon, Pentagon, C=C Bond, and C-C Bond up orientations the relative rotation between the top and bottom faces is 60°, 72°, 0°, and 180°, respectively. All 3D atomic geometry visualizations in this work were created using OVITO [97].

In this computational work, C_{60} is adsorbed on the Cu(111)-(4x4) surface in the following orientation; a C_{60} molecule oriented to present a hexagonal face (C_{60}-h) to a face centred cubic hollow site on the Cu(111) surface (Cu(111)-fcc). This results in a hexagonal face of the C_{60} molecule oriented down towards the surface, and upwards towards any simulated SPM tip **(Figures 4.7 & 4.17)**. This orientation was selected as it was found to be the most energetically favorable in the DFT calculations, and best replicates the experimental SPM images in **Chapter 2**. While the face the C_{60} presents to the surface is kept constant in this work, the azimuthal adsorption angle of the C_{60} is varied, which has the effect of rotating the presenting face parallel to the surface. In this section **(Section 4.2.3)** the adsorption angle of a C_{60}-h molecule adsorbed on a Cu(111)-fcc site of the Cu(111)-(4x4) surface, and the corresponding nomenclature, is described. In **Section 4.2.3.1** we will find the azimuthal adsorption angle the system converges on is dependent on the initial angle, the underlying surface reconstruction, and the vdW correction implemented in the calculations. Furthermore, in **Section 4.3.4**, the effect of the relative azimuthal angle between two interacting gaseous C_{60} molecules will be investigated, and correlated with simulated force spectra.

Figure 4.14 describes the symmetry of a face centred cubic hollow site on the Cu(111) surface (Cu(111)-fcc) and a C_{60} molecule oriented to present a hexagonal face (C_{60}-h). Both systems can be described as having 120° rotational symmetry with three vertical mirror planes containing the axis of rotation (C_{3v}). In **Figure 4.14** the vertical planes of symmetry are pictorially represented as dashed lines, and the 120° rotational symmetry is depicted as shaded regions.

Figure 4.15 describes the azimuthal rotation of a C_{60}-h molecule adsorbed on a Cu(111)-fcc site. Looking at **Figures 4.15&4.7**, there are three contributing patterns within the system:

1. The underlying Cu(111) surface exhibits C_{3v} symmetry.
2. A C_{60}-h exhibits C_{3v} symmetry, where this symmetry arises from both the bond order and the C atom positions.
3. The periodic boundary conditions of the system. This can be thought of as the sections of the C_{60} molecule being presented to the replicated C_{60} molecules. As the C_{60} molecule is azimuthally rotated, the periodic replications also rotate.

Figure 4.15 displays a simplified description of $C_{60,u}$ and $C_{60,r}$ systems. However, the $C_{60,r}$ system has the additional reconstructed layer of Cu atoms, which may also affect the azimuthal angle of adsorption. Looking at **Figure 4.15,** the following observations for the simplified system can be made (the red angles D correspond to the red adsorption angles in **Figure 4.15**):

1. A 120° rotation of the Cu(111)-fcc or C_{60} molecule returns an identical geometry.

2. All unique geometries can be found within the rotation range $-60° \leq D \leq 60°$. With a negative angle corresponding to the C=C bonds located over the Cu atoms, and a positive angle corresponding to the C-C bonds located over the Cu atoms.

3. All unique interactions between the C_{60}-h molecule and the Cu(111)-fcc adsorption site (C_{60}-h–Cu(111)-fcc interactions) can be found within the rotation range $-30° \leq D \leq 30°$. The rotation ranges $-30° \geq D \geq -60°$ and $30° \leq D \leq 60°$ contain unique mirror geometries corresponding to C_{60}-h–Cu(111)-fcc interactions equivalent to those found within the rotation range $-30° \leq D \leq 30°$.

4. The mirror geometries arise from the system being symmetric under rotations about $D = \pm 30°$. For example, rotations of $\pm 15°$ about $D = 30°$ will produce the geometries corresponding to $D = 15°$ and $D = 45°$, which are the mirror geometries to each other. The geometries $D = \pm 30°$ are special as they correspond to the vertical mirror planes of the Cu(111)-fcc site, and the C_{60}-h molecule, aligning (compare **Figures 4.14** and **4.15**). The mirror planes align when the C-C or C=C bonds are located exactly above the Cu atoms.

5. The effect of the mirror geometries is a smaller angle range can be used to simulate all unique C_{60}-h-Cu interactions ($-30° \leq D \leq 30°$ rather than $-60° \leq D \leq 60°$).

6. The geometries corresponding to $D = \pm 60°$ are equivalent, and the mirror geometry of $D = 0°$.

7. The system exhibits C_{3v} symmetry only for geometries corresponding to $D = 30° \pm 60n°$ where $n = 0, 1, 2...\infty$. This means all geometries corresponding to $D = 30° \pm 60n°$ contain in the same C_{60}-h-Cu(111)-fcc interactions, but are not necessarily the same geometries.

8. The system exhibits 120° rotational symmetry with no mirror planes (C_3) symmetry for geometries not corresponding to $D = 30° \pm 60n°$ (mathematically denoted as $D \neq 30° \pm 60n°$), where $n = 0, 1, 2...\infty$.

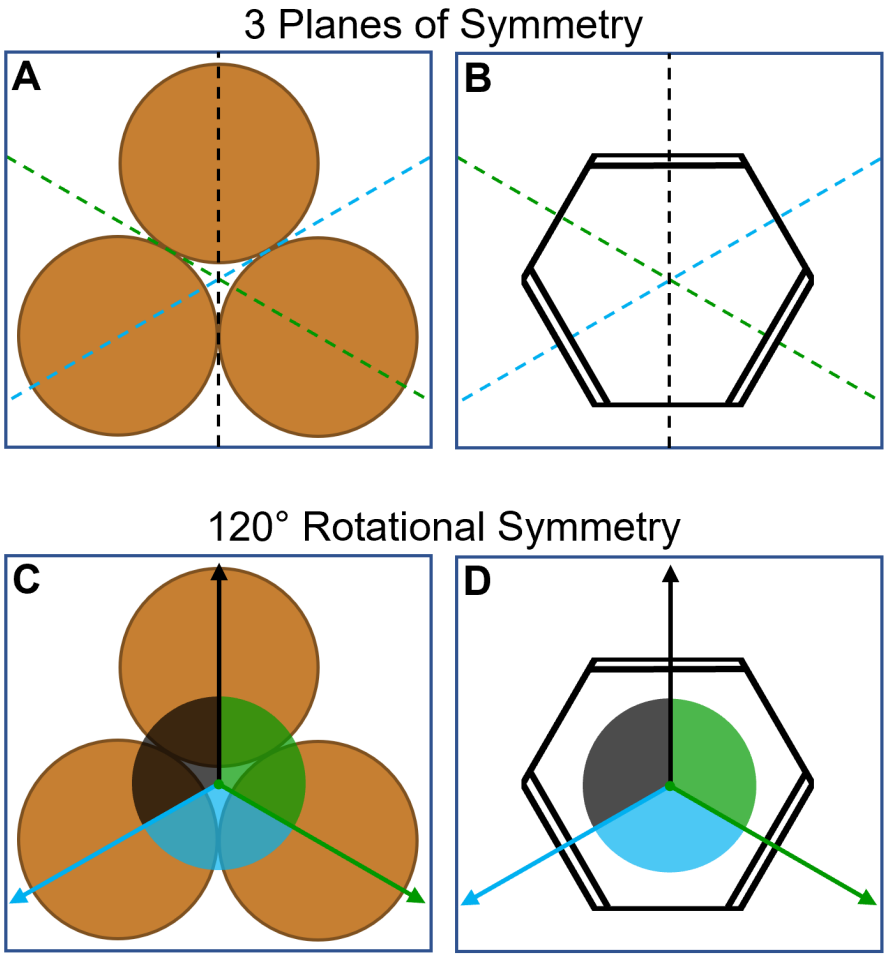

4.18

Figure 4.14: Diagrams displaying the planes of symmetry **(A&B)**, and rotational symmetry **(C&D)**, for a hollow site on the Cu(111) surface **(A&C)** and a C_{60}-*h* **(B&D)**. The black, blue, and green dashed lines in **(A&B)** represent the three planes of symmetry for the two systems. The black, blue, and green arrows and shaded regions represent the 120° rotational symmetry of the two systems. The C_{60}-*h* is shown as a black hexagon, with single and double lines representing C-C and C=C bonds respectively. The three brown circles represent the three Cu atoms forming a hollow site on the Cu(111) surface.

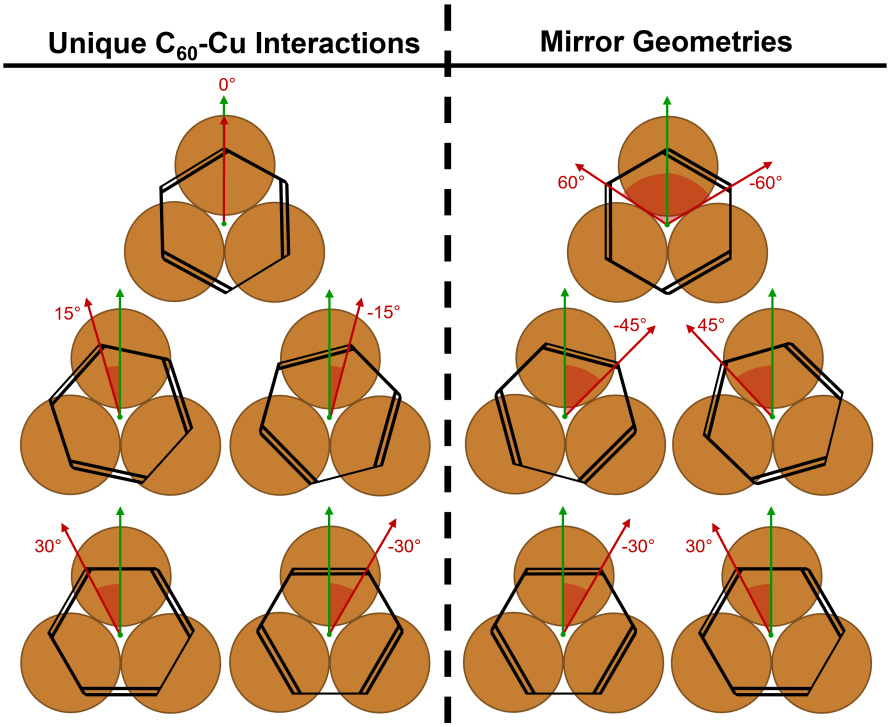

Figure 4.15: Diagrams of the geometries corresponding to unique C_{60}-Cu interactions, and their corresponding mirror geometries, formed by C_{60}-*h* adsorbing atop a hollow site on the Cu(111) surface. The geometries are described by the relative azimuthal angle between the adsorbed C_{60} and the underlying Cu(111) surface (red shaded region). The C_{60}-*h* is shown as a black hexagon, with single and double lines representing C-C and C=C bonds respectively. The three brown circles represent the three Cu atoms forming the hollow site. The green arrow represents the orientation of the Cu(111) surface, the red arrow represents the orientation of the C_{60}-*h*, and the red shaded region represents the angle of adsorption with respect to the underlying Cu(111) surface. The origin of the coordinate system is placed at the center of mass of the C_{60} and the Cu(111) hollow cite (green dot), with a positive angle corresponding to an anticlockwise rotation. The black dashed line in the center of the image is the mirror plane which maps the geometries corresponding to unique C_{60}-Cu interactions onto the mirror geometries.

4.2.3.1 *Adsorption Angle with TS*

Figure 4.16 displays adsorption data for C_{60} relaxing on the both the Cu_u and Cu_r surfaces **(Figures 4.16 A&B** respectively**)**. The initial azimuthal angle (D_i) is varied between $D_i = +60°$ and $D_i = -60°$, and the C_{60} molecule allowed to relax freely onto the surface. The initial and final adsorption angles are defined by the red angles in **Figure 4.15**, and the angles are calculated using the same reference atom in the C_{60} molecule. This data was generated in FHI-aims using the TS vdW correction with the Cu-Cu TS interactions turned off, and an $n = 7$ Cu(111)-(4x4) slab. The FHI-aims convergence criteria are given in **Table 4.5**. The starting height of the C_{60} molecule for any given rotation was in the range $0.2\text{Å} \leq h_{start} \leq 1\text{Å}$, where h_{start} is the starting height of the C_{60} relative to the calculated adsorption height. It was noticed the FHI-aims relaxation algorithm would lower the C_{60} molecule to the adsorption height, followed by an azimuthal rotation at an approximately constant height. Therefore, h_{start} was found to have little to no effect on the final rotation for the values tested ($h_{start} \gtrsim 0.2\text{Å}$). Due to this finding, the initial h_{start} was reduced to save computational time, resulting to the h_{start} range given above.

When looking at the plots in **Figure 4.16**, the following should be taken into consideration:

1. The individual points are the local energy minima found by the FHI-aims relaxation algorithm. The plots **do not** show the energy barriers for rotation between these converged geometries. Research into the energy barrier for azimuthal rotations has been carried out by Jeremy Leaf [116][58][96][115]. No data exists for the white space between the points.

2. The regions shaded red indicate that *the geometry was not converged at that azimuthal rotation*, but otherwise have no physical meaning.

3. It is plausible using different relaxation algorithms and/or convergence parameters could result in the system converging on more, or less, local energy minima, however these changes should not significantly affect the global degenerate energy minima at $D \backsimeq 0° \pm 60n°$ where $n = 0, 1, 2...\infty$.

4. The error on each quoted angle is approximately $\pm 3°$. The error estimate is calculated from the spread of angles created when multiple unique starting geometries converged on approximately the same final adsorption angle in **Figure 4.16 A**.

Looking at both **Figures 4.15 & 4.16** one can observe the *Relative Adsorption Energy* and *Charge Transfer* on adsorption data, in **Figure 4.16**, follows the same trends observed in the symmetry of the system in **Figure 4.15**. In addition, the *Relative Adsorption Energy* is calculated

to be lower for positive angles, suggesting the system is more stable with the C-C bonds being located over the Cu atoms, rather than the C=C bonds. Further observations can also be made about **Figure 4.16**. **Figure Figure 4.16 B** shows the global minimum *adsorption energy* for the $C_{60,r}$ system is located at $D_{r,min} = 0° \pm 60n°$ where $n = 0, 1, 2...\infty$ (also expressed as $D_{r,min} = (30° \pm 30°) \pm 120n°$). Whereas **Figure 4.16 A** shows the global minimum *adsorption energy* for the $C_{60,u}$ system is located at $D_{u,min} = (30° \pm 26°) \pm 120n°$. The $4°$ difference between the two systems is likely due to the effect of the additional 7 Cu atoms in the Cu_r surface. In the $C_{60,u}$, system it is possible inter-molecular interactions have an effect on the azimuthal adsorption angle. Whereas for the $C_{60,r}$ system, the additional Cu atoms form lateral chemical bonds with the $C_{60,r}$ molecule. These chemical bonds will be the dominant interaction over the much weaker inter-molecular C_{60} interactions.

Computational results similar to **Figure 4.16** have been published in the literature. The FCC adsorption site data in **Figure 2b** of Cheng *et al* [58] agrees with the findings from **Figure 4.16 A** for the $C_{60,u}$ system; geometries corresponding with C atoms located above Cu atoms are the degenerate global energy minima of the system. Their work also showed the same is true for the hexagonal close packed adsorption site. More contemporary computational results from Wang *et al* [115] are available for the $C_{60,r}$ system. Wang's work also found the system to have global degenerate energy minima for all geometries with C atoms directly above Cu atoms, in agreement with **Figure 4.16 B**.

Finally, by comparing the orange dots and blue crosses in **Figure 4.16**, one can observe the effects of using the less computationally expensive LSS over the more computationally TSS. Using LSS over TSS had a minimal effect on the adsorption data. There is no significant difference in the *Relative Adsorption Energy* between the simulations performed *LSS* and TSS. In addition, the difference in calculated *charge transfer* is $< 0.02e$, which was shown to be insignificant in **Section 4.2.1.1**. This suggests LSS are adequate for simulating C_{60} adsorbing on the Cu(111)-(4x4) when looking at the *relative adsorption energy* and the *charge transfer* on adsorption.

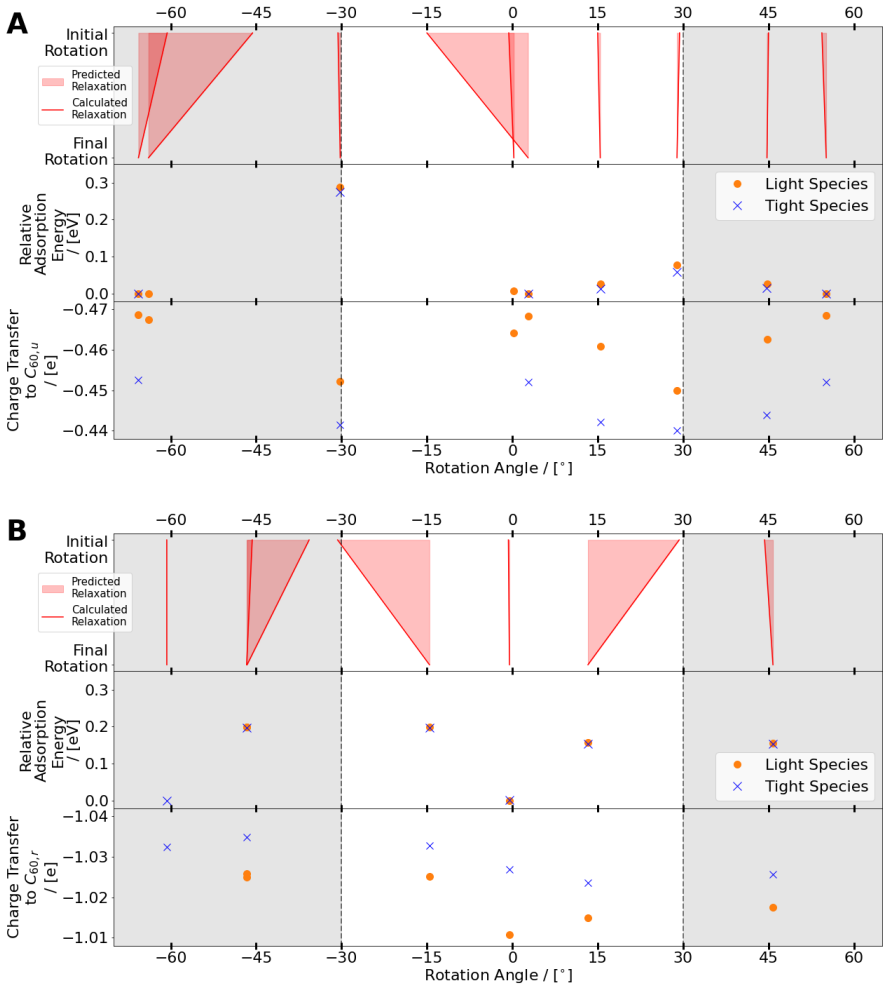

Figure 4.16: Rotation on adsorption, adsorption energy, and charge transfer (to the C_{60} molecule) calculated with HPA for C_{60} adsorbed on Cu(111) surface at various initial and relaxed azimuthal angles. **A:** Azimuthal rotation data for the $C_{60,u}$ system. **B:** Azimuthal rotation data for the $C_{60,r}$ system. The top plots in **A&B** show the azimuthal rotation angle of the initial and relaxed geometries (red lines and shaded regions), where the relaxation was performed using LSS. Dark red lines show the path from the initial angle to the relaxed angle, shaded red regions show the angle that theoretical initial angles are predicted to relax to. Where a positive rotation angle is calculated anticlockwise from the vertical (**Figure 4.15**). The red and black dots mark 15° intervals, which correspond to the diagrams in **Figure 4.15**. The middle and bottom plots in **A&B** display the adsorption energy and charge transfer for the relaxed geometry, with orange dots and blue crosses representing LSS and TSS data respectively.

FHI-aims Parameter Key	FHI-aims Parameter Value	Comments
`xc`	`pbe`	
`charge`	`0`	
`spin`	`none`	
`relativistic`	`atomic_zora scalar`	
`adjust_scf`	`always 2`	
`occupation_type`	`gaussian 0.1`	
`mixer`	`pulay`	
`n_max_pulay`	`8`	
`sc_accuracy_etot`	10^{-6}	
`sc_accuracy_eev`	10^{-3}	
`sc_accuracy_forces`	10^{-4}	
`sc_accuracy_rho`	`default`	See manual for default values
`relax_geometry`	`trm` 10^{-2}	
`k_grid`	`8 8 1`	As discussed in **Section 4.1.1**

Table 4.5: Simulation parameters for C_{60} on Cu(111)-(4x4) azimuthal rotation testing

4.2.3.2 *Adsorption Angle with MBD*

The results presented in **Chapter 6** of this work suggested that the TS vdW correction overestimates the interaction between two C_{60} molecules, and thus is not the ideal vdW correction to use for systems involving C_{60} molecules. As a result of this finding, further DFT work was completed using the MBD vdW correction. When transitioning from the TS to the MBD vdW correction, it was found the vdW correction can effect the adsorption geometry.

The azimuthal adsorption angle of the $C_{60,r}$ system did not change, likely because the geometry of this system is dominated by chemical bonding between the reconstructed surface and the C_{60} molecule. However, the azimuthal adsorption angle of the $C_{60,u}$ system changed from $D_{u,min} = (54 \pm 3)^\circ$ to $D_{u,min} = 44^\circ$. It is hypothesized the adsorption angle of the $C_{60,u}$ system was able to change because it is more dependent on vdW interactions than the $C_{60,r}$ system, as there is no lateral chemical bonding between the C_{60} molecule and Cu surface in the $C_{60,u}$ system. As the interactions between neighbouring C_{60} molecules is a long range interaction, it will be affected by a change to the long range vdW corrections. The adsorption angle calculated with the MBD vdW correction is considered the most reliable value. The simulated force spectra in **Chapter 6** found better agreement with the experimental dtaa when implementing the MBD correction rather than the TS. Furthermore, as described in **Section 3.6**, the MBD approach includes a more theoretically complete description of long range vdW interactions.

4.3 SYSTEMS FOR SIMULATED NC-AFM

4.3.1 *C_{60} Tip*

The model C_{60} functionalized AFM tip (C_{60} Tip) was created by rotating the $C_{60,r}$ system 180°about the X axis, followed by a 60° degree rotation about the Z axis, to produce the geometry shown in **Figure 4.17 A**. The choice of the $C_{60,r}$ system as the model C_{60} Tip was influenced by a number of factors:

1. Experimental data given in **Section 7.2.1** of the thesis by Simon Taylor [117] suggests a C_{60} adsorbed on a blunt Cu base produces a more stable C_{60} functionalized tip. This contributes to the decision to model the C_{60} functionalized AFM tip (C_{60} Tip) as being adsorbed on a slab of Cu rather than a pyramid of Cu.

2. To create the C_{60} Tip experimentally, an adsorbed C_{60} must be picked off the Cu(111) surface. Therefore it is logical to assume the bonding between the Cu tip, and the lifted C_{60}, must be stronger than the bonding between the adsorbed C_{60} molecule and the Cu(111) surface in the experimental $C_{60,u}$ system. Therefore the $C_{60,r}$ system was chosen over the $C_{60,u}$ system as the model C_{60} functionalized AFM tip (C_{60} Tip).

3. The periodicity of the tip must match the periodicity of the sample as periodic boundary conditions were used during the simulated force spectra.

4. Convergence testing has already been performed for the $C_{60,r}$ system. As the relative positions of the atoms in the unit cell remain unchanged, the convergence testing detailed in **Section 4.2** can be directly applied to the C_{60} Tip system.

Figure 4.17 B&C visualize the systems used to simulate AFM force spectra taken with a C_{60} Tip over an adsorbed $C_{60,u}$ and $C_{60,r}$ molecule respectively. **Figure 4.17 D&E** represent the true periodic nature of the systems **Figure 4.17 B&C** respectively. As the DFT systems in **Figure 4.17 B&C** are periodic within the simulation, the simulated force spectra are simulations of a mono-layer of $C_{60,r}$ approaching a mono-layer of $C_{60,u}$ or $C_{60,r}$. The effect of the periodicity on the force spectra is quantified in **Chapter 6, Sections 6.2.4&6.2.5**. However, the periodicity also means if the tip or sample C_{60} molecule rotates, the simulation is no longer valid when compared to the experimental data because during the simulations in this work the entire mono-layer rotates in unison.

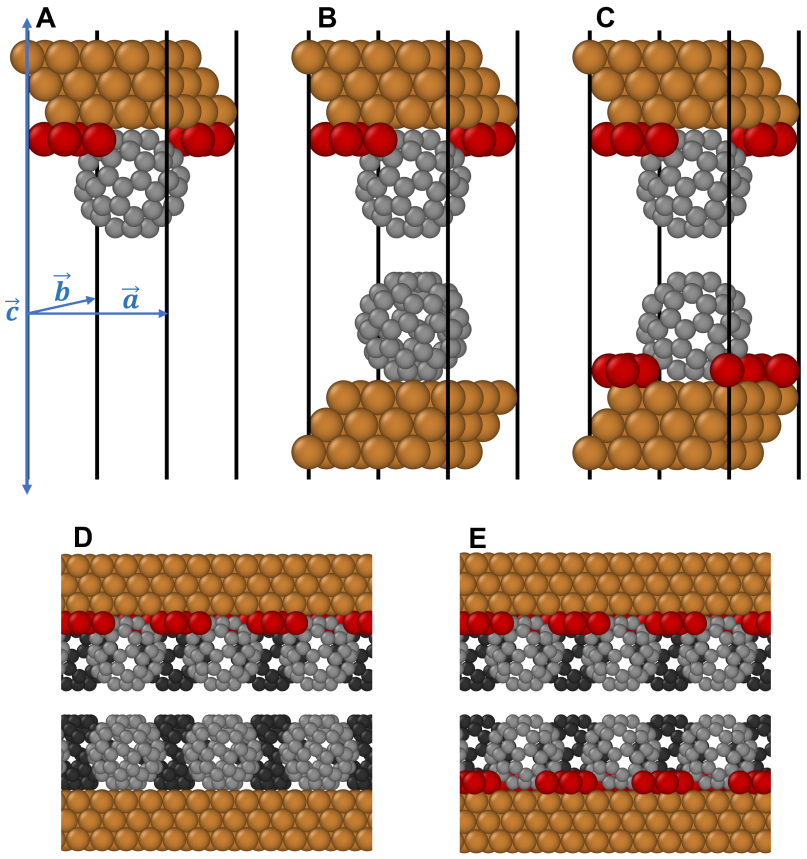

Figure 4.17: (**A**) Visualization of the simulated C_{60} functionalized AFM tip (C_{60} Tip), (**B**) the simulated C_{60} functionalized AFM tip (C_{60} Tip) combined with the simulated $C_{60,u}$ surface, (**C**) the simulated C_{60} functionalized AFM tip (C_{60} Tip) combined with the simulated $C_{60,r}$ surface. **D&E** display **B&C** replicated infinitely along $\overrightarrow{a}$ and twice along $\overrightarrow{b}$ to visualize how the system was simulated as two infinite mono-layer approaching each other. Atoms are represented as spheres, with orange, red, grey, and dark grey representing Cu, Cu in the surface reconstruction, C in the first repeat of C_{60} molecules along the $\overrightarrow{b}$ direction, and C in the second layer of C_{60} molecules along the $\overrightarrow{b}$ direction, respectively. All 3D atomic geometry visualizations in this work were created using OVITO [97].

4.3.2 *Cu(111) and CO Tips*

The model copper functionalized AFM tip (*Cu* Tip) was created by generating a Cu(111) slab of $a_{Cu} = 3.6310$Å and selectively removing atoms from the system. A three layer pyramid tapering to a single atom apex, sitting upon a two layer thick Cu(111) slab, was the chosen *Cu* Tip (**Figure 4.18 A**). A pyramid tapering to a single atom is a commonly used design [118][119][120][121][33][122][123][124][125], used to mimic the ideal experimental AFM tip. Furthermore, the pyramid was placed upon an $n = 2$ thick slab as it has been shown the electric field generated by the slab can be significant when simulating SPM experiments [125]. The tip was created from a Cu(111) slab as this ensured the periodicity of the tip structure agreed with the periodicity of the unit cell and the Cu(111) slab forming part of the surface. **Figure 4.17 B&C** visualize the systems used to simulate AFM force spectra taken with a *Cu* Tip over an adsorbed $C_{60,u}$ and $C_{60,r}$ molecule respectively. **Figure 4.17 D&E** represent the true periodic nature of the systems **Figure 4.17 B&C** respectively. As the DFT systems in **Figure 4.17 B&C** are periodic within the simulation, the simulated force spectra are actually a mono-layer of *Cu* Tips approaching a mono-layer of adsorbed $C_{60,u}$ or $C_{60,r}$. The CO functionalized AFM tip (*CO* Tip) tip was generated by adsorbing a CO molecule onto the *Cu* Tip apex in a vertical orientation, as shown in **Figure 4.19**.

Although extensive convergence testing was not performed for the *Cu* Tip, the data from **Section 4.2** can be applied to this new system. The data in **Section 4.2** suggests three layers of Cu(111) are adequate for the system to convergence with respect to adsorption energy and charge transfer. Looking at the *Cu* Tip, there are five layers of Cu(111); three layers within the tip pyramid, and two layers of Cu(111)-(4x4). Furthermore, one can think of the Cu pyramid as a Cu 'molecule' adsorbed on the slab, partially decoupling the tip-sample interaction from the slab thickness of the tip.

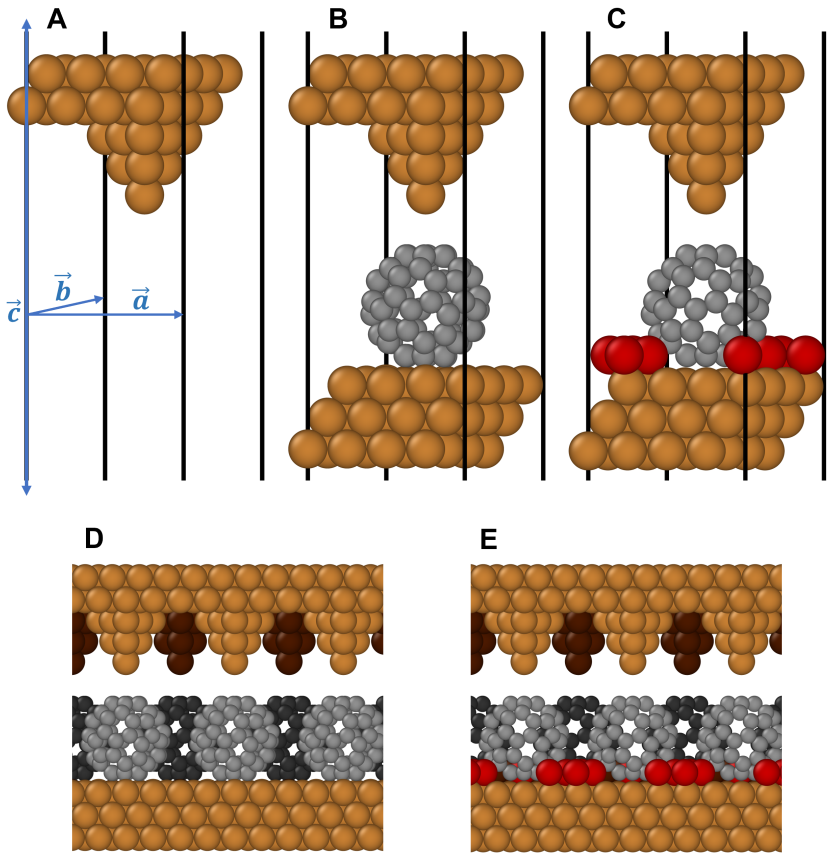

Figure 4.18: (**A**) Visualization of the simulated Cu Tip, (**B**) the simulated Cu Tip combined with the simulated $C_{60,u}$ surface, (**C**) the simulated copper functionalized AFM tip (Cu Tip) combined with the simulated $C_{60,r}$ surface. **D&E** display **B&C** replicated infinitely along $\vec{a}$ and twice along $\vec{b}$ to visualize how the system was simulated as two infinite mono-layers approaching each other. Atoms are represented as spheres, with orange, red, grey, and dark grey representing Cu, Cu in the surface reconstruction, C in the first layer of C_{60} molecules, and C in the second layer of C_{60} molecules, respectively. Dark brown represents Cu in the second layer of Cu tips, positioned above the second layer of C_{60} molecules (dark grey). All 3D atomic geometry visualizations in this work were created using OVITO [97].

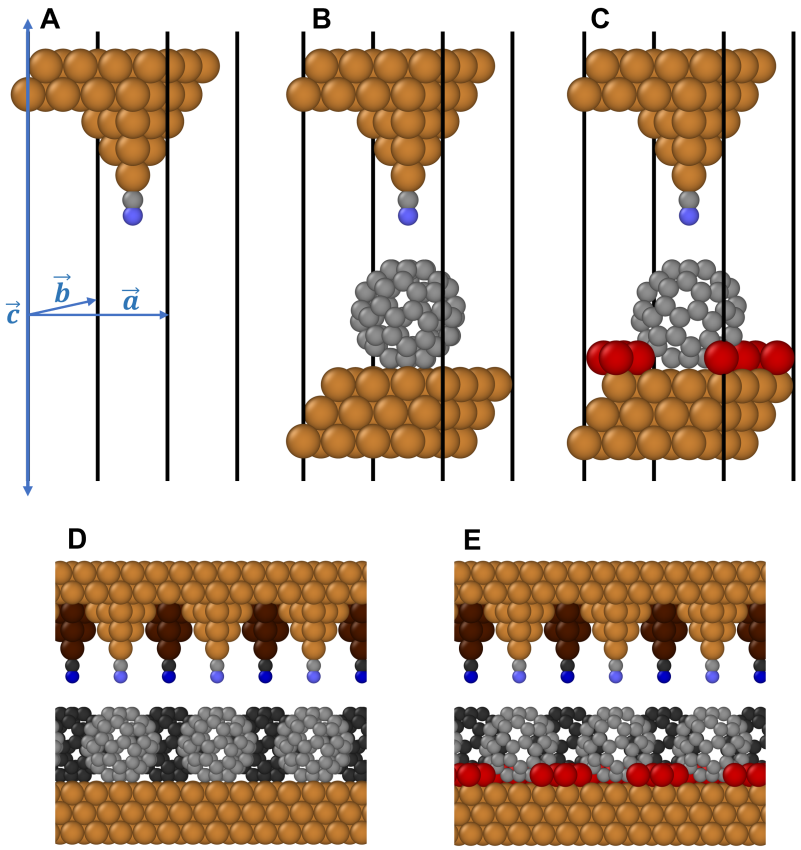

Figure 4.19: (**A**) Visualization of the simulated *CO* Tip, (**B**) the simulated *CO* Tip combined with the simulated $C_{60,u}$ surface, (**C**) the simulated CO functionalized AFM tip (*CO* Tip) combined with the simulated $C_{60,r}$ surface. **D&E** display **B&C** replicated infinitely along $\vec{a}$ and twice along $\vec{b}$ to visualize how the system was simulated as two infinite mono-layers approaching each other. Atoms are represented as spheres, with orange, red, grey, and dark grey representing Cu, Cu in the surface reconstruction, C in the first layer of C_{60} and CO molecules, and C in the second layer of C_{60} and CO molecules, respectively. Dark brown and dark blue represent Cu and O in the second layer of CO tips, positioned above the second layer of C_{60} molecules (dark grey). Light blue represent the O of the CO tips positioned in the first layer. All 3D atomic geometry visualizations in this work were created using OVITO [97].

4.3.3 $H_2O@C_{60}$

Small molecules such as H_2O and HF can be trapped within a C_{60} cage [126]. For the case of H_2O contained within a C_{60} cage, with the resulting molecular complex is referred to as $H_2O@C_{60}$. In this work the notation has been extended to include information about the surface; $H_2O@C_{60,u}$ for the $H_2O@C_{60}$ molecular complex adsorbed on the Cu_u surface ($H_2O@C_{60,u}$), $H_2O@C_{60,r}$ for the $H_2O@C_{60}$ molecular complex adsorbed on the Cu_r surface ($H_2O@C_{60,r}$), and $H_2O@C_{60,g}$ for the $H_2O@C_{60}$ molecular complex in a gaseous state ($H_2O@C_{60,g}$). The H_2O molecule was positioned in the previously relaxed $C_{60,u}$ and $C_{60,r}$ geometries to recreate the same relative H_2O and C_{60} positions as described by Sader *et al* [126]. The system was then allowed to relax during the force spectra, with only the top and bottom slab layers of the tip and sample being confined, consistent with the other simulated force spectra in this work.

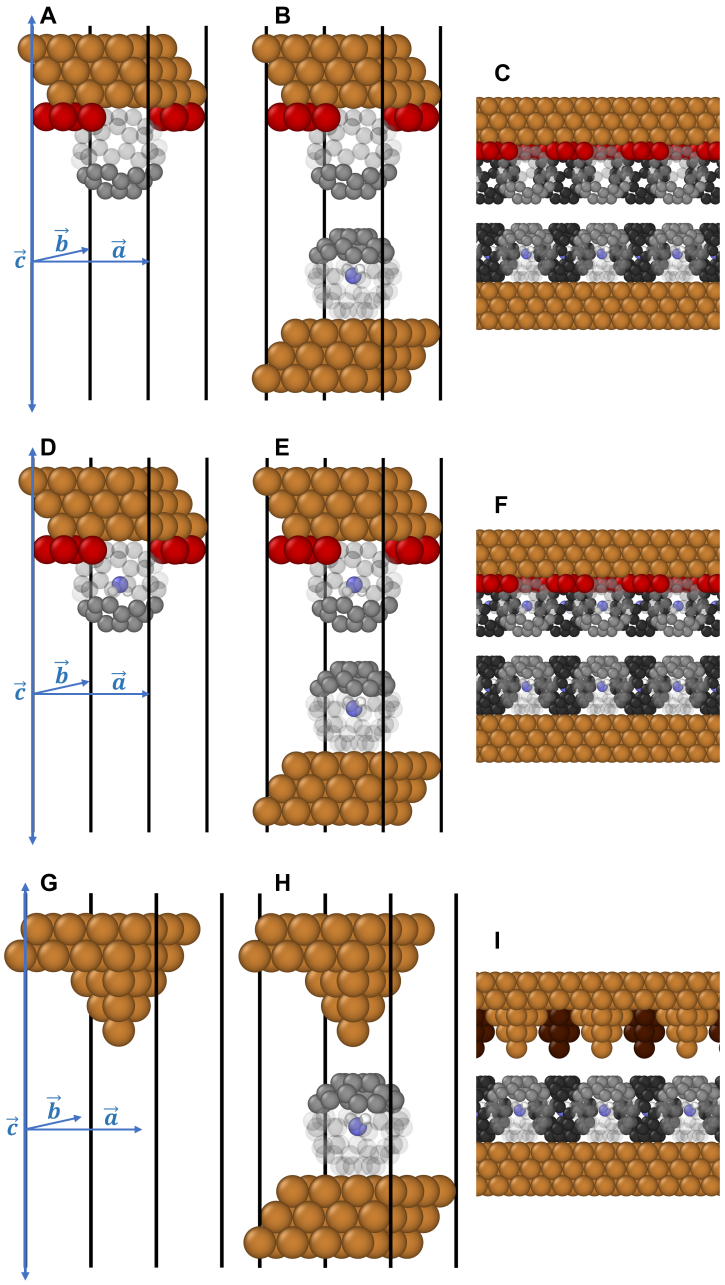

Figure 4.20: Visualization of the three AFM systems used to simulate force spectra over a $H_2O@C_{60}$ molecule. **{A, B, C}**: $C_{60,r}$ AFM tip. **{D, E, F}**: $H_2O@C_{60,r}$ AFM tip. **{G, H, I}**: Cu AFM tip. Where **{A, D, G}** contain just the tip, **{B, E, H}** contain the full system, and **{C, F, I}** the full system replicated infinitely along $\vec{a}$ and twice along $\vec{b}$. Atoms are represented as spheres, with orange, red, grey, and dark grey representing Cu, Cu in the surface reconstruction, C in the first layer of C_{60} and CO molecules, and C in the second layer of C_{60} and CO molecules, respectively. White and light blue represent the H and O in H_2O, and dark brown the Cu in the second layer of Cu tips, positioned above the second layer of C_{60} molecules (dark grey). The bottom two thirds of the front most C_{60} molecules are transparent to allow the contained H_2O molecule visible. All 3D atomic geometry visualizations in this work were created using OVITO [97].

4.3.4 *Gaseous Systems*

Systems involving C_{60} and $H_2O@C_{60}$ were also simulated as gaseous molecules approaching each other. In this gaseous regime the systems were simulated without the presence of a metal surface, as cluster calculations (no repeating unit cell). This greatly reduces the computational cost of such calculations, allowing more spectra to be simulated. In addition, as the calculations are not periodic, effects such as the unit cell interacting with itself are no longer an issue. The effect of the relative rotation between the tip and sample C_{60} molecules on the calculated force spectra was investigated using this gaseous system.

Figure 4.21 details how the system geometries described in **Section 4.3.4** were made. The following describes points **1***, **2*** and **3*** from **Figure 4.21**;

1. The 6 Carbon atoms forming the bottom hexagon of the $C_{60,g}$ were confined along the Z direction, but not the X and Y directions. All other atoms were allowed to relax freely. This formed a flat face to confine the $C_{60,g}$ molecule from during the spectra, without incorporating strain into the system from the confined atoms.

2. The H_2O molecule was given the same initial orientation as in **Figure 4.20**. As with step **1***, The 6 C atoms forming the bottom hexagon of the $H_2O@C_{60,g}$ were confined along the Z direction, but not the X and Y directions. All other atoms were allowed to relax freely.

3. The 6 Carbon atoms in the bottom hexagon of the *surface* molecular complex, and top hexagon of the *tip* molecular complex, were confined along the X, Y, and Z directions. These are the C atoms previously confined in the Z direction only.

4.3.4.1 $C_{60,g}$ *Approaching* $C_{60,g}$

Figure 4.14 shows how a C_{60} molecule presenting a C_{60}-*h* face has the same C_{3v} symmetry as a hollow site on the Cu(111) surface. Therefore, the geometry of a C_{60}-*h* face approaching a C_{60}-*h* face **(Figure 4.22)** can be thought of as having the same symmetries as the system described in **Figure 4.15**;

1. Geometries corresponding to unique tip-sample interactions can be found in the relative rotation range $-30° \leq D \leq 30°$.

2. Mirror geometries corresponding to equivalent tip-sample interactions can be found in the relative rotation ranges $-30° \geq D \geq -60°$ and $30° \leq D \leq 60°$.

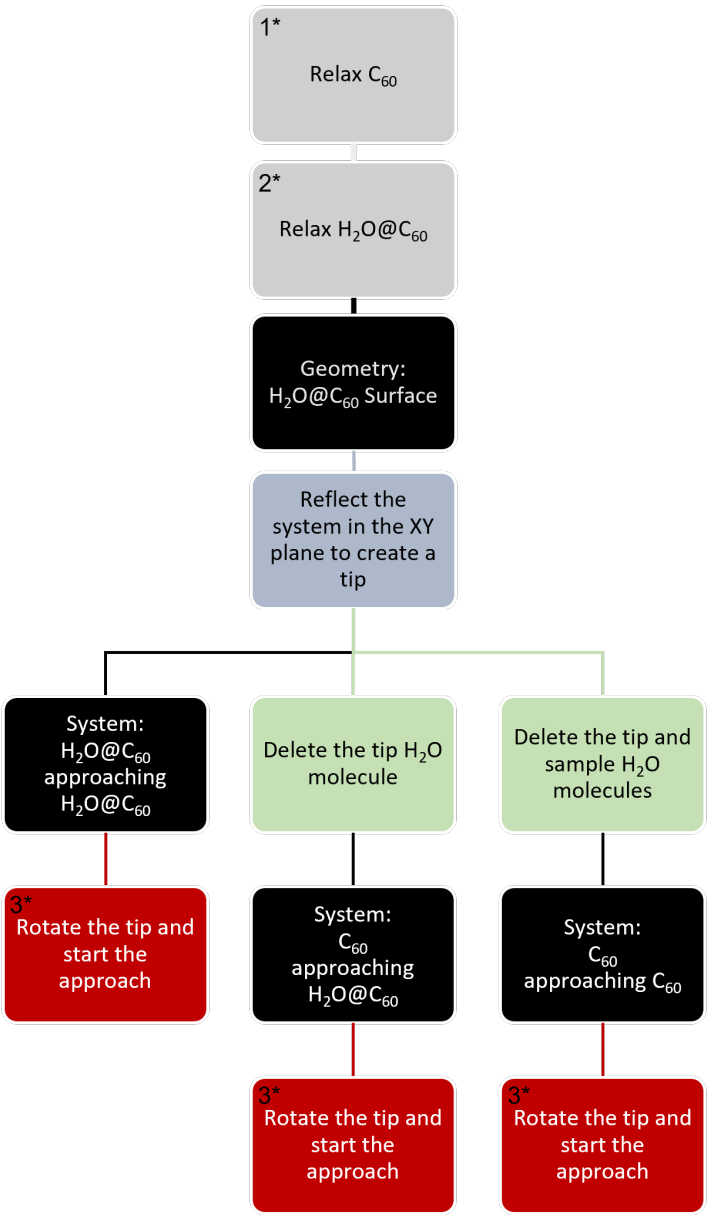

Figure 4.21: Flow diagram describing how the $C_{60,g}$ and $H_2O@C_{60,g}$ system geometries were made. The points marked 1*, 2* and 3* are further explained in the main text **(Section 4.3.4)**.

3. A 120° rotation of the tip or sample produces an identical geometry.

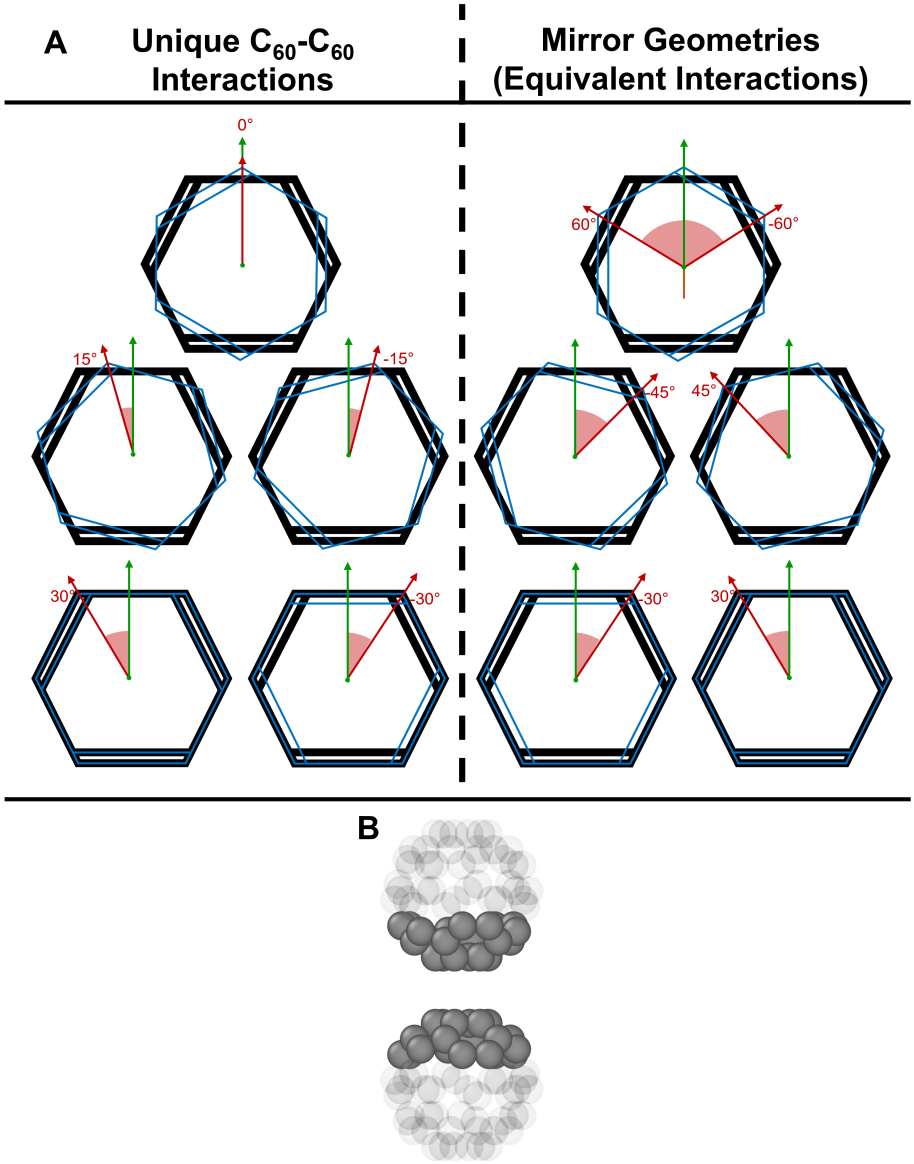

Figure 4.22: **A:** Possible geometries for the interaction of a C_{60}-h approached by a second C_{60_g} molecule in the C_{60}-h orientation. The surface and tip molecules are represented by the black and blue hexagons respectively. Double and single lines represent C=C and C-C bonds. The red and green arrows represent the orientation of the tip and sample molecules respectively, the red shaded regions gives the relative angle between the two molecules. The black dashed line in the center of **A** is the mirror plane in which maps the geometries corresponding to unique C_{60}-h - C_{60}-h interactions onto the mirror geometries. **B:** Diagram of the full C_{60_g} molecular system. Grey spheres represent C atoms, some of the C atoms have been rendered as partially transparent. All 3D atomic geometry visualizations in this work were created using OVITO [97].

$C_{60,g}$ *Approaching* $H_2O@C_{60,g}$

The trapping of a H_2O molecule in a $C_{60,g}$ to form the $H_2O@C_{60}$ molecular complex in a gaseous state ($H_2O@C_{60,g}$) breaks the C_{3v} symmetry of the system. As a result, the hexagonal face of a $H_2O@C_{60}$ molecule ($H_2O@C_{60}$-h) no longer has rotational symmetry, but still possesses a single vertical plane of mirror symmetry. However, the pattern of unique geometries and mirror domains obtained by combining two systems is determined by the highest order of symmetry of the constituent systems. Therefore, replacing the C_{60}-h surface with a $H_2O@C_{60}$-h surface **(Figure 4.23)** produces the same pattern of unique geometries and mirror domains demonstrated in **Figures 4.15&4.22**.

$H_2O@C_{60,g}$ *Approaching* $H_2O@C_{60,g}$

In this system both the tip and the sample molecular complexes are $H_2O@C_{60,g}$ molecules. This results in no azimuthal rotational symmetry in the full system as the constituent $H_2O@C_{60,g}$ molecules have no rotational symmetry. Therefore, the pattern of unique and mirror geometries are different to the systems described in **Sections 4.3.4.1 & 4.3.4.1**;

1. Geometries corresponding to unique tip-sample interactions can be found in the relative rotation range $-90° \leq D \leq 90°$ **(Figure 4.24)**.

2. Mirror geometries corresponding to equivalent tip-sample interactions can be found in the relative rotation ranges $-90° \geq D \geq -180°$ and $90° \leq D \leq 180°$, where the geometries corresponding to $D = \pm 180°$ are the same geometries.

3. A full $360°$ rotation of the tip or sample is required to produce an identical geometry.

A system comprising of $H_2O@C_{60}$-h approaching $H_2O@C_{60}$-h was simulated **(see Figure 4.24)**. In the experimental system, where the $H_2O@C_{60}$ molecular complex is adsorbed on a metal substrate or metal SPM tip base, the H_2O molecule is thought to orient so the H atoms point away from the metal substrate **[126]**. Therefore, the initial orientation of the tip $H_2O@C_{60}$-h was set to mimic this.

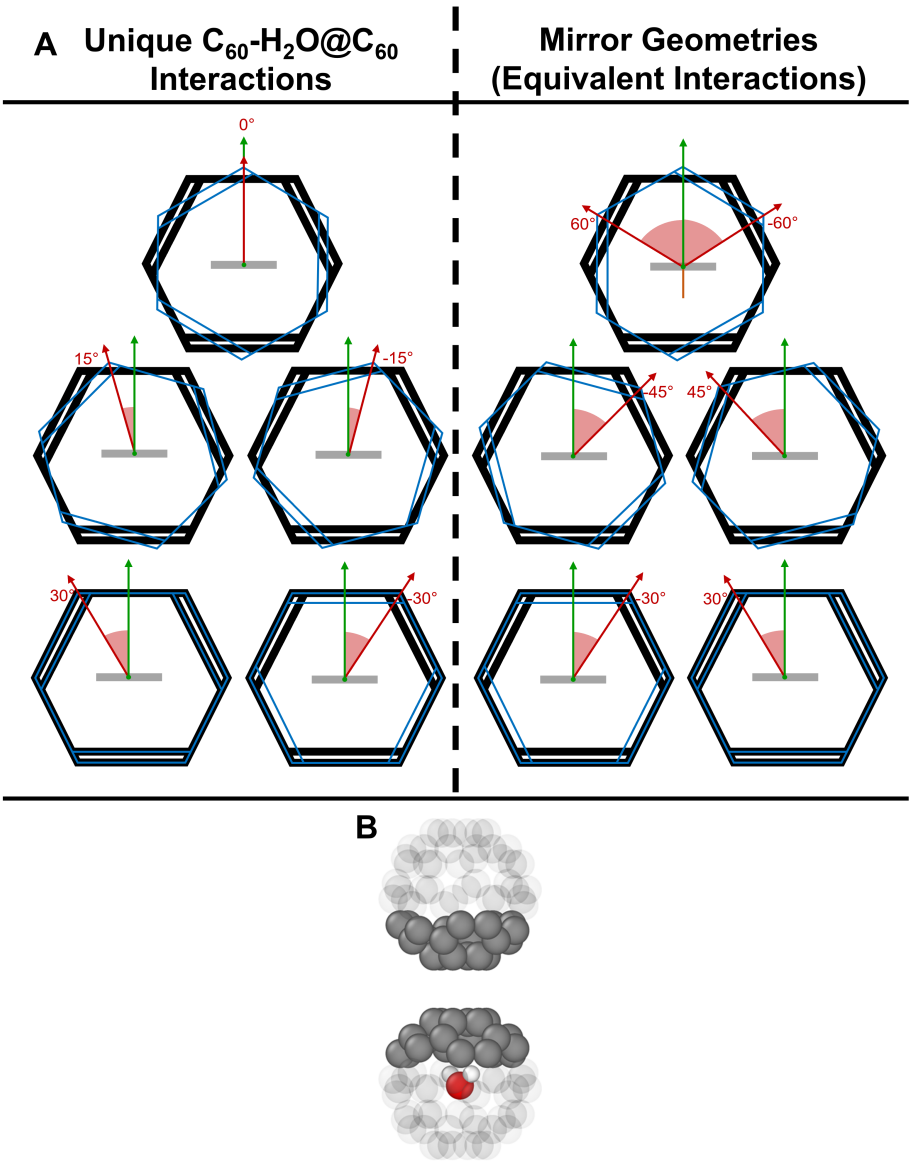

Figure 4.23: **A:** Possible geometries for the interaction of a C_{60}-*h* approaching a $H_2O@C_{60}$-*h* from a $H_2O@C_{60,g}$ molecule. The surface and tip molecules are represented by the black and blue hexagons respectively, with the grey line representing the long axis of the H_2O molecule contained within the surface $H_2O@C_{60,g}$ molecule. The red and green arrows represent the orientation of the tip and sample molecules respectively, the red shaded regions gives the relative angle between the two molecules. Double and single lines represent C=C and C-C bonds. The black dashed line in the center of **A** is the mirror plane in which maps the geometries corresponding to unique C_{60}-*h* - $H_2O@C_{60}$-*h* interactions onto the mirror geometries. **B:** Diagram of the full molecular system. Grey, red, and white spheres represent C, O, and H atoms respectively. Some of the C atoms have been rendered as partially transparent to make the encapsulated H_2O molecule is visible. All 3D atomic geometry visualizations in this work were created using OVITO [97].

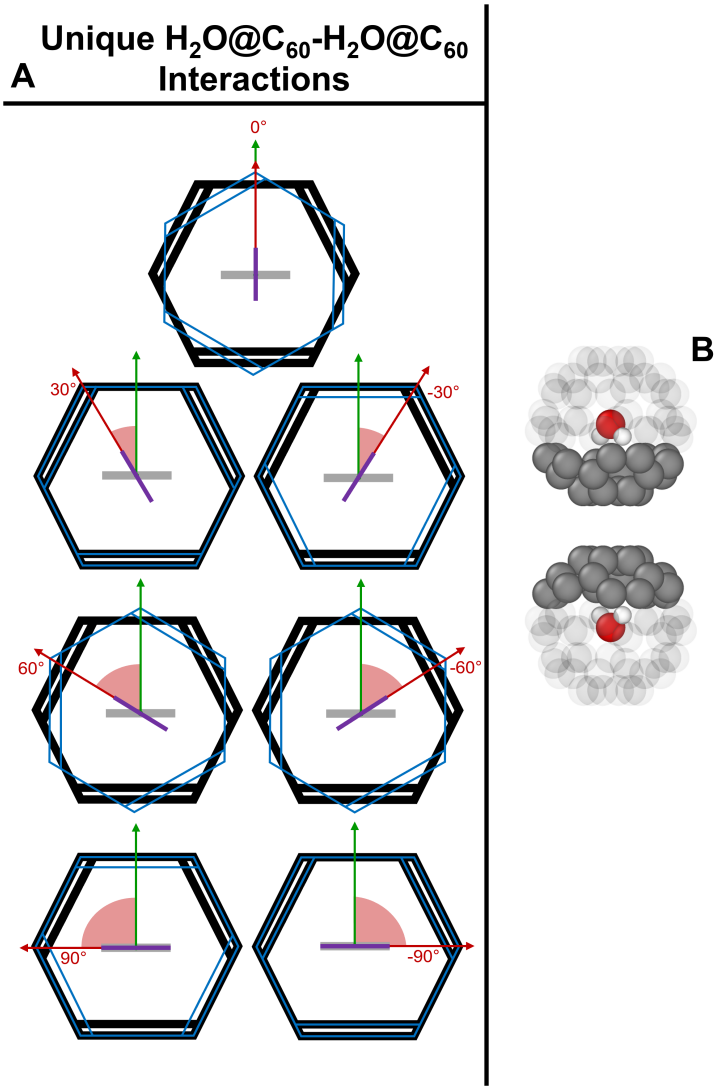

Figure 4.24: **A:** Geometries for a $H_2O@C_{60}$-*h* approaching a $H_2O@C_{60}$-*h* of a second $H_2O@C_{60,g}$ molecule. The surface and tip molecules are represented by the black and blue hexagons respectively, with the grey and orange lines representing the long axis of the H_2O molecules contained within the surface and tip $H_2O@C_{60,g}$ molecules, respectively. The red and green arrows represent the orientation of the tip and sample molecules respectively, the red shaded regions gives the relative angle between the two molecules. Double and single lines represent C=C and C-C bonds. **B&C:** Diagrams of the full molecular systems involving $H_2O@C_{60,g}$ approaching $H_2O@C_{60,g}$. Grey, red, and white spheres represent C, O, and H atoms respectively. Some of the C atoms have been rendered as partially transparent to make the encapsulated H_2O molecules visible. Mirror geometries corresponding to equivalent tip-sample interactions ($-180° \leq D \leq -90°$ and $90° \leq D \leq 180°$) have not been displayed as they were not simulated. All 3D atomic geometry visualizations in this work were created using OVITO [97].

5

SIMULATED NC-AFM METHODS

5.1 SYSTEM COMPONENTS

Figure 5.1 defines key groups of atoms within a Simulated Non-Contact Atomic Force Microscopy ($_s$NC-AFM) system. A $_s$NC-AFM system can be broken down into components; a $_s$NC-AFM tip ($_s$Tip), and a $_s$NC-AFM surface ($_s$Surface). If the $_s$Tip is a functionalized metal tip, then we can break down the $_s$Tip into the metal section of the $_s$NC-AFM tip, which can be further functionalized with additonal molecules (such as C_{60}, CO, or Cu tip apex) ($_s$Tip Base), and the molecule adsorbed on the functionalized $_s$Tip Base ($_s$Tip Molecule). All $_s$Tips have a $_s$Tip Apex, which we define as the atoms in the $_s$Tip involved in short range interactions with the $_s$Surface ($_s$Tip Apex). Examples of short range interactions being pauli repulsive forces, and covalent or metallic bonding. A similar set of component definitions can also be made for the $_s$Surface. If the $_s$Surface is simulating molecule adsorbed on a surface, then we can further break down the $_s$Surface into the the underlying surface, analogous to the experimental surface ($_s$Surface Base) and the the molecule adsorbed on the underlying surface, analogous to the deposited molecule in an experiment ($_s$Surface Molecule). Furthermore, like with the $_s$Tip, all $_s$Surfaces have a $_s$Surface Apex, which we define as the atoms in the $_s$Surface involved in short range interactions with the $_s$Tip ($_s$Surface Apex).

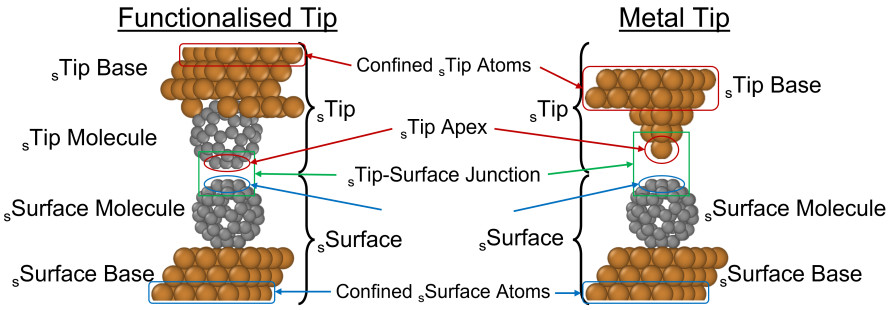

Figure 5.1: Definitions of the components forming the $_s$Tip and $_s$Surface in $_s$NC-AFM systems. The components have been defined pictorially for both a simulated metal tip, and a simulated functionalized metal tip. All 3D atomic geometry visualizations in this work were created using OVITO [97].

5.2 FORCE SPECTRA IN FHI-AIMS

When calculating $_s$NC-AFM with DFT, implemented in FHI-aims, there are three methods for calculating the force and corresponding potential spectra. The Fritz Haber Institute *ab initio* molecular simulations System Energy method (FHI-aims-SE) **(see Section 5.4)**, the Fritz Haber Institute *ab initio* molecular simulations Tip Forces method (FHI-aims-TF) **(see Section 5.5)**, and the Fritz Haber Institute *ab initio* molecular simulations Surface Forces method (FHI-aims-SF) **(see Section 5.5)**. **Section 5.3** describes how the Z scale for a $_s$NC-AFM is defined, and **Section 5.6** details how the the three possible approaches for calculating the $_s$NC-AFM force and potential spectra were applied in this work. Where the $_s$NC-AFM spectrum is built from a series of well defined DFT simulations, calculated by FHI-aims.

The general procedure for calculating a $_s$NC-AFM force spectra with FHI-aims is as follows:

1. The geometry for the $_s$Tip and $_s$Surface are created and geometrically relaxed in separate calculations. The converged systems should be checked for resultant force along the Z direction. If a resultant force is found, the system should be relaxed again with tighter force convergence criteria.

2. The converged $_s$Tip and $_s$Surface geometries are combined into one system. The $_s$Tip is positioned so the $_s$Tip Apex is located at the desired initial tip-sample separation, over the correct site on the $_s$Surface (the correct X,Y and Z coordinates). The full system is allowed relax, governed by the supplied convergence criteria. Some atoms, in both the $_s$Tip Base and $_s$Surface Base, must be confined in all three directions to calculated a valid force spectrum.

3. The $_s$Tip atoms from the converged geometry of the previous system are stepped towards the surface atoms by a desired amount. The X and Y coordinates of $_s$Tip are not changed during the step towards the surface. The new system is relaxed.

4. Repeat step 3 until the $_s$Tip atoms have approached the $_s$Surface to the desired tip-sample separation.

The Z scale, along with the force and potential data, is extracted and calculated from this series of converged simulations using the methods described below. The methods have been selected and designed to be as analogous to the $_e$NC-AFM experiments as possible.

In addition to using the converged geometry from the previous step to create the geometry for the current step, the solved electronic structure from the previous step was also used as a starting point to find the electronic structure for the new geometry. This technique was performed using the **`elsi_restart`** and **`elsi_restart_use_overlap`**

options, and resulted in significant savings of computational resources. It allows the solution of a similar geometry to be extrapolated to the current geometry, rather than starting from the gaseous orbitals of the isolated atoms. For a detailed explanation see the FHI-aims manuals for the releases used in this works [86][87][84].

5.3 Z SCALE

In Experimental Non-Contact Atomic Force Microscopy ($_e$NC-AFM), the Z scale is defined from the position of the cantilever base, which in turn is defined/controlled by the piezoelectric crystal extension. This Z scale is independent of both the oscillation amplitude, and the geometric relaxations occurring in the system. The Z scale can be further be offset to define $Z = 0$ at a sensible point using STM or $_e$NC-AFM.

When calculating $_s$NC-AFM spectra in DFT (or molecular mynamics), the Z scale needs to be defined to match the experiment. In this work, the Z scale is defined from the highest confined atom in the $_s$Tip, which is all the Cu atoms in the top layer of the $_s$Tip Base. This Z scale is then offset so that the Z coordinate at the point of largest tip-sample separation is approximately equal to the atomic core separation between the $_s$Tip Apex and the $_s$Surface Apex. With this approach, $Z = 0$ would correspond to the $_s$Tip Apex overlapping with the $_s$Surface Apex, if the system does not relax. This approach is analogous to the experimental definition of the Z scale as it is independent of geometric relaxations occurring in the system during the force spectrum.

5.4 FHI-AIMS SYSTEM ENERGY

The FHI-aims-SE method calculates a $_s$NC-AFM force spectra using the total energy of the system. This total energy includes the contributions from both the vdW correction and the DFT calculation. The potential spectrum is given by plotting the system energy against the Z scale described in **Section 5.3**. Each point in the spectrum corresponds to a single, converged, DFT calculation. To calculate a force spectrum from this data, the energy is differentiated with respect to the Z scale. As this method only relies on atomic coordinates and the converged energy of the system, it is widely applicable to other DFT and molecular dynamics programs. The zero energy point needs to be set when the potential spectrum is calculated this way. This is done by setting the initial tip-sample separation to a large enough value that it approximates a tip-sample separation of ∞, this allows the first point of the spectrum to be set as the zero energy point. $2\,nm$ was found to be adequate for $_s$NC-AFM spectra this work.

However, there are both benefits and limitations to using this approach. The system energy is calculated using every atom in the

system, with each atom having an equal weighting. Therefore, the FHI-aims-SE provides the most complete picture of the system. Unfortunately this can result in the DFT calculation diverging from the experimental data, due to the nature of how $_e$NC-AFM measures the tip-sample force. In $_e$NC-AFM, the recovered force is only sensitive to interactions between the tip and sample along the direction of tip oscillation, which is assumed to be vertical. Furthermore, due to the experimental off-curve subtraction, the captured interaction is dominated by the interaction between the experimental tip apex and surface apex. The FHI-aims-SE method is equally affected by interactions occurring between the $_s$Tip Apex and $_s$Surface Apex as it is by interactions between the $_s$Surface Base and $_s$Surface Molecule. In other words, when using the FHI-aims-SE method, interactions occurring far away from the $_s$Tip-Sample Junction have equal weighting to interactions occurring at the $_s$Tip-Sample Junction, even when those interactions are not between the $_s$Tip and $_s$Surface. Furthermore, the system energy value exacted from each individual calculation has no directionality. Therefore, the FHI-aims-SE method is sensitive to changes lateral interactions in addition to changes in vertical interactions. The increased sensitivity of the FHI-aims-SE method is most noticeable when relatively large geometrical relaxations occur at points of interest in the force spectrum, such as the force minimum. When comparing the origins of the measurements obtained from the $_e$NC-AFM to that simulated by FHI-aims-SE, we can see the increased sensitivity of the FHI-aims-SE (relative to the experiment) reduces how analogous the simulation is to the experiment. This sensitivity can be amplified when differentiating the potential to calculate the force. A small change in the gradient of the potential induced by a geometrical relaxation can have a small effect on the total potential, but a large effect on the differential of the potential (the force). Finally, the resolution of the simulated spectrum can have large effects on calculated force because the force is calculated from the differential of the energy. If a low resolution is used, the differential will be less accurate.

In summary, the FHI-aims-SE approach should be used in the following situations:

1. When the simulated $_s$NC-AFM Z resolution is too low to accurately integrate the FHI-aims-TF to calculate the potential energy.

2. If there is an offset in FHI-aims-TF that can not be corrected in post-processing.

5.5 FHI-AIMS FORCES

The Fritz Haber Institute *ab initio* molecular simulations Tip Forces method (FHI-aims-TF) and Fritz Haber Institute *ab initio* molecular simulations Surface Forces method (FHI-aims-SF) methods calculate $_s$NC-AFM

force spectra using the resultant force acting on each individual atom. The vertical component of the resultant force acting on every atom in the $_s$Tip (or $_s$Surface) are summed over to produce the force acting on the whole of the $_s$Tip (or $_s$Surface),

$$F_{z,tip} = \sum_{i_{tip}=0}^{tip\,atoms} F_{z,i_{tip}} \tag{5.1}$$

$$F_{z,surface} = \sum_{i_{surface}=0}^{surface\,atoms} F_{z,i_{surface}} \tag{5.2}$$

with $F_{z,i_{tip}}$, $F_{z,i_{surface}}$, $F_{z,tip}$, $F_{z,surface}$ representing the vertical component of the resultant force acting on the i^{th} atom in the tip, the vertical component of the resultant force acting on the i^{th} atom in the surface, the total (resultant) vertical force acting on the $_s$Tip, and the total (resultant) vertical force acting on the $_s$Surface, respectively.

In the ideal situation, the system will be perfectly relaxed and only the confined atoms will experience a resultant force. However, this is not possible within a computational simulation. Therefore we set a convergence criteria to define the maximum tolerated resultant force on a 'relaxed' atom. In FHI-aims, this convergence parameter is called **`sc_accuracy_forces`**. This value should be set sufficiently small enough to not (significantly) affect the converged geometry of the system, and therefore approximate the ideal situation of zero resultant force acting on a relaxed atom. In this work it was noticed some of the information about the long range vdW interaction, between the $_s$Tip and $_s$Surface, was contained within these very small resultant forces. Therefore, when calculating a $_s$NC-AFM force spectrum, it is important to sum over all the atoms in the $_s$Tip (or $_s$Surface), and not just the confined ones. The force spectrum is given by plotting the summed force against the Z scale described in **Section 5.3**. Each point in the spectrum corresponds to a single, converged, DFT calculation. To calculate the corresponding potential spectrum, the force is integrated using the trapezium rule [127] (with respect to the Z scale).

There are benefits and limitations to using the FHI-aims-TF and FHI-aims-SF approaches. These methods are only sensitive to forces acting in the vertical direction, and the force specifically acting on the $_s$Tip (and only the $_s$Tip) is calculated using the FHI-aims-TF method. This is analogous to the sensitivity of the $_e$NC-AFM spectrum (discussed in **Section 5.4**). Furthermore, as the force is being calculated directly from each simulation, the resolution of the spectrum will not effect the calculated force value. This allows a lower resolution to be used at large tip-sample separation, saving computational resources. Newtons 3rd law suggests the FHI-aims-TF and FHI-aims-SF methods should produce the same value, however this is not always the case. In addition, residual strain in the system (that is within the simulation convergence criteria) is integrated when calculating the corresponding potential

spectrum, potentially leading to inaccurate potential values. This issue can be approximately accounted for by offsetting the spectrum by the initial force value, under the assumption the tip-sample separation is large enough that the initial force value should be $F_{z,tip} = 0\,nN$ (or $F_{z,surface} = 0\,nN$). However, the potential spectrum is still strongly effected by the resolution of the spectrum.

In summary, the FHI-aims-TF and FHI-aims-SF approaches should be used in the following situations in the following ways:

1. **The FHI-aims-TF should be used by default to calculate the $_s$NC-AFM force spectrum and integrated to calculate the $_s$NC-AFM potential spectrum. Spectra calculated with the FHI-aims-SF should be in agreement with those calculated with the FHI-aims-TF, and can be used as a consistency check for the simulations.**

2. If the tail of the FHI-aims-TF force spectrum $\neq 0$ at a tip-sample separation of $\gtrsim 20\,$Å, and it does not agree with the FHI-aims-SF force spectrum, then the FHI-aims-TF and FHI-aims-SF spectra should be offset to remove the initial strain in the system. This offset should be applied before integrating the force spectrum to calculate the corresponding potential spectrum.

3. If the FHI-aims-TF and FHI-aims-SF approaches do not produce the same spectrum (after applying the offset), then one of two approaches can be taken. The FHI-aims-TF and FHI-aims-SF methods can be used to compare spectra calculated using the same tip geometry, and the same surface geometry respectively. Or, the FHI-aims-SE method can be used, assuming no large geometrical relaxations.

4. If the Z resolution is low, the FHI-aims-SE method should be used to calculate the potential energy spectrum.

5.6 METHODS FOR CHAPTERS 6 & 7

The force spectra detailed in **Chapters 6 & 7** were calculated using the FHI-aims-TF method described in **Section 5.5**, or the FHI-aims-SE method described in **Section 5.4**. The FHI-aims-TF method was used by default, however for some comparisons the FHI-aims-SE method was more appropriate. The corresponding potential spectra were always calculated using the FHI-aims-SE method described in **5.4**. The approaches used in this work were determined to be the best compromise for producing experimentally analogous, accurate, and computationally affordable $_s$NC-AFM spectra, on low to mid tier UK supercomputers.

5.6.1 *Resolution*

Ideally, a Z resolution (Z_{res}) of $Z_{res} \leq 10\,pm$ would be used for the full $_s$NC-AFM spectrum. Unfortunately, this approach is computationally expensive. Furthermore, the majority of the data of interest is found about the force minimum at $Z \backsimeq 3\,\text{Å}$, rather than the weakly interacting tail of the spectrum at $5\,\text{Å} < Z < 20\,\text{Å}$. Therefore, one could potentially define this approach as wasteful. After taking this into account, a lower resolution ranging from $0.2\,\text{Å} \leq Z_{res} \leq 10\,\text{Å}$ was used at the start of the spectrum, and Z_{res} was gradually decreased [1] as the $_s$Tip approached the force minimum, and the gradient of the spectrum increased.

5.6.2 *Potential Spectra*

To compensate for the low resolution, the FHI-aims-SE method was used to calculate the potential spectrum. As discussed in **Section 5.4**, the FHI-aims-SE is not ideal for $_s$NC-AFM as it is more sensitive than the $_e$NC-AFM setup. However, data at the potential minima is not affected by the low Z_{res} used in the tail of the spectrum. Therefore inaccuracies of the FHI-aims-SE approach were deemed to be smaller than those introduced by the integration of the FHI-aims-TF data over a low Z_{res}.

5.6.3 *Force Spectra*

The FHI-aims-TF method was used by default to calculate the force spectra. The force values at the force minimum are not effected by the low resolution at larger Tip-Sample separations. An offset of ~30pN was applied to the FHI-aims-TF force spectra to compensate for strain in the system when simulating a C_{60} Tip. No offset was needed for the Cu Tip. After the offset, the junction separation of ~15 Å (C_{60} Tip) or ~20 Å (Cu Tip) corresponded to a force between the tip and sample of $0\,nN$ **(see Section 5.5)**. The offset changed the absolute values of the force minima by ~30 pN but did not significantly change the difference in the force minima between the $C_{60,u}$ and $C_{60,r}$ systems. Furthermore, results obtained using the FHI-aims-TF method agreed with results obtained using the FHI-aims-SF method.

In **Chapter 7**, the FHI-aims-SE method was used to calculate both the force and potential spectra. This was due to a strain in the H_2O contained within a C_{60} molecule ($H_2O@C_{60}$) causing inaccuracies FHI-aims-TF method. Attempts to resolve the strain were made by specifying tighter convergence criteria. However, these attempts spread the strain out over more atoms, rather than releasing the strain from the system.

1 A decrease in Z_{res} results in a higher sampling rate, and a more accurate $_s$NC-AFM spectrum.

5.6.4 *Types of System*

FHI-aims is able to perform DFT calculations on two different types of system; as a *cluster* calculation, or a *periodic* calculation with periodic boundary conditions. In a *cluster* calculation, the atoms of the system are suspended in an infinitely large environment, therefore the system can be considered as *isolated*. In a *periodic* system, periodic boundary conditions are applied. This requires unit vectors along the $\overrightarrow{a}$, $\overrightarrow{b}$, & $\overrightarrow{c}$ directions to be supplied, along with the system geometry. The system is then infinitely repeated along the supplied unit vectors, allowing the unit cell to interact with itself. To avoid the *periodic* systems in this work interacting with themselves along the Z direction, a very large unit vector along the Z direction was used of $\overrightarrow{c} = 100\,\text{Å}$.

Furthermore, in this work, *gaseous* and *full* systems are considered. The *full* system is the most experimentally analogous system, involving metal surfaces acting as the ${}_s$Tip Base and ${}_s$Surface Base **(see Figure 5.1)**. The *gaseous* systems only include the ${}_s$Tip Molecule and ${}_s$Surface Molecule, as if they were in a gaseous state. These *gaseous* calculations exclusively involve C_{60} (or $H_2O@C_{60}$) molecules approaching each other in this work.

5.7 OFF-CURVE SUBTRACTION

This Section details an optimized methodology for performing ${}_s$NC-AFM force spectroscopy in DFT. This is achieved through the introduction of an experimentally analogous, simulated, Off-Curve subtraction. In this section we will show how in order to produce an accurate, experimentally analogous, force and potential spectra, one sometimes needs to simulate both the On-Curve and Off-Curve. Furthermore, it is explained how this requirement arises due to the unique geometries of the $C_{60,u}$ and $C_{60,r}$ systems. In this work we define the On-Curve and Off-Curve as; NC-AFM spectra taken over a site of interest (On-Curve), and, NC-AFM spectra taken over the (usually unperturbed) substrate to remove the long range background interaction (Off-Curve). Without a simulated Off-Curve subtraction, an experimentally analogous comparison between the force and potential minima of the $C_{60,u}$ and $C_{60,r}$ systems is not possible. This need stems from the 7 displaced surface atoms in the $C_{60,r}$ system, and how those displaced surface atoms interact with the experimental off-curve subtraction **(Figure 5.2)**.

In the experimental case, the NC-AFM spectra taken over the (usually unperturbed) substrate to remove the long range background interaction (Off-Curve)s for both systems are taken over the bare Cu(111) substrate. This Off-Curve is a good match for the $C_{60,u}$ system because the same number of Cu atoms exist in the On-Curve as they do the Off-Curve. However, for the $C_{60,r}$ system, the Off-Curve contains more

Cu atoms than the On-Curve. This discrepancy occurs because the surface reconstruction has displaced 7 surface atoms from the top layer of the Cu surface. In the Off-Curve for the $C_{60,r}$ system, these atoms have not been displaced. Therefore, the experimental Off-Curve for the $C_{60,r}$ system can be thought of as an *overestimate*. When this system is translated to DFT, this *overestimate* should be replicated to allow direct comparison between the experimental and computational results. This has been accomplished by *filling in* the 7 missing Cu surface atoms when producing the $C_{60,r}$ Off-Curve system. This *filling in* has two main effects on the $C_{60,r}$ Off-Curve system, relative to the $C_{60,u}$ Off-Curve system. The effect is the $C_{60,r}$ Off-Curve system has an additional Cu layer relative to the $C_{60,u}$ Off-Curve system. Furthermore, the location of the additional Cu layer means the simulated NC-AFM tip approaches closer to the surface in the $C_{60,r}$ Off-Curve system **(see Figure 5.2)**. This closer approach is analogous to experiment, where the $C_{60,r}$ molecules appear lower down than the $C_{60,u}$ molecules, relative to the surrounding surface. Thus, both the On-Curve and Off-Curve spectra taken atop the $C_{60,r}$ molecules are taken closer to the surface.

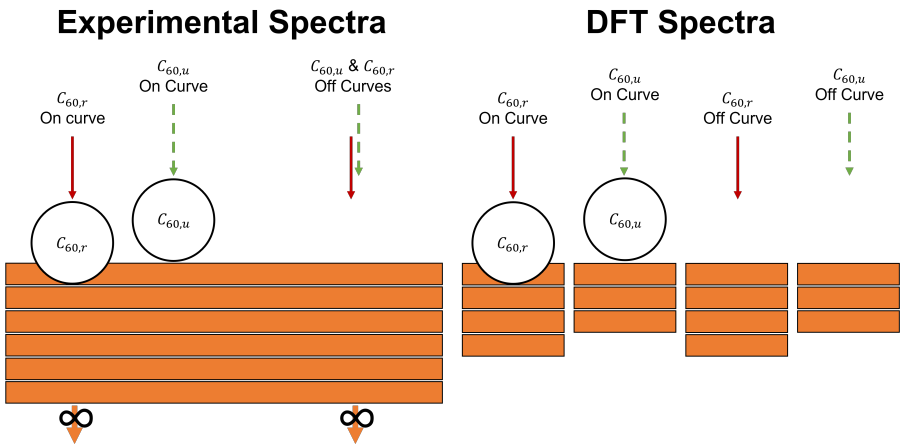

Figure 5.2: Geometries corresponding to $_{e}$NC-AFM and $_{s}$NC-AFM force spectra for an NC-AFM tip approaching the $C_{60,u}$ and $C_{60,r}$ molecules. The orange rectangles represent layers of the Cu(111) surface, the black circles represent adsorbed C_{60} molecules on the Cu(111) surface. The solid red and green dashed lines represent the tip trajectory during spectra, relative to the Cu(111) surface and adsorbed $C_{60,u}$ and $C_{60,r}$ molecules.

6

SIMULATED NC-AFM RESULTS: C_{60} ON CU(111)

6.1 METAL TIP

This section details results of Simulated Non-Contact Atomic Force Microscopy ($_s$NC-AFM) force spectroscopy calculated for a *Cu* Tip approaching C_{60} adsorbed Cu(111)-(4x4) surface. See **Section 4.3** for diagrams of the systems. For a detailed description of the methods used to calculate the $_s$NC-AFM spectrum in DFT, implemented in FHI-aims, see **Chapter 5**.

6.1.1 *Force and Potential Spectra*

Simulated Non-Contact Atomic Force Microscopy ($_s$NC-AFM) force spectroscopy was calculated with a *Cu* Tip over four unique spectrum sites for both the $C_{60,u}$ and $C_{60,r}$ systems (described in **Figure 4.18**). The initial tip position in each spectrum was created by positioning the atomic core of the (single atom) *Cu* Tip apex ~20 Å above one of the following spectrum sites; the centre, a C=C bond, a C-C bond, and a C atom, of the upwards presenting hexagonal face of the adsorbed $C_{60,u}$ or $C_{60,r}$ (see inset for **Figure 6.1 A**).

Looking at **Figure 6.1**, the force minimum values for the C-C bond, C=C bond, and C atom sites all lie within the range $-1.495\,nN$ to $-1.504\,nN$. This $9\,pN$ variation is ~0.5 % of the force minima, and likely not experimentally detectable. During the spectrum simulated over the C=C site, the adsorbed $C_{60,u}$ moves to allow a single C atom to bond with the *Cu* Tip apex atom. In contrast, the *Cu* Tip apex atom remains located over the desired site during the spectra simulated over the C-C bond and C atom sites. This variation in movement by the adsorbed $C_{60,u}$ molecule explains why the shape of the spectra simulated over the C=C bond and C atom sites are similar to each other, but different to the shape of the spectrum simulated over the C-C bond site **(see Figure 6.1 D)**. The inflection visible in the final point of the C=C bond site spectrum is caused by the $C_{60,u}$ molecule moving so the *Cu* Tip apex atom is located over the C=C bond once more. The spectrum simulated over the centre of the $C_{60,u}$ molecule has a force minimum of $-0.737\,nN$, ~$0.76\,nN$ less than the force minima of spectra simulated over the other sites. The inflection which occurs in the spectrum simulated over the centre of the $C_{60,u}$ corresponds to the $C_{60,u}$ moving such that a C=C bond is located directly below the *Cu* Tip apex atom. However, this movement causes the $C_{60,u}$ to move sideways by ~1 Å in the X and Y direction **(see Figure 6.6)**. The periodicity of the simulations means this lateral movement reduces the reliability of the simulation at these points, as the whole mono-layer of $C_{60,u}$ moves in unison. This results in adjacent $C_{60,u}$ molecules (periodic replications) being moved out of the way by the adjacent *Cu* Tips (periodic replications), as the mono-layer of $C_{60,u}$ molecules moves in the same direction. The $_s$NC-AFM spectra simulated with a

Cu Tips were not continued to include the potential minima as this was not possible during the corresponding experiments in **Chapter 2**.

Looking at **Figure 6.2**, there are both similarities and differences between the data presented in **Figure 6.1** for the $C_{60,u}$ system compared to the data presented in **Figure 6.2** for the $C_{60,r}$ system. A clear similarity between the $C_{60,u}$ and $C_{60,r}$ systems is the force spectra taken at the centre site is ~50 % less attractive then the other three sites. In contrast, the force minimum values for the C-C bond, C=C bond, and C atom sites are more spread out for the $C_{60,r}$ system, existing within the range of $-1.475\,nN$ to $-1.594\,nN$. This $119\,nN$ variation is ~7 % of the force value at the minima. Furthermore, there are no inflections in the spectra taken over the $C_{60,r}$ molecule **(see Figure 6.3 A&B)**. Finally, the spectrum taken over the C=C bond site is $90\,pN$ more attractive for the $C_{60,r}$ system **(see Figure 6.3 B)**. This $90\,pN$ variation is likely significant within the DFT simulations, and, could be experimentally detectable as this variation is ~6 % of the force minimum value.

The interaction between a *Cu* Tip and a C_{60}-*h* molecule was measured experimentally by Hauptmann *et al* [35] [1] to lie in the range of $-1.25\,nN$ to $-1.75\,nN$, with the lower bound estimate measured using a predicted off-curve calculated from a long range fit.

Theoretical and experimental work on the forces between metal tips and fullerenes or other similar carbon allotropes has been carried out. DFT simulations carried out by Ondracek *et al* [120] [2] involving Tungsten tips interacting with graphene and carbon nanotubes found the the force minimum between the tip and hollow sites, or atom C atoms, to lie in the range of $-1.25\,nN$ to $-1.8\,nN$.

1 The calculations were performed with the DFT-FIREBALL [128] code using a local density approximation for the exchange and correlation potential. A vdW correction was estimated with a semi-empirical correction based on the London expression [129].

2 The simulations referenced in this work were calculated using the PBE xc functional, along with a vdW correction by Grimme *et al* [130] which was a precursor to the well known D3 vdW correction [83].

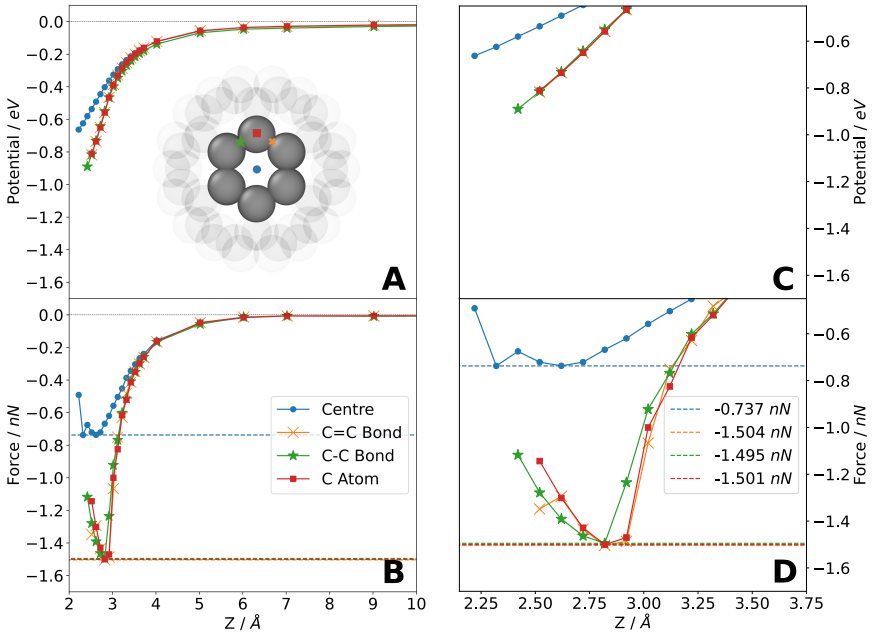

Figure 6.1: $_s$NC-AFM force (and corresponding potential) spectra for a *Cu* Tip approaching the $C_{60,u}$ system which is detailed in **Figure 4.18 B**. Each of the four spectra is simulated over a unique site (see inset diagram in **A**); the centre (blue dots), a C=C bond (orange crosses), a C-C bond (green stars), and a C atom (red squares), of the upwards presenting hexagonal face of the adsorbed $C_{60,u}$. **A&B:** The spectra are displayed on a Z scale ranging from a large tip-sample separation (where the interaction is ~ 0) to a small tip-sample separation (which probes past the force minimum). **C&D:** The data from **A&B** has been cropped about the force minima to highlight the differences between the spectra simulated over the different sites. The blue, orange, green, and red horizontal dashed lines mark the force minimum of the blue dotted, orange crossed, green starred, and red squared lines, respectively. The values of the dashed lines are also given numerically in the legends. The solid lines and markers correspond to DFT data, with each marker representing the converged data from a single DFT simulation. The data in **Figure 6.1** is calculated using the Fritz Haber Institute *ab initio* molecular simulations Tip Forces method (FHI-aims-TF). All 3D atomic geometry visualizations in this work were created using OVITO [97].

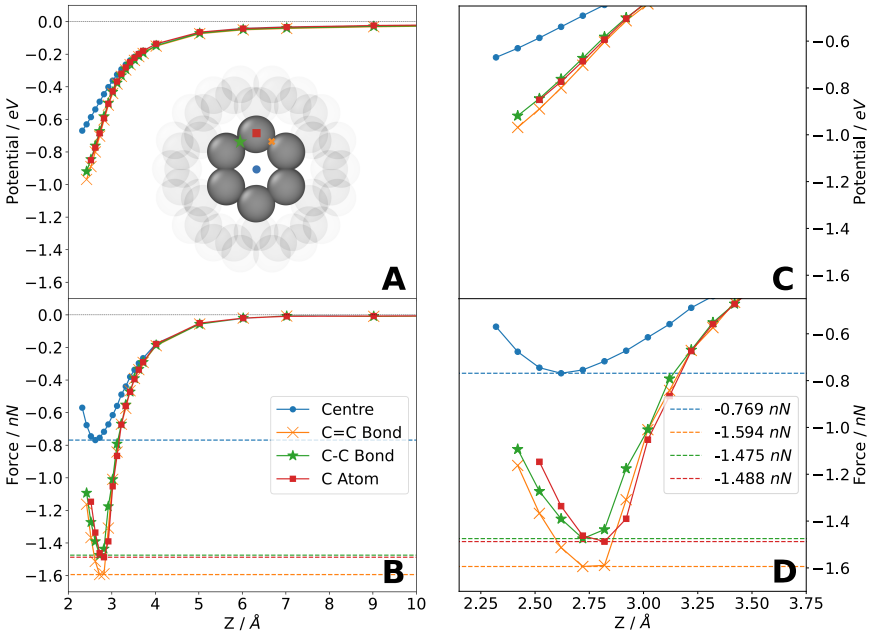

Figure 6.2: $_s$NC-AFM force (and corresponding potential) spectra for a *Cu* Tip approaching the $C_{60,r}$ system which is detailed in **Figure 4.18 B**. Each of the four spectra is simulated over a unique site (see inset diagram in **A**); the centre (blue dots), a C=C bond (orange crosses), a C-C bond (green stars), and a C atom (red squares), of the upwards presenting hexagonal face of the adsorbed $C_{60,r}$. **A&B:** The spectra are displayed on a Z scale ranging from a large tip-sample separation (where the interaction is ~ 0) to a small tip-sample separation (which probes past the force minimum). **C&D:** The data from **A&B** has been cropped about the force minima to highlight the differences between the spectra simulated over the different sites. The blue, orange, green, and red horizontal dashed lines mark the force minimum of the blue dotted, orange crossed, green starred, and red squared lines, respectively. The values of the dashed lines are also given numerically in the legends. The solid lines and markers correspond to DFT data, with each marker representing the converged data from a single DFT simulation. The data in **Figure 6.2** is calculated using the Fritz Haber Institute *ab initio* molecular simulations Tip Forces method (FHI-aims-TF). All 3D atomic geometry visualizations in this work were created using OVITO [97].

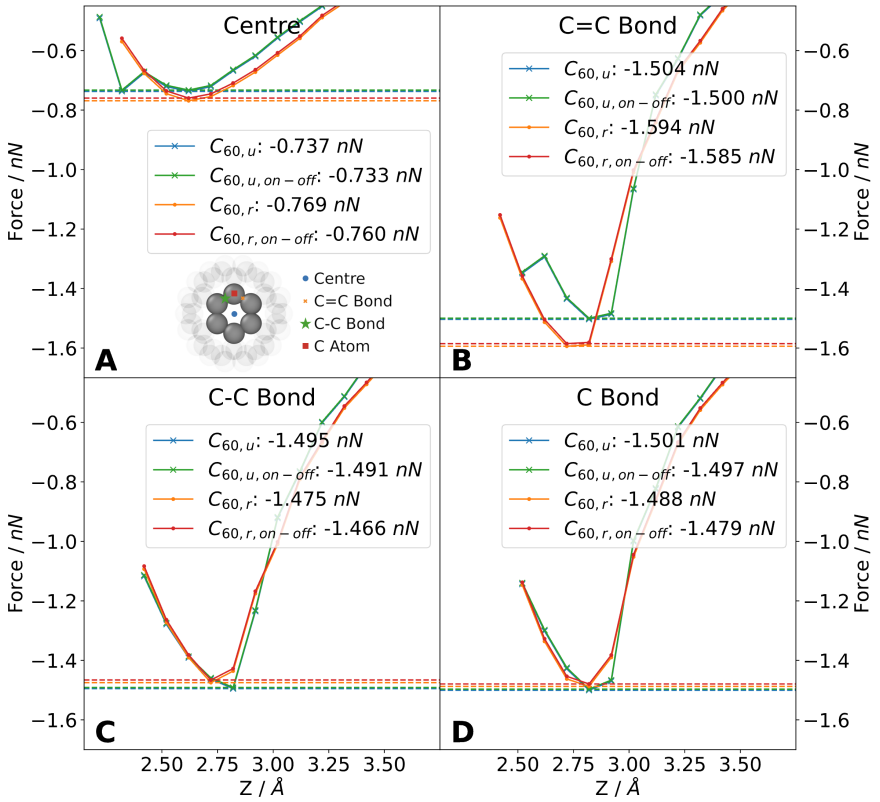

Figure 6.3: $_s$NC-AFM force spectra for a Cu Tip approaching the $C_{60,u}$ (blue crossed) and $C_{60,r}$ (orange dots) systems which are detailed in **Figure 4.18**. Each of the four plots **(ABCD)** contains spectra simulated over a unique site (see inset diagram in **A**); the centre **(A)**, C=C bond **(B)**, C-C bond **(C)**, and C atom **(D)**, of the upwards presenting hexagonal face of the adsorbed C_{60} molecules. The blue and orange horizontal dashed lines mark the force minimum of the $C_{60,u}$ and $C_{60,r}$ systems respectively. The values of the dashed lines are also given numerically in the legends. The solid lines and markers correspond to DFT data, with each marker representing the converged data from a single DFT simulation. The data in **Figure 6.3** is calculated using the Fritz Haber Institute *ab initio* molecular simulations Tip Forces method (FHI-aims-TF). All 3D atomic geometry visualizations in this work were created using OVITO [97].

The differences between spectra taken over the $C_{60,u}$ and $C_{60,r}$ systems can be explained by a greater mobility of the C_{60} molecule when adsorbed on the Cu_u surface compared to the Cu_r surface. Comparing **B** and **C** in **Figure 4.18**, one can see the adsorbed $C_{60,r}$ molecule is embedded 1 atomic layer into the Cu_r surface, whereas the $C_{60,u}$ molecule sits atop the relatively unperturbed Cu_u surface. This increases the contact area between the $C_{60,r}$ molecule and the Cu_r surface, relative to the $C_{60,u}$ system, and thus the interaction strength. This increased interaction strength between the $C_{60,r}$ and Cu_r more strongly confines the $C_{60,r}$ molecule, particularly in the lateral direction, compared to the $C_{60,u}$ molecule. As a result, with the $C_{60,r}$ system, the *Cu* Tip apex remains located over the desired spectrum site during all the simulated spectra. In contrast, for the $C_{60,u}$ system, the adsorbed C_{60} molecule moved so the *Cu* Tip apex was located above a C atom during the spectrum simulated over the C=C site.

6.1.2 C_{60} *Mobility*

The movement of the adsorbed C_{60} molecule, induced by the tip during the $_s$NC-AFM force spectra, is shown in **Figures 6.5** and **6.6**. **Figure 6.5** plots the Δ*Adsorption Height*, defined as the change in the highest atomic coordinate of the adsorbed C_{60} molecule in **Figure 6.4**. **Figure 6.6** plots the Δ*Lateral Adsorption Position*, defined as the average X and Y coordinate of the 6 Carbon atoms forming the hexagonal face of the adsorbed C_{60} molecule, see **Figure 6.4**. Furthermore, the Δ*Lateral Adsorption Position* is calculated separately for the X and Y directions in **Figure 6.6**. Comparing the orange crossed lines to the blue dotted lines in **Figure 6.5**, one can see the $C_{60,r}$ molecule moves upwards approximately 0.1 Å to 0.2 Å less than $C_{60,u}$ molecule during the simulated spectra. Looking at **Figure 6.6**, one can see the $C_{60,u}$ molecule is also more mobile in the X and Y directions than the $C_{60,r}$ molecule.

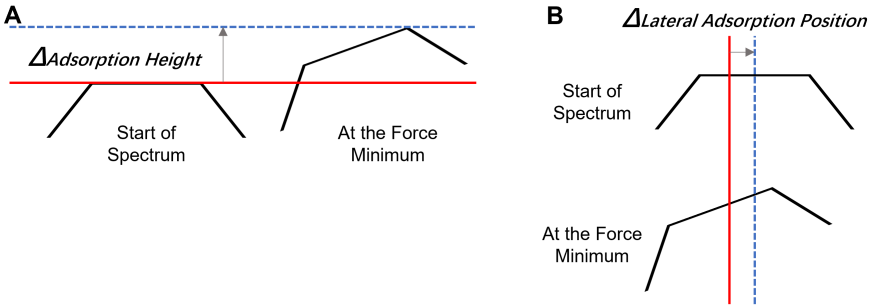

Figure 6.4: Diagrams of how the $\Delta Adsorption\ Height$ **(A)** and $\Delta Adsorption\ Lateral\ Position$ **(B)** are defined. The black half-hexagons represent the top of an adsorbed C_{60} molecule, the red lines show the initial $\Delta Adsorption\ Height$ and $\Delta Adsorption\ Lateral\ Position$ values, and the blue lines show the $\Delta Adsorption\ Height$ and $\Delta Adsorption\ Lateral\ Position$ values at a later point in the spectrum. The C_{60} movement depicted in **Figure 6.4** is an exaggerated example of the mobility of the $C_{60,u}$ molecule.

6.2 C_{60} TIP

This section details results of Simulated Non-Contact Atomic Force Microscopy ($_s$NC-AFM) force spectroscopy calculated for a C_{60} Tip approaching C_{60} adsorbed Cu(111)-(4x4) surface. See **Section 4.3** for diagrams of the systems. For a detailed description of the methods used to calculate the $_s$NC-AFM spectrum in DFT, implemented in FHI-aims, see **Chapter 5**.

6.2.1 *Force and Potential Spectra*

Simulated Non-Contact Atomic Force Microscopy ($_s$NC-AFM) force spectra involving Cu slabs and adsorbed C_{60} molecules, in the C_{60} Tip and the surface, were calculated for a single spectrum site at the centre of the adsorbed C_{60} molecule. The system was simulated with a relative azimuthal angle of $\sim 30°$ between the tip and sample C_{60}-*h* oriented molecules. See **Figure 4.17** for a pictorial description of the system. The effect of the relative orientation between the tip and adsorbed C_{60} molecules was investigated in **Section 4.3.4.1** using less computationally expensive cluster calculations, without the presence of Cu. The initial $_s$Tip position in each spectrum was created by positioning the $_s$Tip Apex ~15 Å above the top of the $_s$Surface Apex. Where the $_s$Tip Apex is defined as the average atomic core coordinate of the six C atoms forming the downwards facing hexagon in the $_s$Tip Molecule, and the $_s$Surface Apex is defined as the average atomic core position of the six C atoms forming the upwards facing hexagon of the $_s$Surface Molecule.

Looking at **Figures 6.7 A, B, C, & D** one can see the spectra taken over the $C_{60,u}$ and $C_{60,r}$ molecules are similar both quantitatively

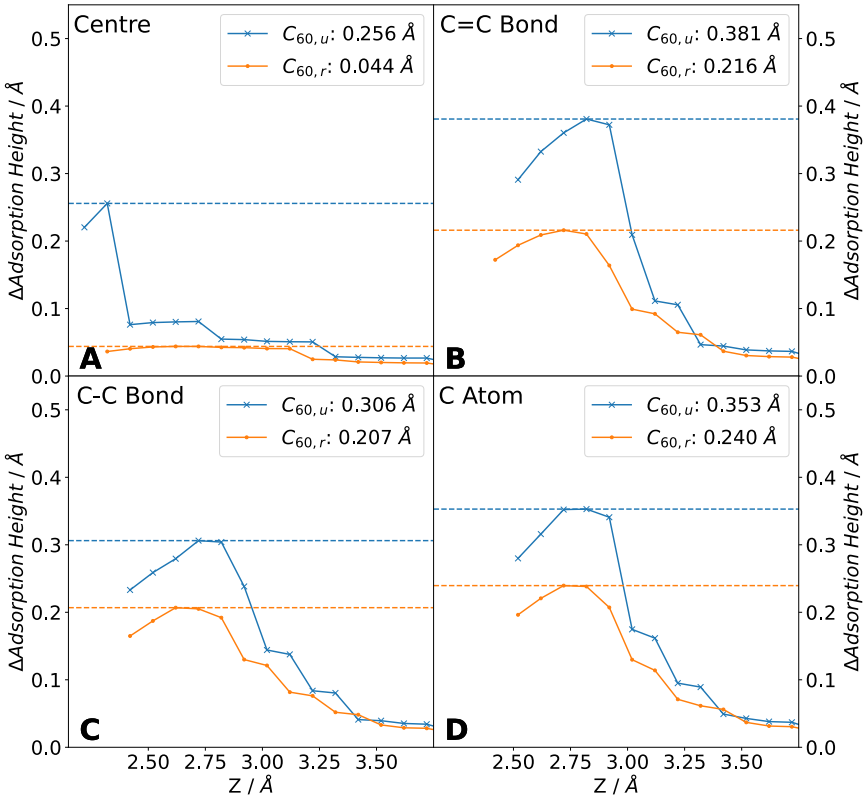

Figure 6.5: Relative surface height data for the $_s$NC-AFM force spectra presented in **Figure 6.3**. The blue crossed and orange dotted lines represent the $C_{60,u}$ and $C_{60,r}$ systems detailed in **Figure 4.18**. Each of the four plots **(ABCD)** contains spectra simulated over a unique site; the centre **(A)**, C=C bond **(B)**, C-C bond **(C)**, and C atom **(D)**, of the upwards presenting hexagonal face of the adsorbed C_{60} molecules. The blue and orange horizontal dashed lines mark the relative maximum surface height of the $C_{60,u}$ and $C_{60,r}$ systems respectively. The values of the dashed lines are also given numerically in the legends. The solid lines and markers correspond to DFT data, with each marker representing the converged data from a single DFT simulation.

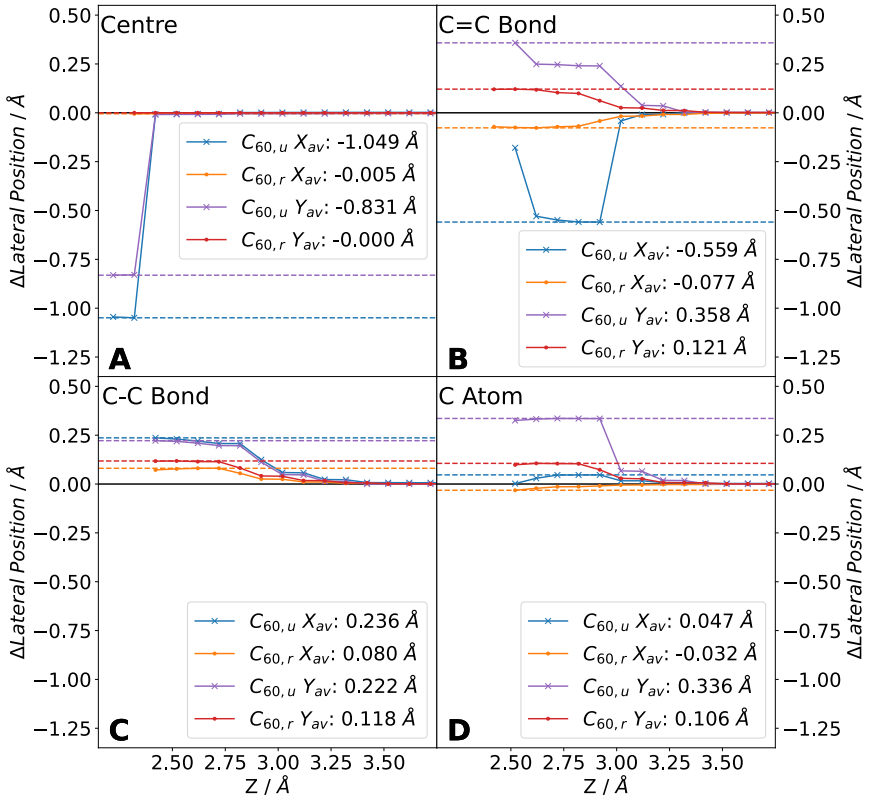

Figure 6.6: Relative X and Y coordinate data for the $_s$NC-AFM force spectra presented in **Figure 6.3**. Each of the four plots **(ABCD)** contains spectra simulated over a unique site; the centre **(A)**, C=C bond **(B)**, C-C bond **(C)**, and C atom **(D)**, of the upwards presenting hexagonal face of the adsorbed C_{60} molecules. Blue and purple crossed lines correspond to movement of the $C_{60,u}$ molecule in the X and Y directions. Orange and red dotted lines correspond to movement of the $C_{60,r}$ molecule in the X and Y directions. The horizontal dashed lines mark the point of maximum movement along the X and Y directions for each system, 0 Å is the initial movement the X and Y directions. The values of the dashed lines are also given numerically in the legends. The solid lines and markers correspond to DFT data, with each marker representing the converged data from a single DFT simulation.

and qualitatively, with force and potential minima of approximately $F_{z,min} \simeq -0.33\,nN$ and $U_{z,min} \simeq -0.44\,eV$. It was found the spectrum taken over the $C_{60,r}$ molecule is more attractive, by $7\,pN$ and $6\,meV$ at the force and potential minima respectively. However, if an experimentally analogous Off-Curve subtraction for both the $C_{60,u}$ and $C_{60,r}$ systems is simulated and performed, the difference in the force minima is removed and both systems return a force minimum of $F_{z,min} = -0.323\,nN$ for the off-curve subtracted spectra (**Figures 6.7 C&D)**. There is still a small difference at the potential minimum, with the $C_{60,u}$ system being $4\,meV$ more attractive. **Figure 6.8** displays the partial charge assigned to each atom as calculated by the HPA scheme [79]. Looking at **Figure 6.8**, one can see the adsorbed C_{60} as a whole accumulates a negative charge, however this charge is located in the bottom half of the molecule for both surface reconstructions. As $_s$NC-AFM and $_e$NC-AFM can only probe the reactivity of the top half of the C_{60} cage, the techniques are unable to detect the effects of the underlying surface on the lower half of the adsorbed C_{60} molecule.

In **Sections 6.2.4 & 6.2.5** a further correction was made to the spectra in **Figure 6.7** to correct for the periodicity of the $_s$Tip. This correction came to approximately $-16\,pN$ at the force minimum. The same value is used for both the $C_{60,u}$ and the $C_{60,r}$ systems, therefore it does not change the relative force difference.

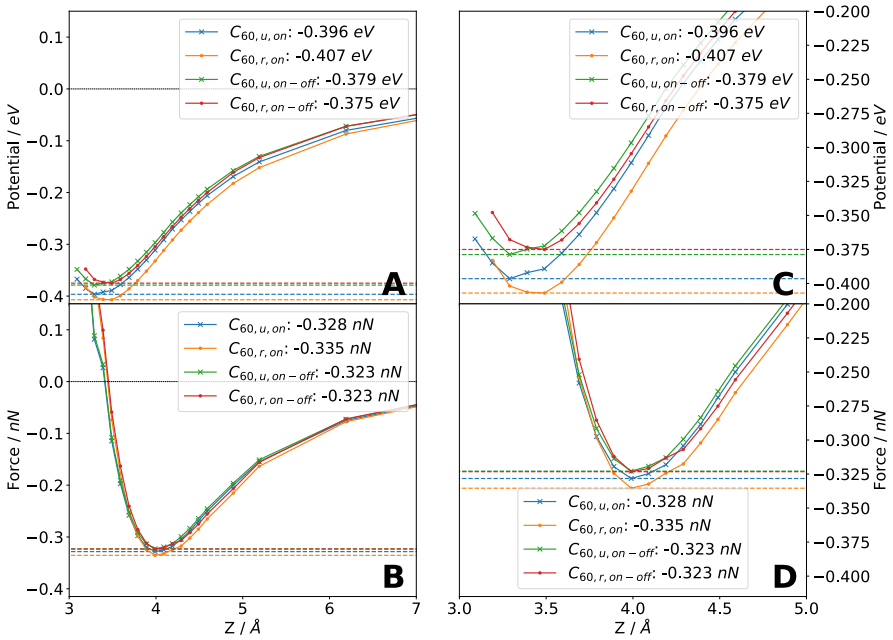

Figure 6.7: sNC-AFM force spectra for a C_{60} Tip approaching the $C_{60,u}$ and $C_{60,r}$ systems. Blue crosses and orange dots correspond to On-Curve spectra for the $C_{60,u}$ and $C_{60,r}$ systems. Green crosses and red dots correspond to off-curve subtracted spectra for the $C_{60,u}$ and $C_{60,r}$ systems. For information on the systems see **Figure 4.17**. **Figure 6.7** contains data from spectra simulated with the downwards presenting hexagonal face of the tip C_{60} molecule approaching the centre of the upwards presenting hexagonal face of the surface C_{60} molecule. The relative rotation of the two C_{60} molecules is $\sim 30°$ as defined in **Figure 4.22**. **A&C:** Potential spectra, **B&D:** Force spectra. **C&D:** The data in **A&B** has been cropped about the force and potential minima to highlight the similarities and differences between the spectra. In **A, B, C, & D** the blue and orange horizontal dashed lines mark the force and potential minima of the $C_{60,u}$ and $C_{60,r}$ system On-Curves. The green and red horizontal dashed lines mark the force and potential minima of the $C_{60,u}$ and $C_{60,r}$ system off-curve subtracted On-Curves. The values of the dashed lines are also given numerically in the legends. The solid lines and markers correspond to DFT data, with each marker representing the converged data from a single DFT simulation. The force data in **Figure 6.7** is calculated using the FHI-aims-TF, the potential data using the FHI-aims-SE.

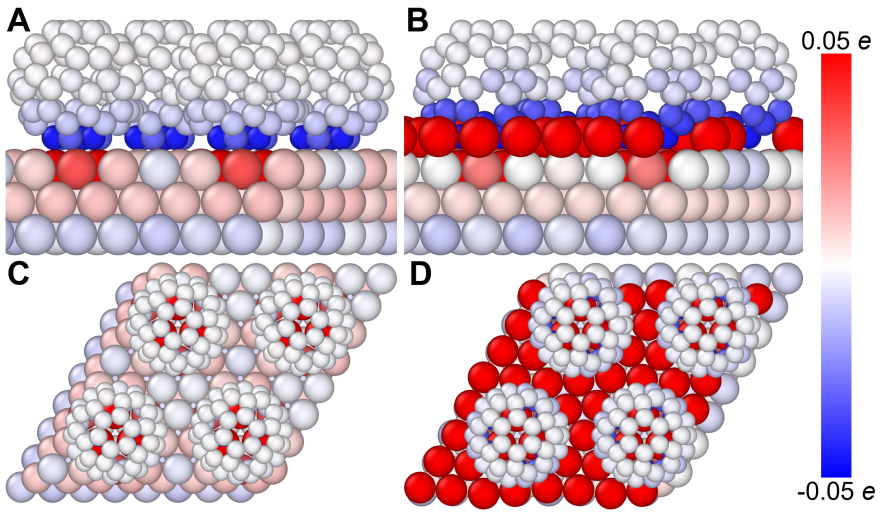

Figure 6.8: Heat maps of the partial charge on each atom after C_{60} is adsorbed on the Cu_u **(A&C)** and Cu_r **(B&D)** surfaces. The partial charge values were calculated with the Hirshfeld Population Analysis (HPA) scheme [79]. Blue indicates an electron transfer onto the atom (net negative charge), and red indicates an electron transfer out of the atom (net positive charge). White indicates a neutral charge. All 3D atomic geometry visualizations in this work were created using OVITO [97].

6.2.2 C_{60} *Mobility*

Figure 6.9 plots the relative surface height of the adsorbed $C_{60,u}$ and $C_{60,r}$ molecules during the $_s$NC-AFM spectra. The relative surface height is defined as the highest atomic coordinate in the $_s$Surface atoms. The value at the largest tip-sample separation is set to zero, and all other points are given relative to this value. Looking at the blue crossed line one can see a relatively large geometrical relaxation [3] occurs at both the force minimum and the potential minimum of the $C_{60,u}$ spectrum. Comparing **Figure 6.9** to **Figure 6.5**, one can see the vertical displacement of the adsorbed C_{60} molecules interacting with a C_{60} Tip is smaller than the vertical displacement calculated for the adsorbed molecules interacting with a Cu Tip. The maximum perturbation to the adsorption height of the adsorbed $C_{60,u}$ and $C_{60,r}$ molecules, caused by the C_{60} Tip, is approximately 3 pm and 1 pm **(Figure 6.9)**. Whereas, for the Cu Tip, the maximum perturbation to the adsorption height is approximately 35 pm and 22 pm. This is a difference of an order of magnitude, which is consistent with the order of magnitude difference in the calculated force minimum for the adsorbed C_{60} molecules interacting with a C_{60} Tip compared to a Cu Tip. When making this comparison, the C=C

3 in this context define a relatively small geometrical relaxation as a couple of atoms in the system moving a couple of pm, and a relatively large geometrical relaxation as the whole C_{60} molecule moving a couple of pm.

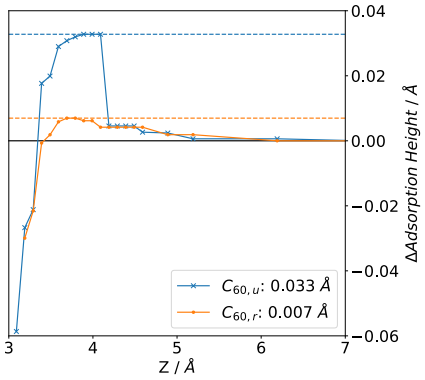

Figure 6.9: Relative surface height data corresponding to the $_s$NC-AFM force spectra for a C_{60} Tip approaching the $C_{60,u}$ (blue crosses) and $C_{60,r}$ (orange dots) systems displayed in **Figure 6.7**, detailed in **Figure 4.17**. The blue and orange horizontal dashed lines mark the highest atomic core coordinate of the $_s$Surface atoms during the $_s$NC-AFM spectra, for the $C_{60,u}$ and $C_{60,r}$ systems, respectively. The values of the dashed lines are also given numerically in the legends. The solid lines and markers correspond to DFT data, with each marker representing the converged data from a single DFT simulation.

bond, C-C bond, and C atom sites in **Figure 6.5**, were considered as those sites replicate the experimental data most accurately.

6.2.3 $_s$*NC-AFM Methods*

The force spectra shown in **Figure 6.7** were calculated using the FHI-aims-TF method described in **Section 5.5**. An offset of ~30pN was applied to the FHI-aims-TF force spectra to compensate for strain in the system. The offset changes the absolute values of the force minima by ~30 pN but does not significantly change the difference in the force minima between the $C_{60,u}$ and $C_{60,r}$ systems. A similar force difference of 11 pN was calculated using the FHI-aims-SF method.

The potential spectra were calculated using the FHI-aims-SE method. However, the accuracy of the FHI-aims-SE method is reduced for the $C_{60,u}$ spectrum due to a relatively large geometrical relaxation occurring at the potential minimum **(see Figure 6.9).** Despite this, it was decided the uncertainties caused by the geometrical relaxation were smaller than those introduced by integrating the FHI-aims-TF over a low resolution. It is theorized the FHI-aims-SE data is more greatly effected by the relaxation than the FHI-aims-TF data because the data obtained by the FHI-aims-SE method is equally effected by small changes in the molecule-surface interaction than by small changes in the tip-sample interaction.

6.2.4 *Periodicity Correction: Theory*

"The universe required correction"

— Thanos, Endgame (2018). Defending the principle of The Snap, moments before his passing on Planet 0259-S.

Due to the limited resources available when calculating the $_s$NC-AFM spectra in this work, compromises between experimental comparability and computational cost were made. The $_s$NC-AFM system discussed in this work should be thought of as a mono-layer of adsorbed C_{60} approaching another mono-layer of adsorbed C_{60}. This is not strictly analogous to the experimental situation. In the experiment, the tip is comprised of a single C_{60} molecule forming the NC-AFM tip apex, and this tip can approach anything from an isolated adsorbed C_{60}, to an island of adsorbed C_{60}, to a mono-layer, or n-layer thick coverings of adsorbed C_{60}. From this simple description alone, one can see the simulated C_{60} Tip in a periodic system is larger (infinite) compared to the experimental C_{60} Tip. This unwanted periodicity of the simulated C_{60} Tip arises from the requirement for the tip to have the same periodicity as the surface.

In this section, I investigate the extent to which the periodicity of periodic systems can cause an overestimate of the attractiveness of experimental $_e$NC-AFM spectra. In this work, the mathematics and assumptions being implemented are tailored to systems involving C_{60} adsorbed on a surface, interacting with a C_{60} Tip. The analytical equations are written in full, along with the logic behind them. Furthermore, the approximations made, along with any numerical reasoning for the validity of said approximations, are clearly stated and described. In **Section 6.2.6** the validity of some of the applied approximations are tested.

6.2.4.1 *Theory*

"You simply lack the strength to wield it: your bodies would crumple as your minds collapsed into madness."

— Thor, Infinity War (2018). Acquisition of Stormbreaker.

Figure 6.10 A, pictorially describes how a $_s$NC-AFM system can be broken down into groups of atoms. The system has been broken down into the $_s$Tip and $_s$Surface, and then further split into the constituent parts of the $_s$Tip and $_s$Surface. In this work, we define the $_s$Tip Base as the metal section of the $_s$NC-AFM tip, which can be further functionalized with additonal molecules (such as C_{60}, CO, or Cu tip apex) ($_s$Tip Base), and the $_s$Tip Molecule as the molecule adsorbed on the functionalized $_s$Tip Base ($_s$Tip Molecule). We also define the $_s$Surface Base as the underlying surface, analogous to the experimental surface ($_s$Surface Base), and the $_s$Surface Molecule as the molecule adsorbed

on the underlying surface, analogous to the deposited molecule in an experiment ($_s$Surface Molecule).

The interactions occurring between these groups of atoms can be partitioned into two categories: Intra-Cellular **(B)**, or Inter-Cellular **(C)**. Where we define Intra-Cellular as the interactions between groups of atoms occurring within a Cluster Calculation, or the original unit cell of a Periodic System (Intra-Cellular), and Inter-Cellular as the interactions between groups of atoms in a Periodic System, where one of the interacting groups exists in the original unit cell, and the other group of atoms exists in the periodic replications of the unit cell (Inter-Cellular). Given the complexity and number of Inter-Cellular interactions, we choose to further categorize them as periodic replications of the $_s$Tip interacting with the original $_s$Surface (PT-OS), or periodic replications of the $_s$Surface interacting with the original $_s$Tip (PS-OT) **(C)**. In **(C)**, the Inter-Cellular interactions have been pictorially drawn, with separate diagrams for the PT-OS and PS-OT interactions. The Inter-Cellular interactions have been drawn out and labeled for a single repetition of the infinitely repeating unit cell.

Looking at **Figure 6.10 B**, one can deduce that performing the off-curve subtraction in **Figure 6.7** removes the interactions between the $_s$Tip and the $_s$Surface Base. Therefore this leaving only interactions between the $_s$Tip and the $_s$Surface Molecule. However, the off-curve subtracted spectrum is not equivalent to a gaseous C_{60} approaching a gaseous C_{60}. For a cluster calculation (non periodic), the interactions occurring in the system, and the interactions removed by the off-curve subtraction, are straight forward **(Figure 6.10 B, Equations 6.1 & 6.2 below)**. However, when dealing with periodic systems with small unit cells, the situation becomes complex **(Figure 6.10 C, Equations 6.4 & 6.5 below)**.

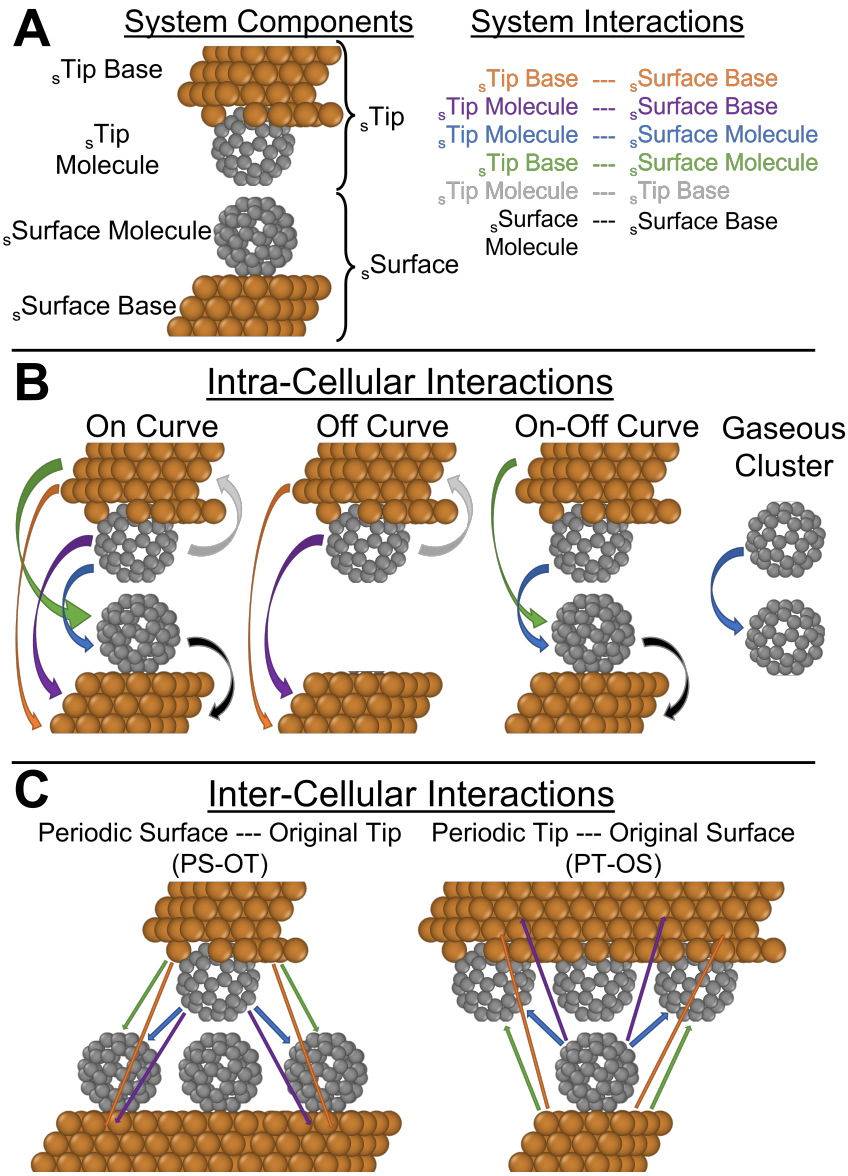

Figure 6.10: Definitions of the components and interactions between the tip and sample in $_s$NC-AFM systems, specifically a C_{60} tip probing a C_{60} surface. **(A) System Components:** Pictorial definitions of the $_s$Tip, $_s$Surface, and the components that make them. **(A) System Interactions:** A color coded key defining the tip-surface interactions the coloured lines correspond to. **(B) Intra-Cellular Interactions:** Pictorial definitions of the components forming tip-surface interactions in the original unit cell of $_s$NC-AFM systems. **(C) Inter-Cellular Interactions:** Pictorial definitions of the components forming the PS-OT and PT-OS interactions in $_s$NC-AFM systems. All 3D atomic geometry visualizations in this work were created using OVITO [97].

This work aims to produce experimentally analogous $_s$NC-AFM spectra using the FHI-aims DFT package. Within FHI-aims, one can simulate systems in two distinct ways; as a cluster calculation, or a periodic system. For a cluster calculation, the interactions occurring between the $_s$Tip and $_s$Surface are all Intra-Cellular, and thus relatively simple to describe. **Equation 6.1** describes how an Off-Curve subtraction is performed to produce the off-curve subtracted $_s$NC-AFM force spectrum calculated with a cluster calculation ($F_{OCS,CL}$),

$$F_{OCS,CL} = F_{on,CL} - F_{off,CL}, \tag{6.1}$$

where F_{on} and F_{off} are the corresponding On-Curve and Off-Curves. Using **Figure 6.10**, we can expand F_{on} and F_{off} in terms of their component interactions;

$$\begin{aligned} F_{on,CL} &= F_{TB-SB} + F_{TB-SM} + F_{TM-SB} + F_{TM-SM} \\ F_{off,CL} &= F_{TB-SB} + F_{TM-SB}, \end{aligned} \tag{6.2}$$

where we define F_{TB-SB} as the Intra-Cellular interaction between the original $_s$Tip Base and the original $_s$Surface Base (TB-SB), F_{TB-SM} as the Intra-Cellular interaction between the original $_s$Tip Base and the original $_s$Surface Molecule (TB-SM), F_{TM-SB} as the Intra-Cellular interaction between the original $_s$Tip Molecule and the original $_s$Surface Base (TM-SB), and F_{TM-SM} as the Intra-Cellular interaction between the original $_s$Tip Molecule and the original $_s$Surface Molecule (TM-SM) **(see Figure 6.10 B)**. By substituting **Equations 6.2** into **Equation 6.3,** and canceling like terms, we can express $F_{OCS,CL}$ as a summation of it's constituent interactions;

$$\begin{aligned} F_{OCS,CL} &= \underbrace{F_{TB-SB} + F_{TB-SM} + F_{TM-SB} + F_{TM-SM}}_{F_{on}} - \left(\underbrace{F_{TB-SB} + F_{TM-SB}}_{F_{off}} \right) \\ &= \cancel{F_{TB-SB}} + F_{TB-SM} + \cancel{F_{TM-SB}} + F_{TM-SM} - (\cancel{F_{TB-SB}} + \cancel{F_{TM-SB}}) \\ F_{OCS,CL} &= F_{TB-SM} + F_{TM-SM}. \end{aligned} \tag{6.3}$$

From **Equation 6.3** we learn that the off-curve subtracted interaction between the $_s$Tip and the $_s$Surface, for a cluster calculation, can be expressed as just two Intra-Cellular interactions; the TB-SM and TM-SM interactions. However, the systems in this work are periodic. Therefore, we need to consider the additional Inter-Cellular components which arise from the periodicity of the system. Moving forward in this work, we make the assumption *the intra-cellular interactions for a periodic system are the same as the iterations within a cluster calculation of the same unit cell*. This is not strictly true as the local bonding environment of an atom has the potential to affect the interactions involving the atom, when the interactions are calculated by DFT or a vdW correction scheme.

Thus, the atoms at the edge of the cluster are not exactly equivalent to those at the edge of the periodic unit cell. **Equation 6.4** describes the Off-Curve subtraction for a periodic system

$$F_{OCS,PBC} = F_{on,PBC} - F_{off,PBC}. \tag{6.4}$$

As with the cluster calculation, we can express $F_{on,PBC}$ and $F_{off,PBC}$ as summations of their constituent interactions;

$$\begin{aligned} F_{on,PBC} = & \underbrace{F_{TB-SB} + F_{TB-SM} + F_{TM-SB} + F_{TM-SM}}_{F_{on,CL}} + \\ & \underbrace{F_{TB_{PBC}-SB} + F_{TB_{PBC}-SM} + F_{TM_{PBC}-SB} + F_{TM_{PBC}-SM}}_{\text{PT-OS terms}} + \\ & \underbrace{F_{TB-SB_{PBC}} + F_{TB-SM_{PBC}} + F_{TM-SB_{PBC}} + F_{TM-SM_{PBC}}}_{\text{PS-OT terms}} \\ F_{off,PBC} = & \underbrace{F_{TB-SB} + F_{TM-SB}}_{F_{off,CL}} + \\ & \underbrace{F_{TB_{PBC}-SB} + F_{TM_{PBC}-SB}}_{\text{PT-OS terms}} + \\ & \underbrace{F_{TB-SB_{PBC}} + F_{TM-SB_{PBC}}}_{\text{PS-OT terms}}. \end{aligned} \tag{6.5}$$

Where we define the Inter-Cellular PT-OS terms; $F_{TB_{PBC}-SB}$ as the the interaction between the periodic replications of the $_s$Tip Base and the original $_s$Surface Base (TB$_{PBC}$-SB), $F_{TB_{PBC}-SM}$ as the the interaction between the periodic replications of the $_s$Tip Base and the original $_s$Surface Molecule (TB$_{PBC}$-SM), $F_{TM_{PBC}-SB}$ as the the interaction between the periodic replications of the $_s$Tip Molecule and the original $_s$Surface Base (TM$_{PBC}$-SB), and $F_{TM_{PBC}-SM}$ as the the interaction between the periodic replications of the $_s$Tip Molecule and the original $_s$Surface Molecule (TM$_{PBC}$-SM). We also define the Inter-Cellular PS-OT terms; $F_{TB-SB_{PBC}}$ as the the interaction between the original $_s$Tip Base and the periodic replications of the $_s$Surface Base (TB-SB$_{PBC}$), $F_{TB-SM_{PBC}}$ as the the interaction between the original $_s$Tip Base and the periodic replications of the $_s$Surface Molecule (TB-SM$_{PBC}$), $F_{TM-SB_{PBC}}$ as the the interaction between the original $_s$Tip Molecule and the periodic replications of the $_s$Surface Base (TM-SB$_{PBC}$), and $F_{TM-SM_{PBC}}$ as the the interaction between the original $_s$Tip Molecule and the periodic replications of the $_s$Surface Molecule (TM-SM$_{PBC}$). Compared to **Equations 6.2**, **Equations 6.5** are comprised of significantly more terms, where the extra terms arise from the periodic replications of the system interacting with the original unit cell. Furthermore, in keeping with **Figure 6.10**, we have described these Inter-Cellular interactions as PT-OS or PS-OT interactions.

Like with the cluster calculation, we can express $F_{OCS,PBC}$ as a sum of its constituent interactions by substituting **Equations 6.5** into **Equation 6.4**, and canceling like terms;

$$
\begin{aligned}
F_{OCS,PBC} &= F_{on,PBC} - F_{off,PBC} \\
&= \underbrace{F_{TB-SB} + F_{TB-SM} + F_{TM-SB} + F_{TM-SM}}_{F_{on,CL}} + \\
&\quad \underbrace{F_{TB_{PBC}-SB} + F_{TB_{PBC}-SM} + F_{TM_{PBC}-SB} + F_{TM_{PBC}-SM}}_{\text{PT-OS terms}} + \\
&\quad \underbrace{F_{TB-SB_{PBC}} + F_{TB-SM_{PBC}} + F_{TM-SB_{PBC}} + F_{TM-SM_{PBC}}}_{\text{PS-OT terms}} - \\
&\quad \left(\underbrace{F_{TB-SB} + F_{TM-SB}}_{F_{off},CL} + \underbrace{F_{TB_{PBC}-SB} + F_{TM_{PBC}-SB}}_{\text{PT-OS terms}} + \underbrace{F_{TB-SB_{PBC}} + F_{TM-SB_{PBC}}}_{\text{PS-OT term}} \right) \\
&= \underbrace{\cancel{F_{TB-SB}} + F_{TB-SM} + \cancel{F_{TM-SB}} + F_{TM-SM}}_{F_{on,CL}} + \\
&\quad \underbrace{\cancel{F_{TB_{PBC}-SB}} + F_{TB_{PBC}-SM} + \cancel{F_{TM_{PBC}-SB}} + F_{TM_{PBC}-SM}}_{\text{PT-OS terms}} + \\
&\quad \underbrace{\cancel{F_{TB-SB_{PBC}}} + F_{TB-SM_{PBC}} + \cancel{F_{TM-SB_{PBC}}} + F_{TM-SM_{PBC}}}_{\text{PS-OT terms}} - \\
&\quad \left(\underbrace{\cancel{F_{TB-SB} + F_{TM-SB}}}_{F_{off},CL} + \underbrace{\cancel{F_{TB_{PBC}-SB} + F_{TM_{PBC}-SB}}}_{\text{PT-OS terms}} + \underbrace{\cancel{F_{TB-SB_{PBC}} + F_{TM-SB_{PBC}}}}_{\text{PS-OT terms}} \right) \\
F_{OCS,PBC} &= \underbrace{F_{TB-SM} + F_{TM-SM}}_{F_{on,CL}} + \underbrace{F_{TB_{PBC}-SM} + F_{TM_{PBC}-SM}}_{\text{PT-OS terms}} + \underbrace{F_{TB-SM_{PBC}} + F_{TM-SM_{PBC}}}_{\text{PS-OT terms}}
\end{aligned}
\tag{6.6}
$$

Thus we see that $F_{OCS,PBC}$ contains all the interactions from $F_{on,CL}$, plus some PT-OS and PS-OT interactions. This work aims to produce experimentally analogous $_s$NC-AFM spectra, which further complicates the situation, as some of the PT-OS and PS-OT interactions are experimentally analogous, whereas others are not.

In the remainder of this section, we will show the mathematics needed to produce a correction term for the components of the PT-OS and PS-OT interactions which have no experimental counterpart. In doing so, we also set the practical limitation that the correction term should be calculable from computationally affordable DFT simulations.

Above we have described two methods for calculating off-curve subtracted $_s$NC-AFM spectra. One method using periodic boundary conditions, another method using cluster calculations. In the ideal world, where the systems can be infinitely large, the two methods should produce the same result. However, in reality, the size of our systems is limited by computational feasibility. Each method has it's

own advantages and disadvantages, however neither method is an exact analogy to experimental $_e$NC-AFM spectra at an affordable computational cost. $F_{OCS,CL}$ from **Equation 6.3** is more suited to modeling an idealized $_e$NC-AFM tip [4], however, this approach is less suited to modeling an infinite experimental surface. This leads to the conclusion; $F_{OCS,CL}$ is either an underestimate of the experimental spectrum, but adequate if the certain interactions involving the $_s$Surface can be considered insignificant. $F_{OCS,PBC}$ from **Equation 6.6** is more suited to modeling the surface of an $_e$NC-AFM experiment as the periodic boundary conditions allow for the computationally efficient treatment of mono-layers, and an experimentally analogous infinite $_s$Surface Base. However, the entire system needs to be periodic. Therefore the $_s$Tip is also replicated and one is actually simulating a mono-layer of $_s$Tip approaching an infinitely repeating $_s$Surface (the approach taken in this work). This leads to to the conclusion F_{PBC} is likely an overestimate of the true experimental spectrum. As the size of the system increases, both F_{CL} and F_{PBC} will approach the true value of the $_s$NC-AFM spectrum, which in turn should agree with the experimental NC-AFM spectrum. We can express the logic above as **Equations 6.7 & 6.8** below;

$$F_{OCS,FHI}(z) = F_{OCS,CL}(z) + C_{CL}(z) \tag{6.7}$$

and

$$F_{OCS,FHI}(z) = F_{OCS,PBC}(z) - C_{PBC}(z). \tag{6.8}$$

where $F_{OCS,FHI}$ represents the *true value* of the off-curve subtracted $_s$NC-AFM one would obtain with FHI-aims if computational resources do not limit the size of the system. $C_{OCS,CL}(z)$ is the z dependent correction term for the cluster calculation approach, and $C_{OCS,PBC}(z)$ is the z dependent correction term for the periodic calculation approach. **Equations 6.7 & 6.8** have been given with respect to z to emphasize how the correction term will be a function of z, rather than a constant.

In this work, $_s$NC-AFM spectra involving the metallic $_s$Tip Base and $_s$Surface Base were calculated using periodic boundary conditions. Therefore, only the $C_{PBC}(z)$ correction term is going to be determined. Furthermore, we are going to apply a Large Separation Approximation (LSA) moving forwards. C_{60} is a relatively large molecule, approximately $1\,nm$ in diameter. Therefore, the groups of atoms defined in **Figure 6.10** are often separated by large distances, allowing for some of the interactions to be classified as insignificant (the LSA). Using the LSA, we can hypothesize the following interactions can be ignored: the interaction between the original $_s$Tip Base and the original $_s$Surface Base (TB-SB), the interaction between the original $_s$Tip Base and the

4 a long, narrow, metal Tip Base, which reduces the long range interaction between the tip and the surface

periodic replications of the $_s$Surface Molecule (TB-SM$_{PBC}$), the interaction between the original $_s$Tip Base and the periodic replications of the $_s$Surface Base (TB-SB$_{PBC}$), the interaction between the original $_s$Tip Molecule and the periodic replications of the $_s$Surface Base (TM-SB$_{PBC}$), the interaction between the periodic replications of the $_s$Tip Base and the original $_s$Surface Molecule (TB$_{PBC}$-SM), the interaction between the periodic replications of the $_s$Tip Base and the original $_s$Surface Base (TB$_{PBC}$-SB), and the interaction between the periodic replications of the $_s$Tip Molecule and the original $_s$Surface Base (TM$_{PBC}$-SB). Essentially, all the periodic interactions involving the $_s$Tip Base, the $_s$Surface Base, and the TB-SB interaction in the original unit cell, have been approximated as insignificant. Applying these approximations to **Equation 6.6** allows us to simplify it down to an equation one can calculate a numerical solution for, using relatively inexpensive additional $_s$NC-AFM spectra;

$$\begin{aligned} F_{OCS,PBC,LSA} &= \underbrace{F_{TB-SM} + F_{TM-SM}}_{F_{on,CL}} + \underbrace{F_{TB_{PBC}-SM} + F_{TM_{PBC}-SM}}_{\text{PT-OS terms}} + \\ &\quad \underbrace{F_{TB-SM_{PBC}} + F_{TM-SM_{PBC}}}_{\text{PS-OT terms}} \\ &\simeq \underbrace{F_{TB-SM} + F_{TM-SM}}_{F_{on,CL}} + \underbrace{\cancel{F_{TB_{PBC}-SM}} + F_{TM_{PBC}-SM}}_{\text{PT-OS terms}} + \\ &\quad \underbrace{\cancel{F_{TB-SM_{PBC}}} + F_{TM-SM_{PBC}}}_{\text{PS-OT terms}} \\ F_{OCS,PBC,LSA} &\simeq \underbrace{F_{TB-SM} + F_{TM-SM}}_{F_{on,CL}} + \underbrace{F_{TM_{PBC}-SM}}_{\text{PT-OS terms}} + \underbrace{F_{TM-SM_{PBC}}}_{\text{PS-OT terms}} \end{aligned} \tag{6.9}$$

Upon inspection of $F_{OCS,PBC,LSA}$, we can see two periodic terms, and two cluster terms, have remained. From the logic described earlier, we know the $F_{TM_{PBC}-SM}$ term has no experimental counterpart as it is classified as a PT-OS interaction, thus we desire to remove it from the $_s$NC-AFM spectra. Therefore, we know part of C_{PBC} in **Equation 6.8** must be $F_{TM_{PBC}-SM}$. In contrast, the implications of the $F_{TM-SM_{PBC}}$ term in **Equation 6.9** are more complex as it is a PS-OT interaction. If one is simulating an experimental NC-AFM Tip approaching a mono-layer (or large island) of adsorbed molecules, then the $F_{TM-SM_{PBC}}$ term becomes experimentally analogous. However, if one is simulating an experimental NC-AFM tip approaching an isolated adsorbed molecule, the $F_{TM-SM_{PBC}}$ term should be removed. To account for this, we also include the $F_{TM-SM_{PBC}}$ in C_{PBC}, however with the additional prefactor A. Where A is a constant which ranges from $A = 0$ (molecule adsorbed in a mono-layer) to $A = 1$ (isolated molecule adsorbed on a surface). In **Equation 6.9** we define $C_{PBC,LSA}(z)$ as the experiment-specific correction term for **Equation 6.8**,

$$C_{PBC,LSA}(z) = F_{TM_{PBC}-SM} + A.F_{TM-SM_{PBC}}, \tag{6.10}$$

where we have relied on the LSA to simplify the problem. However, we still have not determined the value of the $F_{TM_{PBC}-SM}$ and $F_{TM-SM_{PBC}}$ terms.

In **Equation 6.11** we introduce two new, computationally inexpensive, $_s$NC-AFM spectra. $F_{PBC,g}$, which we define as the F_{PBC} system after removing the $_s$Tip Base and $_s$Surface Base atom groups while keeping the periodicity of the system unchanged; and $F_{CL,g}$, which we define as the F_{PBC} system after removing the $_s$Tip Base and $_s$Surface Base atom groups, and simulating the system as a cluster calculation to remove the periodicity. Using the $F_{PBC,g}$ & $F_{CL,g}$ systems, one can calculate approximations for the $F_{TM_{PBC}-SM}$ and $F_{TM-SM_{PBC}}$ terms **(Equation 6.12)**. It shall be stated clearly at this point, that the conclusions from **Section 6.2** have been applied to simplify the theory going forwards; *the interactions between the $_s$Surface Molecule and $_s$Surface Base, and the $_s$Tip Molecule and $_s$Tip Base, do not effect the interaction between the $_s$Tip Molecule and the $_s$Surface Molecule*. Where this further assumption is based on the $C_{60,u}$ and $C_{60,r}$ systems having the same force minima in **Sections 6.1 & 6.2**, and the charge transfer values in **Figure 6.8**. This is a similar approximation to the one applied in experimental $_e$NC-AFM data sets when one performs an off-curve subtraction to isolate the interaction between the experimental Tip and an adsorbed molecule. To aid the validity of the approximation made at this step, the $F_{PBC,g}$ and $F_{CL,g}$ systems are simulated confined to the geometry from the original F_{PBC} system. This also reduces the computational cost as no relaxation steps occur. **Equation 6.11** below defines the terms $F_{PBC,g}$ and $F_{CL,g}$ are comprised of;

$$\begin{aligned} F_{PBC,g} &= F_{TM-SM} + F_{TM_{PBC}-SM} + F_{TM-SM_{PBC}} \\ F_{CL,g} &= F_{TM-SM}. \end{aligned} \quad , \tag{6.11}$$

In **Equation 6.12** we subtract $F_{PBC,g}$ from $F_{CL,g}$,

$$\begin{aligned} F_{PBC,g} - F_{CL,g} &= \underbrace{F_{TM-SM} + F_{TM_{PBC}-SM} + F_{TM-SM_{PBC}}}_{F_{PBC,g}} - \underbrace{F_{TM-SM}}_{F_{CL,g}} \\ &= F_{TM_{PBC}-SM} + F_{TM-SM_{PBC}}, \end{aligned} \tag{6.12}$$

which leaves us with the terms we are looking to isolate and use in **Equation 6.10**. However, for **Equation 6.10** we need the $F_{TM_{PBC}-SM}$ and $F_{TM-SM_{PBC}}$ terms separately, whereas **Equation 6.12** can only calculate the sum of the two terms. Therefore, we make an additional simplification by taking advantage of the symmetry of the system; *systems involving C_{60} approaching C_{60} are approximately symmetric, therefore* $F_{TM_{PBC}-SM} \simeq F_{TM-SM_{PBC}}$. This lets us define the new term $F_{MM_{PBC}}$ which is calculable from **Equation 6.12**,

$$F_{MM_{PBC}} = \frac{F_{TM_{PBC}-SM} + F_{TM-SM_{PBC}}}{2}, \tag{6.13}$$

where $F_{MM_{PBC}}$ is the average of the $F_{TM_{PBC}-SM}$ and $F_{TM-SM_{PBC}}$ interactions. We can then substitute **Equation 6.13** into **Equations 6.12, 6.9, & 6.10;**

$$F_{PBC,g} - F_{CL,g} \simeq 2F_{MM_{PBC}}, \tag{6.14}$$

$$F_{OCS,PBC,LSA} \simeq \underbrace{F_{TB-SM} + F_{TM-SM}}_{F_{on,CL}} + \underbrace{2F_{MM_{PBC}}}_{\text{PT-OS \& PS-OT terms}}, \tag{6.15}$$

and

$$C_{PBC}(z) \simeq (1 + A)F_{MM_{PBC}}. \tag{6.16}$$

We now have the required theory to create a single equation **(Equation 6.17)** which can correct the overestimate of $_s$NC-AFM spectra, involving C_{60} molecules, due to the periodicity of the system. To produce **Equation 6.17,** we start with the general formula for correcting the off-curve subtracted spectra. In lines two and three we apply the LSA from **Equation 6.9**, which in turn simplifies the previously unknown $C_{PBC}(z)$ term to $C_{PBC,LSA}(z)$ from **Equation 6.10**, which we can then express as PT-OS and PS-OT terms. In line four we take advantage of the symmetry of the system to further simply the $C_{PBC,LSA}(z)$ term. This is performed by combining the two periodic terms into one calculable term dubbed $F_{MM_{PBC}}$ (**see Equation 6.13**). Finally, we replace the $F_{MM_{PBC}}$ term with two (computationally inexpensive) additional simulated spectra, $F_{PBC,g}$ and $F_{CL,g}$ (**see Equations 6.11 & 6.12**) to create the calculable form of **Equation 6.17**;

$$\begin{aligned} F_{FHI}(z) &= F_{OCS,PBC}(z) - C_{PBC}(z) \\ &\simeq F_{OCS,PBC} - C_{PBC,LSA}(z) \\ &\simeq F_{OCS,PBC} - (F_{TM_{PBC}-SM} + A.F_{TM-SM_{PBC}}) \\ &\simeq F_{OCS,PBC} - (1 + A)F_{MM_{PBC}} \\ F_{FHI}(z) &\simeq F_{OCS,PBC} - (1 + A)\frac{F_{PBC,g} - F_{CL,g}}{2}. \end{aligned} \tag{6.17}$$

Where $A = 0$ when simulating a tip approaching a mono-layer, $A = 1$ when simulating a tip approaching an isolated C6o adsorbed on a surface, and $A = 0.5$ when simulating a tip approaching a C_{60} adsorbed on the edge of an island/monolayer.

6.2.5 *Periodicity Correction: Application*

Figure 6.11 displays the $_s$NC-AFM data needed apply the periodicity correction detailed in **Equation 6.17** to the $C_{60,r}$ system. There are four spectra displayed in **Figure 6.11**; $F_{OCS,PBC}$: Red dots correspond to the off-curve subtracted spectra for the $C_{60,r}$ system detailed in **Figure 4.17**. $F_{PBC,g}$: Purple dots correspond to $_s$NC-AFM data for a gaseous C_{60} molecule approaching a gaseous C_{60} molecule. The data was calculated using the periodic unit cell used in $F_{OCS,PBC}$, the C_{60} molecules were confined to the converged geometries from the F_{PBC} $_s$NC-AFM. $F_{CL,g}$: Brown stars correspond to to $_s$NC-AFM data for a gaseous C_{60} molecule approaching a gaseous C_{60} molecule in a cluster calculation. Like with the $F_{PBC,g}$ data, the C_{60} molecules were confined to the converged geometries from the F_{PBC} $_s$NC-AFM. $F_{FHI}(z)$: Green stars correspond to the corrected $F_{OCS,PBC}$. The data has been corrected using **Equation 6.17**, with $A = 0$ to match the experimental situation of an experimental C_{60} Tip approaching a mono-layer of adsorbed C_{60} molecules. Comparing the force and potential minima of the $F_{OCS,PBC}$ and $F_{FHI}(z)$ spectra, we can see the correction for the unwanted *PT-OS* interactions has reduced the force and potential minima by $17\,pN$ and $38\,meV$. If we were to correct our $_s$*NC-AFM* spectrum to simulate a C_{60} Tip approaching an isolated adsorbed C_{60} molecule, the correction will be double in magnitude, changing the force and potential minima by approximately $34\,pN$ and $76\,meV$. Or to rephrase the result, the theory predicts a $17\,pN$ force difference at the force minimum, when comparing a C_{60} molecule adsorbed in a mono layer to an isolated adsorbed C_{60} molecule. Furthermore, this theory suggests the $_s$NC-AFM are indeed an over-estimate of the $_e$NC-AFM, due to the periodicity of the system. Where for a C_{60} Tip, this overestimate is 5% to 10% of the force minimum. However, if the periodicity correction for a *Cu* Tip is similar in magnitude than that for a C_{60} Tip, the overestimate is insignificant relative to the magnitude of the force minimum ($\sim 1.5\,nN$).

Figure 6.11 can also be used to check if **Equation 6.17** is overestimating the periodicity correction. We expect **Equation 6.18**

$$F_{FHI}(z) \geq F_{CL,g}, \tag{6.18}$$

to be true for all values of A, as $F_{FHI}(z)$ should contain additional interactions between the $_s$Surface Base and the $_s$Tip, and between the $_s$Tip Base and the $_s$Surface. As calculated above, for $A = 1$, periodicity correction is $34\,pN$ at the force minimum. Therefore, **Equation 6.18** is satisfied.

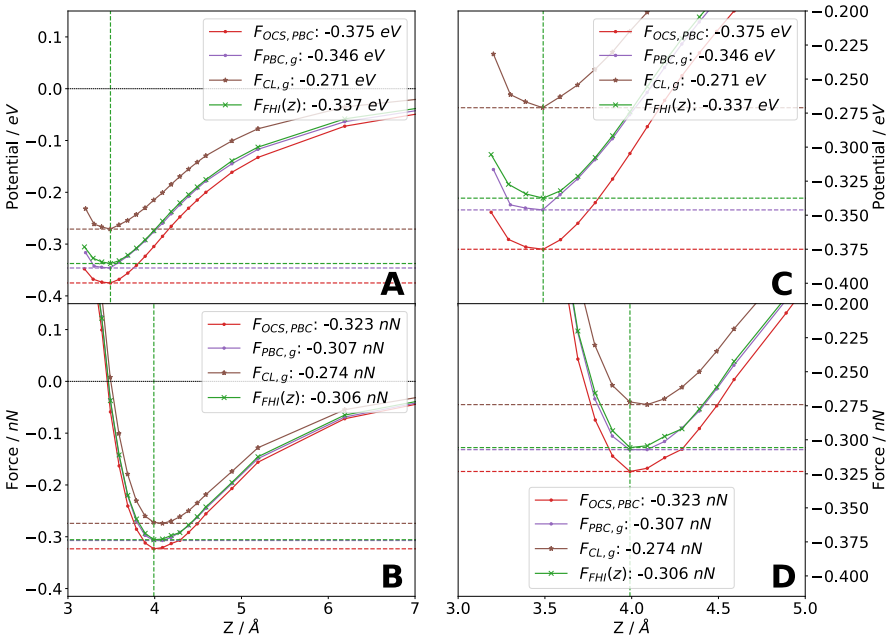

Figure 6.11: $_s$NC-AFM force spectra involving C_{60} Tip approaching a C_{60} molecule on a surface. $F_{OCS,PBC}$: Red dots correspond to the off-curve subtracted spectra for the $C_{60,r}$ system detailed in **Figure 4.17**. $F_{PBC,g}$: Purple dots correspond to $_s$NC-AFM data for a gaseous C_{60} molecule approaching a gaseous C_{60} molecule. The data was calculated using the periodic unit cell used in $F_{OCS,PBC}$, the C_{60} molecules were confined to the converged geometries from the F_{PBC} $_s$NC-AFM. $F_{CL,g}$: Brown stars correspond to to $_s$NC-AFM data for a gaseous C_{60} molecule approaching a gaseous C_{60} molecule in a cluster calculation. As with the $F_{PBC,g}$ data, the C_{60} molecules were confined to the converged geometries from the F_{PBC} $_s$NC-AFM. $F_{FHI}(z)$: Green stars correspond to the corrected $F_{OCS,PBC}$. The data has been corrected using **Equation 6.17**, with $A = 0$ to match the experimental situation of an experimental C_{60} Tip approaching a mono-layer of adsorbed C_{60} molecules. **A&C:** Potential spectra, **B&D:** Force spectra. **C&D:** The data in **A&B** has been cropped about the force and potential minima to highlight the differences and similarities between the spectra. The green, red, purple, and brown horizontal dashed lines mark the force and potential minima in of the plotted $_s$NC-AFM spectra. The values of the horizontal dashed lines are also given numerically in the legends. The solid lines and markers correspond to DFT data, with each marker representing the converged data from a single DFT simulation. The force data in **Figure 6.11** is calculated using the FHI-aims-TF method, the potential data using the FHI-aims-SE method. The vertical green dashed line marks the Z coordinate of the force and potential minima of the $F_{FHI}(z)$ data. The same line has also been plotted in **Figure 6.12**.

6.2.6 *Large Separation Approximation Validity*

A number of approximations were performed in the above theory. Fortunately, it is possible to test the validity of the LSA used with this system without performing additional simulations. See **Figure 6.2.6** for the plots testing the validity of the LSA. In **Equation 6.19** we subtract $F_{PBC,g}$ from $F_{OCS,PBC}$ (see **Section 6.2.4** for definitions of $F_{PBC,g}$ and $F_{OCS,PBC}$);

$$\begin{aligned} F_{OCS,PBC} - F_{PBC,g} &= F_{TM-SM} + F_{TB-SM} + F_{TB_{PBC}-SM} + \\ &\quad F_{TM_{PBC}-SM} + F_{TB-SM_{PBC}} + F_{TM-SM_{PBC}} - \\ &\quad (F_{TM-SM} + F_{TM_{PBC}-SM} + F_{TM-SM_{PBC}}) \\ &= \cancel{F_{TM-SM}} + F_{TB-SM} + F_{TB_{PBC}-SM} + \\ &\quad \cancel{F_{TM_{PBC}-SM}} + F_{TB-SM_{PBC}} + \cancel{F_{TM-SM_{PBC}}} - \\ &\quad (\cancel{F_{TM-SM}} + \cancel{F_{TM_{PBC}-SM}} + \cancel{F_{TM-SM_{PBC}}}) \\ F_{OCS,PBC} - F_{PBC,g} &= F_{TB-SM} + F_{TB_{PBC}-SM} + F_{TB-SM_{PBC}}. \end{aligned} \tag{6.19}$$

However, can further simplify **Equation 6.19** down to just the F_{TB-SM} term by applying the LSA;

$$\begin{aligned} F_{OCS,PBC} - F_{PBC,g} &= F_{TB-SM} + F_{TB_{PBC}-SM} + F_{TB-SM_{PBC}} \\ &\simeq F_{TB-SM} + \cancel{F_{TB_{PBC}-SM}} + \cancel{F_{TB-SM_{PBC}}} \\ F_{OCS,PBC} - F_{PBC,g} &\simeq F_{TB-SM}. \end{aligned} \tag{6.20}$$

Looking at the terms in the Off-Curve from **Equation 6.5**, we can also remove most of the terms using the LSA (see **Section 6.2.4** for the definition of $F_{off,PBC}$);

$$\begin{aligned} F_{off,PBC} &= F_{TB-SB} + F_{TM-SB} + F_{TB_{PBC}-SB} + \\ &\quad F_{TM_{PBC}-SB} + F_{TB-SB_{PBC}} + F_{TM-SB_{PBC}} \\ &\simeq \cancel{F_{TB-SB}} + F_{TM-SB} + \cancel{F_{TB_{PBC}-SB}} + \\ &\quad \cancel{F_{TM_{PBC}-SB}} + \cancel{F_{TB-SB_{PBC}}} + \cancel{F_{TM-SB_{PBC}}} \\ F_{off,PBC} &\simeq F_{TM-SB}. \end{aligned} \tag{6.21}$$

We can now apply the symmetry of the system once more to say $F_{TB-SM} \simeq F_{TM-SB}$, and therefore produce a criteria for checking the LSA applied to this system;

$$F_{off,PBC} \simeq F_{OCS,PBC} - F_{PBC,g}, \tag{6.22}$$

where if **Equation 6.22** holds true, the LSA used to produce **Equation 6.17** is valid.

Figure 6.22 displays the $_s$NC-AFM data needed to test the validity of the LSA, and the calculated C_{PBC} correction term applied in **Figure 7.1**. The vertical green line indicates the z coordinate of the force and

potential minima for the corrected $F_{FHI}(z)$ data in **Figure 7.1**. The values quoted in the legends of **Figure 6.12** are the values of the data at the force minimum of $F_{FHI}(z)$. If the LSA is valid, **Equation 6.22** suggests the $F_{off,PBC}$ and $F_{PBC} - F_{PBC,g}$ data should be approximately equal. Looking at **Figure 6.22** we can see the $F_{off,PBC}$ and $F_{PBC} - F_{PBC,g}$ data varies by 4 pN and 3 meV at the minimas, which suggests the LSA is adequate.

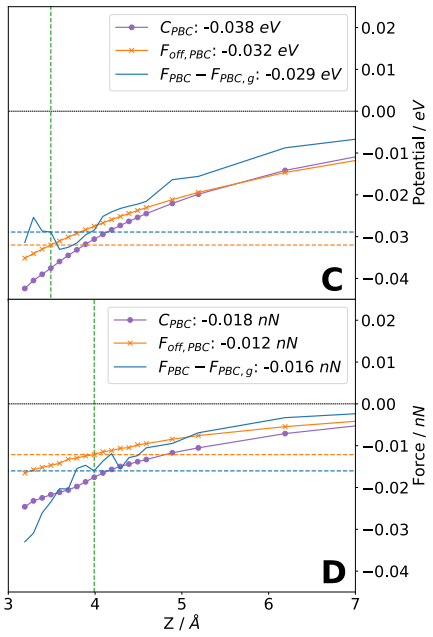

Figure 6.12: sNC-AFM force spectrum data related to **Equation 6.17**, and testing the validity of the LSA with **Equation 6.22**. $F_{off,PBC}$: Orange crosses represent the experimentally analogous sNC-AFM Off-Curve, calculated with a C_{60} Tip. C_{PBC}: Purple dots represent the correction term from **Equation 6.17** for $A = 1$, calculated using $F_{PBC,g}$ and $F_{CL,g}$. $F_{PBC} - F_{PBC,g}$: The Blue line shows a comparison term from **Equation 6.22**, used to test the validity for the LSA. **A:** Potential spectra. **B:** Force spectra. The vertical green dashed lines mark the z coordinate for the force and potential minima of the $F_{FHI}(z)$ data plotted in **Figure 7.1**. The values given in the legend are the values of the plotted data at the point of intersection with the vertical dashed green line. The solid lines and markers correspond to DFT data, with each marker representing the converged data from a single DFT simulation. The force data in **Figure 6.12** is calculated using the FHI-aims-TF method, the potential data using the FHI-aims-SE method.

6.2.7 *Effect of the Surface*

In **Section 6.2** it was discussed that a change in reactivity of the adsorbed C_{60} molecule, induced by the underlying Cu(111) surface reconstruction, was not detectable when probing the adsorbed C_{60} molecule with $_s$NC-AFM using a Cu Tip or C_{60} Tip. Thus one would also expect the reactivity of the adsorbed C_{60} molecule to be unchanged by the underlying Cu(111) surface reconstruction in $_e$NC-AFM spectra, when probed with an experimental C_{60} Tip. However, the series of $_s$NC-AFM spectra in **Chapter 6**, and the experimental $_e$NC-AFM in **Chapter 2**, are not able to tell us the how the Cu_r or Cu_u surface perturbs the reactivity of the adsorbed C_{60} molecule relative to a gas phase C_{60} molecule.

We can computationally construct a series of systems, based on the experiment, which allow us to investigate the question; *how is the reactivity of the adsorbed C_{60} molecule perturbed relative to a gas phase C_{60} molecule*. We do this by building upon the theory developed in **Section 6.2.4**. As discussed in **Section 3.6**, a contemporary DFT calculation involving a geometrical relaxation often includes a vdW correction. The vdW correction is applied to increase the accuracy of the calculation, as it is well understood the purely DFT part of the calculation does not include long range vdW interactions between atoms. Although the system is geometrically relaxed using the resultant force of the DFT and vdW correction, it is possible to decompose the total force back into it's components, as defined in **Equation 6.23** for the F_{PBC} and $F_{PBC,g}$ systems from **Section 6.2.4**;

$$\begin{aligned} F_{PBC} &= F_{PBC,DFT} + F_{PBC,vdW} \\ F_{PBC,g} &= F_{PBC,g,DFT} + F_{PBC,g,vdW}. \end{aligned} \tag{6.23}$$

Where we define F_{PBC} as the full $C_{60,r}$ system comprised of a $_s$Tip Base, $_s$Tip Molecule, $_s$Surface Base, and $_s$Surface Molecule, with $F_{PBC,DFT}$ and $F_{PBC,vdW}$ being the DFT and vdW correction components respectively. We also define $F_{PBC,g}$ as the F_{PBC} system after removing the $_s$Tip Base and $_s$Surface Base atom groups, while keeping the periodicity of the system unchanged, and the Carbon atoms confined to their original positions. $F_{PBC,g,DFT}$ and $F_{PBC,g,vdW}$ are the DFT and vdW correction components respectively for the $F_{PBC,g}$ system. As the DFT force component only acts over a shot range, we can presume the DFT component only includes interactions between the top half of the $_s$Surface Molecule, and bottom half of the $_s$Tip Molecule. If the presence of the $_s$Surface Base does not effect the reactivity of the $_s$Surface Molecule, when probed with a C_{60} molecule, then we can state

$$F_{PBC,DFT} \simeq F_{PBC,g,DFT}, \tag{6.24}$$

and create the further test case

$$F_{PBC} = F_{PBC,DFT} + F_{PBC,vdW} \simeq F_{PBC,g,DFT} + F_{PBC,vdW}. \tag{6.25}$$

In **Figures A&B**, the force and corresponding energy components from **Equation 6.23** have been plotted for the $C_{60,r}$ system in **Figure 4.17**. An approximately 30 pN offset was applied to the $F_{PBC,DFT}$ component, as the offset discussed in **Section 6.2.3** arises from the DFT component. There was no offset in the $F_{PBC,g}$ data. In **Figure C&D** the force and corresponding energy calculated using **Equation 6.25** has been plotted along with the original $C_{60,r}$ spectrum. One can see that $F_{PBC,DFT} = F_{PBC,g,DFT}$ for the forces calculated with the FHI-aims-TF method, however, the $F_{PBC,DFT} = F_{PBC,g,DFT}$ relationship is not met as well for the the potential calculated with the FHI-aims-SE method. Thus, **Equation 6.25** holds for the forces calculated with the FHI-aims-TF method, but not for the potential calculated with the with the FHI-aims-SE method. This is a result of the FHI-aims-SE including the $_s$Surface Molecule – $_s$Surface Base interactions **(black lines in Figure 6.10 B)**, whereas the FHI-aims-TF method does not. Furthermore, the difference in result between the FHI-aims-SE and FHI-aims-TF methods is consistent with **Figures 4.10 & 6.8**. **Figure 4.10** suggests the electronic structure of the adsorbed C_{60} molecule has been perturbed from the has phase C_{60} molecule. However, **Figure 6.8** suggests changes to the electronic structure are localized to the lower half of the C_{60} molecule, which is not probed by $_s$NC-AFM. **Figure 6.13** further confirms this as the $_s$NC-AFM method sensitive to $_s$Surface Molecule – $_s$Surface Base interactions (FHI-aims-SE) is able to detect the presence of the Cu_r surface, whereas the $_s$NC-AFM method primarily sensitive to $_s$Tip Apex – $_s$Surface Apex interactions (FHI-aims-TF) was unable to detect the presence of the Cu_r surface.

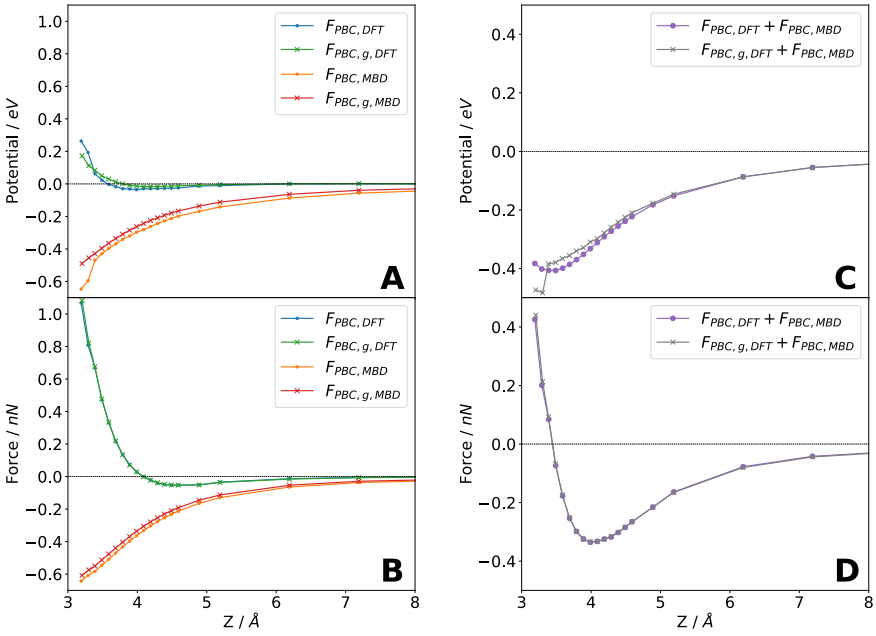

Figure 6.13: $_s$NC-AFM force spectra corresponding to **Equations 6.23 & 6.25**. In **A&B** the DFT and vdW components from **Equation 6.23** have been plotted for the F_{PBC} and $F_{PBC,g}$ systems. In **C&D Equation 6.25** has been plotted. The force data in **Figure 6.13** is calculated using the FHI-aims-TF, the potential data using the FHI-aims-SE.

6.2.8 *Predicting* 'Does the Bottom Effect the Top?'

Given the FHI-aims-TF method is the most experimentally analogous **(Chapter 5)**, the following discussion is only considering the FHI-aims-TF data. As $F_{PBC,DFT} = F_{PBC,g,DFT}$ holds true, **Equation 6.25** holds true. This suggests the presence of the Cu_r surface has not changed the reactivity of the C_{60} molecule relative to the gas phase C_{60} molecule, when probed with a C_{60} Tip. As we have applied this analysis to the $C_{60,r}$ system, we can also conclude the surface reconstruction has not significantly effected the force and potential minimum, and the prescence of the Cu_u surface will also not significantly effect the reactivity of the section of the C_{60} molecule being perturbed by the C_{60} Tip. When we also look at the charge distributions plotted in **Figure 6.8**, we can conclude this result can be predicted using charge transfer values; *if the charge transferred to the adsorbed molecule does not exist around the section of the molecule being probed by $_s$NC-AFM, and the atoms within the molecule are not geometrically displace by the presence of the surface, then $_s$NC-AFM will likely not detect the presence of the surface in the reactivity of the adsorbed molecule*. As the $_s$NC-AFM in this work has been focused on replicating $_e$NC-AFM, we also extend this conclusion to $_e$NC-AFM.

6.3 CO TIP

Simulated NC-AFM force spectra, calculated using a *CO* Tip, for both the $C_{60,u}$ and $C_{60,r}$ systems (described in **Figure 4.19**), were simulated for a single spectrum site located at the centre of the adsorbed C_{60} molecules. The initial tip position in each spectrum was created by positioning the atomic core of the Oxygen atom in the tip apex ~17 Å above the top of the surface. The top of the surface is defined as the average atomic core position of the six C atoms forming the upwards facing hexagon in the surface. Looking at **Figures 6.14 A&B**, one can see the spectra taken over the $C_{60,u}$ and $C_{60,r}$ molecules are similar, with force and potential minima of approximately $U_{z,min} \simeq -0.135\,eV$ and exactly $F_{z,min} \simeq -0.105\,nN$. A small difference of $1\,nN$ and $3\,eV$ the two systems was detected in the potential minimum was detected, it is possible this effect is caused by an integration of the uncertainty in the force. Pawlak *et al* reported experimental force minima with a *CO* functionalized tip of ~$50\,pN$ for various sites over the C_{60} molecule [131].

The force and potential spectra shown in **Figure 6.7** were calculated using the FHI-aims-SE method (described in **Section 5.2**) as it was determined to be the most reliable method for the *CO* Tip systems. There was an uncertainty in the tail of the spectra when it was calculated with the FHI-aims-TF and FHI-aims-SF methods. It is theorized the uncertainty arises from a combination of the convergence criteria used, and the low resolution used for large tip-sample separations. With the FHI-aims-TF and FHI-aims-SF methods, the potential is calculated using an integral of the force. Therefore the uncertainty is also integrated, and thus has a relatively large effect on the potential minima values. In contrast, when using the FHI-aims-SE approach, the calculated force and potential values at the minima are unaffected by the data at the tail of the spectrum. Furthermore, there are no large geometrical relaxations in the spectrum, and a high resolution is used about the force minima, which allows an accurate differential of the potential to be calculated.

Figure 6.14 C plots the change in the highest atomic coordinate of the surface atoms for the two systems. Comparing **Figure 6.14 C** to **Figures 6.5 and 6.7 C**, one can see the vertical displacement for both the $C_{60,u}$ and $C_{60,r}$ systems is smaller. This is likely due to the maximum attractive force between the tip and sample for the *CO* Tip being approximately $\frac{1}{3}$ and $\frac{1}{10}$ value simulated with the *Cu* Tip and C_{60} Tips respectively. Despite the overall small tip-sample interaction strength, the $C_{60,u}$ molecule still rises off the surface further than the $C_{60,r}$ molecule.

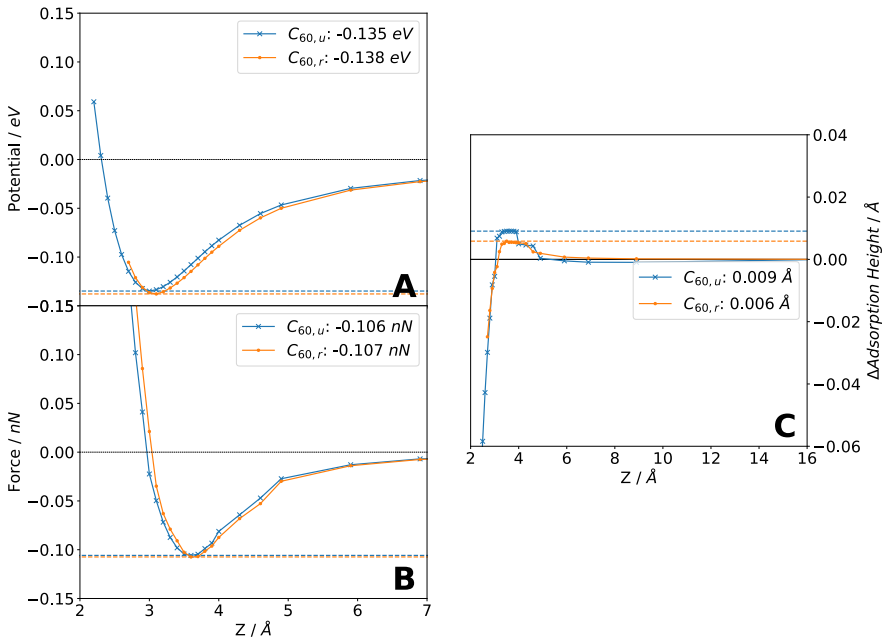

Figure 6.14: Simulated NC-AFM force spectra for a *CO* Tip approaching the $C_{60,u}$ (blue crosses) and $C_{60,r}$ (orange dots) systems, detailed in **Figure 4.19**. Plots **A, B, & C** contain data from spectra simulated with the O atom of the tip approaching the centre of the upwards presenting hexagonal face of the surface C_{60} molecule. **A:** Potential spectra, **B:** Force spectra, **C:** Relative surface height data. The blue and orange horizontal dashed lines mark the force and potential minima in **A&B**, and the surface height maxima in **C,** of the $C_{60,u}$ and $C_{60,r}$ systems respectively. The values of the dashed lines are also given numerically in the legends. The solid lines and markers correspond to DFT data, with each marker representing the converged data from a single DFT simulation. The data in **Figure 6.14** is calculated using the Fritz Haber Institute *ab initio* molecular simulations System Energy method (FHI-aims-SE).

6.4 $H_2O@C_{60}$ ON CU(111)

This section details results of Simulated Non-Contact Atomic Force Microscopy ($_s$NC-AFM) force spectroscopy calculated for systems involving H_2O contained within a C_{60} molecule ($H_2O@C_{60}$), see **Section 4.3** for diagrams of the systems. For a detailed description of the methods used to calculate the $_s$NC-AFM spectrum in DFT, implemented in FHI-aims, see **Chapter 5**. It has been known for more than a decade that small molecules, such as H_2 [132] and H_2O, [133] can be encapsulated within a C_{60} molecule. Furthermore, the $H_2O@C_{60}$ molecular complex has been previously investigated with both Nuclear Magnetic Resonance [134], and STM [135]. **Section 6.4** aims to test the feasibility of detecting the encapsulated H_2O through experimental $_e$NC-AFM, by first probing the $H_2O@C_{60}$ molecular complex in $_s$NC-AFM. The initial orientation of the H_2O molecule within $H_2O@C_{60}$ molecular complex was replicated from the work by Jarvis *et al* [126], which considered $H_2O@C_{60}$ deposited on the similar Ag(111) surface.

6.4.1 *C_{60} and $H_2O@C_{60}$ Tips*

$_s$NC-AFM force spectra were carried out for three systems involving C_{60} and $H_2O@C_{60}$ adsorbed on the Cu_u and Cu_r surfaces. The systems are comprised of a $C_{60,r}$ approaching a $C_{60,u}$ **(**blue dots, **Figure 4.17)**, a $C_{60,r}$ approaching a $H_2O@C_{60,u}$ **(**orange crosses, **Figure 4.20)**, and a $H_2O@C_{60,r}$ approaching a $H_2O@C_{60,u}$ **(**green stars, **Figure 4.20)**, and all three spectra were simulated at the spectrum site defined as the centre of the adsorbed $C_{60,u}$ or $H_2O@C_{60,u}$ molecules. The initial tip position in each spectrum was created by positioning the $_s$Tip Apex ~15 Å above the top of the $_s$Surface Apex. Where the $_s$Tip Apex is defined as the average atomic core coordinate of the six C atoms forming the downwards facing hexagon in the $_s$Tip Molecule, and the $_s$Surface Apex is defined as the average atomic core position of the six C atoms forming the upwards facing hexagon of the $_s$Surface Molecule.

The $C_{60,r}$ approaching a $C_{60,u}$ system is the same data presented in **Figure 6.7**. This system acts as a control for the systems involving the $H_2O@C_{60}$ molecular complexes. Looking at **Figures 6.15**, one can see each encapsulated H_2O molecule increases the attractiveness of the force minimum by $4\,pN \leq F_{diff} \leq 9\,pN$, and increases the attractiveness of the potential minimum by $6\,eV \leq U_{diff} \leq 7\,eV$, a similar result to the gaseous simulations presented in **Section 4.3.4**. Given well designed $_e$NC-AFM experiments have measured tip-sample interactions in the sub pN regime [136], these simulations suggest detecting the difference between the C_{60} and $H_2O@C_{60}$ molecular complexes in $_e$NC-AFM experiments is experimentally feasible. Although the increase in attractiveness at the force minimum appears to be larger when moving from the blue dotted line to the orange crossed line, compared

to moving from the orange crossed line to the green starred line, it is unclear if this difference is a real effect, or an artifact from the method used to calculate the force spectrum data. However, as the two encapsulated H_2O molecules are aligned such that they should repel one another, we can conclude the increase in attractiveness is due to the additional vdW interactions involving the H_2O molecules.

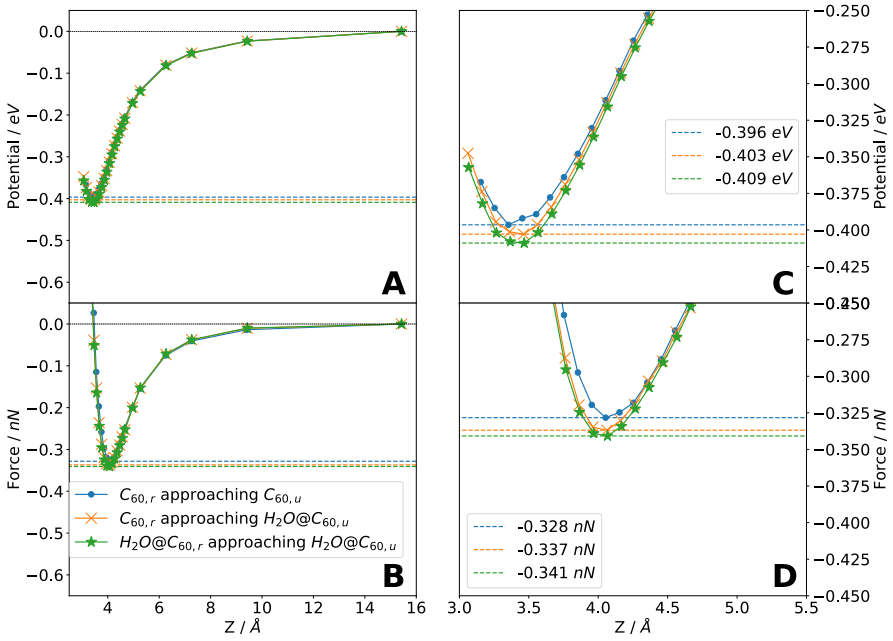

Figure 6.15: Simulated NC-AFM force (and corresponding potential) spectra for three systems involving C_{60} and $H_2O@C_{60}$ adsorbed on the Cu_u and Cu_r surfaces. The systems are comprised of a $C_{60,r}$ approaching a $C_{60,u}$ **(**blue dots, **Figure 4.17)**, a $C_{60,r}$ approaching a $H_2O@C_{60,u}$ **(**orange crosses, **Figure 4.20)**, and a $H_2O@C_{60,r}$ approaching a $H_2O@C_{60,u}$ **(**green stars, **Figure 4.20)**. **A&B:** The spectra are displayed on a Z scale ranging from a large tip-sample separation (where the interaction is $\sim$ 0) to a small tip-sample separation (which probes the repulsive interaction). **C&D:** The data from **A&B** has been cropped about the force minima to highlight the differences between spectra simulated over different sites. The blue, orange, and green horizontal dashed lines mark the force minimum of the blue dotted, orange crossed, and green starred lines respectively. The values of the dashed lines are given numerically in the legends. The solid lines and markers correspond to DFT data, with each marker representing the converged data from a single DFT simulation. The force data in **Figure 6.7** is calculated using the FHI-aims-TF, the potential data using the FHI-aims-SE.

6.4.2 *Methods*

The force spectra shown in **Figure 6.15** were calculated using the FHI-aims-TF method, the potential data was calculated using the FHI-aims-SE method (methods described in **Section 5.2**). Unfortunately, none of the three methods proposed in **Section 5.2** are ideal for the comparisons made in **Figure 6.15**. The tip and sample atoms being summed over are not consistent for the three systems being compared, and the FHI-aims-SE method is unreliable for the $C_{60,r}$ approaching $C_{60,u}$ system due to the relatively large geometrical relaxation at the force minimum **(see Section 6.2.2)**. As none of the three methods are ideal, the same methods used in **Section 6.2** were used to keep consistency.

The FHI-aims-SF method produces similar results to the FHI-aims-TF, with each H_2O molecule increasing the attractiveness of the force minimum. Furthermore, the differences are larger at the force minima when calculated with the FHI-aims-SF method. This suggests the FHI-aims-TF method provides a lower bound estimate for the effects of the encapsulated H_2O molecules.

6.4.3 *Cu Tip*

Simulated NC-AFM force spectra were carried out for a Cu Tip approaching the C_{60} **(**blue dots, **Figure 4.18)**, and $H_2O@C_{60}$ **(**orange crosses, **Figure 4.20)** molecular complexes adsorbed on the Cu_u surface. Both spectra were simulated over the C atom spectrum site, with the initial tip position in each spectrum created by positioning the atomic core of the (single atom) Cu Tip apex ~20 Å above the same C atom in the upwards facing hexagon of the $C_{60,r}$ or $H_2O@C_{60,r}$ molecular complexes. Looking at **Figures 6.16**, one can see each encapsulated H_2O molecule decreases the attractiveness of the force minimum by 3 pN. Given the force minimum of ~1.5 nN, this 0.2% difference is likely not experimentally detectable. The potential minimum was not simulated as it is not experimentally obtainable.

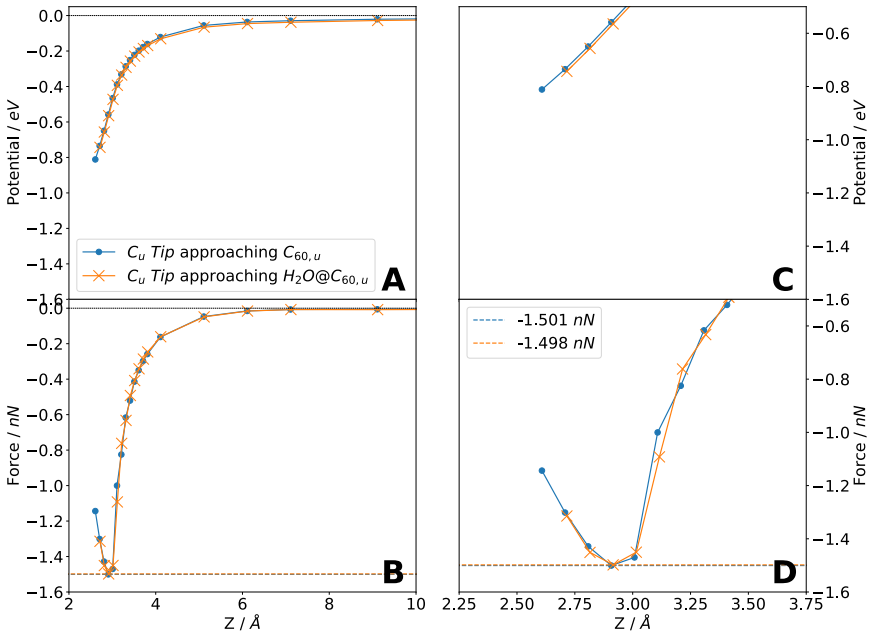

Figure 6.16: Simulated NC-AFM force (and corresponding potential) spectra for two systems; a Cu Tip approaching a $C_{60,u}$ (blue dots, **Figure 4.18**), and a Cu Tip approaching a $H_2O@C_{60,u}$ (orange crosses, **Figure 4.20**). **A&B:** The spectra are displayed on a Z scale ranging from a large tip-sample separation (where the interaction is ~ 0) to a small tip-sample separation (which probes the repulsive interaction). **C&D:** The data from **A&B** has been cropped about the force minima to highlight the differences between spectra simulated over different sites. The blue and orange horizontal dashed lines mark the force minimum of the blue dotted and orange crossed lines. The values of the dashed lines are given numerically in the legends. The solid lines and markers correspond to DFT data, with each marker representing the converged data from a single DFT simulation. The data in **Figure 6.16** is calculated using the Fritz Haber Institute *ab initio* molecular simulations Tip Forces method (FHI-aims-TF).

7

SIMULATED NC-AFM RESULTS: GASEOUS C_{60}

This section details the results for the $_s$NC-AFM force spectra involving the gaseous systems described in **Section 4.3.4**. For a full analysis of the methods used to calculate a $_s$NC-AFM spectrum, see **Chapter 5**.

Figure 7.1 displays $_s$NC-AFM spectra for the C_{60}-h approaching C_{60}-h system. The $D = 30°, 0°, -30°$ systems were selected as they correspond to all unique tip-sample interactions **(see Figure 4.22, Figure 7.1 A inset)**. Comparing **Figure 7.1** to **Figure 4.22,** we can conclude the most attractive C_{60}-h – C_{60}-h interaction occurs when the double bonds of the tip molecule approach the single bonds of the sample molecule, and the least attractive configuration corresponds to the double bonds of the tip molecule approaching the double bonds of the sample molecule. However, this difference is only $10\,pN$ and $13\,meV$. This difference is smaller than the experimental accuracy demonstrated by the scatter plots of **Chapter 2**. **Figure 7.2** displays $_s$NC-AFM spectra for the C_{60}-h approaching C_{60}-h, C_{60}-h approaching H_2O@C_{60}-h, and H_2O@C_{60}-h approaching H_2O@C_{60}-h systems, for the relative azimuthal angle of $D = 0°$. Looking at the force and potential minima, one can see each encapsulated H_2O molecule increases the attractiveness of the force and potential minima by $6\,pN$ and $5\,meV$. The effect of the encapsulated H_2O molecule on the force and potential minima is consistent with **Section 6.4.1**, despite there being no $_s$Tip Base and $_s$Surface Base present. As the two encapsulated H_2O molecules are in an opposing configuration, this further suggests the C_{60} molecule is screening the electrostatic interaction of the H_2O molecules, and the force difference is due to the additional vdW interactions in the system.

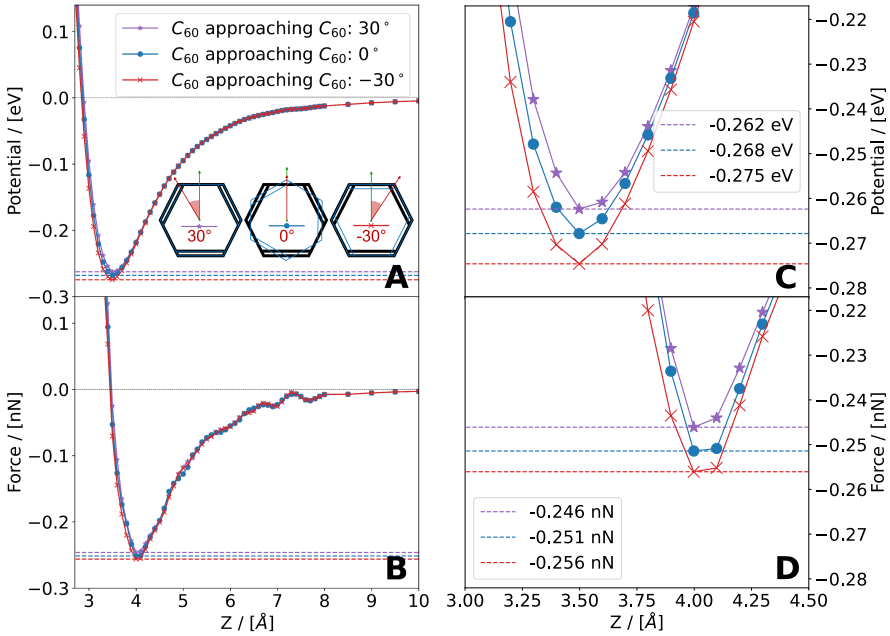

Figure 7.1: Simulated NC-AFM force (and corresponding potential) spectra for the C_{60}-h approaching C_{60}-h system detailed in **Figure 4.22**. Data corresponding to the relative azimuthal angles $D = -30°, 0°, 30°$ has been plotted. **A&B:** The spectra are displayed on a Z scale ranging from a large tip-sample separation (where the interaction is ~ 0) to a small tip-sample separation (which probes the repulsive interaction). **C&D:** The data from **A&B** has been cropped about the force and potential minima to highlight the differences between the three spectra. The blue dotted, red crossed, and purple starred lines, represent data taken with the relative azimuthal angles of $D = -30°, 0°, 30°$ respectively. With the blue, red, and purple, dashed horizontal lines highlighting the respective force and potential minima. The values of the dashed lines are also given numerically in the legends. The solid lines and markers correspond to DFT data, with each marker representing the converged data from a single DFT simulation. The data in **Figure 7.1** is calculated using the Fritz Haber Institute *ab initio* molecular simulations System Energy method (FHI-aims-SE).

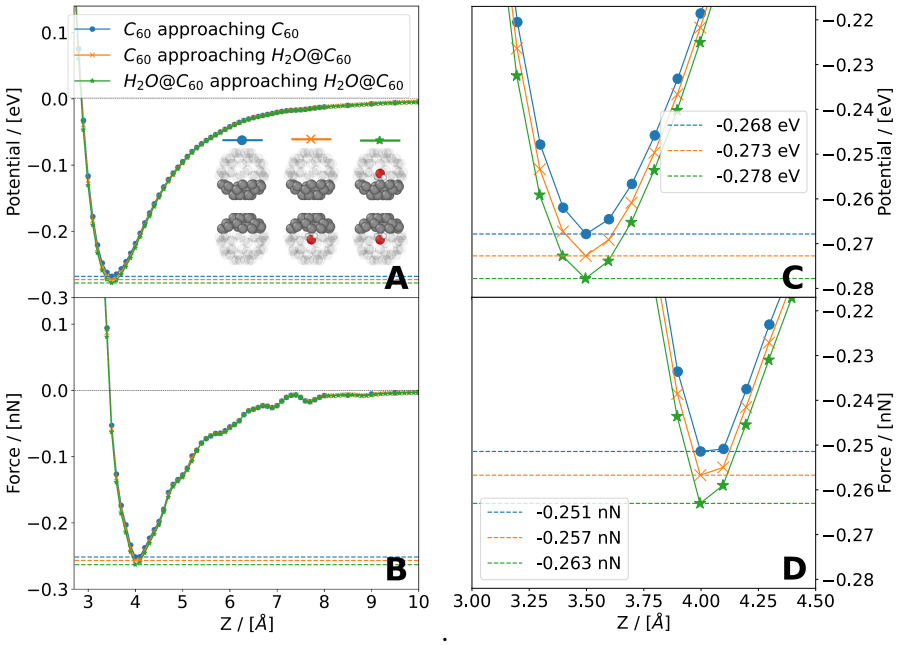

Figure 7.2: Simulated NC-AFM force (and corresponding potential) spectra for the systems in **Section 4.3.4**, oriented with the relative azimuthal angle $D = 0°$ (defined in **Figures 4.22, 4.23, & 4.24**). **A&B:** The spectra are displayed on a Z scale ranging from a large tip-sample separation (where the interaction is ~ 0) to a small tip-sample separation (which probes the repulsive interaction). **C&D:** The data from **A&B** has been cropped about the force and potential minima to highlight the differences between the three spectra. The blue dotted, orange crossed, and green starred lines, represent data for the C_{60}-*h* approaching C_{60}-*h*, C_{60}-*h* approaching $H_2O@C_{60}$-*h*, and $H_2O@C_{60}$-*h* approaching $H_2O@C_{60}$-*h* systems respectively, with the blue, orange, and green, dashed horizontal lines highlighting their respective minima. The values of the dashed lines are also given numerically in the legends.The solid lines and markers correspond to DFT data, with each marker representing the converged data from a single DFT simulation. The data in **Figure 7.2** is calculated using the Fritz Haber Institute *ab initio* molecular simulations System Energy method (FHI-aims-SE). All 3D atomic geometry visualizations in this work were created using OVITO [97].

Overall, simulated NC-AFM force spectra were carried out with the C_{60}-h approaching C_{60}-h, C_{60}-h approaching $H_2O@C_{60}$-h, and $H_2O@C_{60}$-h approaching $H_2O@C_{60}$-h systems for the relative azimuthal angles of $D = -90°$, $-60°$, $-30°$, $0°$, $30°$, $60°$. The force and potential minima of all these spectra have then been calculated, and plotted in **Figure 7.3**. Comparing the blue dots and orange crosses in **Figure 7.3** to the geometries corresponding to unique interactions and equivalent interactions in **Figures 4.22 and 4.23,** one can see the force and potential minima data follows the patterns laid out by the unique and equivalent interactions in the geometry diagrams. All unique force and potential minima are found within the angle range $-30° \leq D \leq 30°$, the angles $D = -60°, 0°, 60°$ have the same force and potential minima values, and the force and potential minima values for $D = -90°$ and $D = 30°$ (120° rotation) are the same as the geometries are equivalent. When looking at the data for the $H_2O@C_{60}$-h approaching $H_2O@C_{60}$-h system (green stars), the results are more complex. The trends in the data for the $H_2O@C_{60}$-h approaching $H_2O@C_{60}$-h system are the same as the trends in the data for the C_{60}-h approaching C_{60}-h, C_{60}-h approaching $H_2O@C_{60}$-h systems. However, the geometry patterns laid out in **Figure 4.24** does not predict this. Therefore, the data suggests the relative azimuthal orientation of the encapsulated H_2O is not detectable in the simulated NC-AFM force and potential spectra. However, the presence of the encapsulated H_2O is detectable as the spectra become $\sim 6\,pN$ and $\sim 5\,meV$ more attractive per encapsulated H_2O .

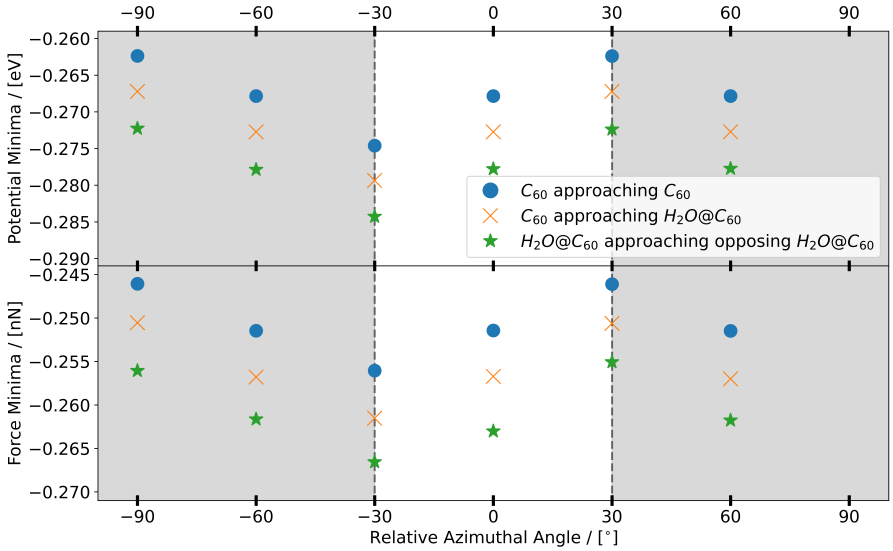

Figure 7.3: Minima values of the simulated NC-AFM spectra for the C_{60}-h approaching C_{60}-h (blue dots), C_{60}-h approaching $H_2O@C_{60}$-h (orange crosses), and $H_2O@C_{60}$-h approaching $H_2O@C_{60}$-h (green stars) systems. The spectra were performed for the relative azimuthal angles of $D = -90°$, $-60°$, $-30°$, $0°$, $30°$, $60°$, as defined in **Figures 4.22, 4.23, and 4.24**. The two vertical dashed lines and shaded regions mark the relative azimuthal rotations corresponding to mirror geometries for the C_{60}-h approaching C_{60}-h, and C_{60}-h approaching $H_2O@C_{60}$-h systems. The data in **Figure 7.3** is calculated using the Fritz Haber Institute *ab initio* molecular simulations System Energy method (FHI-aims-SE).

Part III

DOES THE BOTTOM EFFECT THE TOP?

8

DOES THE BOTTOM EFFECT THE TOP?

Chapter 8 summarizes the experimental and computational results detailed in **Chapters 2** and **Chapters 6 & 7**. The agreement between the experimental and computational results from this work are discussed, then the results calculated in this work are further compared to previous work in the literature. To perform this comparison, published work on computational and experimental systems involving C_{60}, similar to those studied in this work, have been detailed and summarized. Finally, The effect of the underlying surface reconstruction, investigated using ${}_{e}$NC-AFM, ${}_{s}$NC-AFM, and further DFT analysis, shall be discussed.

8.1 C60 TIP

This section summarizes and compares the experimental and computational data from **Chapters 2 & 6** pertaining to force spectra taken over C_{60} molecules adsorbed on the Cu(111) surface, investigated in ${}_{e}$NC-AFM and ${}_{s}$NC-AFM with a C_{60} Tip.

8.1.1 *Experimental Results*

In **Chapter 2**, **Section 2.2**, force spectrum data gathered atop C_{60} molecules adsorbed on the Cu(111) surface, gathered with a C_{60} Tips, was presented. Hundreds of force spectra were taken, over C_{60} adsorbed on the unreconstructed Cu(111) surface ($C_{60,u}$), and C_{60} adsorbed on the 7 atom vacancy Cu(111) surface reconstruction ($C_{60,r}$).

The force spectra were broken down into two sets of data; C_{60} *Tip Dataset 1* and C_{60} *Tip Dataset 2*. For each dataset, the average force minima of the spectra taken over the $C_{60,u}$ and $C_{60,r}$ molecules was calculated separately. The following values were measured;

C_{60} *Tip Dataset 1*:

- $F_{min,r}^{C_{60}\,Tip\,1} = -(0.306 \pm 0.014)\,nN$
- $F_{min,u}^{C_{60}\,Tip\,1} = -(0.298 \pm 0.014)\,nN$

C_{60} *Tip Dataset 2*:

- $F_{min,r}^{C_{60}\,Tip\,2} = -(0.307 \pm 0.014)\,nN$
- $F_{min,u,M1}^{C_{60}\,Tip\,2} = -(0.303 \pm 0.014)\,nN$ **and** $F_{min,u,M2}^{C_{60}\,Tip\,2} = -(0.342 \pm 0.014)\,nN$

Two values were calculated for the $C_{60,u}$ data from C_{60} *Tip Dataset 2* to reflect the bimodal distribution in the data. In the above, $F_{min,r}$ and $F_{min,u}$ denote the average the force minima for spectra taken over the $C_{60,r}$ and $C_{60,u}$ molecules, and $F_{min,u,M1}$ and $F_{min,u,M2}$ denote the two modes of the bimodal distribution in the $C_{60,u}$ data for C_{60} *Tip Dataset 2*.

When looking at the average force minimum values for the $C_{60,r}$ molecules, the measured average force minima for the two datasets ($F_{min,r}^{C_{60}\,Tip\,1}$ and $F_{min,r}^{C_{60}\,Tip\,2}$) are in statistical agreement, with the small force difference of $1\,pN$ (< 1 % of the force minimum) lying within the $28\,pN$ (1 sigma) overlap range of the $14\,pN$ error bars (calculated in **Section 2.4**). However, the story is less clear when looking at the average force minimum values for the $C_{60,u}$ molecules. $F_{min,u,M1}^{C_{60}\,Tip\,2}$ (mode M1 of the bimodal distribution) was measured to be $5\,pN$ more attractive than $F_{min,u}^{C_{60}\,Tip\,1}$, lying within the $28\,pN$ (1 sigma) overlap range of the $14\,pN$ error bars . Whereas $F_{min,u,M2}^{C_{60}\,Tip\,2}$ (mode M2 of the bimodal distribution) was $44\,pN$ more attractive, lying outside the $28\,pN$ (1 sigma) overlap range of the $14\,pN$ error bars. Furthermore the two modes $F_{min,u,M1}$ and $F_{min,u,M2}$ are in disagreement with each other, as they vary by $39\,pN$. This leads to to the following conclusions when comparing the force minima over the $C_{60,r}$ and $C_{60,u}$ molecules:

1. The expected force minimum for a C_{60} Tip interacting with a $C_{60,r}$ is $F_{min,r}^{C_{60}\,Tip} = -(0.306 \pm 0.014)\,nN$.

2. The force minimum for a C_{60} Tip interacting with a $C_{60,u}$ is expected to either lie in on of the following ranges; $F_{min,u}^{C_{60}\,Tip} \simeq -(0.300 \pm 0.014)\,nN$, or $F_{min,u}^{C_{60}\,Tip} = -(0.342 \pm 0.014)\,nN$.

3. The two modes of the bimodal distribution in C_{60} Tip dataset 2 are in disagreement after taking into account the error bars, suggesting the cause was not considered in this work.

4. In summary, the experimental data does not eliminate the possibility of the $C_{60,u}$ and $C_{60,r}$ force minima being the same, or strongly support there being a reproducible difference in the force minima. One could even describe the experimental data as *inconclusive.*

8.1.2 *Computational Results*

Simulations of the experiments detailed in **Chapters 2** were performed with DFT using FHI-aims. In the ideal world, the $_s$Tip would be modeled as a C_{60} molecule adsorbed atop a pyramid of Copper, and the $_s$Surface modeled as an infinite Cu(111) slab topped with the experimental coverage of adsorbed C_{60} molecules. Where the experimental coverage varies from a mono-layer, to large or small islands, to an isolated C_{60} molecule. To make the simulation computationally feasible, the system was simulated as a mono-layer of $C_{60,r}$ approaching a mono-layer of $C_{60,r}$ or $C_{60,u}$ **(Section 4.2)**.

The system was periodic to simulate the $_s$Surface as an infinite Cu(111) surface, and C_{60} molecules were adsorbed onto Cu(111) surface as a mono-layer of either $C_{60,r}$ or $C_{60,u}$. The disadvantage of this approach was the $_s$Tip also needed to be compatible with a periodic system. Therefore, to mimic a copper tip functionalized with a C_{60} molecule, the $_s$Tip was also modeled as the $C_{60,r}$ $_s$Surface **(Chapter 4)**.

Both the On-Curves and Off-Curves for the $C_{60,r}$ and $C_{60,u}$ systems were simulated, and an off-curve subtraction analogous to the experimental off-curve subtraction was applied. This approach was performed to accurately replicate how the off-curve subtraction for the $C_{60,r}$ and $C_{60,u}$ systems is not equivalent **(Section 1.3.3)**. In addition to the off-curve subtraction, theory to quantify the over-estimate of the force minimum caused by the periodicity of the system (in particular the tip replications interacting with the surface) was developed, and a correction term calculated and tested for accuracy **(Sections 6.2.4, 6.2.5 & 6.2.6)**.

Finally, the force and potential minima for a gaseous system, comprised of two interacting C_{60} molecules without the presence of a $_s$Surface Base or $_s$Tip Base, was calculated in **Chapter 7**.

The following results for the $_s$NC-AFM force minima were obtained:

1. The $_s$NC-AFM force minimum for a C_{60} Tip interacting with an adsorbed $C_{60,r}$ molecule is the same as the simulated force minimum for a C_{60} Tip interacting with an adsorbed $C_{60,u}$ molecule once the off-curve subtraction is performed.

2. The simulated force minimum is $F_{min}^{C_{60}\,Tip} = -0.306\,nN$, after performing the off-curve subtraction and the periodicity correction, with the periodicity correction using $A = 0$ to replicate a force spectrum taken over a C_{60} molecule adsorbed in a mono-layer.

3. For a gaseous system, the simulated force and potential minima were calculated to be; $-0.246\,nN \leq F_{min}^{gas} \leq -0.256\,nN$ and $-0.262\,eV \leq U_{min}^{gas} \leq -0.275\,eV$. Where the variation arises from the relative azimuthal orientation of the molecules.

8.1.3 *Comparison of Experimental and Computational Results*

Overall, there is good agreement between the experiments and simulations. **Figure 8.1** displays example $_e$NC-AFM force spectra from C_{60} *Tip Dataset 1* plotted alongside corresponding $_s$NC-AFM force spectra. The spectra have been been aligned along the Z axis to the force minimum of the $_s$NC-AFM force spectra. The simulated force minimum of $-3.06\,nN$ agrees exactly with the average experimental force minima atop a $C_{60,r}$ molecule of $-3.06\,nN$. This simulated value is also in close agreement with the average experimental force minima atop a $C_{60,u}$ molecule. With C_{60} *Tip Dataset 1* producing, $-0.303\,nN$, and the first mode of the bimodal distribution in C_{60} *Tip Dataset 2* producing $-0.298\,nN$. The second mode of C_{60} *Tip Dataset 2* has an larger average force minimum of $-0.342\,nN$, however this is still within ~15% of the computational force minimum.

Furthermore, the computational investigation suggests no difference in the force minima when comparing spectra taken atop the $C_{60,r}$ and $C_{60,u}$. This finding is supported by C_{60} *Tip Dataset 1*, and partially supported by C_{60} *Tip Dataset 2*. Overall however, further experimental data needs to be gathered using working equipment, in a less time constrained setting, to confirm the experimental data agrees with the simulations.

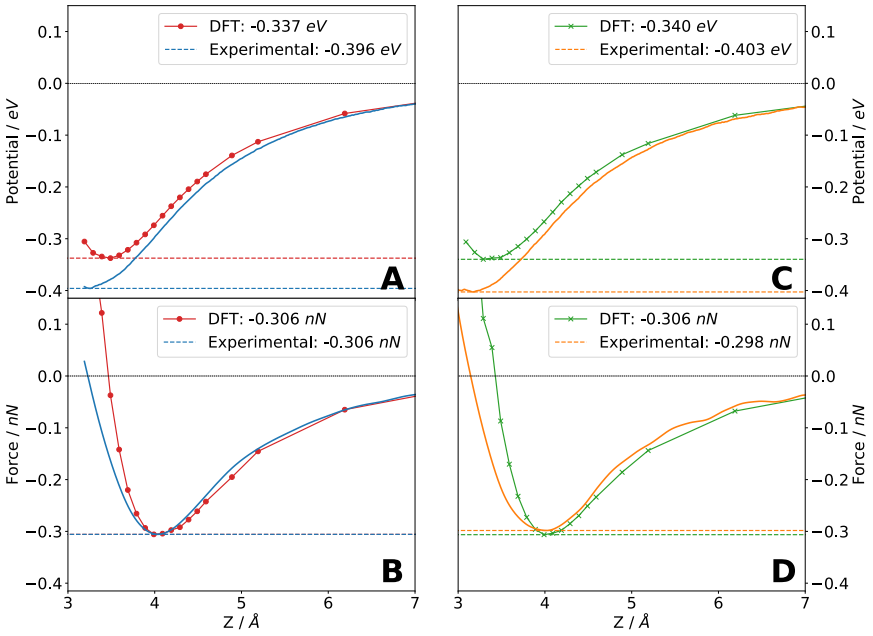

Figure 8.1: Example $_e$NC-AFM force spectra from C_{60} *Tip Dataset 1*, and corresponding $_s$NC-AFM force spectra. Red dots and green crosses correspond to off-curve subtracted, periodicity corrected, $_s$NC-AFM spectra for the $C_{60,r}$ and $C_{60,u}$ systems. Blue and orange lines correspond to off-curve subtracted On-Curve $_e$NC-AFM spectra taken atop adsorbed $C_{60,r}$ and $C_{60,u}$ molecules. **A&B:** Potential and force spectra for the $C_{60,r}$ system. **C&D:** Potential and force spectra for the $C_{60,u}$ system.

8.1.4 *Standing On the Shoulders of Giants*

Earlier DFT simulations of C_{60} on Cu(111) were carried out by Schull *et al* [34] in 2009 [1]. This work calculated a force minimum of $\sim -0.48\,nN$, which is significantly larger than the value of $-0.306\,nN$ calculated in this work. However, $\sim\frac{2}{3}$ of the force minimum was due to the vdW correction, which the authors suggest is prone to overestimating the interaction strength.

Further computational work (involving C_{60} molecules on the Cu(111) surface interacting with C_{60} Tips) was carried out by Hauptmann *et al* [37] [2]. The work reported force minima of approximately $-0.38\,nN$ to $-0.43\,nN$ [37], depending on the relative orientations of the tip and sample C_{60} molecules. These simulations were in agreement with themselves, but less attractive at the force minimum by $50\,pN$ to $100\,pN$ when compared to prior work by Schull *et al* [34]. Compared to the force minimum values reported in this work, the simulated values calculated by Hauptmann *et al* [37] are $-0.75\,nN$ to $-0.125\,nN$ more attractive than the calculated value of $-0.306\,nN$ from this work. Given the simulated force minimum between two interacting C_{60} molecules is largely dominated by the applied vdW correction, these differences are most likely a result of the different vdW corrections used. This explanation is backed up by the choice of vdW correction applied by Hauptmann *et al* [37], as the chosen vdW correction was the same as the one used by Schull *et al* [34], which Schull *et al* [34] suggested overestimates the vdW correction.

Hauptmann *et al* [35] also experimentally measured the force minimum between two interacting C_{60} molecules. Similar to the experiments and simulations in this work, the experiments were performed on the Cu(111) surface. The measured experimental force minimum of $-0.40\,nN$ by Hauptmann *et al* [35] is in agreement with the simulations [37]. However, the measured value of $-0.40\,nN$ is nearly $100\,pN$ more attractive than the value of $-0.306\,nN$ measured in this work. There are however explanations for such a discrepancy. In this work, an off-curve subtraction was performed. However, the force minimum value measured by Hauptmann *et al* [35] was calculated using a predicted Off-Curve, an approach which is less accurate than experimentally measuring the Off-Curve.

More contemporary experimental work involving C_{60} on the Cu(111) surface, published by by Jarvis *et al* [38], and Brand *et al* [4], is in closer agreement with the DFT calculated in this work. They reported

1 The calculations were performed with the SIESTA [137] pseudopotential DFT method and the generalized gradient approximation2 for xc. A vdW correction was estimated with a semi-empirical correction based on the London expression [129].

2 The calculations were performed with the DFT-FIREBALL [128] code using a local density approximation for the exchange and correlation potential. A vdW correction was estimated with a semi-empirical correction based on the London expression [129].

experimental force minima of $-0.34\,nN$, and $\sim -0.35\,nN$, respectively. These values are in close agreement with the second mode C_{60} *Tip Dataset 2* ($-0.342\,nN$), and within approximately $40\,pN$ to $50\,pN$ of the other computational and experimental force minimum values calculated in this work.

Experimental work involving C_{60} adsorbed on the Si(111) surface was carried out by Sweetman *et al* [36]. This work reported the experimental force minimum for C_{60}–C_{60} interactions to be $\sim 0.3\,nN$, and the experimental potential minimum was calculated to vary from $-0.220\,eV \leq U_{min}^{Si(111)-(4x4)} \leq -0.270\,meV$ ($-0.270\,meV$ at the centre), depending on the location atom the adsorbed C_{60} molecule. Furthermore, the Girifalco potential [138] minimum was calculated to be $\sim -0.275\,eV$, in close agreement with the measured experimental value. Later work by Sweetman *et al* [139] involving C_{60} molecules adsorbed on the Ag(111) surface reported a similar experimental C_{60}–C_{60} interaction of $\sim -0.3\,nN$. Further work was performed by Sweetman *et al* [139] involving C_{60} molecules on the Si(111) surface. The work experimentally measured the C_{60}–C_{60} interaction potential minimum to be approximately $-0.26\,eV$. Both the tip and surface molecules had an unknown orientation. In these experiments, the C_{60} molecules where adsorbed on the Si(111) surface, and picked up with a Si AFM tip. This work also extended to computationally calculate the potential minimum. It was found to be $\sim -0.27\,eV$ and $\sim -0.24\,eV$, for a pairwise Lennard Jones potential and DFT simulations respectively.

The experimental force minimum values of $\sim -0.3\,nN$, published by Sweetman *et al* [36][139], are in agreement with the experimental and computational values calculated in this work. It is worth noting the experimental force minimum for two interacting C_{60} molecules has now been measured to be approximately $-0.3\,nN$, for the Cu(111), Ag(111), and Si(111) surfaces. Furthermore, the computational potential minimum values for gaseous systems not involving the surface, were calculated by Sweetman *et al* [139] to be $-0.26\,eV$ and $-0.265\,eV$, using DFT and the Girifalco potential. These values are in agreement with the potential minimum of $-0.262\,eV \leq U_{min}^{gas} \leq -0.275\,eV$ calculated in **Chapter 7** of this work for two interacting gaseous C_{60} molecules, as expected.

However, the potential minimum for two interacting C_{60} molecules, experimentally measured by Sweetman *et al* [5][139], was measured to be $100\,meV$ less than was computationally calculated in this work. This is unexpected as the experimental force minimum, measured by Sweetman *et al* [36][139], were in agreement with the calculated computational (and experimental) force minima. However, the orientations of the two interacting C_{60} molecules were known.

8.2 METAL TIP

This section summarizes and compares the experimental and computational data from **Chapters 2 & 6** pertaining to force spectra taken over C_{60} molecules adsorbed on the Cu(111) surface, investigated in $_e$NC-AFM and $_s$NC-AFM with a *Cu* Tip.

8.2.1 *Experimental Results*

In **Chapter 2**, **Section 6.1**, force spectrum data taken atop C_{60} molecules adsorbed on the Cu(111) surface, gathered with *Cu* Tips, was presented. Hundreds of force spectra were taken, over C_{60} adsorbed on the unreconstructed Cu(111) surface ($C_{60,u}$), and C_{60} adsorbed on the 7 atom vacancy Cu(111) surface reconstruction ($C_{60,r}$).

The force spectra were broken down into two sets of data; *Cu Tip Dataset 1* and *Cu Tip Dataset 2*. For each dataset, the average force minima of the spectra taken over the $C_{60,u}$ and $C_{60,r}$ molecules was calculated separately. The following values calculated;

Cu Tip Dataset 1:

- $F_{min,r}^{Cu\ Tip\ 1} = -(1.72 \pm 0.17)\, nN$
- $F_{min,u}^{Cu\ Tip\ 1} = -(1.44 \pm 0.17)\, nN$

Cu Tip Dataset 2:

- $F_{min,r}^{Cu\ Tip\ 2} = -(1.39 \pm 0.17)\, nN$
- $F_{min,u}^{Cu\ Tip\ 2} = -(1.41 \pm 0.17)\, nN$

The $F_{min,u}^{Cu\ Tip\ 1}$, $F_{min,u}^{Cu\ Tip\ 2}$, and $F_{min,r}^{Cu\ Tip\ 2}$ values agree to within 56 pN (4 % of the force minimum), lying firmly within the 340 pN (1 sigma) overlap range of the 170 pN error bars calculated in **Section 2.4**. Including $F_{min,r}^{Cu\ Tip\ 1}$ makes the results less clear, however all four values ($F_{min,u}^{Cu\ Tip\ 1}$, $F_{min,r}^{Cu\ Tip\ 1}$, $F_{min,u}^{Cu\ Tip\ 2}$, and $F_{min,r}^{Cu\ Tip\ 2}$) still agree within 330 pN, which lies within the (1 sigma) overlap range of the 170 pN error bar. Therefore we can conclude the following; This difference is significant, however the experimental data offers no clear cause for the difference. Therefore, the two datasets are in disagreement;

1. Both *Cu Tip Dataset 1* **and** *Cu Tip Dataset 2* suggest there is not a statistically significant force difference induced by the surface reconstruction
2. The expected force minimum for a *Cu* Tip interacting with a $C_{60,r}$ is $F_{min,u}^{Cu\ Tip} \simeq -(1.43 \pm 0.17)\, nN$.

3. The force minimum for a Cu Tip interacting with a $C_{60,u}$ is expected to either lie in on of the following ranges; $F_{min,r}^{Cu\,Tip} = -(1.72 \pm 0.17)\,nN$, or $F_{min,r}^{Cu\,Tip} = -(1.41 \pm 0.17)\,nN$, with both these values being in agreement with each other after taking into account the 1 sigma overlap of the uncertainties.

In summary, the experimental data supports the idea the underlying surface reconstruction does not effect the force minimum, when measured with a Cu Tip.

8.2.2 *Computational Results*

Simulations of the experiments detailed in **Chapter 2** and **Section 6.1** were performed with DFT using FHI-aims. The system was periodic to simulate the $_s$Surface as an infinite Cu(111) surface, and C_{60} molecules were adsorbed onto Cu(111) surface as a mono-layer of either $C_{60,r}$ or $C_{60,u}$. The disadvantage of this approach was the $_s$Tip also needed to be compatible with a periodic system. However, unlike with the C_{60} Tip, a periodicity correction for the system was not needed. This was due to the strong chemical bonding between the $_s$Tip $_s$Surface dominating the $_s$NC-AFM spectra, making any periodicity correction insignificant.

Both the On-Curves and Off-Curves for the $C_{60,r}$ and $C_{60,u}$ systems were simulated. However, when the off-curve subtraction was performed, it was found to have an insignificant effect on the force minimum. This was because the $_s$NC-AFM spectra was dominated by the strong chemical bonding between the $_s$Tip $_s$Surface. Therefore, for simplicity, analysis of the $_s$NC-AFM spectra was performed without the off-curve subtraction.

$_s$NC-AFM force spectra were simulated at four sites atop both the $C_{60,r}$ and $C_{60,u}$ molecules; over a C atom, over a C-C bond, over a C=C bond, and over the centre of the adsorbed C_{60} molecule. The following results were obtained:

1. The force minimum is approximately $1.5\,nN$ for spectra taken over the over the C atom, over the C-C bond, and over the over the C=C bond.

2. The force minimum is approximately $0.75\,nN$ for spectra taken over the over the centre of the adsorbed C_{60} molecules.

3. There is no significant difference in the force minima, caused by the underlying surface, for spectra taken over the over a C atom, over a C-C bond, C_{60} molecule.

4. The force minimum over the $C_{60,r}$ molecule is $100\,pN$ more attractive at the C=C site. However, this difference is caused by the difference in mobility of two adsorption geometries, rather than a change in reactivity of the adsorbed C_{60} molecule induce by the charge transfer.

8.2.3 *Comparison of Experimental and Computational Results*

Overall, there is good agreement between the experiments and simulations. **Figure 8.1** displays example $_e$NC-AFM force spectra from *Cu Tip Dataset 1* aligned along the Z axis to the force minimum of the corresponding $_s$NC-AFM force spectra. As the site over which the spectra were taken had no detectable effect on the force minimum, the $_s$NC-AFM spectrum over the C atom site was selected and plotted. The rational being the following; The $_s$NC-AFM spectrum data suggests the system conforms to position a C atom underneath the Cu tip. As the $_e$Tip is often less well structured than the $_s$Tip, it is reasonable to assume the system is conforming during the $_e$NC-AFM force spectra to position a C atom underneath the Cu $_e$NTA. This line of thought also explains why the $_s$NC-AFM spectrum force minimum over the centre of the adsorbed C_{60} molecules is ~$0.75\,nN$, significantly less than the experimental force minimum; the $_s$Tip is likely much stiffer than the $_e$Tip, therefore in the experiment the $_e$Tip confirms to bond with a C atom, whereas in the $_s$Tip is unable to do so.

The $_s$NC-AFM data suggests the surface has minimal effect on the NC-AFM, with any effect arising from the difference in mobility of the adsorbed C_{60} molecule, rather than changes to the bonding between the tip and the sample induced by the charge transfer. The $_e$NC-AFM data neither strongly supports or disproves the $_s$NC-AFM data.

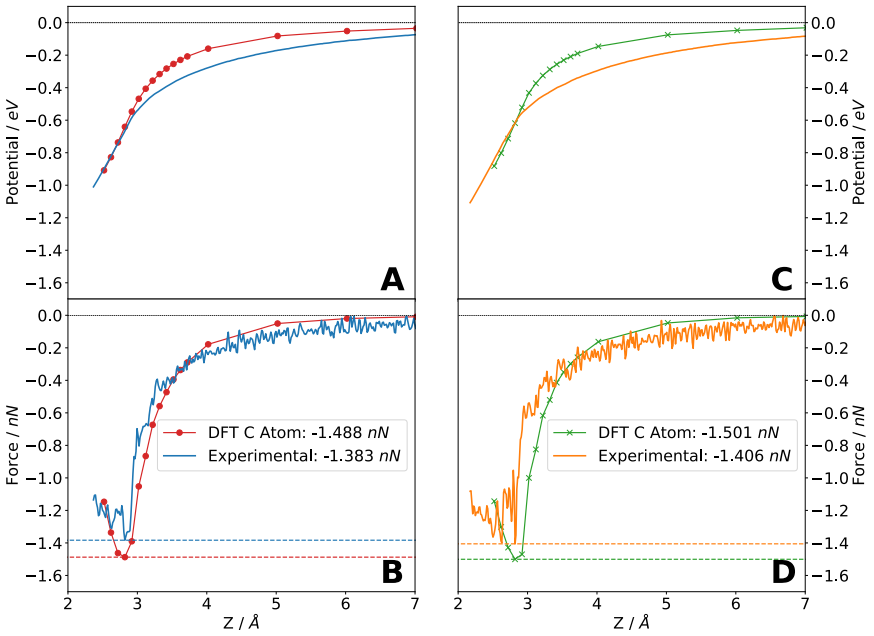

Figure 8.2: Example $_e$NC-AFM force spectra from *Cu Tip Dataset 2*, and corresponding $_s$NC-AFM force spectra. Red dots and green crosses correspond to $_s$NC-AFM spectra for the $C_{60,r}$ and $C_{60,u}$ systems. Blue and orange lines correspond to the off-curve subtracted On-Curve $_e$NC-AFMspectra, taken atop adsorbed $C_{60,r}$ and $C_{60,u}$ molecules. **A&B:** Potential and force spectra for the $C_{60,r}$ system. **C&D:** Potential and force spectra for the $C_{60,u}$ system.

Part IV

APPENDIX

A

APPENDIX

A.1 C_{60} TIP: FULL DATASETS

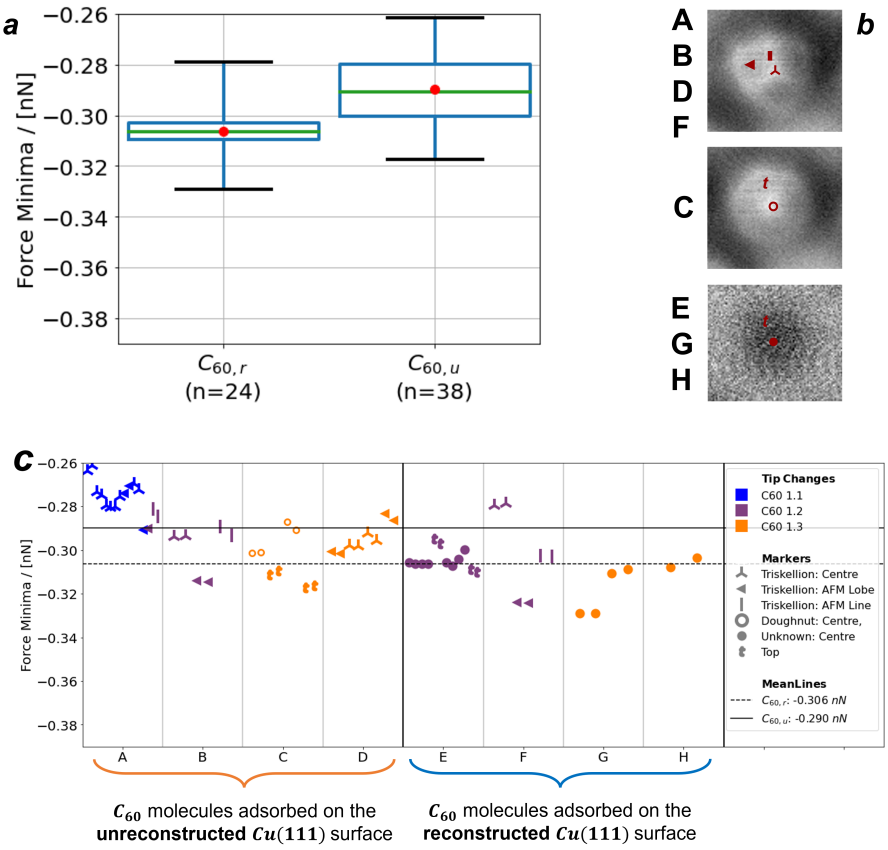

Figure A.1: Box and scatter plots **(*a* & *c*)** of the force minimum data, taken over $C_{60,r}$ and $C_{60,u}$ molecules, with C_{60} Tip 1. In ***a***, the green lines and reds dot correspond to the median and mean values of the spectra, where spectra taken over the $C_{60,r}$ and $C_{60,u}$ molecules have been plotted separately. In ***b***, sites where the spectra were taken have been pictorially defined. In ***c***, the colours correspond to tip changes, and the markers correspond to the site over which the spectrum was taken **(see *b*)**. The solid black and dashed black horizontal lines in ***c*** mark the average force minimum for the spectra taken over the $C_{60,u}$ and $C_{60,r}$ molecules. All the data taken with C_{60} Tip 1 has been plotted, and averaged over, in **Figure A.1**.

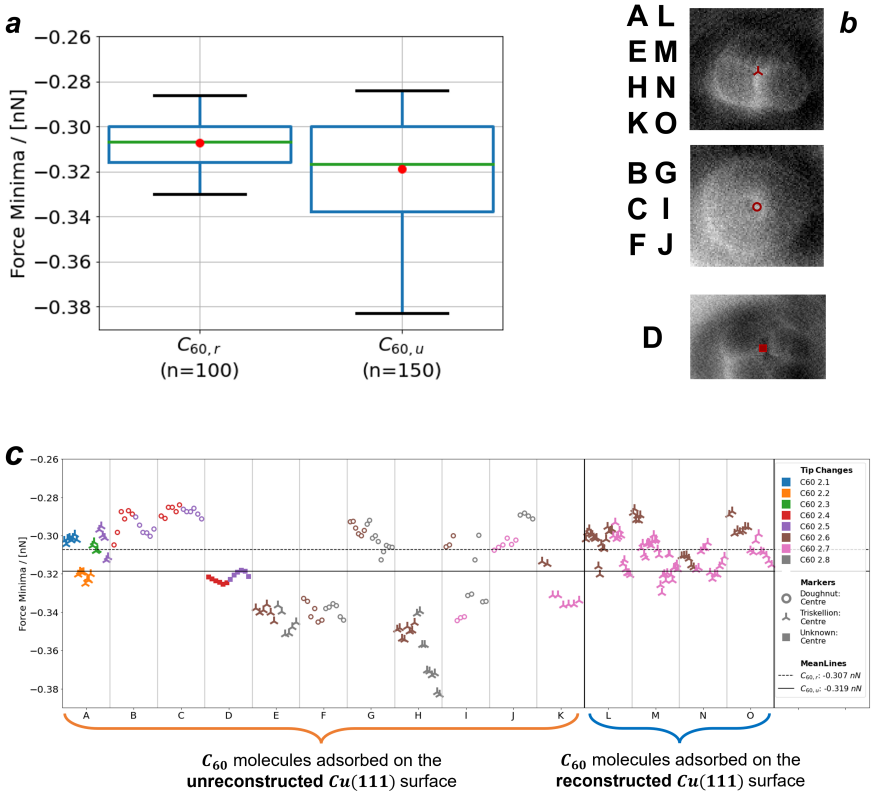

Figure A.2: Box and scatter plots **(*a* & *c*)** of the force minimum data, taken over $C_{60,r}$ and $C_{60,u}$ molecules, with C_{60} Tip 2. In ***a***, the green lines and reds dot correspond to the median and mean values of the spectra, where spectra taken over the $C_{60,r}$ and $C_{60,u}$ molecules have been plotted separately. In ***b***, sites where the spectra were taken have been pictorially defined. In ***c***, the colours correspond to tip changes, and the markers correspond to the site over which the spectrum was taken **(see *b*)**. The solid black and dashed black horizontal lines in ***c*** mark the average force minimum for the spectra taken over the $C_{60,u}$ and $C_{60,r}$ molecules. All the data taken with C_{60} Tip 2 has been plotted, and averaged over, in **Figure A.2**.

A.2 CU TIP: FULL DATASETS

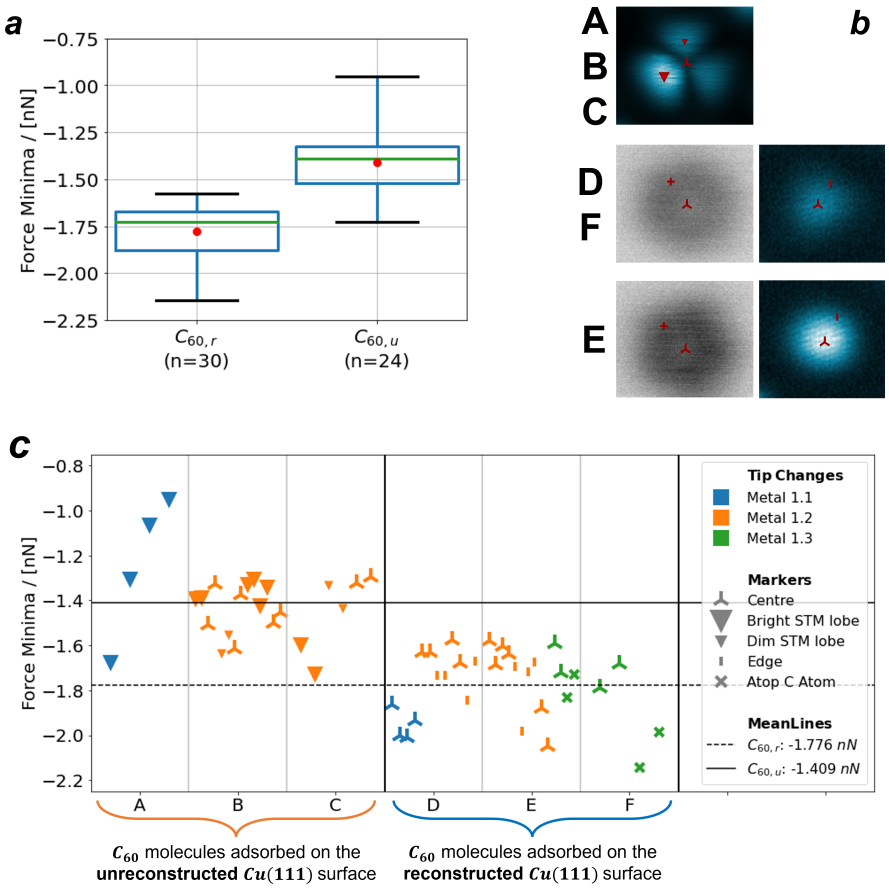

Figure A.3: Box and scatter plots **(*a* & *c*)** of the force minimum data, taken over $C_{60,r}$ and $C_{60,u}$ molecules, with Cu Tip 1. In ***a***, the green lines and reds dot correspond to the median and mean values of the spectra, where spectra taken over the $C_{60,r}$ and $C_{60,u}$ molecules have been plotted separately. In ***b***, sites where the spectra were taken have been pictorially defined. In ***c***, the colours correspond to tip changes, and the markers correspond to the site over which the spectrum was taken **(see *b*)**. The solid black and dashed black horizontal lines in ***c*** mark the average force minimum for the spectra taken over the $C_{60,u}$ and $C_{60,r}$ molecules. All the data taken with C_{60} Tip 1 has been plotted, and averaged over, in **Figure A.3**.

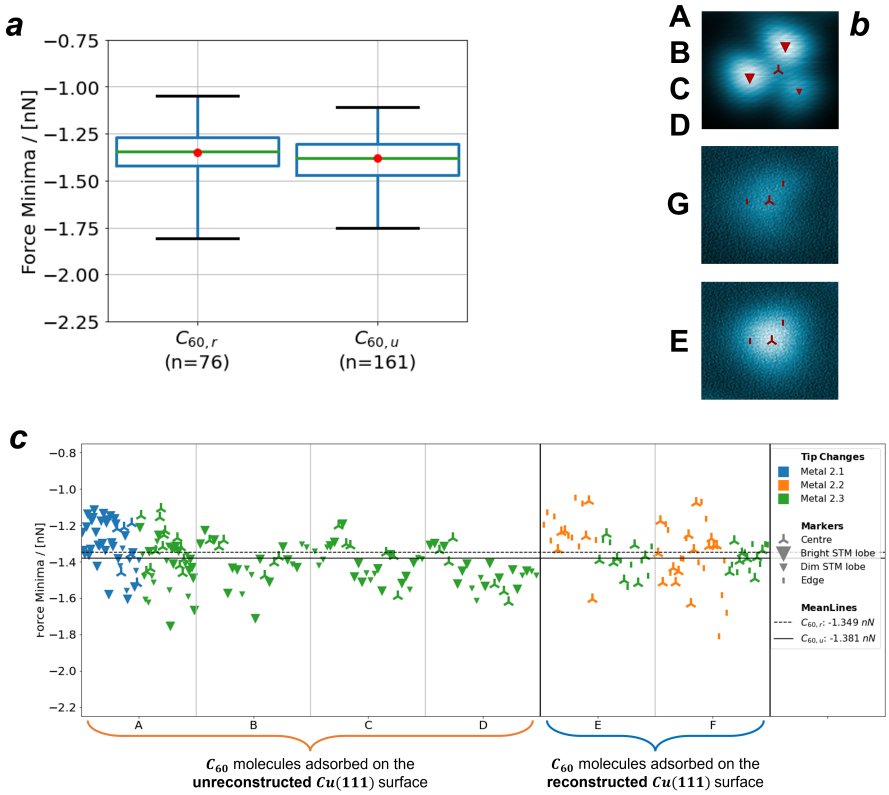

Figure A.4: Box and scatter plots **(*a* & *c*)** of the force minimum data, taken over $C_{60,r}$ and $C_{60,u}$ molecules, with C_{60} Tip 2. In ***a***, the green lines and reds dot correspond to the median and mean values of the spectra, where spectra taken over the $C_{60,r}$ and $C_{60,u}$ molecules have been plotted separately. In ***b***, sites where the spectra were taken have been pictorially defined. In ***c***, the colours correspond to tip changes, and the markers correspond to the site over which the spectrum was taken **(see *b*)**. The solid black and dashed black horizontal lines in ***c*** mark the average force minimum for the spectra taken over the $C_{60,u}$ and $C_{60,r}$ molecules. All the data taken with C_{60} Tip 2 has been plotted, and averaged over, in **Figure A.4**.

BIBLIOGRAPHY

[1] Leo Gross et al. "The Chemical Structure of a Molecule Resolved by Atomic Force Microscopy." In: *Science* 325.5944 (2009), pp. 1110–1114. ISSN: 0036-8075. DOI: 10.1126/science.1176210. eprint: http://science.sciencemag.org/content/325/5944/1110.full.pdf. URL: http://science.sciencemag.org/content/325/5944/1110.

[2] Woei Wu Pai et al. "Optimal Electron Doping of a C_{60} Monolayer on Cu(111) via Interface Reconstruction." In: *Phys. Rev. Lett.* 104 (3 Jan. 2010), p. 036103. DOI: 10.1103/PhysRevLett.104.036103. URL: https://link.aps.org/doi/10.1103/PhysRevLett.104.036103.

[3] Leonardo Forcieri et al. "Origin of C_{60} surface reconstruction resolved by atomic force microscopy." In: *Phys. Rev. B* 104 (20 Nov. 2021), p. 205428. DOI: 10.1103/PhysRevB.104.205428. URL: https://link.aps.org/doi/10.1103/PhysRevB.104.205428.

[4] Jonathan Brand et al. "Nonequilibrium Bond Forces in Single-Molecule Junctions." In: *Nano Letters* 0.0 (0). PMID: 31556298, null. DOI: 10.1021/acs.nanolett.9b02845. eprint: https://doi.org/10.1021/acs.nanolett.9b02845. URL: https://doi.org/10.1021/acs.nanolett.9b02845.

[5] Adam Sweetman et al. "Visualizing the orientational dependence of an intermolecular potential." In: *Nature Communications* 7.1 (Feb. 2016), p. 10621. ISSN: 2041-1723. DOI: 10.1038/ncomms10621. URL: https://doi.org/10.1038/ncomms10621.

[6] G. Binnig et al. "Tunneling through a controllable vacuum gap." In: *Applied Physics Letters* 40.2 (1982), pp. 178–180. DOI: 10.1063/1.92999. eprint: https://doi.org/10.1063/1.92999. URL: https://doi.org/10.1063/1.92999.

[7] G Binnig and H Rohrer. "Scanning Tunneling Microscopy." In: *IBM J. Res. Dev.* 30.4 (July 1986), pp. 355–369. ISSN: 0018-8646. URL: http://dl.acm.org/citation.cfm?id=10869.10870.

[8] G. Binnig et al. "7x7 Reconstruction on Si(111) Resolved in Real Space." In: *Phys. Rev. Lett.* 50 (2 Jan. 1983), pp. 120–123. DOI: 10.1103/PhysRevLett.50.120. URL: https://link.aps.org/doi/10.1103/PhysRevLett.50.120.

[9] Charles A Clifford and Martin P Seah. "Simplified drift characterization in scanning probe microscopes using a simple two-point method." In: *Measurement Science and Technology* 20.9 (July 2009), p. 095103. DOI: 10.1088/0957-0233/20/9/095103. URL: https://doi.org/10.1088%2F0957-0233%2F20%2F9%2F095103.

[10] J. Tersoff and D. R. Hamann. "Theory of the scanning tunneling microscope." In: *Phys. Rev. B* 31 (2 Jan. 1985), pp. 805–813. DOI: 10.1103/PhysRevB.31.805. URL: https://link.aps.org/doi/10.1103/PhysRevB.31.805.

[11] J. Bardeen. "Tunnelling from a Many-Particle Point of View." In: *Phys. Rev. Lett.* 6 (2 Jan. 1961), pp. 57–59. DOI: 10.1103/PhysRevLett.6.57. URL: https://link.aps.org/doi/10.1103/PhysRevLett.6.57.

[12] M. F. Crommie, C. P. Lutz, and D. M. Eigler. "Imaging standing waves in a two-dimensional electron gas." In: *Nature* 363.6429 (June 1993), pp. 524–527. ISSN: 1476-4687. DOI: 10.1038/363524a0. URL: https://doi.org/10.1038/363524a0.

[13] G. Binnig, C. F. Quate, and Ch. Gerber. "Atomic Force Microscope." In: *Phys. Rev. Lett.* 56 (9 Mar. 1986), pp. 930–933. DOI: 10.1103/PhysRevLett.56.930. URL: https://link.aps.org/doi/10.1103/PhysRevLett.56.930.

[14] Franz J. Giessibl. "Atomic Resolution of the Silicon (111)-(7x7) Surface by Atomic Force Microscopy." In: *Science* 267.5194 (1995), pp. 68–71. ISSN: 0036-8075. DOI: 10.1126/science.267.5194.68. eprint: https://science.sciencemag.org/content/267/5194/68.full.pdf. URL: https://science.sciencemag.org/content/267/5194/68.

[15] Adam Sweetman et al. "Intramolecular bonds resolved on a semiconductor surface." In: *Phys. Rev. B* 90 (16 Oct. 2014), p. 165425. DOI: 10.1103/PhysRevB.90.165425. URL: https://link.aps.org/doi/10.1103/PhysRevB.90.165425.

[16] Leo Gross et al. "Organic structure determination using atomic-resolution scanning probe microscopy." In: *Nature Chemistry* 2.10 (Oct. 2010), pp. 821–825. ISSN: 1755-4349. DOI: 10.1038/nchem.765. URL: https://doi.org/10.1038/nchem.765.

[17] Percy Zahl and Yunlong Zhang. "Guide for Atomic Force Microscopy Image Analysis To Discriminate Heteroatoms in Aromatic Molecules." In: *Energy & Fuels* 33.6 (2019), pp. 4775–4780. DOI: 10.1021/acs.energyfuels.9b00165. eprint: https://doi.org/10.1021/acs.energyfuels.9b00165. URL: https://doi.org/10.1021/acs.energyfuels.9b00165.

[18] Prokop Hapala et al. "Mapping the electrostatic force field of single molecules from high-resolution scanning probe images." In: *Nature Communications* 7.1 (May 2016), p. 11560. ISSN: 2041-1723. DOI: 10.1038/ncomms11560. URL: https://doi.org/10.1038/ncomms11560.

[19] Kota Iwata et al. "Chemical structure imaging of a single molecule by atomic force microscopy at room temperature." In: *Nature Communications* 6.1 (July 2015), p. 7766. ISSN: 2041-1723. DOI: 10.1038/ncomms8766. URL: https://doi.org/10.1038/ncomms8766.

[20] Shigeki Kawai et al. "Multiple heteroatom substitution to graphene nanoribbon." In: *Science Advances* 4.4 (2018), eaar7181. DOI: 10.1126/sciadv.aar7181. eprint: https://www.science.org/doi/pdf/10.1126/sciadv.aar7181. URL: https://www.science.org/doi/abs/10.1126/sciadv.aar7181.

[21] Tim Brown et al. "Intramolecular force mapping room temperature." In: *In submission* (2022).

[22] T. R. Albrecht et al. "Frequency modulation detection using high-Q cantilevers for enhanced force microscope sensitivity." In: *Journal of Applied Physics* 69.2 (1991), pp. 668–673. DOI: 10.1063/1.347347. eprint: https://doi.org/10.1063/1.347347. URL: https://doi.org/10.1063/1.347347.

[23] F. J. Giessibl. "A direct method to calculate tip–sample forces from frequency shifts in frequency-modulation atomic force microscopy." In: *Applied Physics Letters* 78.1 (2001), pp. 123–125. DOI: 10.1063/1.1335546. eprint: https://doi.org/10.1063/1.1335546. URL: https://doi.org/10.1063/1.1335546.

[24] H Ö Özer et al. "Low-amplitude, force gradient imaging of Cu(100) surface using tunnel current feedback." In: *Nanotechnology* 15.2 (Dec. 2003), S5–S8. DOI: 10.1088/0957-4484/15/2/002. URL: https://doi.org/10.1088/0957-4484/15/2/002.

[25] Daniel Martin-Jimenez et al. "Bond-Level Imaging of the 3D Conformation of Adsorbed Organic Molecules Using Atomic Force Microscopy with Simultaneous Tunneling Feedback." In: *Phys. Rev. Lett.* 122 (19 May 2019), p. 196101. DOI: 10.1103/PhysRevLett.122.196101. URL: https://link.aps.org/doi/10.1103/PhysRevLett.122.196101.

[26] A. Hinaut et al. "NC-AFM Study of the Adsorption of Hexamethoxytriphenylene on KBr(001)." In: *The Journal of Physical Chemistry C* 115.27 (2011), pp. 13338–13342. DOI: 10.1021/jp202873f. eprint: https://doi.org/10.1021/jp202873f. URL: https://doi.org/10.1021/jp202873f.

[27] Hal Edwards et al. "Fast, high-resolution atomic force microscopy using a quartz tuning fork as actuator and sensor." In: *Journal of Applied Physics* 82.3 (1997), pp. 980–984. DOI: 10.1063/1.365936. eprint: https://doi.org/10.1063/1.365936. URL: https://doi.org/10.1063/1.365936.

[28] Seizo Morita et al. *Noncontact Atomic Force Microscopy: Volume 3*. Springer, 2015.

[29] Hatem Labidi et al. "New fabrication technique for highly sensitive qPlus sensor with well-defined spring constant." In: *Ultramicroscopy* 158 (2015), pp. 33–37. ISSN: 0304-3991. DOI: https://doi.org/10.1016/j.ultramic.2015.06.008. URL: https://www.sciencedirect.com/science/article/pii/S0304399115001424.

[30] Jacob N Israelachvili. *Intermolecular and surface forces*. Academic press, 2011.

[31] Tadashi Shiota and Keiji Nakayama. "The Effect of an Electrostatic Force on Imaging a Surface Topography by Noncontact Atomic Force Microscope." In: *Japanese Journal of Applied Physics* 40.Part 2, No. 9A/B (Sept. 2001), pp. L986–L988. DOI: 10.1143/jjap.40.l986. URL: https://doi.org/10.1143/jjap.40.l986.

[32] M. Guggisberg et al. "Contrast inversion in nc-AFM on Si(111)7×7 due to short-range electrostatic interactions." In: *Applied Physics A* 72.1 (Mar. 2001), S19–S22. ISSN: 1432-0630. DOI: 10.1007/s003390100629. URL: https://doi.org/10.1007/s003390100629.

[33] Michael Ellner et al. "The Electric Field of CO Tips and Its Relevance for Atomic Force Microscopy." In: *Nano Letters* 16.3 (2016). PMID: 26840626, pp. 1974–1980. DOI: 10.1021/acs.nanolett.5b05251. eprint: https://doi.org/10.1021/acs.nanolett.5b05251. URL: https://doi.org/10.1021/acs.nanolett.5b05251.

[34] Guillaume Schull et al. "Passing Current through Touching Molecules." In: *Phys. Rev. Lett.* 103 (20 Nov. 2009), p. 206803. DOI: 10.1103/PhysRevLett.103.206803. URL: https://link.aps.org/doi/10.1103/PhysRevLett.103.206803.

[35] Nadine Hauptmann et al. "Force and conductance during contact formation to a C60 molecule." In: *New Journal of Physics* 14.7 (July 2012), p. 073032. DOI: 10.1088/1367-2630/14/7/073032. URL: https://doi.org/10.1088/1367-2630/14/7/073032.

[36] C. Chiutu et al. "Precise Orientation of a Single C_{60} Molecule on the Tip of a Scanning Probe Microscope." In: *Phys. Rev. Lett.* 108 (26 June 2012), p. 268302. DOI: 10.1103/PhysRevLett.108.268302. URL: https://link.aps.org/doi/10.1103/PhysRevLett.108.268302.

[37] Nadine Hauptmann et al. "Interactions between two C60 molecules measured by scanning probe microscopies." In: *Nanotechnology* 26.44 (Oct. 2015), p. 445703. DOI: 10.1088/0957-4484/26/44/445703. URL: https://doi.org/10.1088%2F0957-4484%2F26%2F44%2F445703.

[38] Samuel Paul Jarvis et al. "Intermolecular artifacts in probe microscope images of C_{60} assemblies." In: *Phys. Rev. B* 92 (24 Dec. 2015), p. 241405. DOI: 10.1103/PhysRevB.92.241405. URL: https://link.aps.org/doi/10.1103/PhysRevB.92.241405.

[39] Franz J. Giessibl. "Forces and frequency shifts in atomic-resolution dynamic-force microscopy." In: *Phys. Rev. B* 56 (24 Dec. 1997), pp. 16010–16015. DOI: 10.1103/PhysRevB.56.16010. URL: https://link.aps.org/doi/10.1103/PhysRevB.56.16010.

[40] John E. Sader and Suzanne P. Jarvis. "Accurate formulas for interaction force and energy in frequency modulation force spectroscopy." In: *Applied Physics Letters* 84.10 (2004), pp. 1801–1803. DOI: 10.1063/1.1667267. eprint: https://doi.org/10.1063/1.1667267. URL: https://doi.org/10.1063/1.1667267.

[41] John E. Sader and Suzanne P. Jarvis. "Interpretation of frequency modulation atomic force microscopy in terms of fractional calculus." In: *Phys. Rev. B* 70 (1 July 2004), p. 012303. DOI: 10.1103/PhysRevB.70.012303. URL: https://link.aps.org/doi/10.1103/PhysRevB.70.012303.

[42] S. H. Ke, T. Uda, and K. Terakura. "Quantity measured in frequency-shift-mode atomic-force microscopy: An analysis with a numerical model." In: *Phys. Rev. B* 59 (20 May 1999), pp. 13267–13272. DOI: 10.1103/PhysRevB.59.13267. URL: https://link.aps.org/doi/10.1103/PhysRevB.59.13267.

[43] U. Dürig. "Relations between interaction force and frequency shift in large-amplitude dynamic force microscopy." In: *Applied Physics Letters* 75.3 (1999), pp. 433–435. DOI: 10.1063/1.124399. eprint: https://doi.org/10.1063/1.124399. URL: https://doi.org/10.1063/1.124399.

[44] Stefan Kuhn et al. "Identifying the absolute orientation of a low-symmetry surface in real space." In: *Phys. Rev. B* 90 (19 Nov. 2014), p. 195405. DOI: 10.1103/PhysRevB.90.195405. URL: https://link.aps.org/doi/10.1103/PhysRevB.90.195405.

[45] Andrew Stannard and Adam Sweetman. "A Considered Approach to Force Extraction from Dynamic Force Microscopy Measurements." In: Jan. 2015, pp. 63–79. ISBN: 978-3-319-17400-6. DOI: 10.1007/978-3-319-17401-3_4.

[46] John E. Sader et al. "Interatomic force laws that evade dynamic measurement." In: *Nature Nanotechnology* 13.12 (Dec. 2018), pp. 1088–1091. ISSN: 1748-3395. DOI: 10.1038/s41565-018-0277-x. URL: https://doi.org/10.1038/s41565-018-0277-x.

[47] Ferdinand Huber and Franz J. Giessibl. "Experimental use of the inflection point test for force deconvolution in frequency-modulation atomic force microscopy to turn an ill-posed situation into a well-posed one by proper choice of amplitude." In:

Journal of Applied Physics 127.18 (2020), p. 184301. DOI: 10.1063/5.0003291. eprint: https://doi.org/10.1063/5.0003291. URL: https://doi.org/10.1063/5.0003291.

[48] Yoshiaki Sugimoto et al. "Simultaneous AFM and STM measurements on the Si(111)-(7x7) surface." In: *Phys. Rev. B* 81 (24 June 2010), p. 245322. DOI: 10.1103/PhysRevB.81.245322. URL: https://link.aps.org/doi/10.1103/PhysRevB.81.245322.

[49] John E. Sader and Yoshiaki Sugimoto. "Accurate formula for conversion of tunneling current in dynamic atomic force spectroscopy." In: *Applied Physics Letters* 97.4 (2010), p. 043502. DOI: 10.1063/1.3464165. eprint: https://doi.org/10.1063/1.3464165. URL: https://doi.org/10.1063/1.3464165.

[50] Jarvis Samuel. "The effect of tip structure in atomic manipulation: a combined DFT and AFM study." Thesis. 2013.

[51] Mircea Fotino. "Tip sharpening by normal and reverse electrochemical etching." In: *Review of Scientific Instruments* 64.1 (1993), pp. 159–167. DOI: 10.1063/1.1144419. eprint: https://doi.org/10.1063/1.1144419. URL: https://doi.org/10.1063/1.1144419.

[52] Inger Ekvall et al. "Preparation and characterization of electrochemically etched W tips for STM." In: *Measurement Science and Technology* 10.1 (1999), p. 11. URL: http://stacks.iop.org/0957-0233/10/i=1/a=006.

[53] D. K. Biegelsen, F. A. Ponce, and J. C. Tramontana. "Simple ion milling preparation of (111) tungsten tips." In: *Applied Physics Letters* 54.13 (1989), pp. 1223–1225. DOI: 10.1063/1.100722. eprint: https://doi.org/10.1063/1.100722. URL: https://doi.org/10.1063/1.100722.

[54] G. N. Phillips et al. "High resolution magnetic force microscopy using focused ion beam modified tips." In: *Applied Physics Letters* 81.5 (2002), pp. 865–867. DOI: 10.1063/1.1497434. eprint: https://doi.org/10.1063/1.1497434. URL: https://doi.org/10.1063/1.1497434.

[55] Moh'd Rezeq, Jason Pitters, and Robert Wolkow. "Tungsten nanotip fabrication by spatially controlled field-assisted reaction with nitrogen." In: *The Journal of Chemical Physics* 124.20 (2006), p. 204716. DOI: 10.1063/1.2198536. eprint: https://doi.org/10.1063/1.2198536. URL: https://doi.org/10.1063/1.2198536.

[56] A. Tamai et al. "Electronic structure at the C_{60}/metal interface: An angle-resolved photoemission and first-principles study." In: *Phys. Rev. B* 77 (7 Feb. 2008), p. 075134. DOI: 10.1103/PhysRevB.77.075134. URL: https://link.aps.org/doi/10.1103/PhysRevB.77.075134.

[57] Atsushi Ogawa et al. "Orbital Interactions between a C60 Molecule and Cu(111) Surface." In: *The Journal of Physical Chemistry B* 107.46 (2003), pp. 12672–12679. DOI: 10.1021/jp0303220. eprint: https://doi.org/10.1021/jp0303220. URL: https://doi.org/10.1021/jp0303220.

[58] Lin-Lin Wang and Hai-Ping Cheng. "Rotation, translation, charge transfer, and electronic structure of C_{60} on Cu(111) surface." In: *Phys. Rev. B* 69 (4 Jan. 2004), p. 045404. DOI: 10.1103/PhysRevB.69.045404. URL: https://link.aps.org/doi/10.1103/PhysRevB.69.045404.

[59] Cornelius Lanczos. *Applied analysis*. Courier Corporation, 1988.

[60] Carl de Boor. *A Practical Guide to Spline*. Vol. Volume 27. Jan. 1978. DOI: 10.2307/2006241.

[61] Richard M. Martin. *Electronic Structure: Basic Theory and Practical Methods*. Cambridge University Press, 2004. DOI: 10.1017/CBO9780511805769.

[62] Frank Jensen. *Introduction to computational chemistry*. Third edition. "John Wiley & Sons", 2017. ISBN: 1-118-82599-3.

[63] David Egger. "Exploring the interactions at metal-organic interfaces with density-functional theory." Thesis. 2013.

[64] Reinhard Johann Maurer. "First-Principles Description of the Isomerization Dynamics of Surface-Adsorbed Molecular Switches." Thesis. 2014.

[65] Shashank Shekhar Harivyasi. "Employing ab-initio methods to study distinct scenarios of adsorption of organic molecules on inorganic surfaces." Thesis. 2018.

[66] Volker Blum et al. "Ab initio molecular simulations with numeric atom-centered orbitals." In: *Computer Physics Communications* 180.11 (2009), pp. 2175–2196. ISSN: 0010-4655. DOI: https://doi.org/10.1016/j.cpc.2009.06.022. URL: https://www.sciencedirect.com/science/article/pii/S0010465509002033.

[67] Kieron Burke and Lucas O. Wagner. "DFT in a nutshell." In: *International Journal of Quantum Chemistry* 113.2 (2013), pp. 96–101. DOI: https://doi.org/10.1002/qua.24259. eprint: https://onlinelibrary.wiley.com/doi/pdf/10.1002/qua.24259. URL: https://onlinelibrary.wiley.com/doi/abs/10.1002/qua.24259.

[68] Pierpaolo Morgante and Roberto Peverati. "The devil in the details: A tutorial review on some undervalued aspects of density functional theory calculations." In: *International Journal of Quantum Chemistry* 120.18 (2020), e26332. DOI: https://doi.org/10.1002/qua.26332. eprint: https://onlinelibrary.

wiley.com/doi/pdf/10.1002/qua.26332. URL: https://onlinelibrary.wiley.com/doi/abs/10.1002/qua.26332.

[69] Stefan Grimme et al. "Dispersion-Corrected Mean-Field Electronic Structure Methods." In: *Chemical Reviews* 116.9 (2016). PMID: 27077966, pp. 5105–5154. DOI: 10.1021/acs.chemrev.5b00533. eprint: https://doi.org/10.1021/acs.chemrev.5b00533. URL: https://doi.org/10.1021/acs.chemrev.5b00533.

[70] M. Born and R. Oppenheimer. "Zur Quantentheorie der Molekeln." In: *Annalen der Physik* 389.20 (1927), pp. 457–484. DOI: https://doi.org/10.1002/andp.19273892002. eprint: https://onlinelibrary.wiley.com/doi/pdf/10.1002/andp.19273892002. URL: https://onlinelibrary.wiley.com/doi/abs/10.1002/andp.19273892002.

[71] P. Hohenberg and W. Kohn. "Inhomogeneous Electron Gas." In: *Phys. Rev.* 136 (3B Nov. 1964), B864–B871. DOI: 10.1103/PhysRev.136.B864. URL: https://link.aps.org/doi/10.1103/PhysRev.136.B864.

[72] L. H. Thomas. "The calculation of atomic fields." In: *Mathematical Proceedings of the Cambridge Philosophical Society* 23.5 (1927), pp. 542–548. DOI: 10.1017/S0305004100011683.

[73] Enrico Fermi. "Statistical method to determine some properties of atoms." In: *Rend. Accad. Naz. Lincei* 6.602-607 (1927), p. 5.

[74] P. A. M. Dirac. "Note on Exchange Phenomena in the Thomas Atom." In: *Mathematical Proceedings of the Cambridge Philosophical Society* 26.3 (1930), pp. 376–385. DOI: 10.1017/S0305004100016108.

[75] W. Kohn and L. J. Sham. "Self-Consistent Equations Including Exchange and Correlation Effects." In: *Phys. Rev.* 140 (4A Nov. 1965), A1133–A1138. DOI: 10.1103/PhysRev.140.A1133. URL: https://link.aps.org/doi/10.1103/PhysRev.140.A1133.

[76] *Chemistry Program, Department of Biomedical and Chemical Engineering and Science at the Florida Institute of Technology*. URL: https://www.fit.edu/engineering-and-science/academics-and-learning/biomedical-and-chemical-engineering-and-sciences/faculty/.

[77] Wei Liu, Alexandre Tkatchenko, and Matthias Scheffler. "Modeling Adsorption and Reactions of Organic Molecules at Metal Surfaces." In: *Accounts of Chemical Research* 47.11 (2014). PMID: 24915492, pp. 3369–3377. DOI: 10.1021/ar500118y. eprint: https://doi.org/10.1021/ar500118y. URL: https://doi.org/10.1021/ar500118y.

[78] Oliver T Hofmann et al. "Interface dipoles of organic molecules on Ag(111) in hybrid density-functional theory." In: *New Journal of Physics* 15.12 (Dec. 2013), p. 123028. DOI: 10.1088/1367-2630/15/12/123028. URL: https://doi.org/10.1088/1367-2630/15/12/123028.

[79] Alexandre Tkatchenko and Matthias Scheffler. "Accurate Molecular Van Der Waals Interactions from Ground-State Electron Density and Free-Atom Reference Data." In: *Phys. Rev. Lett.* 102 (7 Feb. 2009), p. 073005. DOI: 10.1103/PhysRevLett.102.073005. URL: https://link.aps.org/doi/10.1103/PhysRevLett.102.073005.

[80] Victor G. Ruiz et al. "Density-Functional Theory with Screened van der Waals Interactions for the Modeling of Hybrid Inorganic-Organic Systems." In: *Phys. Rev. Lett.* 108 (14 Apr. 2012), p. 146103. DOI: 10.1103/PhysRevLett.108.146103. URL: https://link.aps.org/doi/10.1103/PhysRevLett.108.146103.

[81] Victor G. Ruiz, Wei Liu, and Alexandre Tkatchenko. "Density-functional theory with screened van der Waals interactions applied to atomic and molecular adsorbates on close-packed and non-close-packed surfaces." In: *Phys. Rev. B* 93 (3 Jan. 2016), p. 035118. DOI: 10.1103/PhysRevB.93.035118. URL: https://link.aps.org/doi/10.1103/PhysRevB.93.035118.

[82] Alexandre Tkatchenko et al. "Accurate and Efficient Method for Many-Body van der Waals Interactions." In: *Phys. Rev. Lett.* 108 (23 June 2012), p. 236402. DOI: 10.1103/PhysRevLett.108.236402. URL: https://link.aps.org/doi/10.1103/PhysRevLett.108.236402.

[83] Stefan Grimme et al. "A consistent and accurate ab initio parametrization of density functional dispersion correction (DFT-D) for the 94 elements H-Pu." In: *The Journal of Chemical Physics* 132.15 (2010), p. 154104. DOI: 10.1063/1.3382344. eprint: https://doi.org/10.1063/1.3382344. URL: https://doi.org/10.1063/1.3382344.

[84] *Fritz Haber Institute ab initio molecular simulations: FHI-aims 210716_1*. Manual. July 2021. URL: https://aimsclub.fhi-berlin.mpg.de/club_downloads.php.

[85] A Marek et al. "The ELPA library: scalable parallel eigenvalue solutions for electronic structure theory and computational science." In: *Journal of Physics: Condensed Matter* 26.21 (May 2014), p. 213201. DOI: 10.1088/0953-8984/26/21/213201. URL: https://doi.org/10.1088/0953-8984/26/21/213201.

[86] *Fritz Haber Institute ab initio molecular simulations: FHI-aims 200112_2*. Manual. Apr. 2020. URL: https://aimsclub.fhi-berlin.mpg.de/club_downloads.php.

[87] *Fritz Haber Institute ab initio molecular simulations: FHI-aims 210226*. Manual. Mar. 2021. URL: https://aimsclub.fhi-berlin.mpg.de/club_downloads.php.

[88] Peter Kratzer and Jörg Neugebauer. "The Basics of Electronic Structure Theory for Periodic Systems." In: *Frontiers in Chemistry* 7 (2019), p. 106. ISSN: 2296-2646. DOI: 10.3389/fchem.2019.00106. URL: https://www.frontiersin.org/article/10.3389/fchem.2019.00106.

[89] *Arc4 HPC, University Of Leeds*. URL: https://arcdocs.leeds.ac.uk/systems/arc4.html.

[90] Kumi Motai et al. "C60Grown on the Cu(111)1×1 Surface." In: *Japanese Journal of Applied Physics* 32.Part 2, No. 3B (Mar. 1993), pp. L450–L453. DOI: 10.1143/jjap.32.l450. URL: https://doi.org/10.1143/jjap.32.l450.

[91] A. J. Maxwell et al. "C_{60} on Al(111): Covalent bonding and surface reconstruction." In: *Phys. Rev. B* 52 (8 Aug. 1995), R5546–R5549. DOI: 10.1103/PhysRevB.52.R5546. URL: https://link.aps.org/doi/10.1103/PhysRevB.52.R5546.

[92] Roberto Macovez et al. "Electronic surface reconstruction and correlation in the fcc and dimer phases of RbC_{60}." In: *Phys. Rev. B* 75 (19 May 2007), p. 195424. DOI: 10.1103/PhysRevB.75.195424. URL: https://link.aps.org/doi/10.1103/PhysRevB.75.195424.

[93] H. I. Li et al. "Surface Geometry of $\mathbf{C}_{60}$ on Ag(111)." In: *Phys. Rev. Lett.* 103 (5 July 2009), p. 056101. DOI: 10.1103/PhysRevLett.103.056101. URL: https://link.aps.org/doi/10.1103/PhysRevLett.103.056101.

[94] Bailey C. Hsu et al. "Tailoring thermopower of single-molecular junctions by temperature-induced surface reconstruction." In: *Applied Physics Letters* 101.24 (2012), p. 243103. DOI: 10.1063/1.4769814. eprint: https://doi.org/10.1063/1.4769814. URL: https://doi.org/10.1063/1.4769814.

[95] Qian Wang, Rui Pang, and Xingqiang Shi. "Molecular Precursor Induced Surface Reconstruction at Graphene/Pt(111) Interfaces." In: *The Journal of Physical Chemistry C* 119.39 (2015), pp. 22534–22541. DOI: 10.1021/acs.jpcc.5b06842. eprint: https://doi.org/10.1021/acs.jpcc.5b06842. URL: https://doi.org/10.1021/acs.jpcc.5b06842.

[96] J. Andreas Larsson et al. "Orientation of individual C_{60} molecules adsorbed on Cu(111): Low-temperature scanning tunneling microscopy and density functional calculations." In: *Phys. Rev. B* 77 (11 Mar. 2008), p. 115434. DOI: 10.1103/PhysRevB.77.115434. URL: https://link.aps.org/doi/10.1103/PhysRevB.77.115434.

[97] Alexander Stukowski. "Visualization and analysis of atomistic simulation data with OVITO-the Open Visualization Tool." In: *MODELLING AND SIMULATION IN MATERIALS SCIENCE AND ENGINEERING* 18.1 (JAN 2010). ISSN: 0965-0393. DOI: {10.1088/0965-0393/18/1/015012}.

[98] R. S. Mulliken. "Electronic Population Analysis on LCAO–MO Molecular Wave Functions. II. Overlap Populations, Bond Orders, and Covalent Bond Energies." In: *The Journal of Chemical Physics* 23.10 (1955), pp. 1841–1846. DOI: 10.1063/1.1740589. eprint: https://doi.org/10.1063/1.1740589. URL: https://doi.org/10.1063/1.1740589.

[99] Richard FW Bader. "A quantum theory of molecular structure and its applications." In: *Chemical Reviews* 91.5 (1991), pp. 893–928.

[100] *Bader Charge Analysis*. URL: http://theory.cm.utexas.edu/henkelman/research/bader/.

[101] Graeme Henkelman, Andri Arnaldsson, and Hannes Jónsson. "A fast and robust algorithm for Bader decomposition of charge density." In: *Computational Materials Science* 36.3 (2006), pp. 354–360. ISSN: 0927-0256. DOI: https://doi.org/10.1016/j.commatsci.2005.04.010. URL: https://www.sciencedirect.com/science/article/pii/S0927025605001849.

[102] Edward Sanville et al. "Improved grid-based algorithm for Bader charge allocation." In: *Journal of Computational Chemistry* 28.5 (2007), pp. 899–908. DOI: https://doi.org/10.1002/jcc.20575. eprint: https://onlinelibrary.wiley.com/doi/pdf/10.1002/jcc.20575. URL: https://onlinelibrary.wiley.com/doi/abs/10.1002/jcc.20575.

[103] W Tang, E Sanville, and G Henkelman. "A grid-based Bader analysis algorithm without lattice bias." In: *Journal of Physics: Condensed Matter* 21.8 (Jan. 2009), p. 084204. DOI: 10.1088/0953-8984/21/8/084204. URL: https://doi.org/10.1088/0953-8984/21/8/084204.

[104] Soumen Saha, Ram Kinkar Roy, and Paul W. Ayers. "Are the Hirshfeld and Mulliken population analysis schemes consistent with chemical intuition?" In: *International Journal of Quantum Chemistry* 109.9 (2009), pp. 1790–1806. DOI: https://doi.org/10.1002/qua.21901. eprint: https://onlinelibrary.wiley.com/doi/pdf/10.1002/qua.21901. URL: https://onlinelibrary.wiley.com/doi/abs/10.1002/qua.21901.

[105] L Romaner et al. "Theoretical study of PTCDA adsorbed on the coinage metal surfaces, Ag(111), Au(111) and Cu(111)." In: *New Journal of Physics* 11.5 (May 2009), p. 053010. DOI: 10.1088/1367-

2630/11/5/053010. URL: https://doi.org/10.1088/1367-2630/11/5/053010.

[106] Navaratnarajah Kuganathan, Ratnasothy Srikaran, and Alexander Chroneos. "Stability of Coinage Metals Interacting with C60." In: *Nanomaterials* 9.10 (2019). ISSN: 2079-4991. DOI: 10.3390/nano9101484. URL: https://www.mdpi.com/2079-4991/9/10/1484.

[107] Ku-Ding Tsuei et al. "Photoemission and photoabsorption study of C_{60} adsorption on Cu(111) surfaces." In: *Phys. Rev. B* 56 (23 Dec. 1997), pp. 15412–15420. DOI: 10.1103/PhysRevB.56.15412. URL: https://link.aps.org/doi/10.1103/PhysRevB.56.15412.

[108] C. T. Chen et al. "Electronic states and phases of KxC60 from photoemission and X-ray absorption spectroscopy." In: *Nature* 352.6336 (Aug. 1991), pp. 603–605. ISSN: 1476-4687. DOI: 10.1038/352603a0. URL: https://doi.org/10.1038/352603a0.

[109] M. Svec et al. "van der Waals interactions mediating the cohesion of fullerenes on graphene." In: *Phys. Rev. B* 86 (12 Sept. 2012), p. 121407. DOI: 10.1103/PhysRevB.86.121407. URL: https://link.aps.org/doi/10.1103/PhysRevB.86.121407.

[110] Emilio M. Perez and Nazario Martin. "pi pi interactions in carbon nanostructures." In: *Chem. Soc. Rev.* 44 (18 2015), pp. 6425–6433. DOI: 10.1039/C5CS00578G. URL: http://dx.doi.org/10.1039/C5CS00578G.

[111] T. Hashizume et al. "Intramolecular structures of C60 adsorbed on the Cu(111)1×1 surface studied by the field ion-scanning tunneling microscopy." In: *Journal of Vacuum Science & Technology A* 12.4 (1994), pp. 2097–2100. DOI: 10.1116/1.579143. eprint: https://doi.org/10.1116/1.579143. URL: https://doi.org/10.1116/1.579143.

[112] A. Fartash. "Interfacially ordered C60 films on Cu(111) substrates." In: *Journal of Applied Physics* 79.2 (1996), pp. 742–747. DOI: 10.1063/1.360820. eprint: https://aip.scitation.org/doi/pdf/10.1063/1.360820. URL: https://aip.scitation.org/doi/abs/10.1063/1.360820.

[113] Woei Wu Pai et al. "Structural relaxation of adlayers in the presence of adsorbate-induced reconstruction: C_{60}/Cu(111)." In: *Phys. Rev. B* 69 (12 Mar. 2004), p. 125405. DOI: 10.1103/PhysRevB.69.125405. URL: https://link.aps.org/doi/10.1103/PhysRevB.69.125405.

[114] Nicolas Néel et al. "Conductance of Oriented C60 Molecules." In: *Nano Letters* 8.5 (2008). PMID: 18386913, pp. 1291–1295. DOI: 10.1021/nl073074i. eprint: https://doi.org/10.1021/nl073074i. URL: https://doi.org/10.1021/nl073074i.

[115] Hongxiang Xu et al. "Construction of a Molecular Switch Based on Two Metastable States of Fullerene on Cu(111)." In: *The Journal of Physical Chemistry C* 124.20 (2020), pp. 11158–11164. DOI: 10.1021/acs.jpcc.0c01189. eprint: https://doi.org/10.1021/acs.jpcc.0c01189. URL: https://doi.org/10.1021/acs.jpcc.0c01189.

[116] Leaf Jeremy. "A Study of C60 via Scanning Probe Microscopy, Hückel, and Monte Carlo Methods." Thesis. 2017.

[117] Simon Taylor. "Probing the electronic and geometric structure of adsorbed porphyrins and fullerenes." eng. Thesis. 2016.

[118] Zhixiang Sun et al. "Quantitative Atomic Force Microscopy with Carbon Monoxide Terminated Tips." In: *Phys. Rev. Lett.* 106 (4 Jan. 2011), p. 046104. DOI: 10.1103/PhysRevLett.106.046104. URL: https://link.aps.org/doi/10.1103/PhysRevLett.106.046104.

[119] Markus Ternes et al. "Interplay of Conductance, Force, and Structural Change in Metallic Point Contacts." In: *Phys. Rev. Lett.* 106 (1 Jan. 2011), p. 016802. DOI: 10.1103/PhysRevLett.106.016802. URL: https://link.aps.org/doi/10.1103/PhysRevLett.106.016802.

[120] Martin Ondraifmmode checkcelse vcfiek et al. "Forces and Currents in Carbon Nanostructures: Are We Imaging Atoms?" In: *Phys. Rev. Lett.* 106 (17 Apr. 2011), p. 176101. DOI: 10.1103/PhysRevLett.106.176101. URL: https://link.aps.org/doi/10.1103/PhysRevLett.106.176101.

[121] Joachim Welker and Franz J. Giessibl. "Revealing the Angular Symmetry of Chemical Bonds by Atomic Force Microscopy." In: *Science* 336.6080 (2012), pp. 444–449. DOI: 10.1126/science.1219850. eprint: https://www.science.org/doi/pdf/10.1126/science.1219850. URL: https://www.science.org/doi/abs/10.1126/science.1219850.

[122] Norio Okabayashi et al. "Influence of atomic tip structure on the intensity of inelastic tunneling spectroscopy data analyzed by combined scanning tunneling spectroscopy, force microscopy, and density functional theory." In: *Phys. Rev. B* 93 (16 Apr. 2016), p. 165415. DOI: 10.1103/PhysRevB.93.165415. URL: https://link.aps.org/doi/10.1103/PhysRevB.93.165415.

[123] Shigeki Kawai et al. "Direct quantitative measurement of the C=O – H-C bond by atomic force microscopy." In: *Science Advances* 3.5 (2017), e1603258. DOI: 10.1126/sciadv.1603258. eprint: https://www.science.org/doi/pdf/10.1126/sciadv.1603258. URL: https://www.science.org/doi/abs/10.1126/sciadv.1603258.

[124] Julian Berwanger et al. "Lateral manipulation of single iron adatoms by means of combined atomic force and scanning tunneling microscopy using CO-terminated tips." In: *Phys. Rev. B* 98 (19 Nov. 2018), p. 195409. DOI: 10.1103/PhysRevB.98.195409. URL: https://link.aps.org/doi/10.1103/PhysRevB.98.195409.

[125] Fabian Schulz et al. "Elemental Identification by Combining Atomic Force Microscopy and Kelvin Probe Force Microscopy." In: *ACS Nano* 12.6 (2018), pp. 5274–5283. DOI: 10.1021/acsnano.7b08997. eprint: https://doi.org/10.1021/acsnano.7b08997. URL: https://doi.org/10.1021/acsnano.7b08997.

[126] Samuel P. Jarvis et al. "Chemical shielding of H2O and HF encapsulated inside a C60 cage." In: *Communications Chemistry* 4.1 (Sept. 2021), p. 135. ISSN: 2399-3669. DOI: 10.1038/s42004-021-00569-0. URL: https://doi.org/10.1038/s42004-021-00569-0.

[127] Mary M Tai. "A Mathematical Model for the Determination of Total Area Under Glucose Tolerance and Other Metabolic Curves." In: *Diabetes Care* 17.2 (Feb. 1994), pp. 152–154. ISSN: 0149-5992. DOI: 10.2337/diacare.17.2.152. eprint: https://diabetesjournals.org/care/article-pdf/17/2/152/341381/17-2-152.pdf. URL: https://doi.org/10.2337/diacare.17.2.152.

[128] James P. Lewis et al. "Advances and applications in the FIREBALL ab initio tight-binding molecular-dynamics formalism." In: *physica status solidi (b)* 248.9 (2011), pp. 1989–2007. DOI: https://doi.org/10.1002/pssb.201147259. eprint: https://onlinelibrary.wiley.com/doi/pdf/10.1002/pssb.201147259. URL: https://onlinelibrary.wiley.com/doi/abs/10.1002/pssb.201147259.

[129] F. Ortmann, F. Bechstedt, and W. G. Schmidt. "Semiempirical van der Waals correction to the density functional description of solids and molecular structures." In: *Phys. Rev. B* 73 (20 May 2006), p. 205101. DOI: 10.1103/PhysRevB.73.205101. URL: https://link.aps.org/doi/10.1103/PhysRevB.73.205101.

[130] Stefan Grimme. "Accurate description of van der Waals complexes by density functional theory including empirical corrections." In: *Journal of Computational Chemistry* 25.12 (2004), pp. 1463–1473. DOI: https://doi.org/10.1002/jcc.20078. eprint: https://onlinelibrary.wiley.com/doi/pdf/10.1002/jcc.20078. URL: https://onlinelibrary.wiley.com/doi/abs/10.1002/jcc.20078.

[131] Remy Pawlak et al. "Atomic-Scale Mechanical Properties of Orientated C60 Molecules Revealed by Noncontact Atomic Force Microscopy." In: *ACS Nano* 5.8 (2011). PMID: 21736339, pp. 6349–6354. DOI: 10.1021/nn201462g. eprint: https://doi.org/10.1021/nn201462g. URL: https://doi.org/10.1021/nn201462g.

[132] Elena Sartori et al. "Paramagnet Enhanced Nuclear Relaxation of H2 in Organic Solvents and in H2@C60." In: *Journal of the American Chemical Society* 130.7 (2008). PMID: 18217754, pp. 2221–2225. DOI: 10.1021/ja076071g. eprint: https://doi.org/10.1021/ja076071g. URL: https://doi.org/10.1021/ja076071g.

[133] Kei Kurotobi and Yasujiro Murata. "A Single Molecule of Water Encapsulated in Fullerene C60." In: *Science* 333.6042 (2011), pp. 613–616. DOI: 10.1126/science.1206376. eprint: https://www.science.org/doi/pdf/10.1126/science.1206376. URL: https://www.science.org/doi/abs/10.1126/science.1206376.

[134] Yongjun Li et al. "Comparison of Nuclear Spin Relaxation of H2O@C60 and H2@C60 and Their Nitroxide Derivatives." In: *The Journal of Physical Chemistry Letters* 3.9 (2012). PMID: 26288052, pp. 1165–1168. DOI: 10.1021/jz3002794. eprint: https://doi.org/10.1021/jz3002794. URL: https://doi.org/10.1021/jz3002794.

[135] Satoshi Kaneko et al. "Single Molecular Junction Study on H2O@C60: H2O is "Electrostatically Isolated"." In: *ChemPhysChem* 18.10 (2017), pp. 1229–1233. DOI: https://doi.org/10.1002/cphc.201700173. eprint: https://chemistry-europe.onlinelibrary.wiley.com/doi/pdf/10.1002/cphc.201700173. URL: https://chemistry-europe.onlinelibrary.wiley.com/doi/abs/10.1002/cphc.201700173.

[136] Fabian Stilp et al. "Very weak bonds to artificial atoms formed by quantum corrals." In: *Science* 372.6547 (2021), pp. 1196–1200. DOI: 10.1126/science.abe2600. eprint: https://www.science.org/doi/pdf/10.1126/science.abe2600. URL: https://www.science.org/doi/abs/10.1126/science.abe2600.

[137] Jose M Soler et al. "The SIESTA method for ab initio order-N materials simulation." In: *Journal of Physics: Condensed Matter* 14.11 (Mar. 2002), pp. 2745–2779. DOI: 10.1088/0953-8984/14/11/302. URL: https://doi.org/10.1088/0953-8984/14/11/302.

[138] L. A. Girifalco. "Interaction potential for carbon (C60) molecules." In: *The Journal of Physical Chemistry* 95.14 (1991), pp. 5370–5371. DOI: 10.1021/j100167a002. eprint: https://doi.org/10.1021/j100167a002. URL: https://doi.org/10.1021/j100167a002.

[139] Adam Sweetman et al. "Measuring the reactivity of a silicon-terminated probe." In: *Phys. Rev. B* 94 (11 Sept. 2016), p. 115440. DOI: 10.1103/PhysRevB.94.115440. URL: https://link.aps.org/doi/10.1103/PhysRevB.94.115440.

COLOPHON

This document was typeset using `classicthesis` style developed by André Miede. The style was inspired by Robert Bringhurst's seminal book on typography *"The Elements of Typographic Style"*. It is available for LaTeX and LyX at

https://bitbucket.org/amiede/classicthesis/

Happy users of `classicthesis` usually send the author a real postcard; the collection of postcards received so far is featured at

http://postcards.miede.de/

DECLARATION

Put your declaration here.

England, June 2022

Jack Matthew Leslie Henry